Imperial College London

Imperial College of Science, Technology and Medicine

Department of Materials

Aerosol Processing of Halide Perovskites

Sinclair Ryley Ratnasingham

December 2019

Dissertation submitted in partial fulfilment of the requirements for the degree of Doctor of Philosophy in Material Science

ABSTRACT

Organo-metal halide perovskites (OMHPs) research has progressed rapidly, with photovoltaic (PV) devices reaching over 20% efficiency [1]. However, scalable production of these devices is an ongoing challenge. This study demonstrated the ability to grow halide perovskite films via aerosol assisted chemical vapour deposition (AACVD). AACVD is a scalable deposition process and one advantage of this method compared to conventional CVD is the fact that the precursors do not need to be vapourised. This allows for lower operating temperature, less complex equipment, and therefore lower overall cost [2].

In this thesis, Methylammonium lead-triiodide (MAPI) films were deposited by sequentially passing aerosolized precursor solvent solutions into a reactor containing a heated substrate. In this study two different precursor systems were utilized, one based on lead iodide and the other on lead acetate. The first produced thick films, which were characterized extensively using X-ray diffraction, UV-visible spectroscopy, Kelvin probe measurements, ambient photoemission spectroscopy, time of flight measurements and Hall effect measurements. The second system allowed for the deposition of thinner films, more suitable for photovoltaic applications. These films were again extensively characterised but also allowed for the fabrication of the first working OMHP device utilising AACVD.

Furthermore, this study demonstrated an ability to use aerosols as a scalable post-deposition treatment on existing films, modulating the morphology and boosting the performance of conventionally spin-coated films to over 20% PCE. Treatment of films was accomplished by exposing spin-coated films to aerosolised solvents. Using these treatments, it is shown that the morphology of the films can be drastically and controllably improved. This study also reveals improvements in charge carrier lifetimes and a general improvement in most (PV) parameters. This has further led to experimentation with HTL-free devices and thick OMHP layers, with both showing significant improvements after the aerosol treatment.

DECLARATION

The work presented in this PhD thesis was conducted in two institutions. First, between October 2016 and October 2017, in the School of Materials Science and Engineering at Queen Mary University of London. Then, between November 2017 and December 2019 at the Department of Materials at Imperial College London. The research is my own, and contributions from other people and sources have been appropriately cited.

The copyright of this thesis rests with the author and is made available under a Creative Commons Attribution Non-Commercial No Derivatives licence. Researchers are free to copy, distribute or transmit the thesis on the condition that they attribute it, that they do not use it for commercial purposes and that they do not alter, transform or build upon it. For any reuse or redistribution, researchers must make clear to others the licence terms of this work.

ACKNOWLEDGEMENTS

I would like to thank all supervisors who have helped and supervised me throughout my PhD. Firstly, I offer my sincerest gratitude to my late supervisor and friend Dr Russell Binions. He was a true source of inspiration and encouragement, without him I would have never embarked on this adventure. I will forever remember his many words of wisdom and his incredible kindness.

I would like to offer my gratitude to Dr Martyn McLachlan, who made it possible for me to continue my PhD. When all was lost, he welcomed me into his group and supported me throughout my time at Imperial.

I would like to express a special thank you to Dr Joe Briscoe, who went above and beyond to help. He supported me through some of the toughest times and has helped me achieve many of my goals. I will feel forever grateful for his help and support, one could not ask for a better friend and supervisor.

I would also like to thank all the individuals who helped with the experimental setups. Special thank you to Richard Sweeney, Rory Wilson and Theo Kreouzis who really helped me to understand the equipment and went above and beyond with their support.

Thank you to all my friends and colleagues, who helped me immensely throughout the PhD. I would like to give special thanks to Lokeshwari Mohan, who has been a great source of support and for making the lab fun, regardless of circumstance. I would like to thank Szymon Doszczeczko, and Pavel Victoria, who made the last couple of years an unforgettable experience. I would also like to thank Bethany Miall for her support and care during my studies.

Lastly, I would like to thank my parents Kingsley and Shirani Ratnasingham. They have always supported me with all my endeavors, be it by words of encouragement or by delivering 10 kg bags of rice.

PUBLICATIONS AND PRESENTATIONS

JOURNAL PAPERS

S. R. Ratnasingham and R. Binions, “CHAPTER 9. Hybrid Solar Cells,” RSC Advances, 2017, pp. 298–340.

Y. Wang, M. Daboczi, C. A. Mesa, S. R. Ratnasingham, J. S. Kim, J. R. Durrant, S. Dunn, H. Yan, and J. Briscoe, “Bi2Fe4O9 thin films as novel visible-light-active photoanodes for solar water splitting,” J. Mater. Chem. A, vol. 7, no. 16, pp. 9537–9541, Apr. 2019.

D. G. Georgiadou, Y. H. Lin, J. Lim, S. Ratnasingham, M. A. McLachlan, H. J. Snaith, and T. D. Anthopoulos, “High Responsivity and Response Speed Single-Layer Mixed-Cation Lead Mixed-Halide Perovskite Photodetectors Based on Nanogap Electrodes Manufactured on Large-Area Rigid and Flexible Substrates,” Adv. Funct. Mater., vol. 29, no. 28, p. 1901371, Jul. 2019.

T. Liu, S. Y. Yue, S. R. Ratnasingham, T. Degousée, P. R. Varsani, J. Briscoe, M. A. McLachlan, M. Hu, and O. Fenwick, “Unusual thermal boundary resistance in halide perovskites: A way to tune ultralow thermal conductivity for thermoelectrics,” ACS Appl. Mater. Interfaces, p. acsami.9b14174, Nov. 2019.

T. Du, W. Xu, S.Xu, S. Ratnasingham, C. Lin, J. Kim, J. R. Durrant and M. A. McLachlan, "Light-Intensity and Thickness Dependent Efficiency of Planar Perovskite Solar Cells: Charge Recombination versus Extraction" under review

ORAL PRESENTATIONS

S. R. Ratnasingham, R. Binions, J. Briscoe and M. A. McLachlan, “Aerosol Assisted Chemical Vapour Deposition of Methylammonium Lead-Triiodide” Imperial College Centre for Plastic Electronics Symposium, London, September 2018

S. R. Ratnasingham, R. Binions, J. Briscoe and M. A. McLachlan, “Aerosol Assisted Chemical Vapour Deposition of Methylammonium Lead-Triiodide” European Materials Research Society Fall 2018 Meeting, Warsaw, November 2018

POSTER PRESENTATIONS

S. R. Ratnasingham, R. Binions, “Aerosol Assisted Chemical Vapour Deposition of Methylammonium Lead-Triiodide” EuroCVD-Baltic ALD 2017, Linköping, July 2017

S. R. Ratnasingham, R. Binions, J. Briscoe and M. A. McLachlan, “Aerosol Assisted Chemical Vapour Deposition of Methylammonium Lead-Triiodide” Materials Research Society Fall 2017 Meeting, Boston, November 2017

S. R. Ratnasingham, R. Binions, J. Briscoe and M. A. McLachlan, “Aerosol Assisted Chemical Vapour Deposition of Methylammonium Lead-Triiodide” Imperial College Centre for Plastic Electronics Annual Symposium, London, June 2018 (Awarded flash talk prize)

S. R. Ratnasingham, R. Binions, J. Briscoe and M. A. McLachlan, “Aerosol Assisted Chemical Vapour Deposition of Methylammonium Lead-Triiodide” InnoLAE 2019, Cambridge, January 2019

S. R. Ratnasingham, R. Binions, J. Briscoe and M. A. McLachlan, “Aerosol Assisted CVD of MAPI : Time of Flight Mobility” Imperial College Centre for Plastic Electronics Annual Symposium, London, Sep 2019 (Awarded runner up poster prize)

TABLE OF CONTENTS

Abstract 2

Declaration 3

Acknowledgements 4

Publications and Presentations 5

Journal Papers 5

Oral Presentations 5

Poster Presentations 5

Table of Contents 7

List of Figures 14

List of Tables 22

1 Introduction 23

1.1 The Need for Green Energy 23

1.2 The Potential of Solar Energy 24

1.2.1 Challenges in Photovoltaics 25

1.3 Research Aims and Thesis Structure 27

2 Literature Review 28

2.1 Operation of Photovoltaics (PVs) 28

2.1.1 History of the PV Effect 28

2.1.2 Electronic Band Structure 29

2.1.3 The Band Gap 30

2.1.4 Absorption of Light and Generation of charges 31

2.1.5 Built in Potential- Extracting the Charge 33

2.1.6 The J-V Curve 37

2.1.7 Recombination of Charges, Lifetimes and Mobility 39

2.2 Organo Metal Halide Perovskites 41

2.2.1 History of OMHP 41

2.2.2 The Perovskite Structure 42
2.2.2.1 Common phase transitions 44
2.2.3 Optical Properties of OMHP 44
2.2.4 Charge Carriers in OMHP 45
2.2.5 Device Architecture 46
2.2.5.1 Mesoscopic Cell 47
2.2.5.2 Planar Heterojunctions 48
2.2.5.3 Other Architectures 49
2.2.6 Hysteresis 49
2.2.6.1 Influence of architecture and materials 50
2.2.6.2 Origins of hysteresis 51
2.2.7 Stability 52
2.2.7.1 Moisture instability 53
2.2.7.2 Temperature stability 53
2.2.7.3 Light and oxygen induced degradation 54
2.2.7.4 Material incompatibilities 54
2.2.8 Environmental and toxicological concerns of OMHPs 55
2.2.9 Processing of OMHPs 56
2.2.9.1 Spin coating-based techniques 56
2.2.9.2 Solvent annealing of perovskites 57
2.2.9.3 Chemical vapour deposition (CVD) 58
2.2.9.4 OMHPs and Aerosol assisted chemical vapour deposition (AACVD) 59
2.3 Chemical Vapour Deposition 61
2.3.1 Introduction to CVD 61
2.3.2 The CVD Process 61
2.3.2.1 Thin film growth 62
2.3.2.2 Growth Modes 64
2.3.2.3 Precursor Flow 66

2.3.2.4 Variations of CVD 67
2.3.3 Aerosol Assisted CVD (AACVD) 68
2.3.3.1 Aerosols and generation 69
2.3.3.2 Ultrasonic generation of aerosol 69
2.3.3.3 Aerosol flow in the reactor 69
2.3.3.4 AACVD reaction pathways 70
3 Experimental Apparatus & Methods 72
3.1 Reactor Equipment Design 72
3.1.1 Aerosol Generation 72
3.1.2 Reactor Components 74
3.2 AACVD Experimental 78
3.2.1 Operation of Reactor 78
3.2.2 Precursor Solutions 78
3.2.2.1 PbI_2/DMF 78
3.2.2.2 $Pb(Ac)_2 \cdot 3H_2O$/MeOH 78
3.2.2.3 MAI Solution 79
3.2.2.4 MABr Solution 79
3.2.3 AACVD Substrate and Device Preparation 79
3.2.3.1 FTO substrates & preparation 79
3.2.3.2 Mesoporous TiO_2 Electron Transport Layer (ETL) Layer 80
3.2.3.3 Deposition of HTM Materials 80
3.2.3.4 AACVD Substrate Reactor Placement 80
3.2.3.5 Thermal evaporation of Au electrode & final device dimensions 81
3.3 Spin coating and AASA Experimental 82
3.3.1 ITO Substrate Preparation 82
3.3.2 Glass Substrate Preparation 82
3.3.3 HTM Layers 82
3.3.4 PFN Interlayer 82

3.3.5 MAPI Deposition 82
3.3.6 Mixed Composition OMHP 83
3.3.7 Substrate Placement for AASA Spatial Uniformity 83
3.3.8 Grain Size Evaluation 83
3.3.9 Substrate placement for AASA devices 83
3.3.10 BCP Interlayer 84
3.3.11 Cu electrode evaporation and device 84
3.4 Characterisation Techniques 85
3.4.1 XRD 85
3.4.1.1 Room-temperature XRD 85
3.4.1.2 High-temperature XRD 85
3.4.1.3 Crystallite size 86
3.4.1.4 Lattice Parameter 86
3.4.2 UV-Vis absorption spectroscopy 87
3.4.3 SEM 87
3.4.4 Resistivity & Hall measurements 87
3.4.4.1 Ohmic check 88
3.4.4.2 Van der Pauw and Resistivity 88
3.4.4.3 Measuring Hall voltage 88
3.4.4.4 Sample Preparation 89
3.4.5 ToF 89
3.4.5.1 Excitation Source 89
3.4.5.2 Sample preparation and holder placement 89
3.4.5.3 Signal generator and timing 90
3.4.5.4 Oscilloscope and data collection 90
3.4.6 Dektak Measurments 90
3.4.7 Kelvin Probe / APS 90
3.4.8 AFM and SKPFM 91

3.4.9 TEM & EDS Imaging 91
3.4.10 Device Testing 91
3.4.10.1 J-V Measurements 91
3.4.10.2 MPPT Testing 91
3.4.11 Photoluminescence measurements 92
3.4.12 Curve Fitting and data processing 92
3.5 Summary of Contributions 93
4 Results: AACVD of thick perovskite films 94
4.1 Introduction 94
4.2 2-Step Method and Film Formation 94
4.2.1 1st Step: Growth of PbI_2 film 95
4.2.2 2nd Step: Conversion to MAPI 95
4.2.3 Future Work 100
4.2.4 Film formation summary 100
4.3 XRD studies of AACVD MAPI 101
4.3.1 Peak splitting and texture 101
4.3.1.1 Lattice parameters 103
4.3.2 Thermal XRD studies 104
4.3.2.1 AACVD Phase transition 106
4.3.2.2 Determination of thermal expansion 106
4.3.3 Isothermal XRD studies 109
4.3.4 Future work and improvements 115
4.3.5 XRD study summary 116
4.4 Optoelectronic and Electronic Measurements 116
4.4.1 Time of Flight measurements 116
4.4.1.1 Development of the ToF technique for OMHPs 118
4.4.1.2 Pulse ToF measurements 121
4.4.1.3 ToF future work 125

4.4.1.4 ToF Summary 126
4.4.2 Hall and Electrical Measurments 126
4.4.2.1 Comparison to ToF measurements 128
4.4.2.2 Future Work 129
4.4.2.3 Hall and Electronic Summary 129
4.4.3 Determining the Energy Levels: Kelvin probe, APS and optical band gap 129
4.4.3.1 Kelvin Probe and APS results 129
4.4.3.2 Summary 130
4.5 Applications of Thick AACVD Films 131
4.5.1 Thermal conductivity of AACVD MAPI films 131
4.5.2 Alpha radiation absorption 131
4.6 Chapter 3 Summary 133
5 AACVD Lead Acetate 134
5.1 Introduction 134
5.2 Lead Acetate as a Precursor 134
5.3 Development of the Lead Acetate 2-Step AACVD 134
5.3.1 Determining the deposition parameters 135
5.3.2 Deposition of mesoporous TiO_2 138
5.4 Material characterisation 140
5.5 PV Devices 143
5.5.1 Comparison to spin-coated films 146
5.5.2 Film formation 148
5.6 Methyl Ammonium Lead Bromide 151
5.7 Future work 154
5.8 Chapter 5 Summary 154
6 Aerosol Assisted Solvent Annealing (AASA) 155
6.1 Introduction 155
6.2 Solvent Annealing of Perovskites 155

6.3 Developing The AASA 155
6.4 AASA Devices and Optoelectronic Properties 160
6.4.1 Elucidating the performance increase 161
6.4.2 Future work 163
6.5 Scalability of AASA 165
6.5.1 Uniformity over large areas 165
6.5.2 Large area devices 168
6.5.3 Future Work 170
6.6 Enabling thicker films 170
6.6.1 Future work 174
6.7 AASA Effect on stability 175
6.7.1 Ambient stability via XRD 175
6.7.2 Long-Term Device Stability 176
6.7.3 Future Work 177
6.8 Applicability to Different Architectures and Compositions 179
6.8.1 HTM Free 179
6.8.2 AASA with mixed composition OMHP 180
6.8.3 Future work 180
7 Summary, Conclusions and Research Outcomes 182
7.1 Background and Aims 182
7.2 Research outcomes 182
7.2.1 Chapter 3 182
7.2.2 Chapter 4 183
7.2.3 Chapter 5 184
7.3 Conclusion 187
8 References 188
9 Appendix 209

LIST OF FIGURES

Figure 1-1 World's energy demand measured in TWh, from 1800-2017. Adapted from Hannah Ritchie and Max Roser (2019) - "Energy Production & Changing Energy Sources" [3] 23

Figure 1-2 Map shows the spatially resolved solar irradiance across the globe. Data was collected from the International Satellite Cloud Climatology Project (ISCCP). Adapted from Matthias Loster (2010) [9] 24

Figure 2-1 a) Schematic of Becquerel's 1839 experiment. b) Schematic of Adams' and Day's 1876 experiment. Adapted from M.A. Green (2002) - "Photovoltaics: coming of age" 28

Figure 2-2 Diagram illustrating band structure of metals, semiconductors and insulators. Adapted from Wikimedia [23] 29

Figure 2-3 Sketch illustrating direct and indirect band alignments 31

Figure 2-4 Graph showing absorption coefficient, α, vs incident light wavelength in a variety of semiconductor. Adapted from pveducation.org[28] 32

Figure 2-5 Calculated maximum efficiency vs E_g using the Shockley Queisser model. Solar radiation is approximated as a 6000 K blackbody spectrum. 33

Figure 2-6 Diagram illustrating the effect of p-type and n-type dopants. Adapted from Hyperphysics [33] 34

Figure 2-7 Diagram of p–n junction in thermal equilibrium with zero applied bias. Under the junction, plots for the charge density, electric field, and the voltage. Adapted from Wikimedia [34] 35

Figure 2-8 Schematic of p-i-n junction with zero applied bias. Adapted from Yoshida (2012) - Nanoscale probing of transient carrier dynamics modulated in a GaAs–PIN junction by laser-combined scanning tunnelling microscopy 36

Figure 2-9 J-V behaviour of a non-ideal solar cell in the dark and under illumination. Short-circuit current, J_{sc} , is shown at V = 0 and open-circuit voltage ,V_{oc}, is shown at J = 0. Maximum power density, P_m is shown at the intercepts of J_m and V_m. FF is the ratio between the product of J_{sc} and V_{oc}. 38

Figure 2-10 Effect of parasitic resistances on J-V curve. a) increasing series resistance R_s b) and increasing shunt resistance R_{sh}. The FF is severely affected by both resistances, leading to lower power output. 39

Figure 2-11 Carrier recombination mechanisms in semiconductors [36] 40

Figure 2-12 Crystal structure of methyl ammonium lead tri-iodide (MAPI) 42

Figure 2-13 Structural phase transformations for commonly found within OMHP. Adapted and modified from Chen et al. (2015) [49] 44

Figure 2-14 Band edge positions of various organometal-halide perovskites. The bandgap values are: $MAPbBr_3$ 2.3 eV $MAPbI_3$ 1.5 eV, $FAPbI_3$ 1.5 eV, $MASnI_3$ 1.1 eV. Adapted from Chen et al. (2015 [49] 45

Figure 2-15 Schematic diagrams of common OMHP device architectures. Adapted from Jena et al. [55] 47

Figure 2-16 Example of OMHP hysteresis effect on J-V curve 50

Figure 2-17 Schematic showing the effect of ion migration in p-i-n junction. Adapted from Eames et al. [119] 52

Figure 2-18 Schematic of on-step and two-step spin coating techniques. Adapted from Chen et al. (2015) [49] 56

Figure 2-19 schematic illustration of the CVD steps during deposition [182] 62

Figure 2-20 Dependence of the cluster free energy, ΔG, on the cluster radius, r. The curve illustrates the maximum free energy at the critical cluster size, r_c. 63

Figure 2-21 Schematic showing thin film growth in surface rate reaction limited and mass transport limited systems 64

Figure 2-22 Schematic of different thin-film growth modes 65

Figure 2-23 Development of boundary layer over a flat. Adapted from Flanker (2008) [187] 67

Figure 2-24 Diagram illustrating aerosol reaction pathways with varying temperature and varying drop size. Adapted from Filipovic 2012 [193] 70

Figure 3-1 Schematic of AACVD setup 72

Figure 3-2 a) Schematic of misting bottle b) Photograph of misting bottle 73

Figure 3-3 CAD model of inlet baffle. a) shows complete baffle b) exploded view revealing three main components. c) cutaway view revealing baffle cavities 74

Figure 3-4 a) CAD model of the complete reactor with the baffle mounted b) exploded view of reactor components c)Photograph of assembled reactor with a Quartz tube. 75

Figure 3-5 CFD simulation of nitrogen flow within the AACVD Reactor. a) Simulation run at 0.5 L min^{-1} b) Simulation run at 0.3 L min^{-1} c) £D visualisation of nitrogen flow 77

Figure 3-6 Schematic of FTO substrate used to make AACVD devices 79

Figure 3-7 CFD simulation with grey rectangle indicating substrate position within the reactor 80

Figure 3-8 Schematic of thermally evaporated electrodes 81

Figure 3-9 Schematic of electrode patterns used within AASA devices. a) Schematic of 4 pixel device b) Schematic of large area device 84

Figure 3-10 Schematic of contact placement used for Hall and electrical measurements 87

Figure 4-1 Schematic showing the 2-Step AACVD process 94

Figure 4-2 SEM images of the PbI_2 film deposited during the first step of the AACVD process for reaction durations shown on images. 95

Figure 4-3 Photograph of samples taken at different points of the 2nd step reaction 95

Figure 4-4 Cross-sectional SEM images of the PbI_2 film being converted to MAPI during the second step of the reaction. 96

Figure 4-5 Schematic of the PbI2 to MAPI conversion process 96

Figure 4-6 XRD patterns of substrates taken during the 2nd step AACVD conversion process. Right: Full XRD patterns Left: focusing on PbI_2 100 and MAPI 110 peak. 98

Figure 4-7 a) Absorption spectra of samples removed at different times. b) Tauc plots calculated for direct band gap 99

Figure 4-8 XRD patterns of AACVD, Spin coated and tetragonal reference MAPI 250735-ICSD [132] 101

Figure 4-9 SEM images of (a) spin coated and (b) AACVD films of MAPI 102

Figure 4-10 a) Relative intensity of peaks compared to MAPI reference pattern 250735-ICSD [201]. b) Illustration showing common diffraction planes in relation to perovskite crystal. 103

Figure 4-11 XRD data taken at different temperatures. Tetragonal indices are denoted by the diamond, with major cubic peaks indexed at higher temperatures 105

Figure 4-12 MAPI phase change from tetragonal to cubic upon heating 106

Figure 4-13 Results from AACVD film a) Volume of lattice plotted against temperature. b) Plot focusing on the point of phase change. 108

Figure 4-14 XRD patterns of samples before and after the thermal sweep experiment conducted in section 4.3.2. Figure 4-11 shows the full results of the sweep. 110

Figure 4-15 Isothermal XRD patterns overlaid to show the evolution of the 001 PbI_2 peak in spin-coated MAPI (a) and AACVD MAPI (b). Measurements taken at 150 °C for 93 minutes 111

Figure 4-16 AACVD Isothermal XRD patterns taken from AACVD sample over 93 minutes. Insert shows small peak evolution due to PbI_2 formation. 112

Figure 4-17 Graph showing volume fraction of (001) PbI_2 peak vs (001) MAPI over time for AACVD (a) and spin coated film (b). Below is the $\ln(tx_2\text{-}tx_1)$ vs. 1/RT plots. The gradient of the fitted line gives the activation energy 113

Figure 4-18 Schematic of AACVD ToF sample (a). (b) shows bias applied to FTO to collect holes and (c) shows the collection of electrons by applying the bias to gold. 117

Figure 4-19 Graphical representation of time of flight signal as measured by the oscilloscope. Insert shows determination of arrival time by utilising a double logarithmic plot and the intersection of two tangents. 118

Figure 4-20 Photocurrent transients measured on sample with constant applied bias 118

Figure 4-21 Schematic of ion migration screening with increasing electric field within the ToF sample 120

Figure 4-22 Schematic of voltage pulse timing in relation to photocurrent signal 121

Figure 4-23 Photocurrent transients measured at different pulse delays 122

Figure 4-24 Log-log plots of sample tested with 50 µs and 1000 µs pulse delays. a) Electron signal with a bias pulse time of 1000 µs. b) Electron signal with a bias pulse time of 50 µs. c) Hole signal with a bias pulse time of 1000 µs .d) Hole signal with a bias pulse time of 50 µs. 123

Figure 4-25 Poole-Frenkel of data gathered from ToF measurements. a) 124

Figure 4-26 Poole-Frenkel plot showing combined extracted mobility values of Hall and ToF measurements 128

Figure 4-27 a) Ambient photoemission spectroscopy measurement of AACVD MAPI film. b) Energy level diagram of AACVD MAPI film. Valence band derived from APS measurements, Fermi level from Kelvin probe measurements and conduction band is calculated from the optical band gap 130

Figure 4-28 Thermal conductivity measurements of evaporated (a) and AACVD MAPI (b) [238] 131

Figure 4-29 Average measured ΔI upon exposure to α-radiation, averaged over 16 measurements. 132

Figure 5-1 Chemical formula of lead acetate tri-hydrate ($(Pb(Ac)_2 \cdot 3H_2O)$) 134

Figure 5-2 Schematic showing the 2-Step AACVD process using lead acetate ($Pb(Ac)_2 \cdot 3H_2O$) 135

Figure 5-3 SEM images of films deposited at different first step temperatures using lead acetate $Pb(Ac)_2 \cdot 3H_2O$ a) 100°C, b) 125°C, c) 150°C, d) 175°C, e) 200°C and f) 230°C 136

Figure 5-4 SEM images of films converted at different second step temperatures using lead acetate $Pb(Ac)_2 \cdot 3H_2O$ deposited at 175 °C. a) 220 °C b) 230 °C and 240 °C 137

Figure 5-5 SEM images of films converted at different first step flow rates and concentrations of $Pb(Ac)_2 \cdot 3H_2O$ in MeOH. a) Concentration of 0.066 M with a flow rate of 0.5 l min^{-1}. b) Concentration of 0.198 M a flow rate of 0.5 l $min^{-1.}$ c) Flow rate of 0.25 L min^{-1} with a concentration of 0.33 M d) Flow rate of 1 L min^{-1} with a concentration of 0.33 M 138

Figure 5-6 MAPI film deposited using lead acetate method on mesoporous TiO2 ETL 139

Figure 5-7 XRD patterns of AACVD MAPI and tetragonal MAPI reference pattern [132] 140

Figure 5-8 Relative intensity of peaks compared to MAPI reference pattern [201] 141

Figure 5-9 a) Absorption spectra of AACVD MAPI film deposited from $Pb(Ac)_2 \cdot 3H_2O$. Inset shows Tauc Plot b) Energy band diagram of deposited perovskite. Values were determined by absorption, APS and Kelvin Probe measurements 142

Figure 5-10 a) SEM Cross-section of a cell utilising AACVD MAPI film, with false colouring showing the TCO, ETL active layer and Au electrode. b) Schematic of the cell. c) J-V curve of champion device utilising Spiro-OMeTAD. d) Inset show box plots of data from 12 working cells, measured in a reverse J-V scan 143

Figure 5-11 a) SEM Cross-section of a cell utilising AACVD MAPI film, with false colouring showing the TCO, ETL active layer and Au electrode. b) Schematic of the cell. c) J-V curve of champion device utilising spray-coated CuSCN. d) Inset show box plots of data from 12 working cells, measured in a reverse J-V scan 144

Figure 5-12 J-V curve of champion spin coated device utilising spin- coated spiro-OMeTAD. Inset show box plots of data from 6 working cells, measured in a reverse J-V scan. 146

Figure 5-13 a) J-V curve of champion spin coated device utilising spray-coated CuSCN. Inset show box plots of data from 6 working cells, measured in a reverse J-V scan. b) J-V curve of champion spin

coated device utilising spin- coated CuSCN. Inset show box plots of data from 6 working cells, measured in a reverse J-V scan. 147

Figure 5-14 Photographs of three films removed at different stages of the AACVD deposition. Left: Film after first step. Center: Film halfway through MAI aerosol exposure. Right: Completed MAPI film 148

Figure 5-15 a) XRD patterns correspond to initial lead acetate (PbAc) film, lead iodide intermediary and final methylammonium lead triiodide (MAPI) film b) Tauc plots of film extracted from absorption data 148

Figure 5-16 SEM images of three films removed at different stages of the AACVD deposition. a) Film after first step. b) Film halfway through MAI aerosol exposure. c) Completed MAPI film. 149

Figure 5-17 Schematic illustrating the growth and conversion of the AACVD MAPI film 149

Figure 5-18 Schematic showing the 2-Step AACVD process using lead acetate ($Pb(Ac)_2{\cdot}3H_2O$) and methylammonium bromide 151

Figure 5-19 a) Photograph of resulting MAPbBr film. b) top down SEM image of film and c) cross-section of film. 151

Figure 5-20 XRD patterns of AACVD MAPI and AACVD MAPBr both deposited using led acetate ($Pb(Ac)_2{\cdot}3H_2O$) as the Pb(II) source. Reference pattern ICSD 1446529 152

Figure 5-21 a) Absorption spectra of AACVD MAPBr film deposited from $Pb(Ac)_2{\cdot}3H_2O$. b) Tauc Plot indicating band gap of 2.28 eV 153

Figure 6-1 SEM images of spin coated MAPI films treated with the AASA method. Corresponding cross sections are below each image. a) Untreated control film b) Film treated with 0.1 L min^{-1} c) 0.5 L $min^{-1}$and d) 1 L min^{-1} 156

Figure 6-2 XRD pattern centred around (110) reflection of films treated by AASA with varying aerosol flow rates. 157

Figure 6-3 Radar diagram showing relative peak intensities of films treated with different aerosol flow rates. Only the 0.5l min^{-1}shows a significant difference. 158

Figure 6-4 a) J-V curve of champion treated and untreated champion cells. b) PCE distribution of 24 treated and untreated cells c) Schematic of cell architecture used 160

Figure 6-5 a) Cross-sectional scanning transmission electron microscopy (STEM) images (top row) of complete solar cells, scale bar corresponds to 500 nm. Energy dispersive x-ray spectroscopy (EDS) mapping of the of I/Pb (center row) and Pb/N (bottom row) molar ratio, colour scale bar

corresponds to elemental molar ratio from high (red) to low (blue). b) and c) Histogram of pixels of varied elemental molar ratio. 161

Figure 6-6 Electronic and optoelectronic characterization of untreated perovskite film and AASA treated perovskite film. a) the surface contact potential difference. b) steady-state PL emission spectra of perovskite, HTL/perovskite and perovskite/ETL. c) PL decay dynamics. d) and e) schematic drawing of HTL/perovskite band bending. 162

Figure 6-7 Poole-Frenkel plot of ToF measurements conducted on AASA treated and untreated MAPI films deposited by AACVD. Films were deposited using the method detailed in chapter 4, with the treated films using the 5 minute protocol detailed in this chapter. 164

Figure 6-8 Schematic illustrating petri-dish solvent annealing and the AASA process 165

Figure 6-9 Heatmap showing the average grain size of MAPI films on glass substrates. a) Shows the distribution of grain sizes after the AASA treatment. b) Grain sizes of centre slice of the AASA sample c) Grain size distribution in petri-dish solvent annealed sample 166

Figure 6-10 Box plots of average grain size collected from untreated and treated MAPI films spin-coated on glass 167

Figure 6-11 a) Photograph of device arrangement used to test spatial uniformity. b) Box plot showing PCE distribution of treated devices. c) J-V curves of devices treated by AASA at different reactor positions. d) J-V curves of devices treated by petri dish solvent anneal at different reactor positions. 168

Figure 6-12 a) J-V curves of two-pixel substrates, showing results for AASA treated and untreated films. b) PCE values of devices plotted against area. 169

Figure 6-13 SEM images of thick MAPI films treated with AASA. a) 900 nm film control left and treated right with corresponding cross sections below. b) 1300 nm film control left and treated right with corresponding cross sections below. 171

Figure 6-14 XRD diffractograms of treated and untreated film focusing on the (110) reflection. a) Results for 900 nm film before and after treatment. b) Results of 1300 nm film 172

Figure 6-15 J-V curves of champion devices fabricated from AASA treated and untreated thick perovskite films. Below each curve are the PCE distribution of fabricated cells 174

Figure 6-16 a) Photographs of AASA treated and untreated MAPI films after 48 hours of exposure to ambient air. b) XRD patterns of aged films 175

Figure 6-17 MPP tracking results of AASA treated and untreated devices measured in a) ambient and b) N_2 atmospheres 176

Figure 6-18 a) J-V curves of HTM free devices treated with AASA and untreated. b) Schematic of HTM free device 179

Figure 6-19 Champion J-V curves of AASA treated and untreated devices utilising mixed composition OMHP's. a) J-V curve of film utilsing $Cs_{15}FAPb(I_{0.95}Br_{0.05})_3$. a) J-V curve of film utilsing $MAPb(I_{0.82}Br_{0.12})_3$. a) J-V curve of film utilsing $Cs_{0.15}FA_{0.85}Pb(I_{0.9}Br_{0.1})_3$. 180

Figure 9-1 spin-coated MAPI Isothermal XRD patterns taken from AACVD sample over 93 minutes209

Figure 9-2 ToF table of results, showing arrival times and calculated mobilities of AACVD MAPI film. The film thickness was 6.72 $\pm$ 0.76 µm 210

Figure 9-3 ToF signal before and after pulsing experiments. This shows that the sample did not degrade after the application of a pulsed bias. 211

Figure 9-4 Ohmic check results conducted for Hall measurements. 212

Figure 9-5 Example of neglibile hysteresis within p-i-n cell used in AASA experiments. 213

Figure 9-6 Energy dispersive x-ray spectroscopy (EDS) mapping of the destruction of a) C at%, b) N at% c) I/Pb Ratio d) Pb at%. 214

Figure 9-7 Grain size distribution of untreated MAPI spin coated on glass 215

Figure 9-8 Box-plots of cell parameters of AASA and Petri-dish solvent annealed devices 215

Figure 9-9 Box-plots showing the distribution of cell parameters for AASA treated and untreated thick MAPI devices 216

LIST OF TABLES

Table 2-1 Showing commonly used radii of ions. A-cation are coloured black, B cations are coloured blue and the X anion is green. Table adapted from Chen et al. (2015) [49] 43

Table 2-2 Highest efficiencies reported in publications. Parameters were taken from the reverse scan of the champion device of each study. 47

Table 2-3 Summary of studies utilising AACVD to deposit OMHPs 60

Table 4-1 Deposition parameters used to deposit AACVD MAPI films 94

Table 4-2 Summary of FWHM and crystallite size calculated using Sherer equation. All values were calculated from 110 peaks. 99

Table 4-3 Comparison of lattice parameters between AACVD and spin coated films 103

Table 4-4 Linear thermal expansion coefficients of AACVD film in tetragonal and cubic phase 107

Table 4-5 Volumetric thermal expansion coefficients of AACVD film in tetragonal and cubic phase 108

Table 4-6 Calculated activation energies of degradation for AACVD film and spin coated film 114

Table 4-7 Summary of data collected by Van der Pauw and Hall measurements 126

Table 4-8 Summary of AACVD MAPI film properties measured in Chapter 3. Conduction band, Valence band and Fermi Level values are relative to vacuum level. 133

Table 5-1 Experimental conditions used for the determination of the first step deposition temperature. Notes describe the resulting film. 135

Table 5-2 Calculated lattice parameters of MAPI films deposited using PbI2 and Pb(Ac)2·3H2O 141

Table 5-3 Calculated lattice parameters of AACVD MAPbBr film 152

Table 6-1 FWHM and Crystallite sizes of films treated with varying aerosol flow rates 158

Table 6-2 Lattice parameters calculated from XRD patterns of films treated at different aerosol flow rates 159

Table 6-3 Two-pixel device parameters for AASA treated and untreated films 169

Table 6-4 Lattice parameters for AASA treated and untreated thick perovskite films 173

1 INTRODUCTION

1.1 THE NEED FOR GREEN ENERGY

Over the last 200 years, human energy consumption has risen incredibly rapidly (Figure 1-1). In the early 1800s, before the advent of the industrial revolution, humanity consumed approximately 5.6 PWh (PWh = 10^{15} Wh) per year, but by 2017 this figure was over 150 PWh[3]. This rapid growth in energy usage began during the industrialisation of the western hemisphere in the late 1800s, driven by both an increase in population and per capita increase in energy demand. This is now being further accelerated by the industrialisation of developing economies and even greater energy demands of modern technology. Unfortunately, to date this increasing demand has been met by larger extraction and consumption of fossil fuels. The resulting emissions have had adverse effects on earth's climate and environment, making it imperative that alternative green sources of energy can be found.

Numerous potential green sources of energy have been extensively investigated. At present, technologies harnessing wind, hydrothermal and solar energy make up the bulk of green energy production. However, they still only form a miniscule fraction of total energy production[4] and more investment and research is required to scale up these technologies.

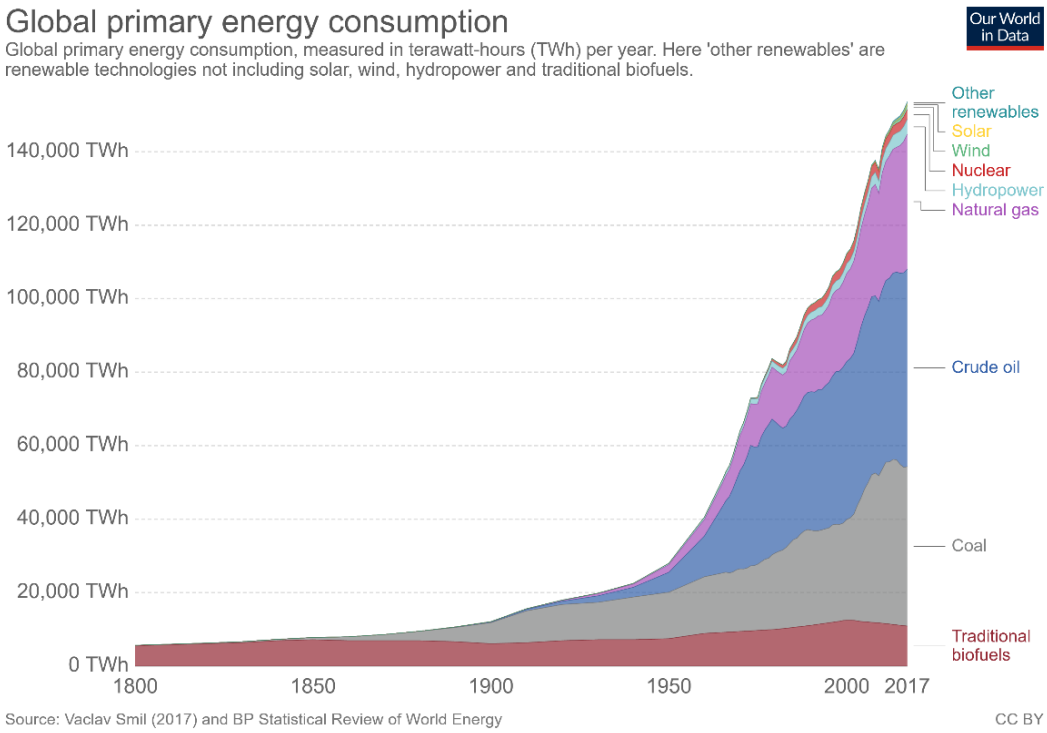


Figure 1-1 World's energy demand measured in TWh, from 1800-2017. Adapted from Hannah Ritchie and Max Roser (2019) - "Energy Production & Changing Energy Sources" [3]

1.2 The Potential of Solar Energy

One of the most promising and abundant renewable energy sources is sunlight. During the course of a year the earth is subjected to over 5 YJ (YJ= 10^{24} J) of solar irradiation, half of which is absorbed or reflected in the atmosphere, leaving 2.7 YJ at the earth's surface[5]. This translates to over 735,000 PWh, or in other terms nearly 5000 times more than the annual global energy demand. Though the potential energy available is large, there are several limiting factors when considering the practicalities of harvesting it.

The intensity of the solar radiation varies greatly; factors such as latitude, season and weather conditions can have dramatic effects. In terms of latitude, areas near the equator can experience the highest levels of approximately 1000W/m^2, which decrease as one approaches the poles of the planet. The global average solar radiation intensity is estimated to be only 184 W/m^2 [6] (Figure 1-2). Furthermore, the local climate can adversely affect the amount of radiation. Areas that regularly have inclement weather will have solar radiation blocked by cloud cover; this reflection of radiation is also known as the cloud albedo [7]. The cloud albedo can reduce the amount of irradiation by up to 80% [8] , and greatly increases the difficulty in harvesting solar power. However, even with all of these potential obstacles, the sheer magnitude of available energy still makes solar energy a worthy endeavour.

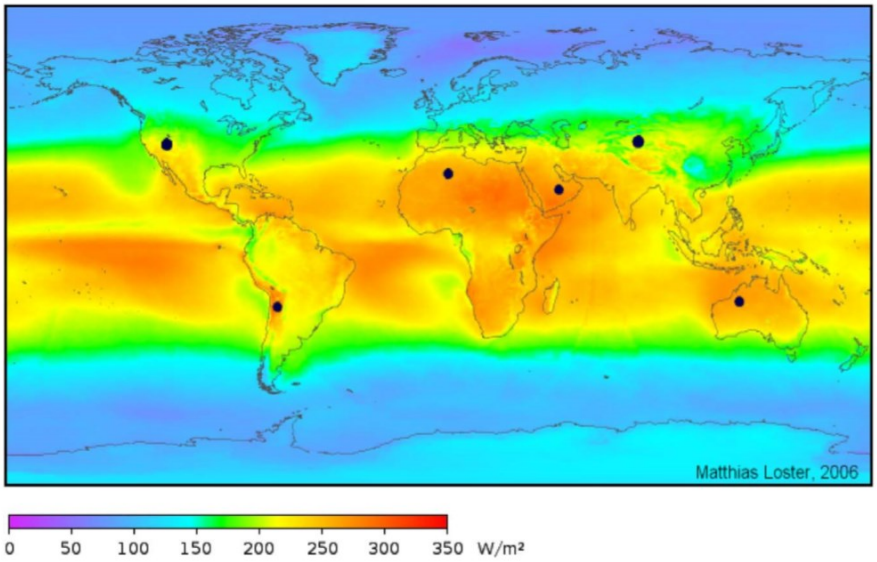


Figure 1-2 Map shows the spatially resolved solar irradiance across the globe. Data was collected from the International Satellite Cloud Climatology Project (ISCCP). Adapted from Matthias Loster (2010) [9]

Currently, there are multiple technologies which can be used to generate power using solar energy. These can be split into two distinct groups: solar thermal and solar PVs . Solar thermal technologies utilise the heat produced by the sun's irradiance. For instance, orientating a building in such a way to maximise solar heating and regulate the internal temperature would be one of the simplest

applications. Generally, solar thermal technologies are used to reduce heating requirements and therefore reduce other energy usage, however, there are technologies which utilise this effect to actively generate power. Central receiver systems (CRS) are an example of this; they use an array of mirrors that concentrate the solar radiation onto a receiver. The receiver contains a liquid, which then becomes heated and vaporises and is used to drive a turbine.[10] Whilst this technology has already been deployed on a large scale, such as in the solar energy generating system (SEGS) solar complex in California, it suffers from a number of drawbacks. These systems require large areas to concentrate enough light and require very intense solar radiation. In comparison to photovoltaics (PV) which convert radiation directly into power, require far less space, have no moving parts and can operate at lower light intensities.

1.2.1 Challenges in Photovoltaics

PV are the dominant solar energy conversion technology, and prices have dropped rapidly since their commercial introduction in the 1970s. In 1977 the average $/W of power generated from silicon (Si) solar cells was $76.67, which by 2012 had dropped to $0.70 [11]. This rapid decrease follows the common model of the learning curve effect, where the cost of a technology reduces as both economy of scale increases and technology advances. This has been partially helped by the semiconductor industry also relying on this material, meaning large investments could be made into producing silicon. As of 2019, solar energy contributes 585 TWh to global energy production, with China alone contributing 177 TWh. Europe in comparison produces 138 TWh with Germany contributing more than a third [4]. Compared to 2018 values, solar energy production has increased by 28.9% and by 2050 is predicted to account for over 20% of the world's energy production[4,12].

Currently, over 90% of this capacity is produced using silicon wafer PV technologies[13]. This is a 1st generation PV technology and over the years has reached solar energy conversion efficiencies over 26%[1]. Whilst this technology has been relatively successful, there is little room left for improvement and the technology is generally considered quite mature.

Several alternative PV technologies have been explored. 2nd generation PV technologies such as thin film solar cells based on CdTe or $CuIn_{1-x}Ga_xSe_2$ (CIGS) offered, as the name implied, thinner and lighter solar cells. Currently, CIGS solar cells hold the record for 2nd generation PVs with an efficiency of 23.4% [1], making them comparable to silicon based PVs. Furthermore, they could be made flexible, potentially allowing them to be used in new applications. The major drawback of this technology was the reliance on expensive and quite toxic elements. To date these types of PVs make up a small proportion of total installed capacity, and over the last couple of years have lost ground to Si based technologies [13]. There are many third generation, also known as emerging, PV technologies currently in development. Dye

sensitised solar cells (DSSCs) use wide bandgap semiconductors, such as TiO_2, coated with organic dyes that absorb sunlight. This technology is neither costly nor toxic and can be readily processed on flexible substrates. However, the major limitation comes from the low efficiencies that this type of cell can achieve. Currently the record efficiency is 14%, far lower than that of silicon or second-generation offerings[14]. Organic photovoltaics are another low-cost emerging technology. These cells are based on various mixtures of organic small molecules and polymers, and again can be manufactured on flexible substrates. With recent advancement, they have achieved a record efficiency of 16.5%[1], making them somewhat more competitive. One of the most promising emerging solar cell technologies are perovskite solar cells, based around organo-metal halide perovskites (OMHP) materials. Perovskite cells are almost matching silicon with efficiencies exceeding 25%[1], achieving this efficiency in only a decade of development. They are relatively low cost and manufactured using abundant, albeit toxic materials. Moreover, this technology has been used to augment existing PV technologies; using a perovskite cell layer on a silicon PV has achieved 28% efficiency, potentially demonstrating an easier route to large scale manufacture by using existing infrastructure [1,15].

One of the main hurdles of any new technology is the scaling up of production and deployment. This is especially true for all the emerging PV technologies. For the gargantuan energy requirement of the world to be fulfilled, production of PVs must take place at incredibly large scales. As perovskites are poised to be one of the main contenders in future PV technologies, a large amount of research and development has taken place on how to realise scalable production. Many of the champion efficiencies quoted use laboratory-scale devices that utilise non-scalable manufacturing techniques, with large-scale devices yet to hit these efficiencies[15]. When comparing this to silicon, the record cell has an area of 79 cm^2, whereas a typical champion perovskite device is likely less than 1 cm^2 [13]. To date, a number of different processes have been developed to deposit perovskite, from inkjet printing to evaporation-based processes, all of which offer a promising pathway to scalable production [16]. This is an area that still requires a large amount of work if perovskites are to become a contender in the competitive solar cell sector. This thesis aims to contribute to this area of research, by investigating the use of aerosols to scalable manufacture and improve perovskite solar cells.

1.3 Research Aims and Thesis Structure

The main aim of this study was to develop scalable routes to OMHP production via the use of aerosol assisted chemical vapour deposition (AACVD) and general aerosol treatments.

The three main areas of study are:

1. Utilising an existing AACVD method to produce thick perovskite films and study their growth and measure key intrinsic material properties.
2. Improving the AACVD method via the use of a novel precursor solvent system and employing it to produce the first working photovoltaic devices using this deposition technique.
3. Using aerosols to treat and modify spin-coated OMHP films to significantly improve photovoltaic performance.

2 LITERATURE REVIEW

2.1 OPERATION OF PHOTOVOLTAICS (PVS)

This section will cover the basic operations of photovoltaic cells as to better understand the detailed concepts behind OMHP PV technology. Photovoltaic cells are one of the most attractive technologies for renewable energy generation. During use PVs produce no emissions, require no moving parts and directly convert sunlight into electricity. To do this they rely on the chemical and electronic properties of the semiconducting materials they are made from.

2.1.1 History of the PV Effect

The PV effect was first demonstrated by Edmond Becquerel in 1839 [17]. In his experiment, silver chloride coated platinum electrodes were placed in an acidic solution and illuminated. He then observed a potential and a small measurable current forming between the electrodes. The same phenomenon was later observed in a solid; in 1876, Adams and Day saw the same effect occur in a bar of selenium under illumination [18] (Figure 2-1). Inventor Charles Fritts then created the first solar cells utilising selenium in 1883.

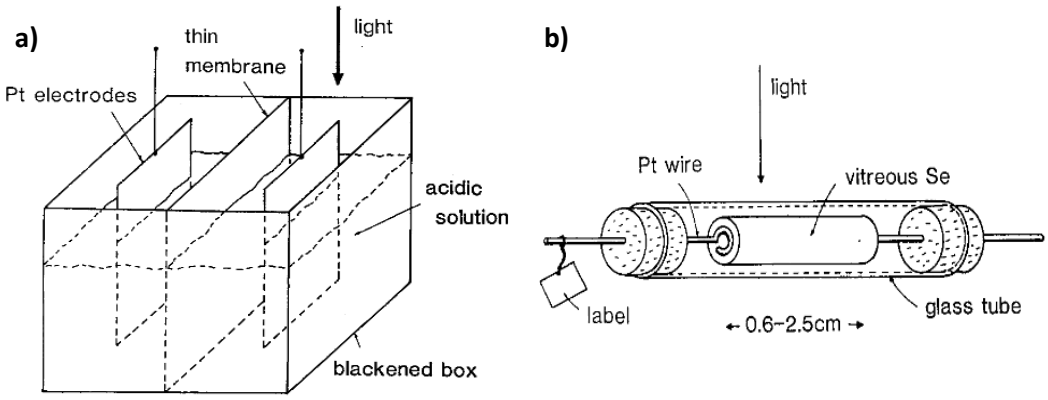


Figure 2-1 a) Schematic of Becquerel's 1839 experiment. b) Schematic of Adams' and Day's 1876 experiment. Adapted from M.A. Green (2002) - "Photovoltaics: coming of age"

A more thorough understanding of this effect was described by Einstein in his 1905 description of the photoelectric effect [19]. His theory stated that if these photons had an energy value above a certain threshold, nowadays known as the work function, they could excite electrons in a metal causing them to be ejected. This was later proven experimentally by R. A. Millikan [20]. This is the cause of the current first observed by Becquerel 65 years before.

The next leap in harnessing this effect came in 1954 from Chapin, Fuller and Pearson's work at Bell Labs [21]. Here they utilised the newly discovered silicon p-n junction to form the first silicon PV, a technology that forms the basis of many modern photovoltaic systems.

2.1.2 Electronic Band Structure

The operation of a modern PV device requires several concepts to be understood. One of the key underlying principles is the formation of the electronic structure of a material and how this structure determines its optical and electronic attributes. In a single atom, electrons occupy atomic orbitals that each have their individual energy level. As atoms are joined to form molecules, these orbitals begin to overlap and form molecular orbitals (MO). These MO consist of lower energy bonding orbitals and a higher energy anti-bonding orbitals.

The Pauli exclusion principle dictates that no two electrons can have the same quantum number. This has the implication that when atoms combine and form molecular orbitals, each of these orbitals will have a slightly different energy level. In a bulk material where there are a vast number of atoms joined together, the orbitals split into many molecular orbitals, however as the number of orbitals is very large the distance between them becomes incredibly small. Therefore, a continuous band of energy is formed [22].

The width of the bands depends on the overlap of the atomic orbitals they originate from. Outer orbitals of atoms overlap heavily with neighbouring outer orbitals of other atoms and therefore have a wider band with more energy states, whereas core orbitals overlap less heavily with neighbouring orbitals and therefore have a narrower band. Due to the finite widths of the bands, certain regions of energy may not be covered leading to what are known as forbidden bands. In a solid there are an infinite number of allowed and forbidden energy bands [22].

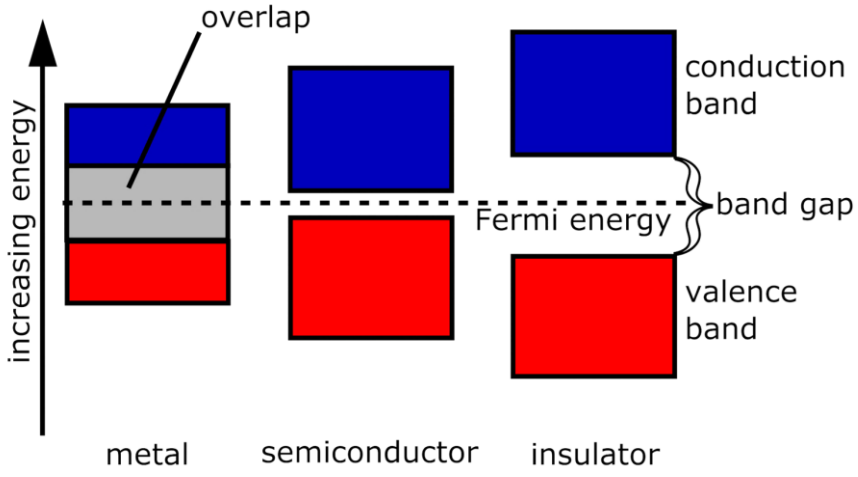


Figure 2-2 Diagram illustrating band structure of metals, semiconductors and insulators. Adapted from Wikimedia [23]

In terms of the material's optoelectrical and electrical properties, the most important those nearest to the Fermi level (E_f). The E_f is derived from the Fermi-Dirac distribution function, which gives the likelihood of filling an energy level with an electron. The Fermi level itself represents the point at which there is a 50% probability of electron occupation at a given temperature [22]. Depending on the nature of the material, the arrangement of the bands around the Fermi level differ. In metallic materials the Fermi level lies within one of the energy bands, and in semiconductors and insulators the Fermi level lies within a band gap (Figure 2-2). The band below the level is termed the valence band (VB), composed of molecular bonding orbitals, and the band above is called the conduction band (CB), composed of molecular anti-bonding orbitals [22].

This arrangement of bands around the E_f gives rise to distinct properties depending on the material. In metals this means that states above the Fermi level are readily accessible to electrons, which means that even with a small amount of energy electrons can be readily to promoted into these empty states. This is the reason why electrons are free flowing in metals, generally making metals good conductors. On the contrary, an insulator is a material that does not readily conduct electricity at room temperature. As the Fermi level lies within a large gap, a large amount of energy would be required to promote an electron into the next free energy level, usually requiring considerable thermal energy to allow for conduction [22].

A semiconductor is a material which have electrical conductivities falling between that of conductors, such as metals, and insulators, such as glass. The band gaps in these materials are smaller than that insulators, with typical values of the band gap ranging between 0.75 eV to 3.90 eV [24]. This causes them to have conducting properties between those of metals and insulators at room temperature, as thermally excited electrons can more easily attain the energy to be promoted to the conduction band. Like insulators, the conductivity also increases with temperature. In PV applications the small E_g is exploited as it allows incident photons to promote electrons into the conduction band gap. This is the same effect first observed by Einstein in metals, however as the electrons do not leave the material it is known as the internal photoelectric effect [25].

2.1.3 The Band Gap

The nature and size of the band gap (E_g) is an important parameter when it comes to how a material responds to light. If a photon possesses energy greater than that of the materials band gap, it can be absorbed by a semiconductor. The photon then transfers its energy to the electron causing it to be promoted into the conduction band (CB). This also causes the formation of a hole, or in other words a lack of an electron leaving behind a space of positive charge. This is known as the formation of an

electron-hole pair. This is the main mechanism behind the generation of electronic charge from sunlight [26].

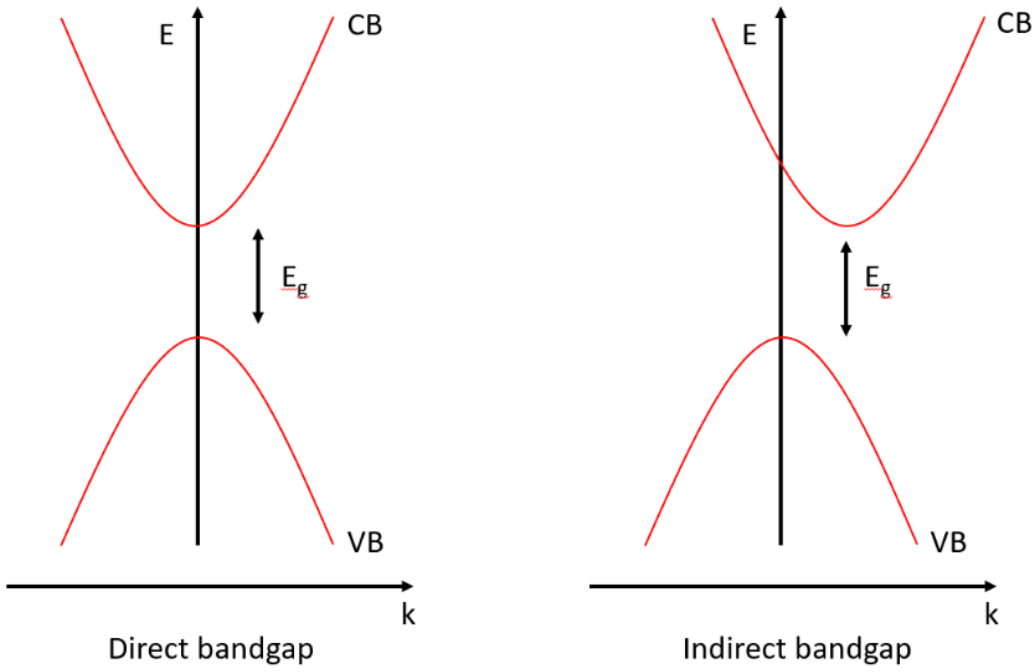


Figure 2-3 Sketch illustrating direct and indirect band alignments

The E_g of a semiconductor can take on two different forms, an indirect band gap or direct band gap (Figure 2-3). This distinction arises due to the nature of how the electron transitions from the valence to the conduction band. In a direct band gap, the electron can directly transition from the valence band to the conduction band as both the conduction band minima and the valence band minima occupy a similar position in k-space. In an indirect band gap, the electron requires a change in momentum before its transition. This is provided in the form of a phonon, or lattice vibration and means that because the process requires multiple components it is less efficient, which has the consequence of reducing the amount of light that a material can absorb in a given thickness. Silicon is an indirect band gap material and therefore suffers from requiring thick absorbing layers (~10-100 µm) [22,27]. In comparison modern direct bandgap technologies such as OMHP PVs, require layers of less than 1 µm thick.

2.1.4 Absorption of Light and Generation of charges

How strongly a material can absorb a certain wavelength/energy of light is determined by the absorption coefficient, α. This is strongly dependant on the band gap of semiconductor, as light with energy below the band gap does not possess enough energy to promote the electron into the

conduction band. Therefore, the photon is not absorbed. Photons with energy above the band gap are readily absorbed giving rise to a sharp increase in absorption (Figure 2-4).

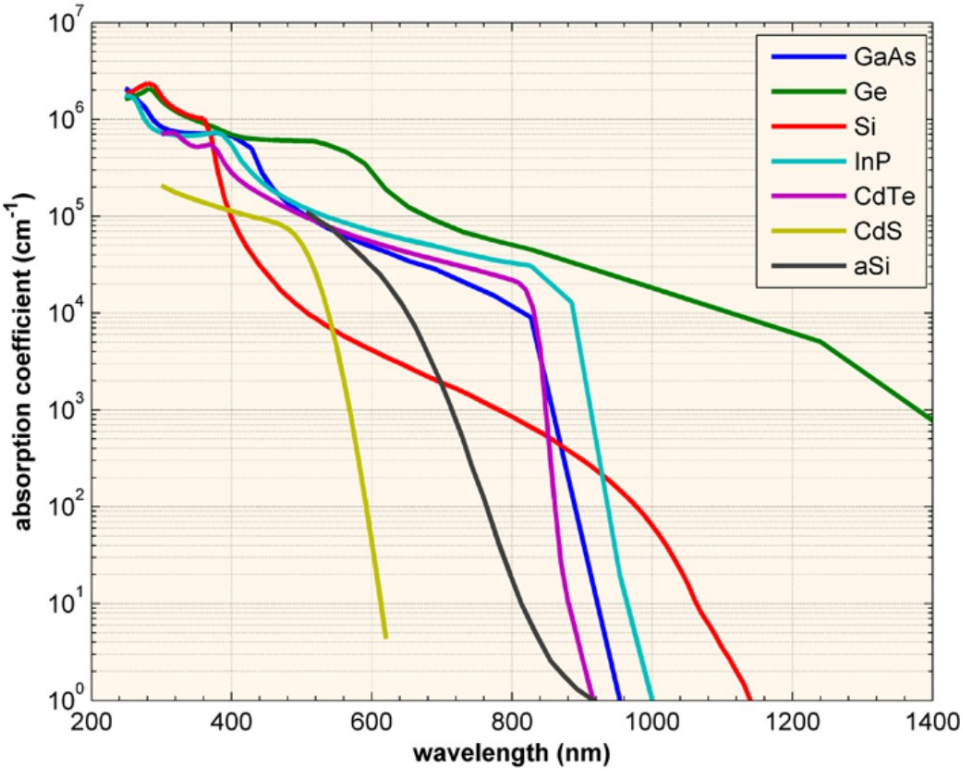


Figure 2-4 Graph showing absorption coefficient, α, vs incident light wavelength in a variety of semiconductor. Adapted from pveducation.org [28]

Therefore, selecting materials with appropriate band gaps, to absorb as much incoming light as possible, is paramount to creating a PV. The Shockley-Queisser Limit can be used to estimate the maximum theoretical efficiency of a solar cell based on the materials band gap. It was first calculated by Shockley and Queisser and estimates that the maximum theoretical efficiency of a single p-n junction solar cell is 33.7%, achieved with a material that has a band gap of 1.34eV [29]. Figure 2-5 shows the theoretical calculated efficiencies of various bandgaps and indicates that values between 1.1 eV and 1.5eV are desirable.

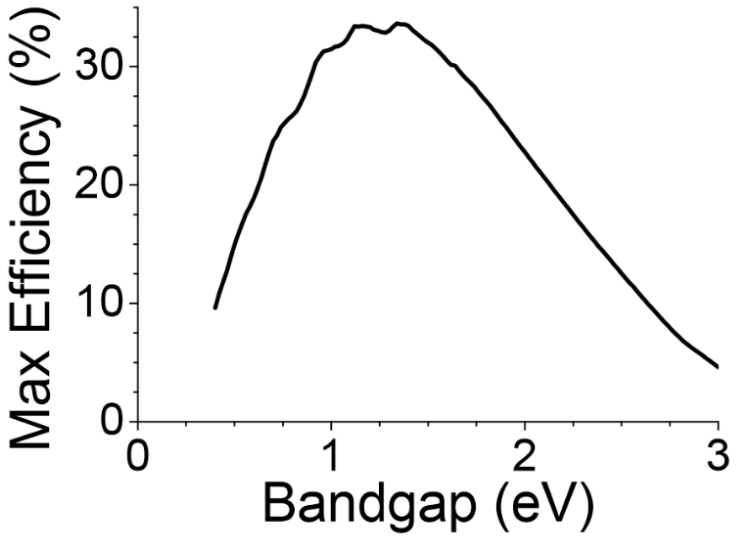


Figure 2-5 Calculated maximum efficiency vs E_g using the Shockley Queisser model. Solar radiation is approximated as a 6000 K blackbody spectrum.

The generation of charge carriers from incident light can be calculated using the absorption coefficient of a material, and the intensity of the incident light [30]:

$$I = I_0 e^{-\alpha x} \quad (2\text{-}1)$$

With α = absorption coefficient (cm^{-1}), x = position in depth of the material, I_0 is the light intensity at the top surface. This assumes that all incident photons produce an electron hole pair. Differentiating this equation will give the generation of electron-hole pairs at any point within a device and yields the generation rate of electron-hole pairs, G:

$$G = \alpha N_0 e^{-\alpha x} \quad (2\text{-}2)$$

With α = absorption coefficient (cm^{-1}), x = position in depth of the material, N_0= photon flux at the surface (photons/unit-area/sec.) As this equation has the form of exponential decay, it also shows that most of the electron-hole generation happens within the surface of the cell [30].

2.1.5 Built in Potential- Extracting the Charge

The generation of charge via the photovoltaic effect alone does not provide enough current necessary for electricity production. Excited electrons tend to have a finite lifetime and will recombine with a hole or thermally relax back into the valence band position. To extract the charges effectively a second mechanism is required: that of a built-in potential barrier.

The original form of this, and the one still used commonly to date, is that of the silicon P-N junction, invented by Ohl in 1939 [31]. To understand the basics of this junction it is necessary to understand semiconductor doping. By introducing impurities, also known as doping, within a semiconductor, new

allowed energy states are introduced within the band gap. Impurities which introduce electronic states near the conduction band edge are called electron donor impurities (n-type doping), whereas impurities that create states near the valence band are called electron acceptor impurities (p-type doping).

For instance, in a perfect silicon lattice each silicon atom shares one of its electrons in the valence shell with another silicon atom, forming four bonds. When one adds a pentavalent element such as phosphorus, four of the electrons form bonds with the remaining electron being free to move in the lattice. These free electrons create the extra energy states near the valence band, which means that they can be readily excited into the conduction band. Conversely, addition of a tri-valent element such as boron creates electron deficiencies, also known as holes. These states are easily filled by electrons in the valence band, leaving mobile holes in the valence band and therefore also improving conductivity. When introducing a large amount of these dopants, enough energy states can be introduced within the E_g to allow for ready conduction at room temperature [32].

By introducing these allowed energy states, dopants have a large effect on the Fermi level of a material. Electron acceptor doped materials (p-type) have their Fermi level close to the valence band, and electron donor doped materials (n-type) have their Fermi level near the conduction band edge (Figure 2-6). Due to the Fermi level needing to be aligned in a system when it is in thermodynamic equilibrium, as the p-type and a n-type material contact each other band bending occurs [26].

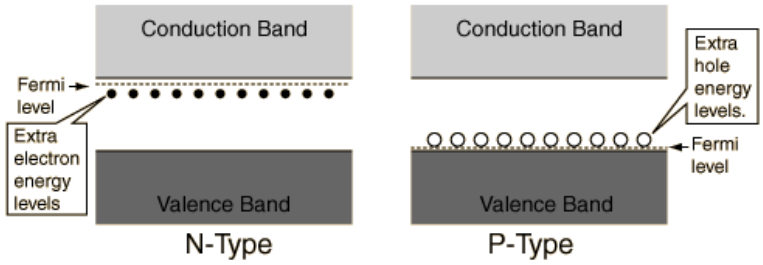


Figure 2-6 Diagram illustrating the effect of p-type and n-type dopants. Adapted from Hyperphysics [33]

At the p-n interface, the free electrons from the n-type are attracted to the excess positive charge in the p-type. This causes them to diffuse into the p-type material and recombine. Conversely, the holes in the p-type drift into the n-type material and screen the charge there. This creates a region of negative charge in the p-type material and a region of positive charge in the p-type material. Both regions together repel mobile charges away due to an electric field, creating a space charge region or potential barrier. This opposes the initial diffusion process, and over time both phenomena counterbalance and reach an equilibrium. This space charge region is what creates the characteristic

diode behaviour of a p-n junction. In forward bias the holes and electrons are pushed into the centre of the junction, reducing the depletion region and allowing the charge carriers to cross easily and current flows more readily. Conversely, in reverse bias charge carriers are pulled away from the centre, creating a larger depletion region making it harder for current to flow [26]. A schematic of a p-n junction can be seen in in Figure 2-7.

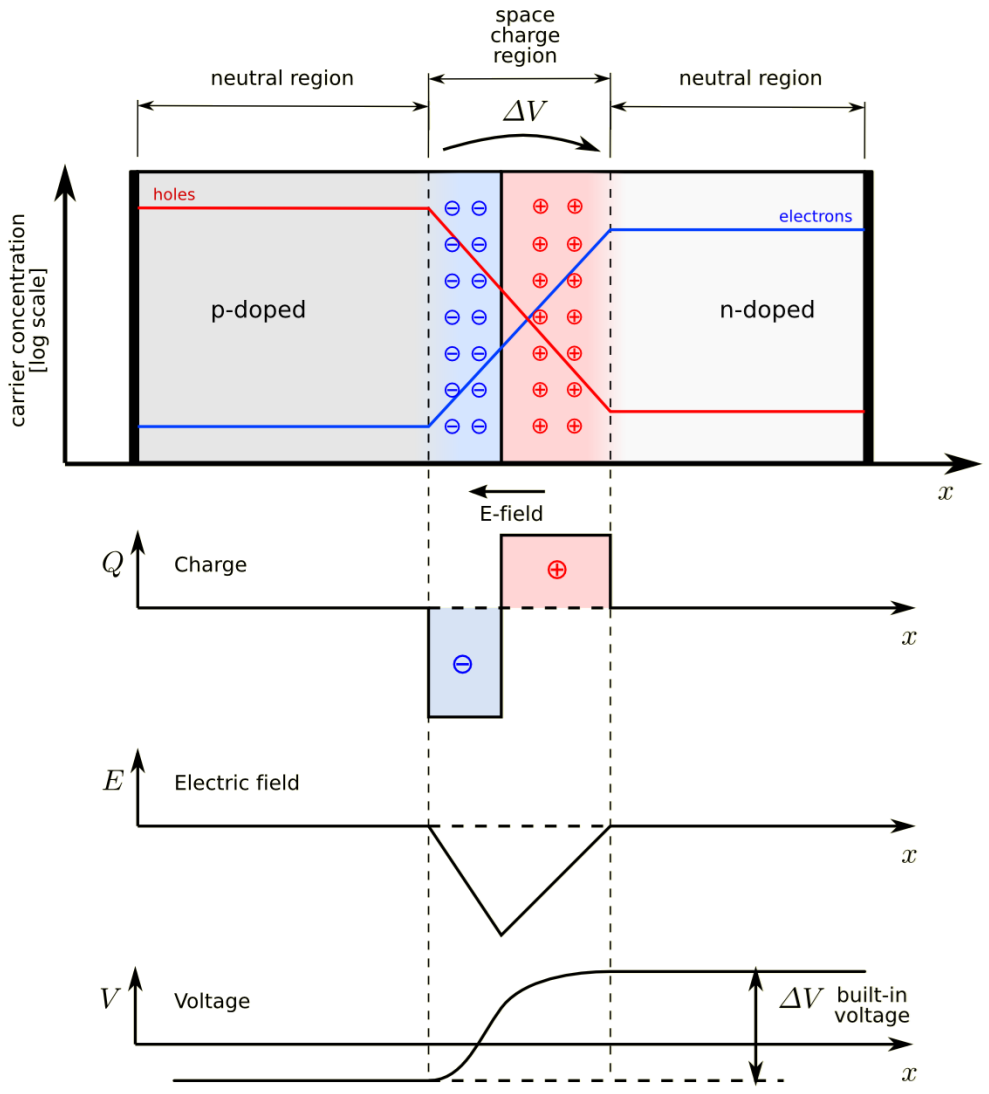


Figure 2-7 Diagram of p–n junction in thermal equilibrium with zero applied bias. Under the junction, plots for the charge density, electric field, and the voltage. Adapted from Wikimedia [34]

Another commonly used variation of the p-n junction is the p-i-n junction, which is the junction commonly implemented in OMHPs. In this junction the perovskite is sandwiched between two semiconducting materials, a p-type and an n-type. The i denotes the intrinsic nature of the perovskite, or in other terms that it is undoped. In this case, the depletion layer is stretched over the larger length and spans the thickness of the intrinsic semiconductor, creating an electric field across the intrinsic material (Figure 2-8). These junctions can also be formed from dissimilar materials with each having

different band gaps and different Fermi-levels; this is referred to as a heterojunction. The energy level diagram of a heterojunction p-n or p-i-n junction look similar to their homo counterparts, however, a key difference is the presence of a discontinuity at the contact of the two materials. This discontinuity can either assist or disrupt the flow of charge carriers depending on the initial band gap levels. In p-i-n junctions this feature can be, for instance, used to block flow of electrons to the side of the cell containing holes, which can reduce recombination of charges.

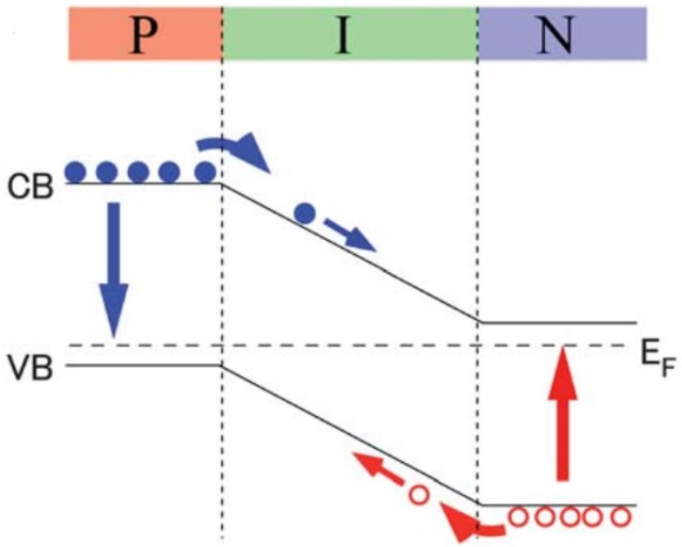


Figure 2-8 Schematic of p-i-n junction with zero applied bias. Adapted from Yoshida (2012) - Nanoscale probing of transient carrier dynamics modulated in a GaAs–PIN junction by laser-combined scanning tunnelling microscopy

When the junction within a solar cell is illuminated, the inbuilt electric field separates the electron-hole pair. The electric filed will cause the electron to drift towards the n-type and the hole will drift towards the p-type, and the charges can be collected. However, the electric field can only influence electron-hole pairs if they are within its influence, meaning the electron-hole pairs have to be within the junction[24]. If electron-hole pairs are formed away from the junction, in the bulk of either semiconductor, then the probability of electron hole separation is lower. The probability of this happening is known as the collection probability and decreases as the distance from the junction increases. This is one major advantage of the p-i-n junction, as the electric field usually stretches across most of the absorbing material and therefore most of the electron hole pairs experience the effect of the electric field [35].

2.1.6 The J-V Curve

The non-linear behaviour of the p-n/p-i-n junction can be described using the diode equation, however when dealing with PVs it is customary to use current density (J) instead of current (I). Under no illumination the equation is as follows:

$$J_{dark}(V) = J_o\left(exp\left(\frac{qV}{nk_bT}\right) - 1\right) \quad (2\text{-}3)$$

J_o is the reverse saturation current density, q is the elementary charge of an electron, V is the applied bias, n is the diode non-ideality factor, k_b is the Boltzmann constant, and T is the temperature in Kelvin [30]. When the junction is illuminated and the terminals are connected in a circuit, a short-circuit current forms. The short circuit current density is defined as:

$$J_{sc} = q\int b_s(E)EQE(E)dE \quad (2\text{-}4)$$

The J_{sc} is defined as the integration of the products of incident spectral flux density, b_s, external quantum efficiency, EQE, across the whole solar spectrum of incident photon energies, E. The spectral flux density is the amount of energy transferred from solar radiation to the cell[30]. The EQE is a measure of the probability of a given photon with energy E creating an electron that is harvested by the circuit. It is also known as the incident photon-to-current conversion efficiency (IPCE). The EQE is dependent on the absorption coefficient of a material and the efficiency of the charge separation[30].

As the junction is illuminated the current formed shifts the diode curve. This can be described by the following modification to the diode equation:

$$J(V) = J_{sc} - J_{dark}(V)$$

$$\rightarrow J(V) = J_{sc-}J_o\left(exp\left(\frac{qV}{nk_bT}\right) - 1\right) \quad (2\text{-}5)$$

This resulting curve can be seen in Figure 2-9 ,which also shows a several other key points on the curve.

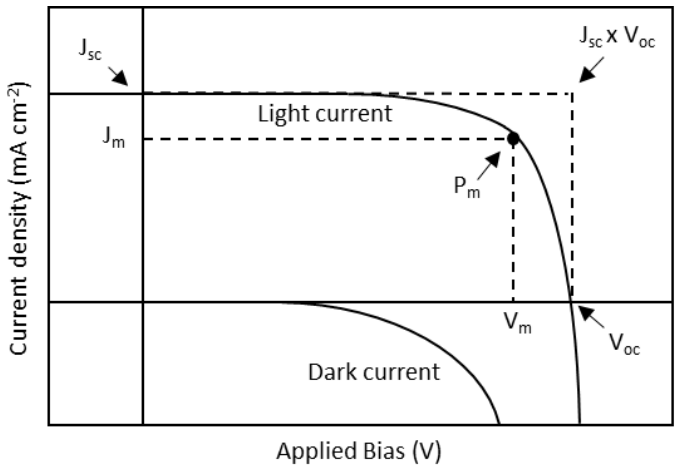


Figure 2-9 J-V behaviour of a non-ideal solar cell in the dark and under illumination. Short-circuit current, J_{sc} , is shown at V = 0 and open-circuit voltage ,V_{oc}, is shown at J = 0. Maximum power density, P_m is shown at the intercepts of J_m and V_m. FF is the ratio between the product of J_{sc} and V_{oc}.

As the current drops to zero it intercepts the abscissa at a given voltage, which is known as the open-circuit voltage, V_{oc}. This is the voltage that the cell generates when the circuit is not completed and stems primarily from the inbuilt potential difference of the junction. Using equation 2.1 the following expression for V_{oc}[30] can be derived:

$$J_{sc} = J_o\left(exp\left(\frac{qV}{nk_bT}\right) - 1\right)$$

$$\rightarrow V_{oc} = \frac{nk_bT}{q} ln\left(\frac{Jsc}{J_0} + 1\right) \qquad (2\text{-}6)$$

Within the region between J_{sc} and V_{oc} the cell is generating power density, P, with the maximum power density, P_m , achieved at a certain combination of current, J_m, and voltage V_m. Another important factor called the fill factor, FF, is calculated using the ratio between the product of the V_{oc} and J_{sc} and the V_m and J_m [30]:

$$FF = \frac{J_m V_m}{J_{sc} V_{oc}} \qquad (2\text{-}7)$$

Using this the overall power conversion efficiency of the cell, η, can be defined as the ratio of P_m and the proportion of incident light power density from solar irradiance, P_{in} [30]. Typically, cells are tested at air mass 1.5 solar irradiance, which equates to a P_{in} of 1000 W/m^2.

$$\eta = \frac{J_m V_m}{P_{in}}$$

$$\rightarrow \eta = \frac{J_{sc} V_{oc} FF}{P_{in}} \qquad (2\text{-}8)$$

In real world operation solar cells experience contact resistances in the contacts and current leakage in the device. These two factors can be quantified by two parasitic resistances, one in series, R_s and one in parallel R_{sh}, also known as the shunt resistance. R_s primarily stems from the resistance of the

cell material to current flow, the current flow to the contacts and the intrinsic resistance of the contacts themselves. Including these resistances, equation 2.3 becomes [30]:

$$J_{sc} = J_o\left(exp\left(\frac{qV}{nk_bT}\right) - 1\right) - \frac{V+JAR_S}{R_{sh}} \qquad (2\text{-}9)$$

The parasitic resistances have a major effect on the FF and therefore can dramatically lower the performance of a device(Figure 2-10).

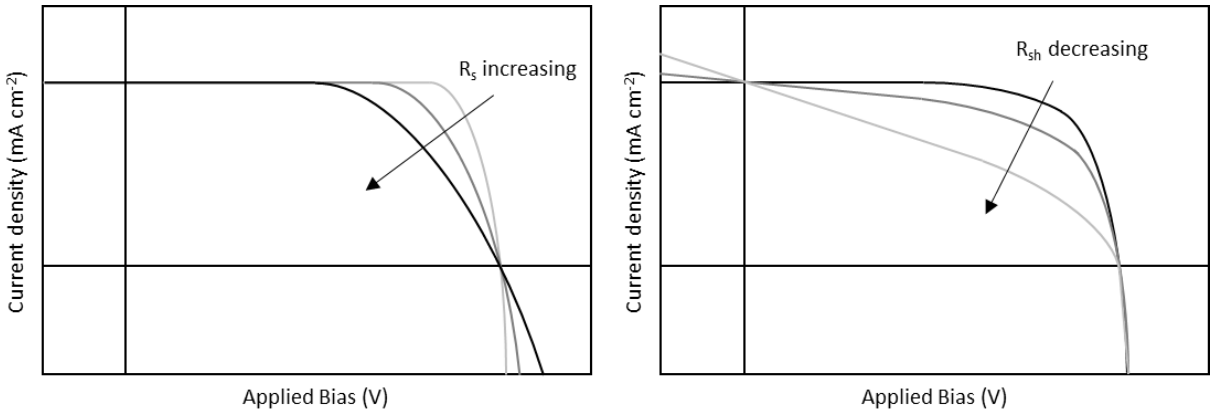


Figure 2-10 Effect of parasitic resistances on J-V curve. a) increasing series resistance R_s b) and increasing shunt resistance R_{sh}. The FF is severely affected by both resistances, leading to lower power output.

2.1.7 Recombination of Charges, Lifetimes and Mobility

Recombination is the opposite of charge generation, in that the excited electrons recombine with holes. This leads to a loss of current from the device and is one of the major losses within solar cells. Recombination is primarily caused due to either intrinsic processes within the material or due to imperfections and interfaces in the material. Radiative recombination is one such intrinsic process, where an excited electron in the conduction band directly recombines with a hole in the valence band, releasing a photon with the energy of the band gap. This is also known as spontaneous photoemission [30]. The other intrinsic process is Auger recombination which involves the recombining of an electron and hole. However the energy is not emitted thermally or as a photon, instead the kinetic energy is transferred to another electron. The electron then loses energy via thermal vibrations and relaxes back into the valence band. Auger recombination dominates in materials with large carrier concentrations, such as heavily doped materials [30]. Recombinations due to imperfections or surfaces occur due to trap states within the band gap. These trap states form at crystal defects and impurities within the material, or at surfaces of the material. The process by which trap states recombine charges is known as Shockley-Read-Hall (SRH) recombination. Here electrons or holes will get trapped at one of the intragap states and either be released due to thermal excitation or recombine with the opposite carrier at the same site [30]. These processes are illustrated in Figure 2-11.

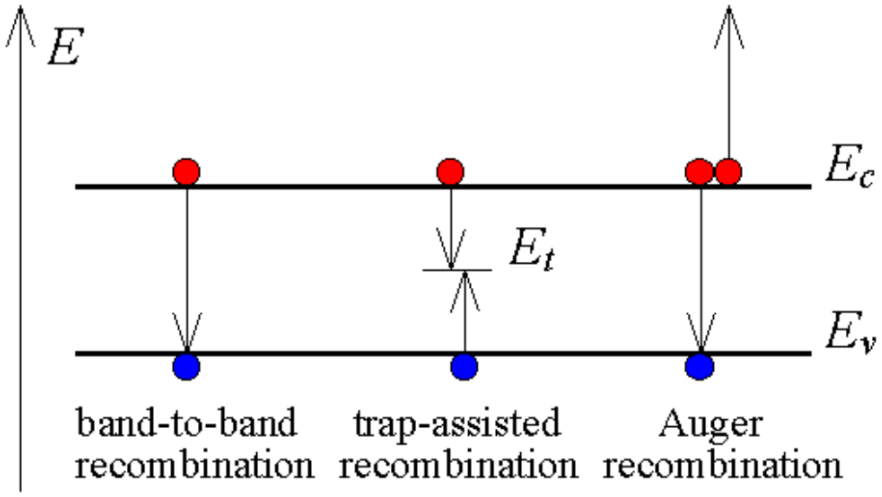


Figure 2-11 Carrier recombination mechanisms in semiconductors [36]

These recombination processes directly affect the lifetime of free charge carriers, which can be described by [37]:

$$\frac{1}{\tau} = \frac{1}{\tau_{rad}} + \frac{1}{\tau_A} + \frac{1}{\tau_{SRH}} \qquad (2\text{-}10)$$

With τ being the total lifetime of the charge, τ_{rad} being the radiative lifetime, τ_A the Auger lifetime and τ_{SRH} SRH lifetime. Charge carrier diffusion length is another parameter that is directly linked to the recombination processes. This describes the average distance a charge carrier can move before it recombines. The diffusion length of the charge will limit the maximum thickness of the solar cell material before it cannot extract charge, as the charge carriers recombine before they reach the contacts. This naturally is linked to the lifetime and the relationship is [30]:

$$L = \sqrt{D\tau} \qquad (2\text{-}11)$$

L is the diffusion length of the charge carrier and D is the diffusivity of the charge carrier, which can be described using the Einstein relation to give another key parameter, the mobility of the charge carrier [38]:

$$D = \frac{k_b T}{q}\mu \qquad (2\text{-}12)$$

The mobility, μ, describes how quickly a charge carrier moves in an electric field and is commonly used as a metric in PV materials to discern how well charges could be extracted from a cell.

2.2 ORGANO METAL HALIDE PEROVSKITES

Organo-metal halide perovskites (OMHP) are a recent development and have garnered a lot of attention in the field of photovoltaics. They were first used as sensitizers in DSSCs, however, now they are considered a separate research entity and show potential for achieving a high efficiency at a low material cost. Over the last 14 years of research perovskite cells have almost matched the record efficiencies of single crystal silicon, as of 2019 exceeding 25% [1]. This in combination with its low material and processing cost, makes it one of the most attractive 3rd generation PV technologies. However, a lot of work remains to be done, especially in the area of scalable depositions techniques. This section of the review will give a brief introduction to OMHP, their properties, the current state of research and how AACVD has been utilised to deposit this material.

2.2.1 History of OMHP

The first use of OMHP in in the field of photovoltaics was in a DSSC solar cell produced by Miyasaka *et.al* in 2009 [39]. In this study, two variations of halide perovskite, methyl ammonium lead tri-bromide (MAPBr) and methyl ammonium lead tri-iodide (MAPI), were used as sensitizers on a mesoporous TiO_2 scaffold. The resulting cells had similar power conversion efficiencies (PCE), with the Br based cell achieving 3.13% and the I cell having 3.83%. Furthermore, a high Voc of 0.96V was realized in the Br based cell. One major drawback reported was the rapid degradation the cell underwent when exposed to light and air, a problem which to date still persists in OMHP.

An evolution of the DSSC based design was demonstrated by Park's research group in 2011 [40] . In this DSSC design, MAPI was deposited in the form of nanocrystal quantum dots (QD), with diameters of 2-3nm. Efficiency of this cell was 6.2 %, with a V_{oc} of 0.629 V and a FF of 0.617. The cell was further improved via the introduction of a $Pb(NO_3)_2$ blocking layer, which reduced recombination. This increased efficiency to 6.5 % and V_{oc} to 0.706 V. However, degradation due to the electrolyte that plagued earlier perovskite DSSC cells was still present.

A big breakthrough in terms of stability and efficiency was the development of solid-state cell (SSC) perovskite devices. The research groups of Park and Snaith both demonstrated cells in which the electrolyte was replaced by the hole transporting polymer 2,2´,7,7´-tetrakis-(N,Ndi-p-methoxyphenylamine)9,9´-spirobifluorene (spiro-OMeTAD). The champion device of Park *et al.* had an efficiency of 9.7 % with a FFof 0.62and a Voc of 0.888 V, exceeding the efficiency achieved by the DSSC counter parts. The biggest improvement due to abandonment of liquid electrolytes was the increased stability. Stability of this cell was analysed and over 500h under illumination only led to a small decrease in J_{sc}[41]. The cell produced by Snaith's group had a very similar structure, however the perovskite was of a mixed halide form ($CH_3NH_3PbI_{3-x}Cl_x$). The cell also had a higher V_{oc}, indicating less

recombination within the cell, and therefore achieved higher efficiencies than its DSSC counterpart, 10.9% [42].Moreover, further investigation into the charge carrier properties, by replacement of the mesoporous TiO_2 layer with a mesoporous Al_2O_3, led to the discovery of the ambipolar charge carrier transport in halide perovskites, long carrier diffusion lengths and high charge carrier mobilities [43–45]. These key discoveries paved the way for OMHPs to become the most rapidly advancing PV technology to date.

2.2.2 The Perovskite Structure

The perovskite structure was first resolved from $CaTiO_2$ 1839 by Gustav Rose and was named perovskite in honour of the Russian Mineralogist L.A Perovski [46]. Halide perovskites were discovered 40 years later, with Wells *et al.* synthesising a series Cs based halide perovskite in 1893. The first OMHP perovskites were synthesised by Weber in 1978, one of which being methyl ammonium lead tri-iodide (MAPI)[47]. This perovskite was used by Miyasaka in 2009 to produce the first OMHP PV, forming the basis of the field [39].

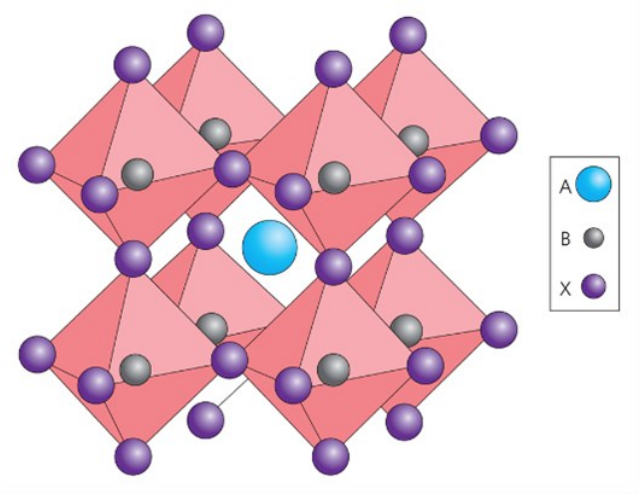


Figure 2-12 Crystal structure of methyl ammonium lead tri-iodide (MAPI)

The general formula of perovskite is ABX_3, where A and B are cations and X is an anion (Figure 2-12). The ideal cubic unit cell (Pm3m) is composed of five atoms, with the A cation occupying the cubo-octahedral site and the B cation occupying the octahedral sites. The X anions occupy the face centred positions [46]. In a typical OMHP the A site is typically occupied by organic cations such as methyl-ammonium ($CH_3NH_3^+$), formamidine ($NH_2CH{=}NH_2^+$) and Guanidium ($C(NH_2)_3^+$). Recent developments have also included the addition of small radii alkali metal ions such as Cs^{1+} and Rb^{1+}. The B site is typically occupied by large divalent metal cations from the carbon group such as Pb^{2+}, Sn^{2+} and Ge^{2+}. The X site is primarily occupied by the three halides, Br^-, Cl^- and I^-. State of the art OMHP employ various mixtures of cations and anions within a single material. One of the simplest ways to determine

if a mixture of ions will form a perovskite the known ionic radii can be used to calculate the Goldschmidt tolerance factor (t) [48] :

$$t = (r_A + r_X)/[\sqrt{2}(r_B + r_X)] \quad (2\text{-}13)$$

R_A is the ionic radius of the A cation, R_b is the radius of B cation and R_x is the radius of the halide ion. A list of typical ionic radii values for OMHP materials can be seen in the following table:

Table 2-1 Showing commonly used radii of ions. A-cation are coloured black, B cations are coloured blue and the X anion is green. Table adapted from Chen et al. (2015) [49]

Species	**Formamidinium (FA)**	**Methylammonium (MA)**	**Cs**	**Pb**	**Sn**	**I**	**Br**	**Cl**	**F**
Size (Å)	1.9 – 2.2	1.8	1.7	1.2	1.1	2.2	2.0	1.8	1.3

When using a mixed composition, a virtual radius must be employed, which considers the fractions of each ion introduced into the system and then uses a weighted average to calculate a final radius for the relevant site. If the value lies between 0.7 and 1.11 it is likely that a perovskite will form. However, as the value deviates from 1, the crystal structure will begin to distort. Values below 0.9 form perovskites with an orthorhombic/rhombohedral structure. Above 1 it may form a tetragonal or hexagonal structure. Furthermore, the size of the A ion can also affect the dimensionality of the perovskite. If the ion is very large, then the three-dimensional (3D) network is broken and two-dimensional (2D) or one-dimensional (1D) structures are formed. Therefore, if t<< 1 the 3D structure will be destroyed. [49] Another value to consider in formability is the octahedron factor,μ, developed by Li *et al.* [50] This factor describes the ratio between the radii of the B cation and the X anion. It is calculated as follows:

$$\mu = r_B/r_X \quad (2\text{-}14)$$

If the value of μ<0.442 then formation of the perovskite will not occur, as the octahedron will be too unstable.[50]

The main caveat with using the Goldschmidt and octahedral factors is the low accuracy with which they can describe OMHP formability. For instance, the Goldschmidt factor tends to only accurately predict 31% of iodide, 51% of chloride and 56% of bromide perovskites. Using modern data analytics Bartel *et al.* have proposed a new tolerance factor that considers the oxidation state of the A site cation [51]:

$$\tau = \frac{r_x}{r_b} - n_A\left(n_A - \frac{r_A/r_B}{ln(r_A/r_B)}\right) \quad (2\text{-}15)$$

Where n_a is the oxidation state of the A site cation. $r_A > r_b$, and $\tau < 4.18$ indicates a stable perovskite. This new tolerance factor can predict the formation of OMHP with over 90% accuracy and has been even extended to low dimensionality perovskites and double perovskite structures.

2.2.2.1 Common phase transitions

As is the case with most materials, external factors such as temperature affect the crystal structure. In OMHP the three dominant crystal systems are cubic (Pm3m), tetragonal (I4/mcm) and orthorhombic (Pnam). As the temperature increases the structure transforms from orthogonal to tetragonal and then to cubic. These phase transformations are classified as follows: high temperature phase α, intermediate temperature phase β and low temperature phase γ (Figure 2-13). MAPI for instance, is tetragonal at room temperature and experiences a phase transition to the tetragonal structure at 400K [52–54].

PVSK	Phase	Temperature (K)	Structure	Space group	Lattice parameters (Å)			Volume (Å^3)
$MAPbI_3$	α	400	Cubic	P4*mm*	*a* = 6.3115	*b* = 6.3115	*c* = 6.3161	251.6
	β	293	Tetragonal	I4*cm*	*a* = 8.849	*b* = 8.849	*c* = 12.642	990
	γ	162–172	Orthorhombic	$Pna2_1$	*a* = 5.673	*b* = 5.628	*c* = 11.182	959.6
$MAPbCl_3$	α	>178.8	Cubic	P*m*3*m*	*a* = 5.675			182.2
	β	172.9–178.9	Tetragonal	P4/*mmm*	*a* = 5.655	*c* = 5.630		180.1
	γ	<172.9	Orthorhombic	$P222_1$	*a* = 5.673	*b* = 5.628	*c* = 11.182	375
$MAPbBr_3$	α	>236.9	Cubic	P*m*3*m*	*a* = 5.901			206.3
	β	155.1–236.9	Tetragonal	I4/*mcm*	*a* = 8.322	*c* = 11.833		819.4
	γ	149.5–155.1	Tetragonal	P4/*mmm*	*a* = 5.8942	*c* = 5.8612		
	δ	<144.5	Orthorhombic	$Pna2_1$	*a* = 7.979	*b* = 8.580	*c* = 11.849	811.1
$MASnI_3$	α	293	Tetragonal	P4*mm*	*a* = 6.2302	*b* = 6.2302	*c* = 6.2316	241.88
	β	200	Tetragonal	I4*cm*	*a* = 8.7577	*b* = 8.7577	*c* = 12.429	953.2
$FAPbI_3$	α	293	Trigonal	P3*m*1	*a* = 8.9817	*b* = 8.9817	*c* = 11.006	768.9
	β	150	Trigonal	P3	*a* = 17.791	*b* = 17.791	*c* = 10.091	2988.4
$FASnI_3$	α	340	Orthorhombic	A*mm*2	*a* = 6.3286	*b* = 8.9554	*c* = 8.9463	507.03
	β	180	Orthorhombic	I*mm*2	*a* = 12.512	*b* = 12.512	*c* = 12.509	1959.2

Figure 2-13 Structural phase transformations for commonly found within OMHP. Adapted and modified from Chen et al. (2015) [49]

2.2.3 Optical Properties of OMHP

Optical properties that make OMHPs ideal for PV applications are their narrow bandgaps 1.1-2.3 eV and high absorption coefficients (10^5 cm^{-1}), allowing for even thin layers to sufficiently absorb a wide range of the solar spectrum. The strong optical absorption arises from their direct band gap nature, which in OMHPs is primarily formed by the molecular orbitals of the B and X site ions [55]. This means that compositional variations of those two sites will heavily affect the light absorbing properties of the material.

For instance, MAPI has a bandgap of ~1.55 eV, meaning that it absorbs light from the near infrared region (800 nm), however, the Sn derivative, $CH_3NH_3SnI_3$, has its absorption onset shifted into the near infrared region, 1000nm, with a band gap of 1.1 eV. Intriguingly, the mixed metal system, $CH_3NH_3Sn_xPb_{1-x}I_3$, has shown red-shifting of the onset towards 1300nm [56]. Changes in the halide can

have a similarly large effect, with the Br substituted derivative, $CH_3NH_3BrI_3$, having a much wider band gap, 2.3 eV. The mixed composition, $CH_3NH_3PbI_{3-x}Br_x$, displays band-gaps between that of the parent systems [57]. However, the addition of Cl ions, forming the mixed halide $CH_3NH_3PbI_{3-x}Cl_x$, displays very little difference in the absorption spectra.[58] Conversely, replacement of the A site cation shows a smaller shift in the absorption. Replacing the MA with FA, forming, $HC(NH_2)_2PbI_3$, has shown the onset shift towards 850nm.[59,60] Additionally, Cs based perovskites such as $CsPbBr_3$ have shown blue shifted absorption onset to 540nm. [61] Recently a study by Grätzel *et al.* showed that a triple cation system containing MA, FA and Cs has an absorption onset of 775nm.[62] A energy diagram of common OMHPs can be seen in Figure 2-14.

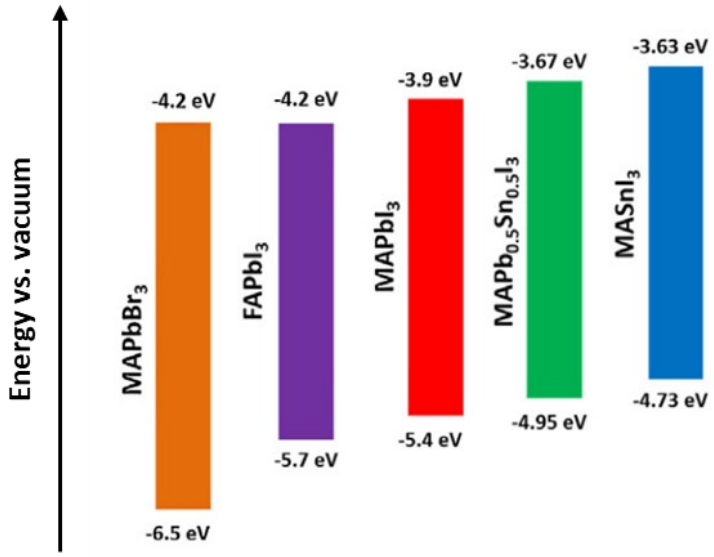


Figure 2-14 Band edge positions of various organometal-halide perovskites. The bandgap values are: $MAPbBr_3$ 2.3 eV $MAPbI_3$ 1.5 eV, $FAPbI_3$ 1.5 eV, $MASnI_3$ 1.1 eV. Adapted from Chen et al. (2015 [49]

2.2.4 Charge Carriers in OMHP

OMHPs exhibit excellent charge carrier properties, having near instantaneous formation of free charge carriers with high mobilities.

Charge carrier generation mechanisms in OMHPs have been shown to behave comparably to that of other semiconductors, such as GaAs. Studies on MAPI have shown that upon illumination, excitons almost immediately disassociate to form free charge carriers [63,64], with Ponseca *et al.* reporting this to occur within 2 ps [65]. In $FAPbI_3$ this has been shown to occur even more rapidly within 1ps[66].

The mobility of these charge carriers has been reported to be between the orders of 10^{-1} to 10^{1} cm^2 $(Vs)^{-1}$ for thin films and up to 10^{3} cm^2 $(Vs)^{-1}$ [67] for single crystals. Interestingly, they have been

shown to have an ambipolar characteristic, with both electrons and holes having similar values. Sn based analogues tend to exhibit higher mobilities in the range of 10^2-10^3 cm^2 / Vs [68,69]. A site modification can also lead to changes in mobility, for example, FA based perovskites tend to exhibit lower mobilities than MA or mixed cation counterparts [67]. Furthermore, addition of Rb leads to increased mobilities, however the mechanisms may be related to trap state reduction rather than intrinsic energetics [70,71]. Substituting I with Br also tends to lead to a lower mobility, with mixed compositions resulting in lower values than either parent system. This is generally attributed to the potential dimensional disorder of the crystal at these compositions [72]. One caveat with most reported mobilities is that they can stem from a variety of analytical techniques. Some techniques, such as time of flight (TOF) and Space Charge Limited Current (SCLC), measure out of plane, akin to what would be found in a device. On the other hand, measuring the field effect mobility via a field effect transistor (FET) or utilising the Hall effect, measure the in-plane mobility. Depending on the axis of measurement, the number of grain boundaries will change, which could lead to different numbers of carriers being trapped at the boundaries, resulting in axis dependant variation in mobilities. Furthermore, decoupling intrinsic factors such as composition and crystal structure from extrinsic factors, such as morphology, defects, and impurities is very challenging. This is because small changes in composition tend to adversely affect the morphology of the films. These are the reasons that true mobilities are hard to ascertain and care must be taken when interpreting results.

A large range of charge carrier diffusion lengths and carrier lifetimes have been reported for OMHPs. Monocrystalline diffusion lengths have been reported to be in the order of several 100 µm [73] , with lifetimes being reported in the µs scale [74]. Recent work by Brenes *et al.* has shown comparable diffusion lengths of 77 µm and lifetimes of 32 µs in thin films after exposing them to humid air, which was shown to reduce surface trap states [75]. However, typical diffusion length results for thin films tend to be < 1µm [44]. When considering that in most devices the active layer is sub 1µm thick, these values show why OMHPs can extract charges very effectively. This is corroborated by the fact that record cells are already approaching the theoretical J_{sc} limit [76–78]. As mobilities are linked to diffusion lengths and carrier lifetimes, the same factors influence the values. Compositional engineering and number of trap states[44,79] heavily influence both factors.

2.2.5 Device Architecture

As previously stated, the typical OMHP cell is formed of an intrinsic perovskite absorber layer sandwiched between two semiconductors, p and n type. When photons are absorbed by the perovskite layer the inbuilt electric field of the junction sweeps charges to the p or n type contacts. Many key properties of the cell performance are linked to the architecture. For instance, the V_{oc}, is governed by the difference in work function of the p and n type materials, and the resulting quasi

Fermi level splitting that occurs at each of the contacts. The FF is affected by the contact resistances of each of the layers and any pinholes or defects that are present. J_{sc} is affected by any recombination losses that can occur due to interfaces between materials. Therefore, it is vital to understand how to structure the OMHP device to maximise the performance. There have been a wide array of materials and architectures studied, which can be categorised mainly by the arrangement of the p and n-type contact materials. An overview of architectures can be seen in Figure 2-15, with leading device performances of each architecture in Figure 2-15.

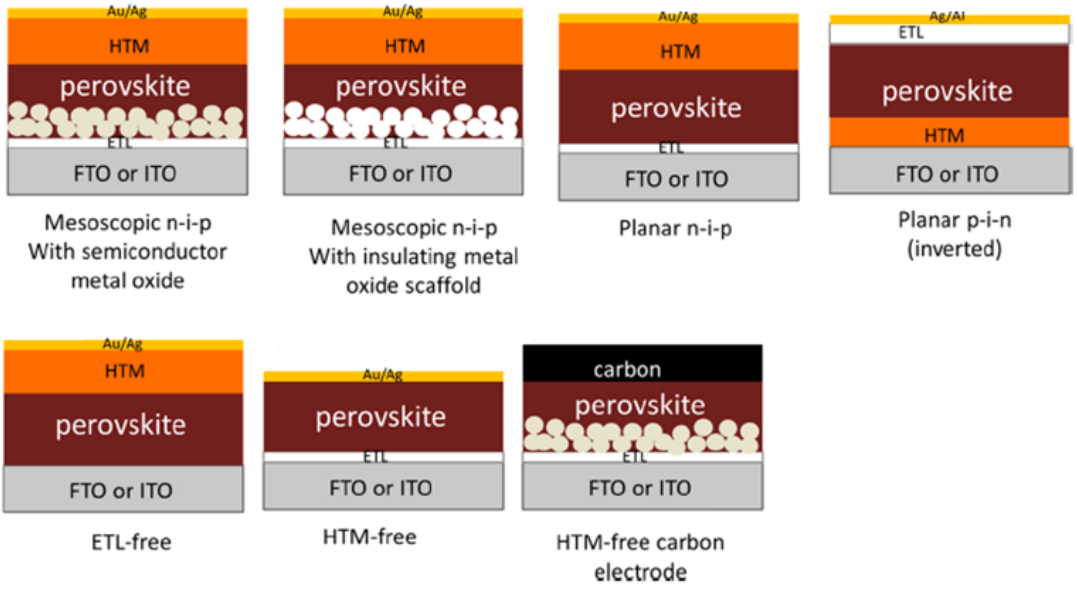


Figure 2-15 Schematic diagrams of common OMHP device architectures. Adapted from Jena et al. [55]

Table 2-2 Highest efficiencies reported in publications. Parameters were taken from the reverse scan of the champion device of each study.

Architecture	Configuration	Composition	PCE (%)	J_{sc} (mA/cm^2)	V_{oc} (V)	FF	Ref
Meso	n-i-p	$(FEA)_2PbI_4/FAPbI_3$	22.1	25.8	1.10	0.78	[80]
Meso	p-i-n	$Cs_xFA_{1-x}PbI_3$	20.13	22.2	1.13	0.80	[81]
Planar	n-i-p	$GA_x(CsFAMA)_{1-x}PbI_3$	21.12	23.7	1.19	0.75	[82]
Planar	p-i-n	$MA_xFA_{1-x}Pb(I_{1-x}Br_x)_3$	20.9	21.9	1.18	0.81	[83]
HTM-Free	i-n	$MAPbI_3$	15.0	21.7	0.96	0.72	[84]
ETL-Free	i-p	$MAPbI_3$	20.1	23.1	1.17	0.74	[85]
C-Electrode	n-i-c	$MAPbI_3$	16.1	20.8	1.05	0.74	[86]
Mesoscopic	infiltrated	$(5\text{-}AVA)_x(MA)_{1-x}PbI_3$	15.7	23.2	0.98	0.69	[87]

2.2.5.1 Mesoscopic Cell

The mesoscopic scaffold type cell is one of the most popular cell architectures used to date and is an evolution of the DSSC structure. The substrate typically is formed of glass coated with a transparent conductive oxide (TCO), such as FTO or ITO. This is then coated with a dense layer of TiO_2 (>100nm), which is an n type material and acts as the electron transporting layer (ETL). This is then covered with

a scaffold of nanostructured TiO_2 (~350 nm). To date several different nanostructures have been investigated, with nanowires, nanorods and nanotubes to name a few [88–90]. The perovskite layer (~350-500 nm) is then deposited and partially infiltrates the scaffold layer. The next layer is typically an organic hole transporting layer (HTL) such as, spiro-OMeTAD. The final layer is a metal contact (~100 nm), although carbon black has been shown to be an effective electrode[49,55]. The resulting cell cross section can be seen in Figure 2-15. During operation, charge carriers are generated in the perovskite sensitizer and swept to n and p type materials due to the inbuilt electric field. Electrons are collected and injected into the mesoporous layer. Holes are transported through the HTL. Moreover, ETL and HTL layers can also act as barriers to non-transported charge carriers, reducing interfacial recombination at the electrodes. Alternative scaffold materials have been studied, such as ZnO, strontium titanate (STO) and barium titanate (BTO)[49,91,92]. Chen *et al.* demonstrated an inverted mesoporous cell utilising $CuGaO_2$. In these cells the mesoporous metal oxide layer forms the p-type material and electron collection is handled by a planar layer of PCBM. This structure has been shown to have increased electron lifetimes and good energy conversion efficiency (20.13%)[81]. Many cells utilising the mesostructured architecture have achieved high efficiencies of over 20% [62,80,93], however it has several drawbacks. Processing of the mesostructured layer is more labour intensive and the high annealing temperatures required to fully process the metal oxide make it less desirable for scale up manufacturing. It has been also shown that during cell operation this type of cell architecture is prone to hysteresis in the J-V scan and, in the case of TiO_2 based structures, degradation, which will be discussed in detail in a later section [94,95].

2.2.5.2 Planar Heterojunctions

Another common architecture is the planar heterojunction. In this architecture the perovskite is still placed between two p and n type materials, however there is no mesostructured component. Instead, all layers are deposited as thin films. Depending on which order the layers are deposited the resulting structure will be p-i-n or n-i-p, note that both still form p-i-n junctions [49]. The naming convention stems from the order of which materials interact with the light. In the n-i-p configuration the ETL is deposited onto the TCO, which can be made of inorganic materials like TiO_2 and SnO_2 or organic materials such as Phenyl-C61-butyric acid methyl ester (PCBM). The absorber layer is similar in thickness to the mesostructured cell (~300-500 nm), however there is no partial infiltration and the perovskite forms a completely planar layer. The hole transport is then handled by a spin coated layer of p-type material. In the inverted, p-i-n configuration the p-type material forms the first layer, which is typically an organic material such as poly(triaryl amine) (PTAA), PTPD or spiro-OMeTAD. One advantage compared to the n-i-p configuration, is the fact that the organic p-type layer can be made thinner as it does not have to ensure coverage on the slightly rougher perovskite surface. As p-type organic materials

typically have low conductivities (~ 10^{-7} S cm^{-1}) a thinner layer would improve series resistance. However, inorganics such as NiO have been shown to be suitable alternatives. This architecture has become one of the most popular as it is highly versatile, allows for easy processing, more consistent performance and is compatible with more deposition techniques [49]. The peak efficiencies of planar structures have lagged that of the mesostructured cell. However, in a recent record set by Wu *et al.* they showed a planar device using colloidal SnO_2 and spiro-OMeTAD reaching over 21.12%[82]. Additionally, this cell architecture has shown improved hysteresis characteristics and stability compared to typical mesostructured cells.

2.2.5.3 Other Architectures

Mesostructured and planar architectures are the most utilised architectures. However there have been many reported variations and novel designs developed. Omission of the HTM has been shown to still yield functioning devices. Li *et al.* utilised an inverted structure design without a p-type material and achieved an efficiency of 15%, which is the highest achieved to date and has been shown to have enhanced stability [84]. Likewise, efficient ETL-free devices have been demonstrated. Huang *et al.* utilised tetramethylammonium hydroxide (TMAH) to treat FTO and used these substrates in a i-p configuration with spiro-OMeTAD to fabricate a cell with 20.1% efficiency [85]. Both architectures are primarily possible due to the ambipolar charge transport properties of OMHPs, which show similar mobilities for electrons and holes. Removing these layers would reduce the complexity and cost of the cell, potentially making scalable manufacturing easier.

Another promising architecture is the carbon-based electrode configuration. Here the perovskite is infiltrated into mesostructured metal oxide, commonly TiO_2. The cell is then completed without HTM, instead a carbon ink is used to form the back contact. Zhang *et al.* utilised a scaffold of CuPc nanorods to record an efficiency of 16.1% [86]. A variation of this architecture, called the mesoscopic cell which utilises screen printed layers of TiO_2, ZrO_2 and carbon which are then infiltrated with perovskite ink, has similar efficiencies with the record being 15.7% [87]. Utilising carbon not only removes the need for an HTM, it removes the need for costly metal back contacts. Furthermore, its inherent hydrophobicity provides a protective barrier for moisture ingress, therefore improving cell stability.

2.2.6 Hysteresis

Reliably evaluating the performance of OMHPs is relatively challenging, primarily due to hysteresis observed during J-V measurements (Figure 2-16). Depending on the scan direction, range and rate, the shape of the curve will change. This leads to different values for key performance metrics and makes it difficult to ascertain the true cell performance. However, recent advances in the field have

not only improved cell efficiency but have also reduced the hysteresis to almost negligible levels. Therefore, it seems that factors governing performance are closely linked to that of hysteresis [96].

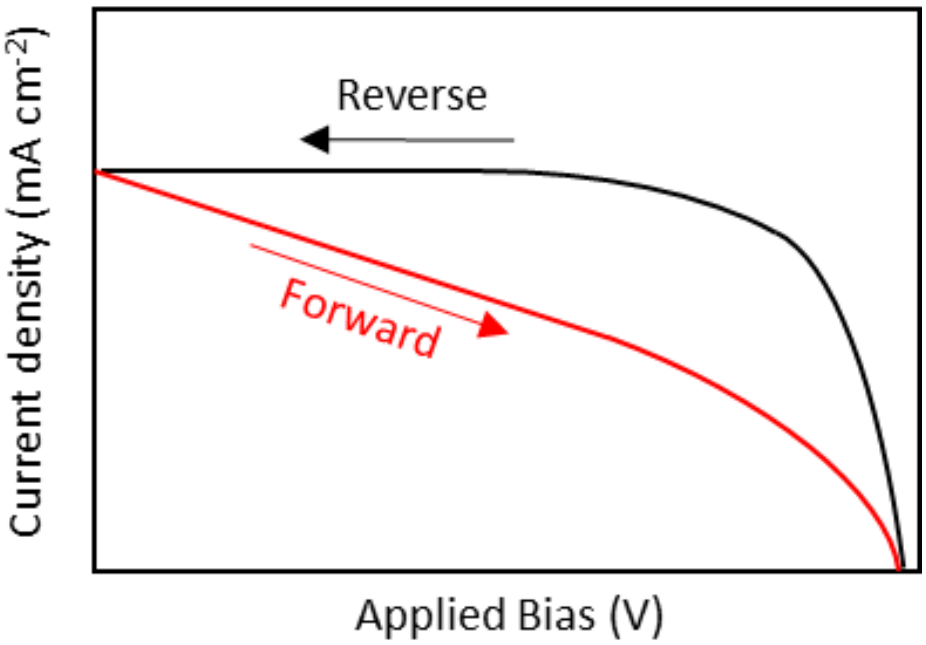


Figure 2-16 Example of OMHP hysteresis effect on J-V curve

Typically, hysteresis manifests itself in three main categories: normal, inverted and mixed. In normal hysteresis the reverse scan shows a higher FF and V_{oc}. Conversely, in inverted hysteresis the forward scan shows higher values [97]. Mixed hysteresis occurs when the forward and reverse scans cross over at a certain point. The severity of hysteresis, also known as the hysteresis index (HI) can be described simply by the ratio of the PCE of the forward and reverse scan:

$$HI = \frac{PCE_{RS} - PCE_{FS}}{PCE_{RS}} \quad (2\text{-}16)$$

where PCE_{RS} is the reverse scan efficiency and PCE_{FS} is the forward scan efficiency. The timescale at which hysteresis occurs is usually within tens of seconds [98–100].

2.2.6.1 Influence of architecture and materials

Different cell architecture and materials show different severities of hysteresis, with the worst generally being planar n-i-p architectures. Sandheep *et al.* conducted a study where they compared mesoporous TiO_2, compact TiO_2 and ETL free cells. Here, the lowest hysteresis was observed on the mesostructured cell, followed by ETL free and then compact TiO_2 [101]. A similar study was conducted by Kim and Park, where they trialled cells containing different mesoporous TiO_2 thicknesses, 220 nm, 110 nm and 0 nm. Their results indicated that thinner layers show more hysteresis, with the ETL free cell showing the highest value. This trend is also present when using SnO_2, with mesoporous architectures

again showing less hysteresis [102]. This effect of mesoporous architectures reducing hysteresis has been linked to the efficient charge carrier collection due to the increased surface area. Intriguingly, inverted planar cells utilising PCBM show very little hysteresis in the planar configuration [103]. This has been attributed to the PCBM diffusing into the perovskite and stabilizing mobile ions [104]. The type of OMHP can also influence the hysteresis; mixed cation perovskite have been shown to have reduced hysteresis [62,70,105]. Furthermore, the nature of the hysteresis has been shown to be inverted [106].

2.2.6.2 Origins of hysteresis

The origin of this effect is a heavily debated area in OMHPs, with several theories being proposed as to a possible cause. As a number of perovskite-structured materials are ferroelectric, it has been suggested that ferroelectricity in OMHPs may be the cause of hysteresis. MAPI for instance has been shown to belong to the non-centrosymmetric space group l4cm crystal group, ascribed to the rotation of the MA^+ ion [107]. Gottesman *et al.* proposed that under the application of a bias the MA^+ dipole would align itself with the field and become polarised [99]. Using density functional theory, Stroppa *et al.* determined the polarisation to be 4.47 $\mu C/cm^2$ [108]. Therefore, it could be theorised that during a J-V measurement the applied bias would pole the perovskite and the resulting polarization field would affect the inbuilt field. Depending on the field direction this would inhibit or enhance charge separation and collection leading to anisotropic J-V behaviour. This could in part explain why planar devices suffer from more hysteresis, as the field will be more unidirectionally applied to the perovskite. However, there are some studies that refute the ferroelectric contribution to hysteresis. Leguy *et al.* have estimated the timescale of ferroelectric domain relaxation to be approximately 0.1-1 ms, faster than the effect observed in the J-V curve [109]. Therefore, whilst some OMHPs may display ferroelectric properties, these may not contribute to the hysteresis in the J-V curve.

Charge accumulation due to unbalanced charge extraction has also been attributed as a cause of the hysteresis. It has been theorised that slow electron extraction leads to a build-up of charge at the n-type contact, creating a capacitance that leads to scan direction/rate dependence [96,110]. Again, this would corroborate the lower hysteresis observed in mesostructured cells, as the large surface area allows for good charge injection into the perovskite.

Another origin may be the trapping and de-trapping of charges at defect sites, occurring at the material interfaces of the cell or at grain boundaries of the OMHP. During the forward sweep, traps at these sites are filled and subsequently released under short circuit conditions, resulting in a hysteresis of the J-V curve[111]. There have been many reports that support this idea. For instance, $TiCl_4$ treatment of the mesoporous TiO_2 has been shown to reduce defects, and lead to cells with better hysteresis

characteristics[112]. Similarly, correctly controlling the annealing of both ETL and OMHP has been shown to reduce traps in the respective materials and reduce hysteresis.

Ion and vacancy migration have been one of the leading theories ascribed to the cause of hysteresis. In OMHPs the ions have been shown to be relatively mobile. Azpiroz *et al.* determined the activation energies of ionic vacancies, in MAPI, using density functional theory (DFT). Iodine vacancies (V_I), MA vacancies (V_{MA}), Pb vacancies (V_{Pb}), and iodine interstitials (I_I), were determined to be 0.08, 0.46, 0.80 and 0.08 eV respectively. Similar values were independently reported by Eames *et al.* and Haruyama *et al.* [113,114]. The low activation energies would mean that with an applied external field, ions could migrate towards the electrodes. This would lead to screening of the internal electric field caused by a build-up of charge at the contacts (see Figure 2-17). Evidence for MA^+ and I^+ migration in a weak electric field has been experimentally observed by several groups [115–117]. Furthermore, external ion migration can occur in cells that utilise certain contact layers. Li^+, H^+ and Na^+ ions have been shown to migrate through the cell during J-V measurements, potentially contributing to the hysteresis [118].

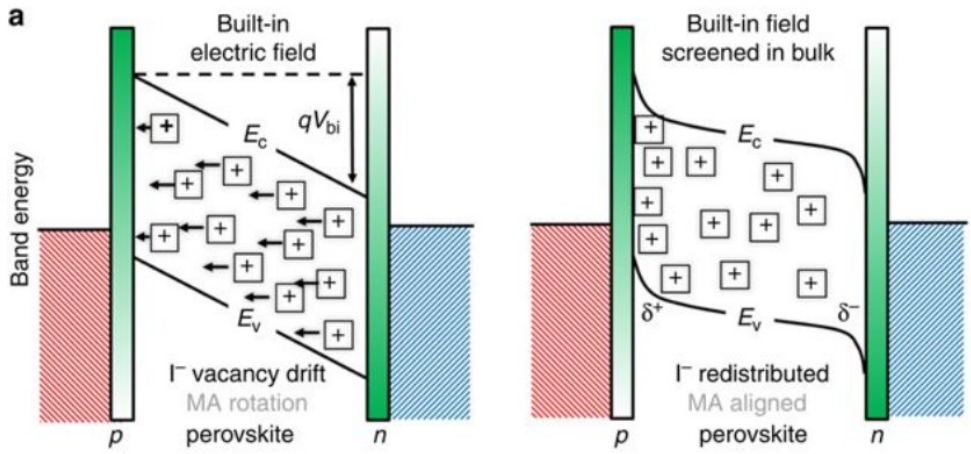


Figure 2-17 Schematic showing the effect of ion migration in p-i-n junction. Adapted from Eames et al. [119]

More recent studies suggest that the hysteresis is a product of several concurrent processes, where the sum of the effects lead to the characteristic curve [120,121].

2.2.7 Stability

One of the most challenging issues facing OMHPs is the environmental and operational instability. These materials have been shown to be susceptible to moisture, temperature, light and chemical incompatibilities with other materials found within a cell. There has been a substantial amount of research effort in this area, leading to significant progress in stability improvements. Recent trials have shown OMHP devices perform for more than 1000 h of continuous operation, whilst retaining over 80% of their initial efficiency [122–124]. However, the lifetime of a solar cell is approximately 25 years, and substantial work is still required to prove and improve their longevity.

2.2.7.1 Moisture instability

The moisture instability of OMHP has been primarily linked with the hygroscopic nature of amine salts, $MA^{+,}$ FA^{+} *etc*. In MAPI, exposure to moisture leads to the formation of a hydrated phase initially, before complete degradation into PbI_2. This process has been determined by Leguy *et al.* and can be described by the following equation [125]:

$$4(CH_3NH_3)PbI_3 + 4H_2O \leftrightharpoons [4(CH_3NH_3)PbI_3 \bullet H_2O] \leftrightharpoons (CH_3NH_3)_4PbI_6 \bullet 2H_2O + 3PbI_2 + 2H_2O \quad (2\text{-}17)$$

The initial hydrated phase is a monohydrate, $(CH_3NH_3)PbI_3 \bullet H_2O$, and continued moisture exposure will create the dihydrate $(CH_3NH_3)_4PbI_6 \bullet 2H_2O$, and finally lead to complete dissolution of the material. The monohydrate formation is reversible and device performance can be revived after drying, albeit with worse J-V characteristics that indicates a loss of film quality [126]. This process can readily occur from humidity found in ambient air. Moreover, recent studies have shown that small levels of humidity during processing can have a beneficial effect during processing, leading to devices with higher and more consistent performance. Snaith *et al.* reported that an ambient humidity of 50% enables the production of higher performance devices due to the removal of excess MA^{+} [127].

Like most properties in OMHP, the compositional can be used to modulate the material property, and this extends into improving the stability. Br substituted perovskites have been shown to be more resilient to moisture, a property attributed to the more contracted lattice due to the introduction of smaller Br ions [128]. Likewise, Cl addition has been also shown to guard against moisture degradation, due to similar effects [129,130].

2.2.7.2 Temperature stability

For OMHP cells to be commercialised they must meet a set of industrial standards. The standard used by most commercial technologies is the IEC 6125, set by the International Electrotechnical Commission (IEC). One of the main stipulations of this standard is the continuous operation of the solar cell at 85 °C for 500 hours [131]. This represents the extreme conditions the cell may undergo during operation. The temperature stability of OMHPs is therefore an important factor, as it would have to survive these elevated temperatures for prolonged periods of time. Thermogravimetric analysis (TGA) has previously shown MAPI to be stable at temperatures in excess of 300 °C, however more recent studies have shown that thermal decomposition occurs at much lower temperatures, between 60 and 140 °C [132–137]. This is well within the typical operating range of a solar cell, which can exceed 60 °C. Kim *et al.* probed the degradation mechanism using in-situ near edge absorption fine structures (NEXAFS) and observed the formation of MA, CH_3I and NH_3, indicating the primary instability is caused by the decomposition of the MA [138]. Further study by Latini *et al.* showed that there are potentially two

competing mechanisms [139]. One produces the aforementioned species, the other produces methylamine and hydrogen-iodide. The degradation pathways can be described as follows:

$$CH_3NH_3PbI_3 \rightarrow PbI_2 + NH_{3(g)} + CH_3I_{(g)} \quad (2\text{-}18)$$

$$CH_3NH_3PbI_3 \rightarrow PbI_2 + CH_3NH_{2(g)} + HI_{(g)} \quad (2\text{-}19)$$

The process described in equation 2-18 is thermodynamically more favourable but is kinetically unfavourable and tends to occur at very high temperatures. The second process, equation 2-19, is thought to be the dominant decomposition route at lower temperatures.

Composition again has a large effect on the stability. Substituting FA, forming $FAPbI_3$, has been shown to drastically improve temperature stability [140–142]. Kovalenko *et al.* demonstrated a perovskite containing guanidinium (GA) and FA to be thermally stable up to 255 °C [143]. Addition of inorganic Cs^+ and Rb^+ has also been shown to improve the temperature stability [61,62,144].

2.2.7.3 Light and oxygen induced degradation

OMHPs have also been shown to be susceptible to UV light exposure. Haque *et al.* exposed films of MAPI to light within a dry atmosphere and observed the formation of CH_3NH_2, PbI_2 and I_2 [145]. Furthermore, they show that the degradation mechanism is mediated through the formation of a reactive superoxide species, that attacks the MA of the perovskite itself. The process can be summarised as follows:

$$CH_3NH_3PbI_3 \xrightarrow{Light} CH_3NH_3PbI_3{}^* \quad (2\text{-}20)$$

$$O_2 \xrightarrow{CH_3NH_3PbI_3{}^*} O_2{}^{\bullet -} \quad (2\text{-}21)$$

$$CH_3NH_3PbI_3 + O_2{}^{\bullet -} \xrightarrow{Deportonation} + CH_3NH_2 + PbI_2 + \frac{1}{2}I_2 + H_2O \quad (2\text{-}22)$$

Here the photoexcited species in MAPI react with molecular oxygen and form an oxygen radical ($O_2^{\bullet -}$). This deprotonates the MA within the perovskite and decomposes it to form methylamine, PbI_2, I_2 and water. The timescales of this degradation have been shown to occur within a few hours to a day, signifying that when incorporated into devices OMHPs would require encapsulation. Light induced degradation has also been shown to occur due to the ETL layer, with TiO_2 producing free radicals that can induce breakdown of OMHPs, creating di-halogens. Furthermore, it has also been shown that light-induced desorption of oxygen species from the TiO_2 itself can rapidly degrade OMHP.

2.2.7.4 Material incompatibilities

At the same time as environmental issues, perovskites are susceptible to chemical exposure from solvents and other materials used during the creation of the cell. It has been reported that 4-tertbutylpyridine (TPB) and acetonitrile, commonly used as additives in organic HTMs, have shown

corrosive effects on perovskite films. [146,147] TPB has been shown to directly attack $CH_3NH_3PbI_3$ and form PbI_2 complexes.[148] Acetonitrile, which is a commonly used solvent for Li-TFSI (Li-bis(trifluoromethanesulfonyl) imide), has also been revealed to directly corrode the perovskite.

The ETL can also induce instabilities. As previously stated, TiO_2 can produce free radicals due to light. This can also occur with ZnO, which also has pH instabilities associated with it. SnO_2 has been shown to be a more stable alternative; due to its wider bandgap it produces less free radicals that can attack the OMHP [149]. Organic ETLs such as PCBM have been shown to be very stable compared to their inorganic counterparts [150].

Electrode materials can be another source of degradation. Commonly utilised metals such as Au and Ag have potential issues with OMHPs. Ag has been shown to react with OMHPs to form silver halides [151]. Au has been shown to diffuse through the HTM and perovskite layers, leading to degradation [152]. However, using Cr interlayers has been shown to prevent this. Moreover, Cu and C based electrode materials have shown much greater compatibility with OMHPs [150,153].

2.2.8 Environmental and toxicological concerns of OMHPs

The instability of OMHPs are not the only concern regarding this technology. Most high performing OMHP compositions use Pb and Sn, both of which have been shown to have detrimental environmental and health effects. Though the concentration of these compounds within a solar panel is in the few 100 mg/m^2, issues with large scale fabrication and implementation should not be overlooked [154]. For instance, the toxicological exposure threshold for PbI_2, a common precursor for MAPI, is only 2.5 mg via ingestion or 0.5 mg via inhalation [154]. In terms of the ecological impact, a study by Li et al. showed the detrimental effect of soil contaminated with perovskite precursor solution. In the study mint plants were grown in soil containing lead at a concentration of up to 250 mg/kg. The plants grown in this contained over 3000 mg/kg of Pb and showed visible deformities [155].

The inherent instability of these cells further exacerbates these concerns, as the degradation products carrying toxic compounds could readily leach into the environment[156]. Therefore, proper encapsulation and sealing of solar cells is imperative.

Due to all these concerns, the decommissioning of OMHPs must also be carefully evaluated and implemented. Several studies have shown the successful extraction of Pb and other raw materials from OMHP cells [157–159]. Furthermore, fabrication of OMHP cells using lead extracted from lead-acid batteries has also been demonstrated [160]. These studies demonstrate the viability of recycling OMHP cells and potentially reducing the impact of toxicity.

2.2.9 Processing of OMHPs

One of the main advantages OMHPs have over 1st and 2nd generation PV technologies, is the relatively inexpensive and diverse processing that can be used to manufacture devices. OMHPs are usually prepared from two main precursors components. The first typically includes an organic halide cation (O_rX^+, X=Cl,Br,I O=FA,MA). The second is an inorganic metal halide species (MX_2, M= Pb,Sn X= Cl,Br,I). These precursors can be mixed to form a variety of different OMHP compounds. The deposition of these precursors can performed via a large variety of processing techniques, such as spin-coating, blade-coating, slot-die coating, inkjet printing, screen printing, chemical vapour deposition and electrodeposition, to name a few [49,161]. The following section will focus on techniques that are most relevant to the thesis.

2.2.9.1 Spin coating-based techniques

Spin-coating was one of the original methods to synthesise perovskites. This method has several advantages due to its low cost and ease of production. However, it suffers from being a non-scalable and wasteful technique. It can be divided into two subcategories, one-step or two-step, depending on how the precursors are mixed and deposited.

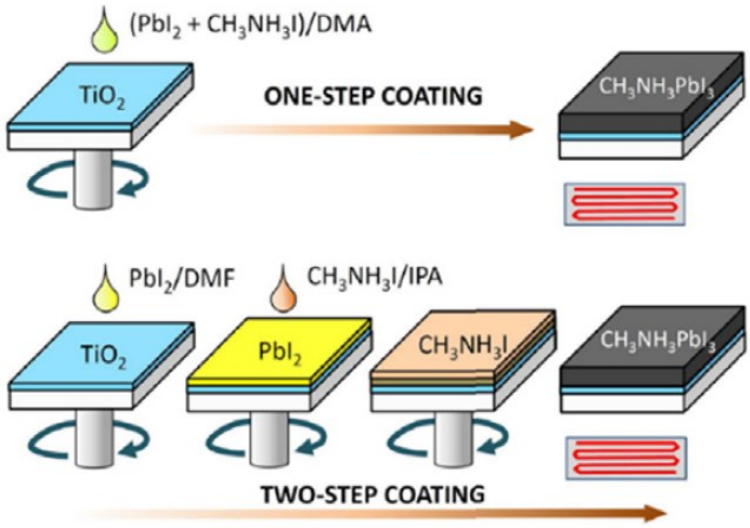


Figure 2-18 Schematic of on-step and two-step spin coating techniques. Adapted from Chen et al. (2015) [49]

One-step processing first involves mixing all the precursors into one solution. Typical solvents used to dissolve the precursors are dimethylformamide (DMF), gamma-butyrolactone (GBL), N-Methyl-2-pyrrolidone (NMP) or dimethyl sulfoxide (DMSO)[49]. The solution is then deposited onto the substrate and spun, forming a thin layer of the precursor solution. It is then annealed at elevated temperatures forming the perovskite (figure 20). Over the last decade, this process has been extensively augmented to improve film quality. Current state of the art methods utilise specific ratios of solvent to control

evaporation rates, therefore allowing for controlled nucleation of perovskite crystals, leading to smoother films with large grains [162]. Moreover, another commonly applied technique is the use of an anti-solvent during the spin-coating. Here an anti-solvent such as toluene, chlorobenzene, isopropanol and diethyl ether is applied to the substrate while it is spinning. This washes away the solvent from the precursor solution, rapidly crystallising the film. This produces very high-quality films, and has been extensively utilised in research [163]. This method is used by Liu *et al.*, who to date have the highest efficiency cell with a published method [80].

In two-step deposition the metal halide component is deposited first, again dissolved in a similar solvent. This is then followed by a deposition of organic halide cation dissolved in a solvent orthogonal to that of the first component, which is usually achieved via spin coating but can also be done by immersing the substrate in the solution. Introduction of the organic precursor leads to rapid crystallization of the perovskite and within a few seconds of annealing the film is formed. This method has been shown to work for both thin-film and mesoporous perovskites, however efficiencies have trailed behind the one step method [49].

2.2.9.2 Solvent annealing of perovskites

Solvent annealing is a commonly employed post deposition treatment and has been shown to improve device efficiencies. It involves the introduction of solvent vapour during the crystallisation process of thin films, which lowers the diffusive energy barrier and allows for the coalescence of grains. It was first discovered as an effective method to increase the crystallinity of organic semiconductors but has since been widely applied to OMHPs.

The first reported application of OMHP solvent annealing was by Huang *et al.* in 2014 [164]. Here, spin coated MAPI films were covered by a petri dish, with 10 µl of DMF applied to the edge of the dish. The films were then annealed at 100 °C for 1 h, allowing the DMF to evaporate and diffuse into the films. The treated films had increased grain sizes in the order of µm's, compared to only 260 nm in untreated films. The resulting devices utilising treated films, showed an improved PCE of 15.6% vs. 13.5% in the untreated devices. This performance uplift was primarily attributed to the reduction of grain boundaries and therefore the reduction of traps, allowing for longer charge carrier lifetimes.

To date, several other solvent vapour systems have been explored, including N_2, H_2O, DMF, γ-butyrolactone (GBL), pyridine, butanol and DMSO [165–168]. However, as yet there have been no devices reported with PCEs exceeding 20 % that have utilised solvent annealing techniques. This lack of performance may be attributed to the difficulty of applying this method consistently, as the evaporation of the solvent cannot be accurately controlled.

2.2.9.3 Chemical vapour deposition (CVD)

Chemical vapour deposition (CVD) has been extensively used in industry to fabricate a variety of thin films over a large area and is considered a relatively mature technology. The details of CVD and the mechanisms will be discussed in later sections. Here, the focus will be on how the method has been utilised to form OMHP. To date, several groups have successfully demonstrated the deposition of OMHP using CVD, however efficiencies have lagged behind those of spin-coated counterparts.

The first application of chemical vapour processing in perovskites is derived from the two-step method. In 2013 Yang *et al.* pioneered the use of the vapour-assisted solution process, a hybrid process utilising aspects of spin-coating and CVD [169]. Here, spin coated films of PbI_2 were placed within a reaction chamber containing a crucible of MAI powder. The chamber was then heated to 150 °C, creating a vapour of MAI. This reacts with the PbI_2, and through a gas-solid reaction it forms MAPI. The resulting films had micron sized grains with cells reaching an efficiency of 12.1%, competitive to many other techniques at the time. An evolution of this technique currently holds the record for CVD processed OMHPs at 18.9% [170]. The main caveat with this method is that it still relies on spin coating of the lead halide, making it less compatible for scale-up production.

The first fully-vapour-processed OMHP were deposited by Qi *et al.* in 2014 [171]. They utilised a hybrid-CVD (HCVD) technique. Here, the lead halide precursor is thermally evaporated at high vacuum, followed by the substrates being placed inside a CVD reactor and being exposed to a MAI vapour. The resulting devices had a champion efficiency of 11.8%. However, this technique is still not a true CVD technique, relying on thermal evaporation to form the lead halide precursor film. This again limits the scalability of this technique, as thermal evaporation requires very high vacuums and is limited by the effective deposition area. Since then, many variations of CVD have been utilised to produce OMHPs, including hybrid physical CVD (HPCVD), in-situ tubular CVD (ITCVD) and low-pressure CVD (LPCVD) [172]. However, most still rely on the prefabrication of a metal halide precursor film using a less scalable deposition technique, negating the advantage of the CVD technique.

Tavakoli *et al.* developed a promising one-step CVD that forms the OMHP without the need for a high vacuum process [173]. This system uses a sealed reaction chamber with two different temperature zones, a low and high zone. The precursors are placed within this chamber in the high temperature zone (up to 360°C) and the substrates are placed in the lower temperature zone (80°). In the high temperature zone, the precursors are evaporated. Argon gas is then passed through the chamber, which transports the evaporated precursors into the low temperature area, where they deposit onto the substrate. Substrates are then annealed, forming the final film. Grain sizes were in the micrometre scale and carrier lifetimes in the nanosecond scale were recorded. The champion efficiency was 11.1%.

2.2.9.4 OMHPs and Aerosol assisted chemical vapour deposition (AACVD)

This section will focus on the progress that has been made to date using AACVD to deposit OMHPs, however key aspects of the technique itself will be discussed in section 2.3.3. OMHP deposition using AACVD is a relatively niche area of research, with only a handful of studies having been published. This is most likely in part due to the challenging nature of controlling the film morphology. At the time of writing, most published research has not shown continuous films and no devices utilising the layers have been reported.

The first deposition via AACVD was done by O'Brien's group in 2014 [174]. In the study they formed $MAPbBr_3$ using a single-step reaction. To form the precursor solution, they mixed an equimolar mixture of $PbBr_2$ and MABr in DMF. This was then diluted in acetonitrile and used as the aerosol. The deposition took place at 250 °C and formed a discontinuous powdery film. They performed XRD, SEM and EDS measurements to confirm composition, showing high phase purity. In the same year Palgrave's group demonstrated the first deposition of $MAPbI_3$, also via single step AACVD [175]. Here they used an undiluted equimolar solution of PbI and MAI in DMF, and carried out the deposition at 200 °C. The material was also characterised via XRD and SEM, but added absorption and XPS measurements. The resulting films showed high phase purity, however, were discontinuous and film thickness was unreported. In 2016 , Nishinaka *et al.* deposited $MAPbBr_{1-x}Cl_x$ [176] using a single step process. In this study they mixed different ratios of $PbBr_2$, MABr and MACl and were able to incorporate 15% of Cl into the structure. Again, the films were discontinuous and not suitable for any devices.

In 2015 the Binions group demonstrated a two-step deposition method, which showed improved continuous film morphology and a film thickness of 1.5 µm[177]. This was the first continuous film to be produced via AACVD. The films were formed by first depositing PbI_2 at 70 °C and then subsequently exposing the film to a MAI aerosol at 230 °C, forming MAPI. The films were characterised by XRD, XPS and absorption measurements. However, no devices were fabricated. More recently, a three-step method was utilised to form films of MAPI [178]. This method is an evolution of the work done by the Binions group and included an intermediary annealing step. This was done between the first and second step to dry the PbI_2 precursor film. The focus of this study was to characterise the compositional variance throughout the surface and to use ellipsometry to measure dielectric and absorption coefficients of the film. The film thickness was stated as being less than 400 nm, however the cross-sectional SEM does not clearly show the film morphology. In a recent study, Flavell *et al.* used lead thiocyanate ($Pb(SCN)_2$) as the metal cation source to form a continuous layer of MAPI from a single step [179]. They report a film thickness of 600 nm, however the film is very rough and has

numerous pinholes. The films showed good ambient stability, remaining stable for one month. Furthermore, they showed a high tolerance to moisture. Again, there were no devices reported.

Recent studies utilising AACVD have been primarily focused on inorganic halide perovskites. A 2017 study synthesised a suspension of $CsPbBr_2I$ nanoparticles, which were then deposited as a thin film using AACVD [180]. The films have a rough surface composed of cubic nanoparticles and were characterised using XRD, SEM and TEM. Moreover, the film thickness was unreported. In 2018 the deposition of Cs_2SnI_6 double perovskite was reported, which marks the first time a double perovskite was deposited using AACVD [181]. Furthermore, the perovskite solutions were modified using hydriodic acid and the resulting films were shown to be stable in ambient conditions. The films were primarily composed of nanoparticles, however they seemed to be quite densely arranged. The thickness was reported to be approximately 1.2 µm. The films were characterised using XRD, SEM, EDS and XPS. These techniques were also used to track changes in the films after 100 days of aging, indicating favourable stability.

To date, there have been only a few studies utilising AACVD for perovskites, with even fewer showing continuous films suitable for PV devices. So far there have been no working devices reported in any form and most of the characterisation is relatively limited. A summary of AACVD in relation to perovskites can be seen in Table 2-3.

Table 2-3 Summary of studies utilising AACVD to deposit OMHPs

Year	Perovskite	Cont. Film	Thickness	Method	Substrate	REF
2014	$MAPbBr_3$	N	NA	1-Step	Glass	[174]
2014	$MAPbI_3$	N	NA	1-Step	Glass + c-TiO_2	[175]
2015	$MAPbI_3$	Y	1.5 µm	2-Step	FTO	[177]
2016	$MAPbBr_{1-x}Cl_x$	N	NA	1-Step	c-TiO_2	[176]
2017	$MAPbI_3$	Y	<500 nm	3-Step	Glass	[178]
2017	$CsPbBr_2I$	N	NA	Colloid+ 1-Step	Glass	[180]
2018	Cs_2SnI_6	N	NA	1-Step	ITO + Au-Si	[181]
2019	$MAPbI_3$	Y	600 nm	1-Step	ITO	[179]

2.3 CHEMICAL VAPOUR DEPOSITION

AACVD is a variation of CVD that relies on aerosol delivery of the precursors. It is a scalable, flexible and low-cost deposition method making it potentially ideal for OMHP deposition. This section will describe the key principles of CVD and thin film growth, with a focus on AACVD.

2.3.1 Introduction to CVD

Chemical vapour deposition (CVD) is one of the most common routes for thin film production in industry. It involves the disassociation and/or chemical reactions of gaseous reactants in an energetic environment, resulting in the formation of a product.

CVD processes can trace back their development to the late 19th century, with the first patents filed by Sawyer and Mann describing a process to coat lamp filaments with metals[182]. Further patents were filed by Lodyguine and Aylesworth for similar uses. In this era, CVD also proved to be an economical way to extract and produce high quality refractory metals, such as Ti, Ni, Zr, and W. However, over the last 50 years CVD has been developed to deposit a variety of materials, including II-V and II-VI materials, carbides, borides, nitrides and oxides. Moreover, since the 1970s CVD has been extensively utilised by the electronics industry to scalably produce high quality thin films from semiconducting materials over. In terms of photovoltaics, CVD has been used to deposit various components of the solar cell, from the TCO to the active layer itself [183].

2.3.2 The CVD Process

A CVD system can be broken down into three main components. The first is the precursor supply system, which is responsible for producing a gaseous reactant species. The second critical component is the reaction chamber; this usually consists of an enclosed vessel where the CVD process itself occurs. It is within this vessel that substrates are placed and heated, facilitating the deposition of the desired material. The final component is the effluent gas handling system. This is responsible for removing the excess reactant from the chamber, but in low pressure CVD systems acts as the vacuum source [182].

The steps within the CVD process can be broken down into the following:

1. Generation of gaseous precursors to form gaseous reactant species.
2. Transportation of these reactant species into the reaction chamber/substrate.
3. The reactants undergo a gas phase reaction forming the intermediary species:
    a. At temperatures above the decomposition temperature of the species, homogenous nucleation can occur. This tends to result in the formation of powders rather than thin films.

b. Below the decomposition temperature, the species diffuse through a boundary layer onto the substrate and undergo steps 4 – 7. The boundary layer effect and its origin will be detailed in section 2.3.2.3.

4. Species are absorbed onto the heated substrate, and heterogenous reactions occur at the substrate surface. This results in a deposit of the desired material.
5. The deposit diffuses along the heated substrate surface and creates a crystallisation centre, from where the film grows.
6. Volatile by-products are removed from the surface by reverse diffusion or convection through the boundary layer.
7. Un-reacted precursor species and by-products are removed from the reaction chamber.

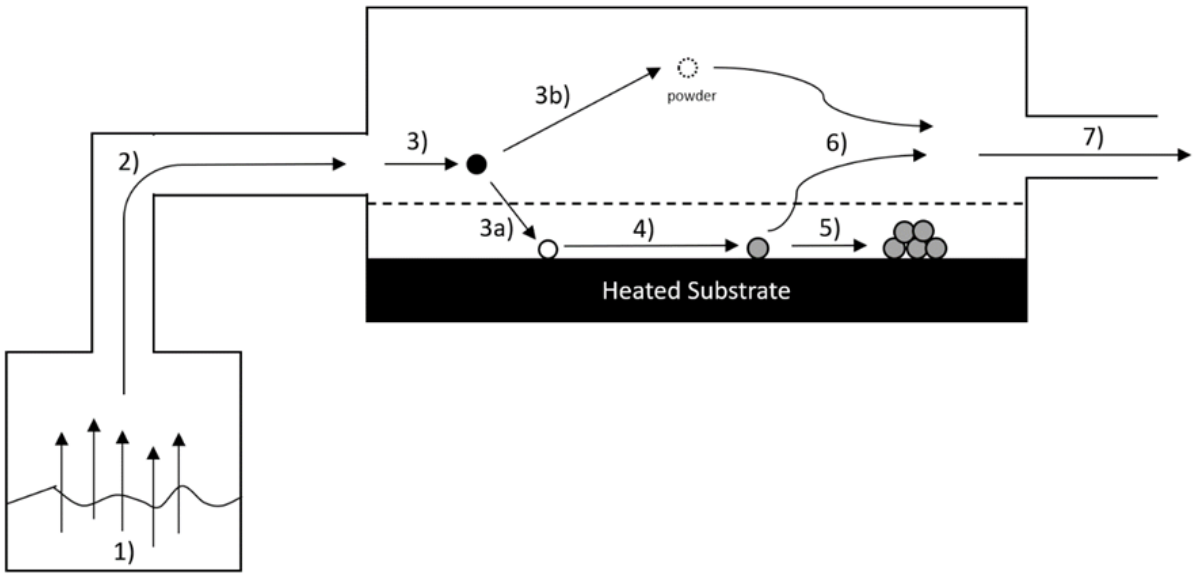


Figure 2-19 schematic illustration of the CVD steps during deposition [182]

2.3.2.1 Thin film growth

For a thin film to form, material must nucleate and grow on the substrate. For this to occur, atoms that adsorb at the surface must reach a critical cluster size before they become thermodynamically stable and allow for further growth. As CVD is a dynamic process, with material being constantly absorbed and desorbed, the critical cluster size is governed by the deposition parameters and the nature of the atomic bonds of the material itself. This process can be described using classical nucleation theory.

The cluster size required, and the Gibbs free energy required to grow from a nucleate can be described by the following equations:

$$\Delta G = \Delta G_s - \Delta G_v \quad (2\text{-}23)$$

Where ΔG_s (J) is the energy requirement to form a new surface, ΔG_v (J) is the free energy contribution when surrounding a particle in a precipitate and ΔG (J) is the total Gibbs free energy. The contributions can be calculated using:

$$\Delta G_s = A_s \gamma \quad (2\text{-}24)$$

$$\Delta G_v = V \Delta g \quad (2\text{-}25)$$

Where A_s (m^2) is the surface area of the cluster, γ (N m^{-1}) is the interfacial energy, V (m^3) is the volume of the cluster and Δg (Jm^{-3}) is the free energy per unit volume. At small cluster sizes the positive ΔG_s term dominates and further nucleation is unfavourable. As the cluster size grows the negative ΔG_v becomes dominant and nucleation and growth becomes more favoured. The critical point ΔG^*, at which formation is stable, is when dG/dr = 0. Figure 2-20 shows the contributions and the location of the critical nucleation energy.

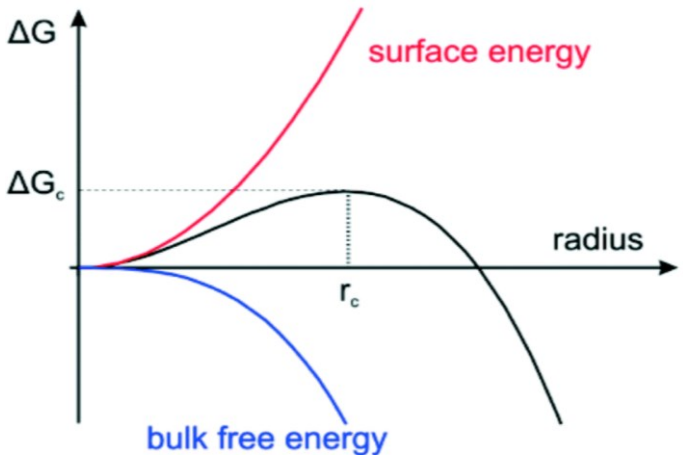


Figure 2-20 Dependence of the cluster free energy, ΔG, on the cluster radius, r. The curve illustrates the maximum free energy at the critical cluster size, r_c.

However, this only describes homogenous nucleation. As nucleation occurs heterogeneously on a flat substrate in CVD it is necessary to consider the surface energy contributions of the substrate:

$$\Delta G_h^* = f(\theta) \Delta G^* \quad (2\text{-}26)$$

$$f(\theta) = \frac{1}{4}(2 + cos\theta)(1 - cos\theta)^2 \quad (2\text{-}27)$$

$$cos\theta = \frac{\gamma_s - \gamma_n}{\gamma_n} \quad (2\text{-}28)$$

Where ΔG_h^* is the critical heterogenous nucleation energy, θ is the contact angle of a liquid on a surface, γ_s (Jm^{-2}) is the surface energy of the substrate, γ_n (Jm^{-2}) is the surface energy of the nucleus, and γ_{sn} (Jm^{-2}) is the interfacial energy between them.

The growth rate of a CVD reaction can be described using the following equation [184]:

$$R = \frac{1}{N}\left(\frac{k_s h_g}{k_s + h_g}\right) C_g \qquad (2\text{-}29)$$

Where R is the growth rate, N is the number of atoms per unit volume of the film, k_s surface reaction rate constant, h_g is the gaseous mass transport coefficient and C_g is the concentration of the precursor.

This growth rate can be simplified depending on if the deposition is mass transport limited ($k_s >> h_g$) or surface reaction limited ($h_g >> k_s$). In mass transport limited cases the surface reactions occur very quickly, and the growth rate is limited by the amount of precursor that can be delivered to the substrate. Here the growth rate can be approximated to [184]:

$$R = \frac{1}{N} h_s C_g \qquad (2\text{-}30)$$

If the reaction is surface reaction rate limited, then the equation can be approximated to:

$$R = \frac{1}{N} k_s C_g \qquad (2\text{-}31)$$

Moreover, in this case the rate can also be described by the Arrhenius equation:

$$k = A e^{\frac{-E_a}{RT}} \qquad (2\text{-}32)$$

Where k is the rate of the reaction, E_a (J mol^{-1}) is the activation energy, R is the universal gas constant, T is temperature and A is a pre-exponential factor.

Depending on which mode the CVD reaction occurs, the resulting morphology of the film can be drastically affected. Mass transport limited systems tend to produce inhomogeneous films, whereas surface reaction rate limited systems tend to produce smooth and uniform films (Figure 2-21).



Figure 2-21 Schematic showing thin film growth in surface rate reaction limited and mass transport limited systems

2.3.2.2 Growth Modes

Films deposited via the CVD process are primarily amorphous polycrystalline in nature (see Figure 2-22). Amorphous films exhibit no long-range order and in terms of electronic properties are generally undesirable. This type of film usually grows at low substrate temperature, where the mobility of the adsorbed species is too low for it to diffuse to more energetic sites and crystallise.

Polycrystalline films form when material nucleates from multiple sites on the substrate and coalesce together to form a film. The arrangement of the crystals in these films tend to either be equiaxial or columnar. Columnar structures consist of highly orientated grains growing from the initially nucleated layer of material. They tend to form due to superstation of the precursor and low substrate temperatures, which limit the nucleation points. Equiaxial structures consist of small randomly orientated grains. Such structures result from very high supersaturation of precursors which forces the precursors to rapidly nucleate before they migrate to a preferential crystal site [182].

Polycrystalline films can also be grown via epitaxy. Epitaxial film growth consists of crystals that have a well-defined orientation with respect to the substrate. The simplest case of this type of growth is when two isomorphic materials, *i.e.* materials with the same crystal structure, are grown on top of one another. Here the crystals in the deposited material will tend to share the orientation of the substrate. Polymorphic materials, *i.e.* materials with the different crystal structures, or even completely dissimilar materials may also have epitaxial effects. For instance, naturally occurring rutile TiO_2 shows epitaxial growth on hematite [185].

They form at low super saturation of precursors and high substrate temperatures. This facilitates the diffusion of the precursor across the surface of the substrate to a preferred nucleation point with the lowest energy. This leads to the growth of the solid from a preferred orientation. Typically, this type of film growth requires the substrate to be free of any contamination, otherwise materials may nucleate from impurities and form a polycrystalline film. Epitaxial films tend to exhibit excellent properties and are desirable for semiconductor applications, however due to the higher temperature and cleanliness requirements they require costly equipment [182].

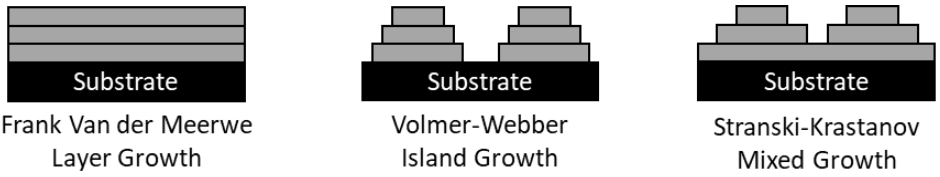


Figure 2-22 Schematic of different thin-film growth modes

The growth mechanism of the thin film can be described by three main classifications: Volmer-Webber (VW), Frank Van Der Merwe (FDM) and Stranski-Krastanov (SK) (Figure 2-22). Volmer-Webber, also known as island growth, describes the process where the material preferentially grows on previously deposited material. This occurs due to more favourable bonding between the deposited material than between the deposited material and the substrate. Films that grow in this fashion tend to have rough surfaces and are either amorphous or polycrystalline in nature. This growth mechanism is typically the least favoured as it produces films with bad homogeneity. Frank Van Der Merwe growth, or layer by

layer growth, is a growth mechanism where the deposition material preferentially deposits onto the substrate, forming a complete layer before the subsequent material is deposited. This mechanism tends to result in films of a high quality and low roughness, ideal for semiconducting applications. Stranski-Krastanov growth is an intermediate mechanism that combines aspects of VW and FDM growth. Here a transition from the initial FDM growth to VW growth occurs at a critical thickness and the transition is primarily affected by the chemical and physical properties of the substrate, such as lattice parameters and surface energy [186].

2.3.2.3 Precursor Flow

Within a CVD reactor, the controlled delivery and flow of the precursor to and over the substrate is critical. The precursor motion must be carefully considered in order to controllably deposit high quality films.

CVD systems typically operate in one of two precursor flow regimes, depending on their operating pressure. In low pressure systems, the mean free path of molecules within the chemical vapour is quite large (>5 cm), and it is said that they operate within a free molecular flow regime. At pressures approaching atmospheric conditions, molecules have a shorter mean free path as collisions readily occur. In this regime the vapour begins to act like a fluid, this is called the continuum flow regime. The Knudsen number (k_n) can be used to determine which regime the system is in [182]. It is the ratio of the gas mean free path and the characteristic reactor dimension:

$$k_n = \frac{w}{x} \qquad (2\text{-}33)$$

Where w is the reactor width and x is the mean free path of the gaseous species. If $k_n >> 1$ the reactor is operating under the continuum regime and when $k_n << 1$ then it is operating in a molecular flow regime. This is typically the regime that AACVD occurs at, with the fluid flow characteristics of the carrier gas directing the precursor flow.

The fluid flow of CVD systems operating in the continuum regime must be carefully controlled to ensure homogenous delivery of the precursor. Typically, the flow of gas over the substrate is laminar rather than turbulent in nature. In other words, the precursor gas smoothly flows over the substrate. The smoothness of this gas flow can be described by the Reynolds number (R_e):

$$R_e = \frac{\rho u L}{\mu} = \frac{uL}{\nu} \qquad (2\text{-}34)$$

Where ρ is the fluid density, u is fluid velocity in respect to substrate, L is a characteristic dimension (*i.e.* reactor length), μ is the dynamic viscosity of the fluid and ν is the kinematic viscosity of the fluid. A high R_e (> 2100) indicates turbulent flow, and a low R_e (>10) indicates laminar flow [182].

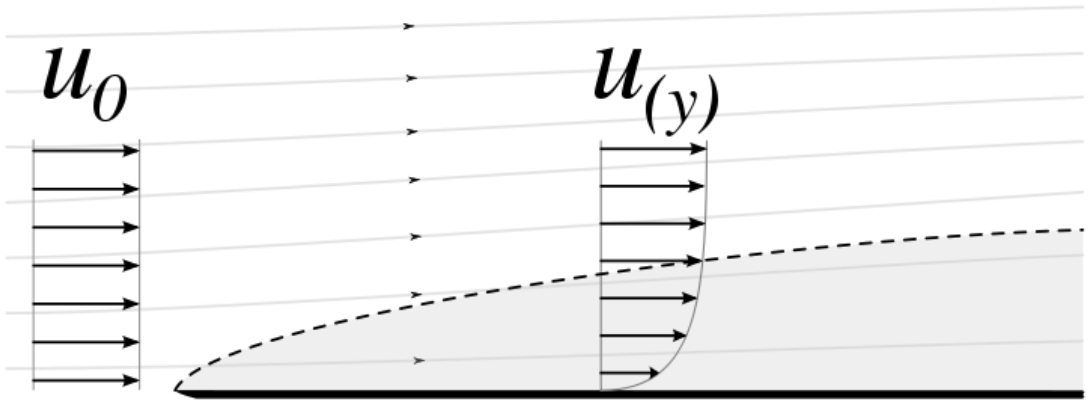


Figure 2-23 Development of boundary layer over a flat. Adapted from Flanker (2008) [187]

As the gas flows, a boundary layer is formed between it and the static substrate. This is a stagnant layer of gas that forms due to aerodynamic effects, as fluid flows over an object. In CVD, precursors must diffuse through this layer to adsorb onto the substrate, hence the thickness of this layer is important to control.

2.3.2.4 Variations of CVD

CVD usually describes the general process, however there are many variations that exist. Most variations are distinguished by their different operating regimes, or their different precursor delivery systems.

The most conventional form of CVD is termed thermally activated CVD (TACVD). Here precursors reactions utilise thermal energy, usually provided by heating the substrate or chamber, to activate the desired chemical reactions. This can be furthered sub-divided depending on their operating pressure during deposition. They are usually classified as atmospheric pressure CVD (APCVD), low pressure CVD (LPCVD) or ultra-high vacuum CVD (UHVCVD). LPCVD systems typical operate at 1-100 Pa and UHVCVD operate below 10^{-6} Pa. Whilst in all cases the reactions are thermally driven, the pressure can significantly alter the way the material grows. For instance, in LPCVD the rate limiting step is the surface reaction at the substrate, as precursor can readily adsorb onto the substrate. Conversely, in APCVD the precursors must diffuse through a boundary layer, making it a mass transport/diffusion limited process [182].

The source for the activation energy of the precursors is also an important differentiator. For instance, utilising plasma (Plasma Enhanced CVD), to provide the activation energy has been demonstrated to allow reactions to occur at much lower temperatures. This enables the use of temperature sensitive substrates, allowing for previously unfeasible material combinations. For instance, it allows the

coating of metal substrates with nitrides [188]. Other sources of activation include light (photo-assisted CVD) and microwave (micro-wave plasma assisted CVD) [182].

The delivery of precursors is another differentiator between CVD systems. In conventional CVD, the precursors are heated and vaporised, before being introduced into the chamber via an inert carrier gas. For instance, in flame-assisted CVD the precursors are delivered by introducing precursors into a flame. Here the flame provides the activation energy and the thermal energy to vaporise the decomposed precursors. Direct liquid injection CVD (DLICVD) utilises liquid precursors, which are introduced into a vaporisation chamber via injectors. This is akin to the process found in common direct injection gasoline engines [189].

2.3.3 Aerosol Assisted CVD (AACVD)

As previously discussed, the precursor delivery is a key way to categorize a CVD method. This study utilises a CVD technique based on aerosolised precursors called aerosol assisted CVD (AACVD). The term aerosol was first coined by Frederick Donnan in the early 19th century, where he used it to describe microscopic particles in air [190]. However, this definition has been expanded to also include liquid droplets suspended in gas. Whilst aerosols are typically associated with synthetic processes, they can also occur naturally. For example, atmospheric dust, fog and clouds are commonly observed aerosols created due to natural phenomena.

The aerosol is typically formed by sub-micrometre precursor droplets that are suspended in an inert carrier gas. The precursor is typically formed by dissolving chemical compounds into suitable solvents. As the aerosol is introduced into the heated reactor, the solvents will rapidly evaporate or combust. The chemicals then decompose and/or react near/on the substrate surface and form the final film [182].

AACVD has several advantages:

1. Aerosol generation is much simpler than the conventional thermal vaporisation methods, therefore reducing complexity and cost.
2. As it uses chemical solvent mixtures as the basis of the aerosol, multiple chemicals can be stoichiometrically mixed and introduced to the chamber in one step. This allows for a more facile deposition of multicomponent systems, as individual components do not have to be separately introduced into the chamber.
3. Deposited material forms rapidly at low temperatures, as the precursors are transported near the substrate surface and only need to diffuse a short distance.
4. It is an atmospheric process and therefore requires no sophisticated reactor or vacuum systems.

2.3.3.1 Aerosols and generation

The method of aerosol generation is very important. Depending on how an aerosol is generated, it can alter the size, distribution and concentration of the aerosol droplets. These parameters heavily influence the deposition of the precursor on the substrate and therefore also affect the film formation. There are several ways in which an aerosol can be generated. The most common methods include pneumatic/collision atomisation, electrostatic atomisation and ultrasonic aerosol generation. Pneumatic/Collison atomisation involves a high-pressure jet of gas passing over an orifice connected to a reservoir of liquid. Due to the Bernoulli principle, the liquid is pulled through the orifice into the stream of gas and is then broken apart into small droplets [191]. Electrostatic atomisation uses a potential applied to a spray nozzle that causes finely charged droplets to be ejected, forming a Taylor cone. Ultrasonic aerosolization utilises a piezoelectric transducer to pulse an ultrasonic wave into the precursor solution, breaking up the surface of the liquid and forming small liquid droplets.

2.3.3.2 Ultrasonic generation of aerosol

Ultrasonic aerosol generation is the method utilised for aerosol generation within this study. In this method the nature of the aerosol produced depends on the nature of the liquid precursor and the properties of the ultrasonic wave used to break up the liquid. Using the following equation established by Lang, the median droplet size due to ultrasonic pulsing [192] can be determined:

$$d = 0.34\left(\frac{8\pi T}{\rho f^2}\right)^{\frac{1}{3}} \qquad (2\text{-}35)$$

Where d is the median droplet size, T is the surface tension of the liquid, ρ is the liquid density and f is the frequency of the excitation wave. From this it can be deduced that a transducer with a narrow excitation frequency would produce an equally narrow distribution of droplet sizes, which is why this method tends to be quite suitable for high quality aerosol generation.

2.3.3.3 Aerosol flow in the reactor

The way a liquid droplet behaves within a gaseous suspension can be described by Knudsen number (k_n).

$$k_n = \frac{2\lambda}{d} \qquad (2\text{-}36)$$

Where λ is the mean free path of the suspending gas and d is the diameter of the aerosol droplet. Similarly, to the flow regimes of gas, droplets can be either in the free molecular regime ($k_n >> 1$) or the continuum regime ($k_n << 1$). In the molecular flow regime, the droplets will behave similarly to the gas molecules and follow the flow of the gas. In the continuum flow regime, gas molecules flow around the droplet and don't readily flow with the stream of gas.

2.3.3.4 AACVD reaction pathways

Once the aerosol is introduced into the reactor it can undergo several possible mechanisms depending on the temperature within the reaction chamber [182]. The processes are illustrated in figure 2-24.

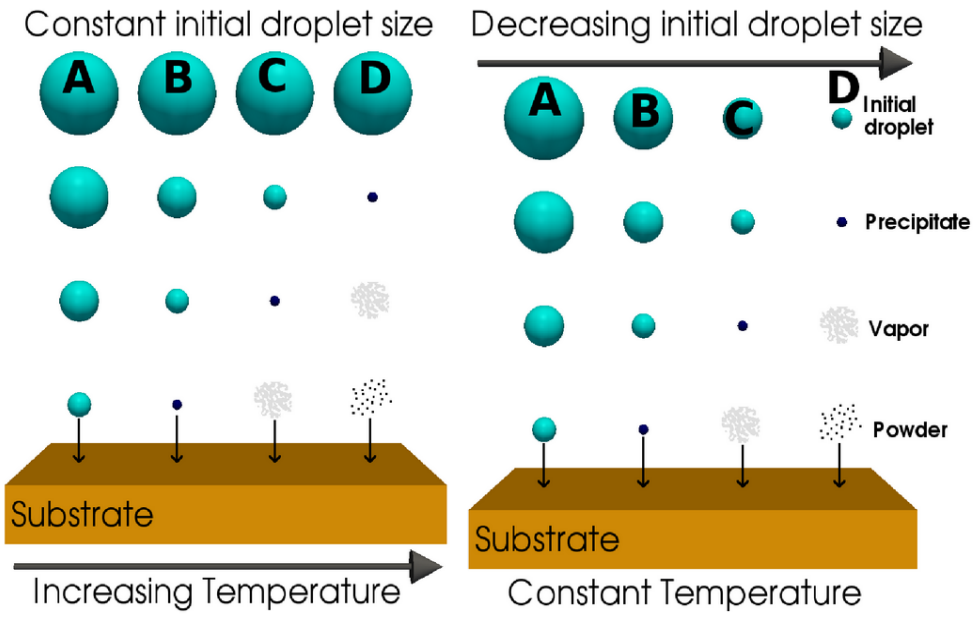


Figure 2-24 Diagram illustrating aerosol reaction pathways with varying temperature and varying drop size. Adapted from Filipovic 2012 [193]

A. In this pathway the aerosol is directly sprayed onto the substrate and the solvent is subsequently removed via evaporation and the precursors decompose to form the final film. This is akin to spray coating and tends to lead to suboptimal film quality, as the continuous wetting and drying of the solvent on the substrate may lead to cracking and roughening of the film.
B. Here the solvent is evaporated before the precursor adsorbs onto the substrate. The precursor typically then undergoes a chemical reaction or decomposes to form the final desired film.
C. Here the solvent is firstly evaporated and then the precursor is also vaporised near the substrate surface. The vaporised precursor then adsorbs onto the surface of the substrate and undergoes the decomposition or chemical reaction to form the final film. This mechanism emulates the heterogenous nucleation typically found in standard CVD systems and produces high quality and dense films.
D. At elevated temperatures the decomposition and reaction of the precursors can occur in gas phase, leading to homogenous nucleation of material. These particles then adsorb on the substrate where they may be sintered together. These films tend have a poor morphology, with a tendency to be porous and have poor substrate adhesion.

Only pathways C and D can be considered true CVD processes, as there is a formation of a chemical vapour that undergoes subsequent chemical reactions. Furthermore, a similar trend would be observed with varying aerosol droplet size. Smaller precursor droplets would evaporate more rapidly, due to their higher surface area to volume ratio, and therefore this would be analogous to the effect of increasing deposition temperature. Therefore, for a given system it is important to try and identify and optimise the processing conditions to allow for deposition of high-quality films.

3 Experimental Apparatus & Methods

This chapter will detail all the experimental setups and methods used within this study. The primary focus will be on the AACVD system, followed by device fabrication methods and characterisation techniques. Additionally, contributions and collaborations will also be detailed.

3.1 Reactor Equipment Design

The AACVD setup consists of two main components, one is the heated reaction chamber and the other is the aerosol precursor delivery system. Figure 3-1 shows a simple schematic of the setup. For this study both components were developed and modified to improve the performance and consistency. This section will briefly cover the designs of both components and the overall setup used in this study.

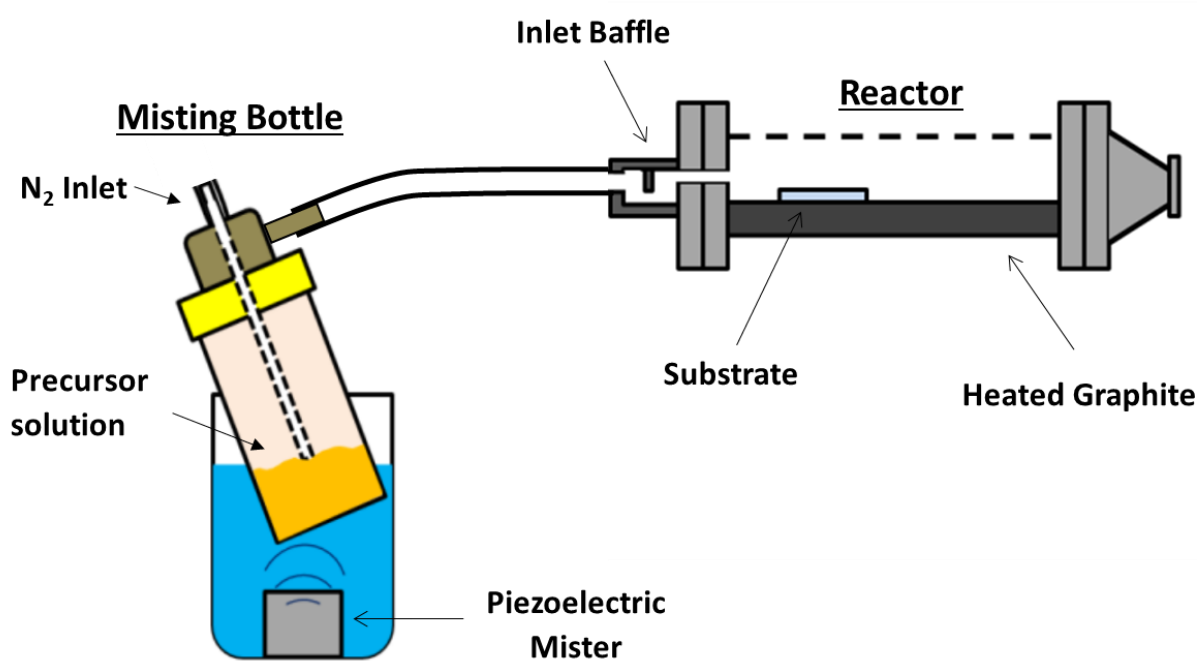


Figure 3-1 Schematic of AACVD setup

3.1.1 Aerosol Generation

This study utilised an ultrasonic piezoelectric mister to create the aerosols. The theory behind this method is detailed in section 2.3.3.2. This mister uses a 20 mm piezoelectric membrane, which is specified to operate at a frequency of 2 MHz. This unit is then placed within a beaker and immersed in water. The misting bottle, containing the precursor solution, is then held above the mister using a clamp. Once the mister is turned on it will begin to aerosolise the solution in the bottle, which is then carried into the reactor using N_2 via Tygon tubing. The nitrogen pressure is set at 1 bar and is controlled via a Patton gas flow meter.

Using the Lang equation (2-35), the expected droplet sizes can be calculated for both MeOH and DMF, the two solvents used in the study. DMF would yield a median droplet of approximately 2 µm and for MeOH it would be 1.9 µm. However, these are estimates for droplet sizes at the point of generation, and do not account for coalescence of droplets as they are flowed in the reactor.

The misting bottle itself was developed specifically for use with high surface tension solvents, such as DMF. Previously, a glass flask was used to hold the solution, however aerosolising solutions proved difficult. This was because the wall thickness of the glass vessels significantly reduced the effect of the ultrasonic pulse. Conversely, this study's misting bottles are made of low-density polyethylene (LDPE), with a thinner wall thickness. This more effectively allowed the ultrasonic pulse to pass though into the solution, creating a better aerosol. Furthermore, the glass vessels were fragile and commonly developed fractures.

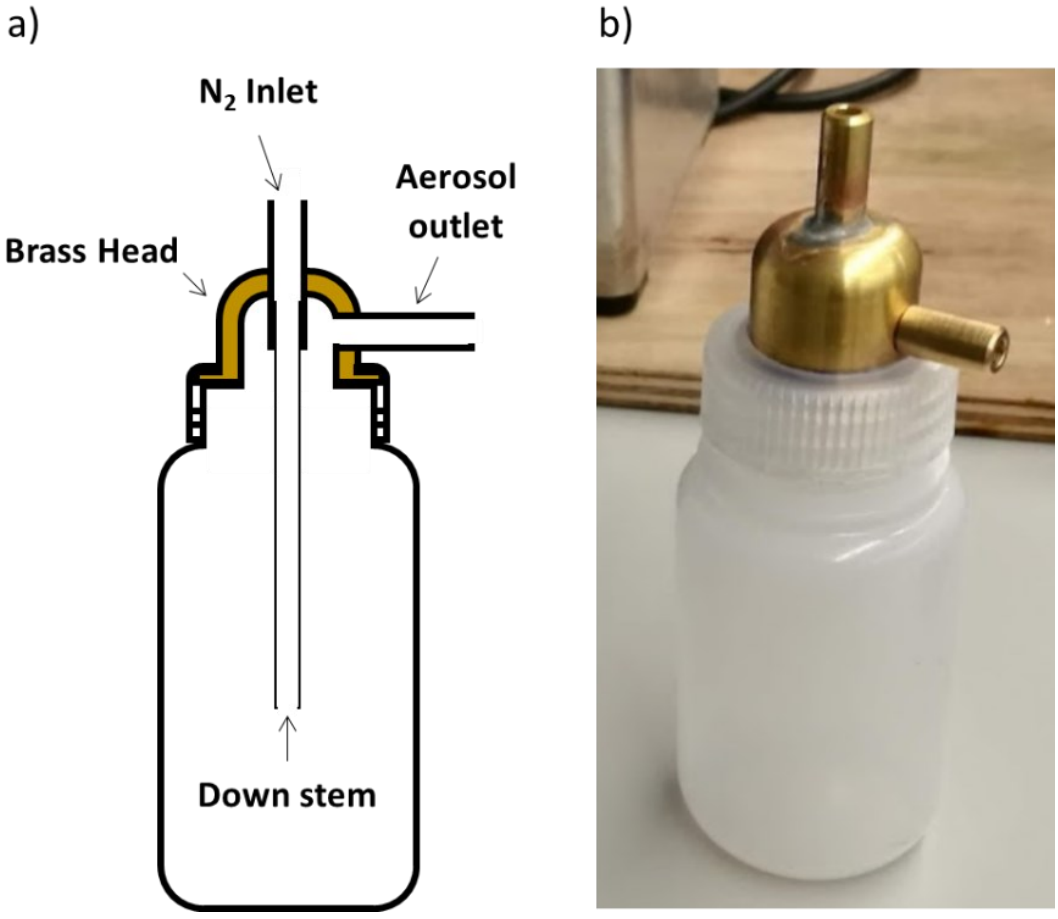


Figure 3-2 a) Schematic of misting bottle b) Photograph of misting bottle

The bottles were designed by using the body and lid of commonly available solvent bottles (VWR 215-343). The inlet and outlet were integrated into a head machined from naval brass (CW712R). CW712R was chosen due to its improved chemical resistance and relatively good machineability. This head was then integrated into the solvent bottle lid by cutting an orifice into the centre of the lid and fitting the

head. This enables use of the existing thread of the bottle lid to screw the head onto the solvent bottle. This design also had several practical advantages as it allowed for facile replacement and cleaning of all components. Another key aspect of this design was the inlet stem, which is designed to allow the carrier gas to push the aerosol out from the bottom of the vessel. In this design the stem is also replaceable. The heads were designed to use leftover needle covers from Braun Sterican 0.8 mm x 120 mm needles, which again simplifies replacement and cleaning. The schematic and image of the bottle lid can be seen in Figure 3-2.

3.1.2 Reactor Components

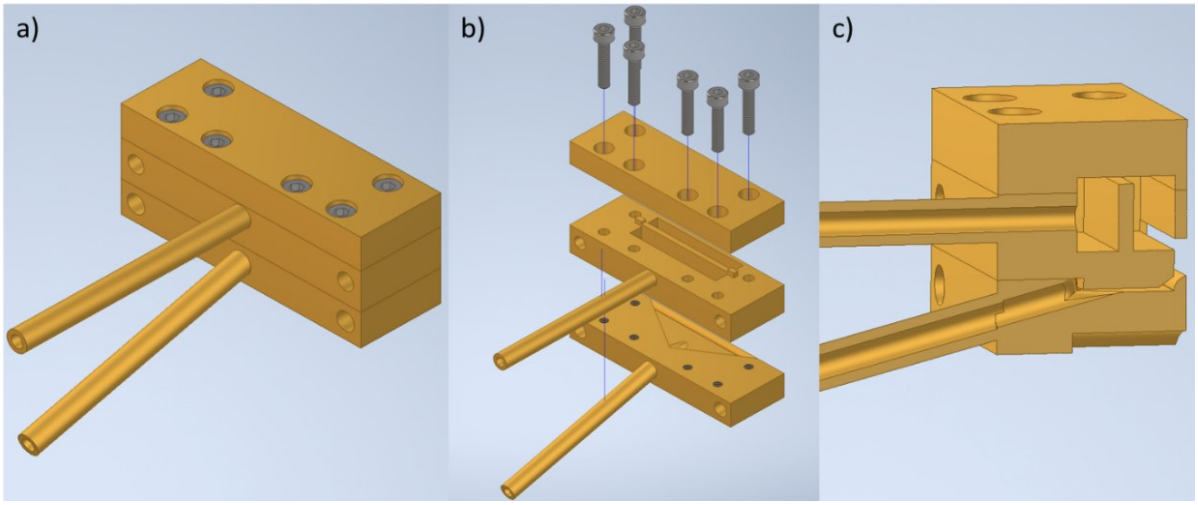


Figure 3-3 CAD model of inlet baffle. a) shows complete baffle b) exploded view revealing three main components. c) cutaway view revealing baffle cavities

For this study a cold wall reactor was constructed based on an existing design within the Binions group. The reactor consists of three major components, the reaction chamber, the heating system and the inlet baffle. Arguably the most important of these is the inlet baffle, which is responsible for planarizing the flow of aerosol. The baffle is constructed from three parts machined from CW712R naval brass and two stainless steel tubes brazed into the baffle. These three parts are then bolted together and form two inlets and baffle cavities. The first cavity is shaped as a rectangular cuboid with a single plate placed perpendicularly to the gas flow. As the gas flows in from the inlet, it flows around the plate and exits through a thin slit, therefore transforming the cylindrical flow of gas into a planar stream. The second cavity, which was not used during this study, is a thin spade shaped cavity. Here the gas enters in at the pointed side and exits through a thin slot at the wide end. A schematic of the cavity and the baffle CAD model can be seen in Figure 3-3.

The second major component is the reaction chamber itself, which consists of a faceplate, a central tube, an exhaust and supports used to mount all the components together. The face plate, exhaust and supports are all machined from 316 stainless steel and the tube is made of quartz. The face is

responsible for mounting the baffle and heater components. Steel rods are used to fasten all these components together to form the complete reactor. Figure 3-4 shows the complete reactor assembly with the baffle fitted.

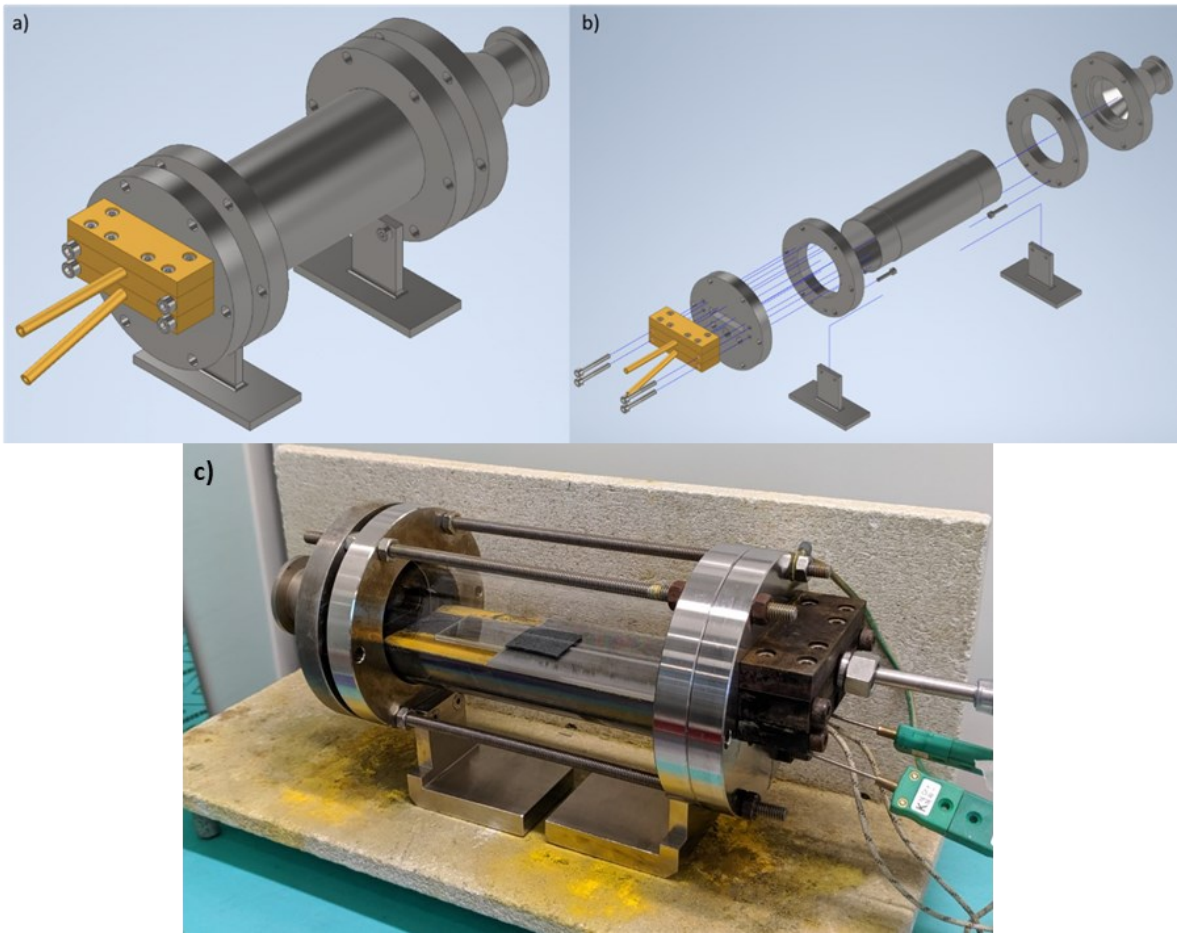


Figure 3-4 a) CAD model of the complete reactor with the baffle mounted b) exploded view of reactor components c)Photograph of assembled reactor with a Quartz tube

The final set of components are all related to the heating system. As stated previously this reactor utilises a cold wall design, meaning that the thermal source is localised and directly heats the substrate. In this design this is achieved via a heated graphite block on which the substrates are placed. The heat source is a Watlow cartridge heater that is mounted to the faceplate and is embedded into the graphite block. Figure 3-4 shows an example of this assembly. To control the heater, two 150 mm type-K thermocouples (RS PRO Type K Thermocouple) connected to a Eurotherm 3126 temperature controller and a Tempatron 4800 were used. The Eurotherm is responsible for setting and controlling the temperature, whilst the Tempatron limits the maximum temperature of the reactor in case of failure. Moreover, the faceplate of the reactor was grounded to reduce the risk of electrical shock and to reduce the build-up of static electricity.

To test this design before fabrication, a simple computational fluid dynamic (CFD) analysis was conducted using Autodesk CFD 2019. The flow of gas was simulated using values for pure N_2 gas, as this is the carrier gas used. The simulation was carried out for 0.3 and 0.5 L min^{-1}, which are the two flow rates primarily used for the AACVD reactions. Figure 3-5 shows the results of the CFD models. Here the action of the baffle, planarizing the cylindrical flow, can be clearly seen. Furthermore, it is evident that this planar gas stream passes over the substrate in a controlled manner, indicating laminar flow.

It can be observed that at 0.5 L min^{-1} the flow velocity is approximately 1 cm s^{-1} over the substrate. At 0.3 L min^{-1} this is reduced to approximately 0.7 cm s^{-1}. Using these velocity values, the equation 2-34 can be applied to calculate the Reynolds number (Re) of the system over the length of the substrate. At the reactor midpoint, 0.3 L min^{-1} and 0.5 L min^{-1} yields Re values of 33 and 47 respectively. These values are well below the turbulent regime that begins at a Re of ~4000. This corroborates the visual information from the CFD model, however, as the model is based on using N_2 and not an aerosol, these results may not be fully representative of the real flow.

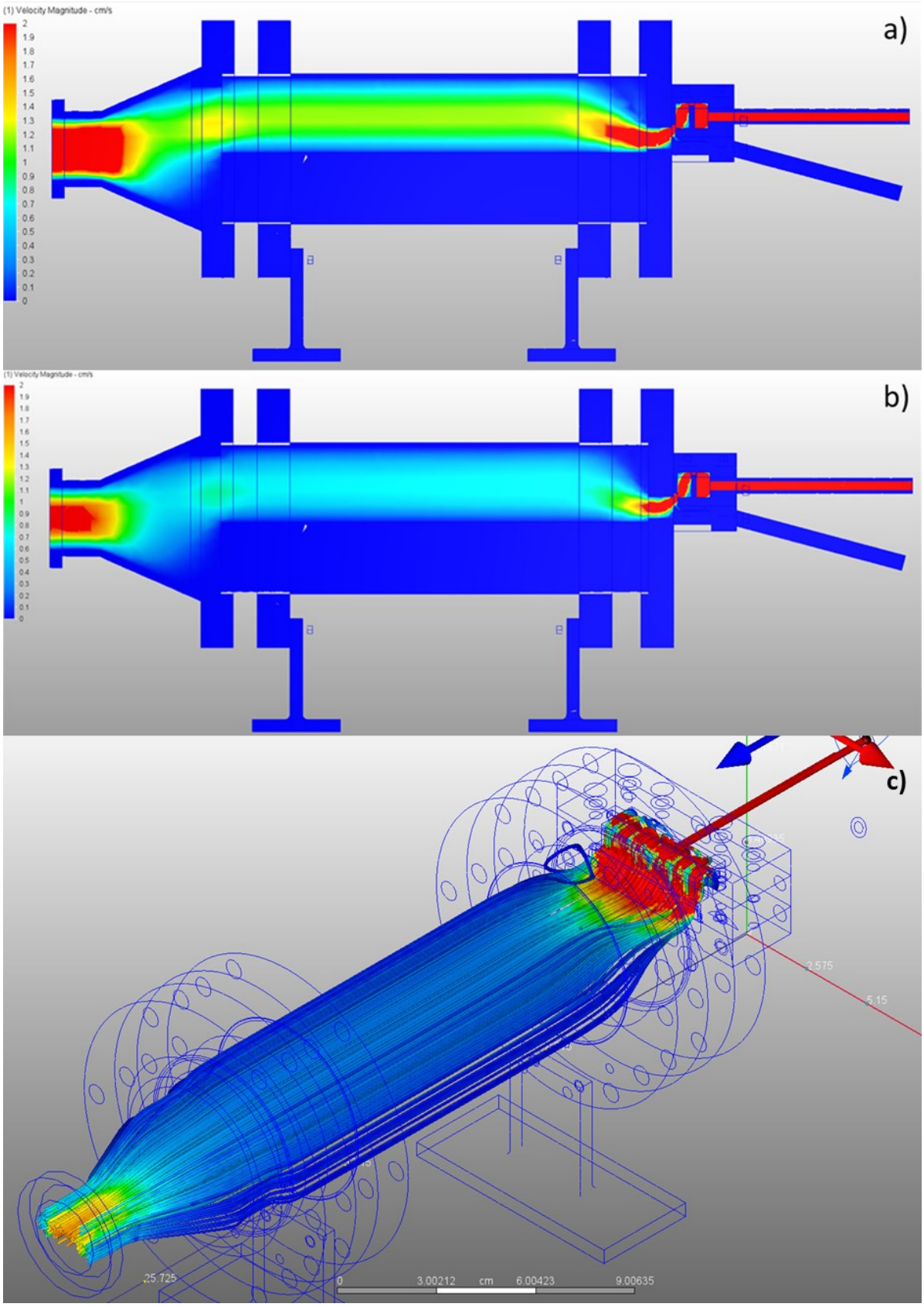


Figure 3-5 CFD simulation of nitrogen flow within the AACVD Reactor. a) Simulation run at 0.5 L min^{-1} b) Simulation run at 0.3 L min^{-1} c) 3D visualisation of nitrogen flow

3.2 AACVD EXPERIMENTAL

This section will describe the methods used to make precursor mixtures and how the experiments were carried out using the AACVD reactor.

3.2.1 Operation of Reactor

The reactor was placed within a fume hood to ensure that all excess aerosol was safely extracted. To complete a deposition, several key steps must be undertaken. Firstly, nitrogen is directly connected to the reactor inlet and the flow is set at 1.0 L min^{-1}. The reactor is then heated to 150°C for 30 minutes, which ensures that any remaining moisture is eliminated from the system. This is a key factor when depositing MAPI, as any remaining moisture can affect the deposition.

In the next step, substrates are placed on the graphite surface and the reactor inlet is connected to the misting bottle outlet. N_2 gas is then connected to the inlet of the misting bottle. The temperature of the chamber is then set using the Eurotherm. Once the set temperature is reached, the piezoelectric mister is turned on. This marks the beginning of the deposition. Once the deposition time has elapsed, the mister is switched off and the N_2 gas is again directly connected to the reactor inlet. This is to ensure that no remaining aerosol continues to flow into the reactor after the set time. The heating is then switched off and the reactor is allowed to cool. Once the temperature has dropped below 50°C, the reactor can be opened and substrates are removed.

3.2.2 Precursor Solutions

All precursors were stored inside a N_2filled glovebox to ensure that no degradation or moisture ingress occurred. Precursor solutions were made in excess for a given reaction time. This was to ensure that the solution did not run out before the reaction time had elapsed. The minimum volume using our bottles is 5 ml, as a lower quantity would not form enough depth in the misting bottle to consistently aerosolise.

3.2.2.1 PbI_2/DMF

In this study only a single concentration of PbI_2 solution was utilised. The solution was created by dissolving 2.4 g of PbI_2 (Merck: 211168) in 15 ml of DMF, creating a 0.035 M solution. This was then heated to 60°C and stirred for 30 minutes to ensure complete dissolution of the PbI_2. The solution was then filtered using a 0.2 µm PTFE filter and cooled to room temperature, before being transferred into the misting bottle.

3.2.2.2 $Pb(Ac)_2{\cdot}3H_2O$/MeOH

The $Pb(Ac)_2$ solution was formed by dissolving a set quantity of $Pb(Ac)_2{\cdot}3H_2O$ (Merck: 467863) in 20 ml anhydrous MeOH (Merck: 322415). As this salt is soluble in MeOH, and due to the low boiling point

of the solvent, the solution was stirred at ambient temperature for 30 min. It was then directly transferred into the misting bottle.

3.2.2.3 MAI Solution

To create the MAI solution, 1.0 g of MAI (Merck: 901434) was dissolved into 30 ml of MeOH. This formed a 0.21 M solution. The solution was stirred at ambient temperature for 30 min and then transferred into a misting bottle.

3.2.2.4 MABr Solution

For the MABr solution, 1.0g of MABr (Merck: 901435) was dissolved into 30 ml of anhydrous MeOH. This formed a 0.29 M solution. The solution was stirred at ambient temperature for 30 min and then transferred into a misting bottle.

3.2.3 AACVD Substrate and Device Preparation

This section will detail the preparation of substrates and devices used in the AACVD experiments of chapters 0 & 5.

3.2.3.1 FTO substrates & preparation

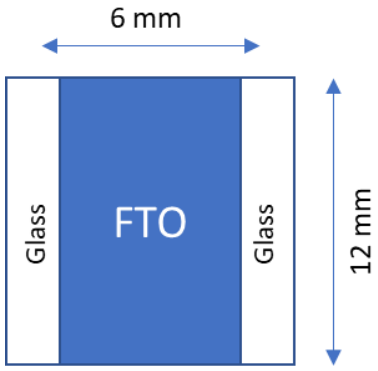


Figure 3-6 Schematic of FTO substrate used to make AACVD devices

Two types of FTO substrates were utilised for these experiments. Non-device depositions used 3 mm thick Pilkington-NSG Tec 15 FTO coated glass. The substrates were cut to size using a diamond scribe and a tile breaker. For ToF measurements we utilised 20 mm x 20 mm sized substrates with 5 mm etched edges.

Devices utilised 2.2 mm thick FTO coated glass substrates. These substrates were pre-cut to 12 mm x 12 mm with 3mm pre-etched edges. Figure 3-6 shows the layout of the patterned FTO.

Substrates were cleaned in 5-steps. Firstly, substrates were washed with acetone, followed by ultrasonication in a mixture of detergent and water. This is followed by two subsequent ultrasonications in acetone and IPA. Lastly, the substrates undergo a 30-minute UV/Ozone treatment.

3.2.3.2 Mesoporous TiO_2 Electron Transport Layer (ETL) Layer

To form the ETL, firstly a layer of compact TiO_2 was deposited. This was formed by spin-coating a 0.2 M titanium isopropoxide (Merck: 377996) solution in absolute ethanol with the addition of 0.02 M HCl at a speed of 5000 rpm. This was then heated to 120°C to dry the layer. MP-TiO_2 was then deposited using a solution of 18-NRT Titania paste (Merck: 791555) diluted in ethanol (1:7 wt%), which was spin-coated at 5000 rpm. The substrates were then annealed at 500°C for 1 hour.

3.2.3.3 Deposition of HTM Materials

AACVD deposited MAPI and reference devices were tested using either Spiro-OMeTAD or CuSCN. CuSCN was deposited on top of the MAPI layer via spray-coating and spin-coating. The spraying solution was formed using a 0.15 M solution of CuSCN (Merck: 298212) in dipropyl sulphide (Merck: P54280). This method was adapted from a previous study [194]. In this study, the substrates were heated to 65°C and 30 spray passes were used. This forms an approximately 300 nm thick layer of CuSCN. The substrates were then stored in a N_2 filled glovebox for one day to allow the layer to dry.

To spin coat CuSCN, 35 mg of CuSCN was dissolved in diethyl sulphide (DES) and dynamically spin coated onto the MAPI layer. The samples were also stored in a N_2 filled glovebox for one day.

3.2.3.4 AACVD Substrate Reactor Placement

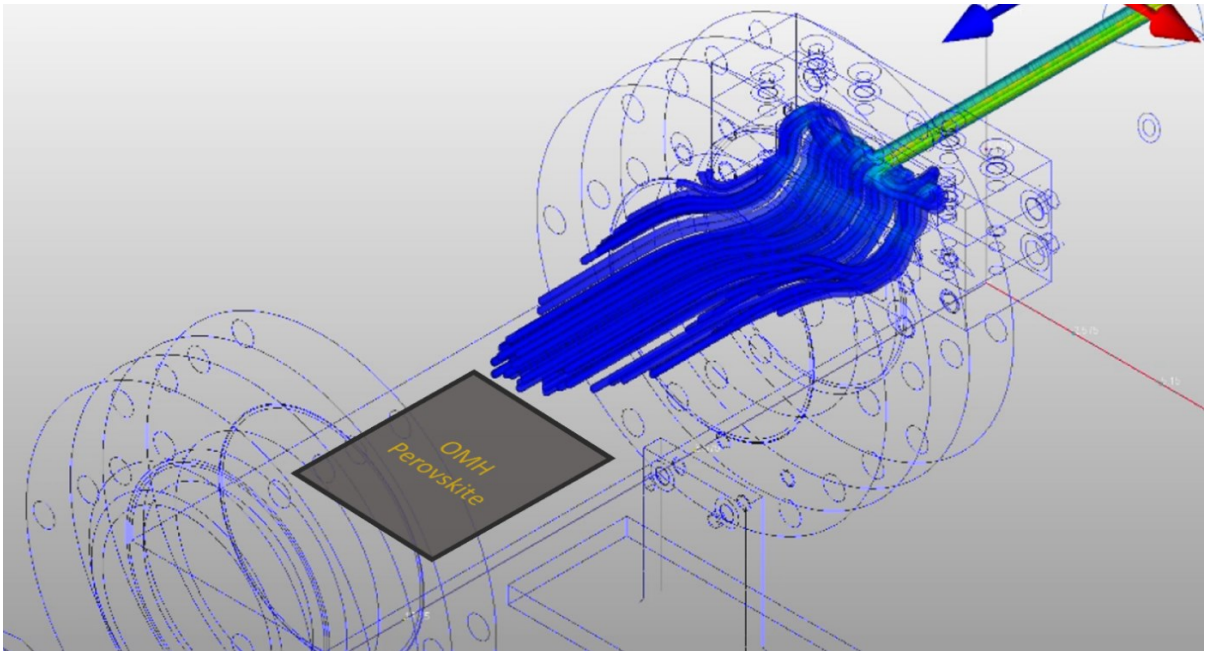


Figure 3-7 CFD simulation with grey rectangle indicating substrate position within the reactor

Reactor position was kept constant to ensure consistent results. For all AACVD experiments only the centre section of the reactor was used, which was approximately 3 cm from the baffle entrance. Figure 3-7 shows the area in which all substrates were placed within the reactor.

Spiro-OMeTAD solution was made by dissolving it in chlorobenzene to form a 70mM solution. This solution was then doped using a 4-tert-butylpyridine (TBP) and bis(trifluoromethane)sulfonimide lithium salt (LI-TFSI). Per ml of Spiro-OMeTAD solution, 30 µl of TBP were added. This was followed by 20 µl of 1.8M Li-TFSI in acetonitrile. The doped solution was then spin coated on the AACVD MAPI at 3000 rpm for 30 s. Samples were then aged for 24 hours in a desiccator to allow for the oxidation of spiro-OMeTAD.

3.2.3.5 Thermal evaporation of Au electrode & final device dimensions

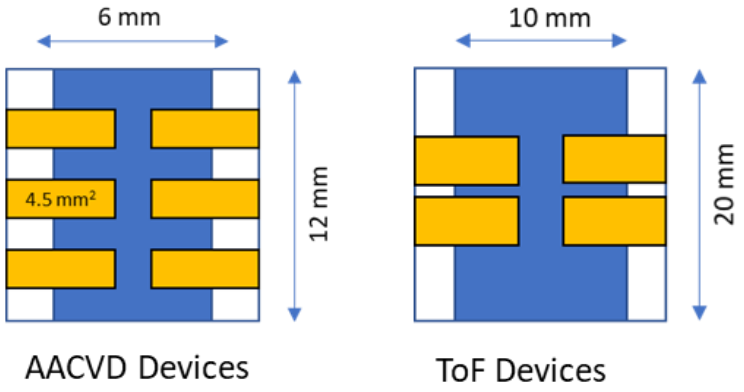


Figure 3-8 Schematic of thermally evaporated electrodes

Cells utilising the AACVD MAPI Layer are n-i-p type devices, which means that holes are collected on the non-illuminated side of the device. Therefore, a metal contact with an appropriate work function is required. A 150 nm thermally evaporated Au was utilised; the thickness of this layer is there to ensure complete coverage over the rough surface. This layer is evaporated at a pressure of 5 x 10^{-6} mBar, with an initial rate of 0.5 nm min^{-1}, which is then increased to 5 nm min^{-1} for the remainder of the thickness. This is to ensure that the HTM layers are not damaged by a large flux of Au metal during the initial parts of the evaporation. The evaporation mask used for these devices produces six electrodes each with a 4.5 mm^2 active area. Figure 3-8 shows the schematic of the device layout.

For ToF samples the same thickness and evaporation procedure were used, however using a four-pixel mask, which can be seen in Figure 3-8.

3.3 SPIN COATING AND AASA EXPERIMENTAL

This section will detail the experimental methods used to produce OMHP films utilised within the AASA experiments in chapter 6. Cells used within this chapter are primarily p-i-n type devices, which were primarily fabricated and measured by Tian Du. The AASA treatment and electrode evaporation was conducted by myself.

3.3.1 ITO Substrate Preparation

To fabricate the devices, patterned ITO substrates were used. Two different substrate dimensions were used. The standard area devices used 12 mm x 12 mm substrates with 3 mm etched edges. Large area devices utilised 20 mm x 20 mm substrates with 3 mm etched edges. The standard substrate layout is identical to the aforementioned FTO based devices. Substrates were cleaned in 5-steps. Firstly, substrates were washed with acetone, followed by ultrasonication in a mixture of detergent and water. This was followed by two subsequent ultrasonications in acetone and IPA. Lastly, the substrates underwent a 10-minute UV/Ozone treatment.

3.3.2 Glass Substrate Preparation

To study the uniformity of the AASA treatment, glass substrates measuring 2.54 cm x 2.54 cm were coated in MAPI. Glass was used instead of ITO, due to the limited availability of large ITO substrates. The cleaning of the substrates and the deposition of MAPI are the identical to that used with ITO substrates.

3.3.3 HTM Layers

Cells used within this chapter are primarily p-i-n type devices. Therefore, the HTM material is spin coated onto the substrate before the OMHP layer. The HTM material used was Poly(4-butylphenyldiphenylamine) (PTPD), which was diluted to 0.25 wt. % in chlorobenzene and spin coated at 5000 rpm for 20 s. This was performed in ambient conditions prior to being transferred into a N_2 filled glovebox.

3.3.4 PFN Interlayer

The wettability of perovskite solutions on PTPD is very poor. Therefore, Poly [(9,9-bis(3'-(N,N-dimethylamino)propyl)-2,7-fluorene)-alt-2,7-(9,9–dioctylfluorene)] (PFN) is used as a surface modifier to enable the spin-coating of perovskite solutions. To apply this layer, a 0.25 wt. % solution of PTAA in chlorobenzene, is spin coated on the HTM at 5000 rpm for 20 s.

3.3.5 MAPI Deposition

The $CH_3NH_3PbI_3$ (MAPI) precursor solution was prepared by dissolving 1.5 M PbI_2 (Alfa Aesar : 12724) and MAI (Merck: 901434) of equal molar ratio in a mixture solvent of N,N-Dimethylformamide (DMF)

and dimethyl sulfoxide (DMSO) (9:1.1 vol). The solution was then filtered using a 0.45 µm PTFE filter. 40 µl precursor solution was dropped onto substrates and spun at 4000 rpm for 30 s. After seven seconds, 0.5 ml diethyl ether was dripped onto the spinning substrate. The substrates were subsequently annealed on a hot plate at 100 °C for 15 minutes.

Thickness was modulated by varying the concentration of precursor in the solution, while the mix of solvent remains constant. 1.5 mol L^{-1}, 1.7 mol L^{-1} and 2.0 mol L^{-1} were used to produce films with thicknesses of 500 nm, 900nm and 1300 nm respectively. This entire process was conducted within a N_2 filled glovebox.

3.3.6 Mixed Composition OMHP

In this study the following mixed composition perovskites were used: $MAPb(I_{0.82}Br_{0.12})_3$, $Cs_{15}FAPb(I_{0.95}Br_{0.05})_3$, and $Cs_{0.15}FA_{0.85}Pb(I_{0.9}Br_{0.1})_3$. The mixed halide solution was made by substituting some MAI, in the aforementioned MAPI solution, with MABr (Merck: 901435). The solution was then spin-coated and annealed using the same protocol as above. The FA based perovskite solution was made by dissolving caesium Iodide (CsI) (Merck : 203033), formamidinium iodide (FAI) (Merck: 806048), PbI_2 and lead bromide ($PbBr_2$) (Merck : 398853) in a mixture of DMF and N-Methyl-2-Pyrrolidone (NMP) (8:2). Films were spin coated using 40 µl precursor solution dropped onto HTM coated substrate and spun at 4000 rpm for 30s. After ten seconds, 0.5 ml diethyl ether was dripped onto the spinning substrate. The substrates were subsequently annealed on a hot plate at 130 °C for 30 minutes. This entire process was conducted within a N_2 filled glovebox.

3.3.7 Substrate Placement for AASA Spatial Uniformity

The spatial uniformity of AASA was tested by placing three MAPI coated glass substrates, measuring 2.54 cm x 2.54 cm substrates, along the length of the reactor. Samples were treated using the protocol described in chapter 6 and immediately moved to a N_2 filled glovebox to await measurement.

3.3.8 Grain Size Evaluation

Substrates were divided into 12 equal sized areas and imaged within the SEM. The grain sizes were evaluated from the centre of each sample, using the intercept technique. This involves drawing a line of a fixed length over the image and counting the number of grain boundaries this line intercepts. This measurement was completed 10 times per image, yielding the average grain size.

3.3.9 Substrate placement for AASA devices

The AASA treatment was carried out after the OMHP films were deposited and annealed. Substrates were placed in the centre of the reactor and treated with the protocol described in chapter 6.

Substrates were then immediately stored in N_2 filled glovebox in preparation for the subsequent HTM and electrode deposition.

3.3.10 BCP Interlayer

Bathocuproine (BCP) is a commonly used interlayer material in photovoltaic devices and is used to improve electron extraction. It achieves this by improving the ohmic contact between the electrode and the ETL layer. To deposit this layer, a fully saturated solution of BCP in MeOH was spin coated at 3000 rpm.

3.3.11 Cu electrode evaporation and device

As devices in the AASA experiments are p-i-n type devices, a 50 nm thick copper (Cu) was used as the top electrode material. This layer is evaporated at a pressure of 5 x 10^{-6} mBar, with an initial rate of 0.5 nm min^{-1}, which is then increased to 5 nm min^{-1} for the remainder of the thickness. This is to ensure that the HTM layers are not damaged by a large flux of Cu metal during the initial parts of the evaporation.

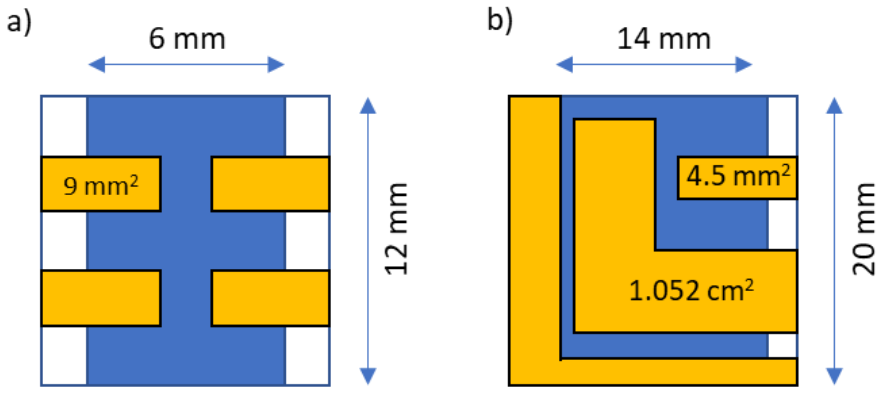


Figure 3-9 Schematic of electrode patterns used within AASA devices. a) Schematic of 4 pixel device b) Schematic of large area device

Two different electrode patterns were used for the AASA devices. The first was a 4-pixel arrangement used on the 12 mm x 12 mm substrates, with each pixel having an area of 9 mm^2. This electrode arrangement can be seen in Figure 3-9. The larger 20 mm x 20 mm substrates used a dual size pixel arrangement, here each substrate contains a 1.052 cm^2 pixel and a second 4.5 mm^2 pixel. This was designed by myself. The L-shape electrode pattern was a result of trying to maximise the pixel area on the existing substrates. Moreover, the L-shape pattern of the collection electrode was designed to minimise resistive losses and to allow for easy connection to the measuring apparatus. Additionally, metal is evaporated on the periphery of the substrate to compensate for contact resistances. Figure 3-9 shows the layout of this device.

3.4 CHARACTERISATION TECHNIQUES

This section will describe how different characterisation techniques were carried out to produce the data shown in this study.

3.4.1 XRD

Within this study two XRD systems were used to measure samples, one for ambient conditions and the other for thermal experiments.

3.4.1.1 Room-temperature XRD

Room-temperature XRD measurements were completed using a PANalytical X'pert^3 Powder diffractometer. The radiation was produced source was a Cu Kα source, with a wavelength of 1.5406 Å. The patterns were collected using the Bragg-Brentano geometry, whilst the sample was rotated with the X-ray source and the detector.

Diffraction patterns were collected from 10-55° 2θ, with a step size of 0.0167° and a collection time of 20 s. The total time for each scan was approximately 8 min. Samples were stored in sealed glass vials and removed just before the measurement was conducted. This was done to minimise the amount of degradation that could occur before the measurement.

3.4.1.2 High-temperature XRD

Sample measurements were conducted by the author, with additional assistance from Afif Aziz in data processing and plotting.

High-temperature XRD measurements were completed using a PANalytical Empyrean diffractometer equipped with an Anton-Paar HTK 1200N high-temperature chamber. Samples were placed within this chamber, which featured environmental heating. This means that the samples are heated externally and not from the substrate surface. The temperature was controlled using the inbuilt Eurotherm system. The chamber is calibrated to remove any thermal expansion artefacts of the stage, meaning that shifts in diffraction patterns are wholly that of the sample. Additionally, the samples were measured entirely in air, to give a more accurate representation of thermal degradation.

XRD measurements were taken using the Bragg-Brentano geometry, with the beam passing through the chamber's polyimide windows. This arrangement limits the temperatures OMHP samples can be heated to, as any material evaporating from the film may condense on the windows and impede the X-ray beam.

Patterns were either collected at various temperatures intervals or, for isothermal measurements, at constant temperatures at set time periods. Scans at different temperature intervals were collected

from 10-55° 2θ, with a step size of 0.0167° and a collection time of 30 s. The longer exposure time was to compensate for the intensity loss of passing the beam through the heating chamber windows. The total time for each scan was approximately 9 min.

For isothermal measurements samples were held at a given temperature and diffraction patterns were collected every 10 minutes. The scan range was limited to 12-16° 2θ to minimise the time lag associated with each scan, with each scan completing in under 2 minutes, therefore giving a more accurate snapshot of the samples diffraction pattern at a given time.

3.4.1.3 Crystallite size

The Scherrer equation was used to calculate the crystallite size of the OMHP films. The equation is as follows:

$$\tau = \frac{K\lambda}{\beta cos\theta} \qquad (3\text{-}1)$$

Where τ is the mean size of ordered crystallite domains, K is the dimensionless shape factor, β is the line broadening at half the maximum intensity (FWHM) and θ is the Bragg angle. In this study a K value of 0.9, which assumes spherical grains. Additionally, the β was taken without including instrumental broadening or strain effects. The FWHM value was taken from the (110) reflection for tetragonal patterns and (100) for cubic patterns. Note, that the instrumental broadening and crystallite stress is not included in the calculation. This means that the calculated crystallite size should not be used as an absolute value, but rather a comparative value.

3.4.1.4 Lattice Parameter

The lattice parameters of OMHP films were calculated from the (110) and (201) peaks in tetragonal systems and the (100) peaks for cubic systems. This calculation is done by first determining the d-spacing of the aforementioned peaks, which was done by using the Bragg equation:

$$2d\ sin\,\theta = n\lambda \qquad (3\text{-}2)$$

Where d is the lattice spacing, θ is the Bragg angle, n is the positive integer and λ is the wavelength of the incident wave. The d-spacing was then applied to the following tetragonal and cubic crystal system equations.

Tetragonal:

$$\frac{1}{d_{hkl}^2} = \left[h^2 + k^2 + l^2\left(\frac{a}{c}\right)^2\right]\frac{1}{a^2} \qquad (3\text{-}3)$$

Cubic:

$$\frac{1}{d_{hkl}^2} = [h^2 + k^2 + l^2]\frac{1}{a^2} \quad (3\text{-}4)$$

For the tetragonal crystal system this involves first solving the equation for the (110) reflection to determine the a lattice parameter. Using a, the equation can be used to solved for c by using the (201) d spacing. For the cubic system, the a parameter was determined by using the single d-spacing value for (100)

3.4.2 UV-Vis absorption spectroscopy

A Shimadzu UV-2600 spectrophotometer was used to collect absorbance data of various samples. The data was collected from 1000 nm to 200 nm. A direct band-gap Tauc plot was used to determine the optical band-gap of the measured samples. The plot shows *hv* (energy of incident wavelength) on the abscissa and $(\alpha hv)^{1/r}$ (where α is absorbance) on the ordinate.

3.4.3 SEM

Scanning electron microscopy (SEM) was carried out with an Inspect F field emission scanning electron microscope. All samples were mounted and grounded using carbon tape. Samples deposited on non-conductive substrates, such as glass, were coated with a 10 nm layer of Au/Pd alloy. This was done to make the sample conductive enough to prevent charging. All imaging was carried out at 5kV to minimise beam damage of samples. This is especially important when imaging the OMHP layers.

To prepare samples' cross-sectional imaging, the substrates were split using a glass scribe and tile breaker. The break was done perpendicularly across an electrode area. The samples were mounted flat and tilted within the SEM to image the cross-section.

3.4.4 Resistivity & Hall measurements

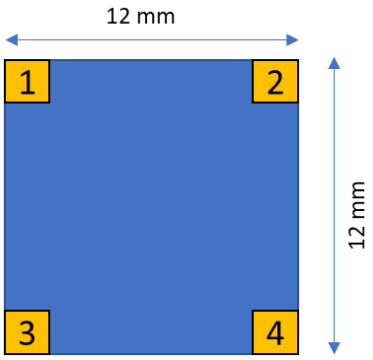


Figure 3-10 Schematic of contact placement used for Hall and electrical measurements

A Lakeshore 8400 HMS system was used to measure the electrical properties and the Hall coefficients of the AACVD MAPI Films. This system utilises the van der Pauw method and a 1.67 T magnetic field to measure the samples. The contact geometry can be seen in Figure 3-10.

3.4.4.1 Ohmic check

To ensure accurate resistivity and Hall measurements an Ohmic contact must be made to the sample. To confirm this, the voltage is measured using different excitation currents. Samples were probed in both diagonal directions (1-3, 2-4) using 0.1 -1 nA .

3.4.4.2 Van der Pauw and Resistivity

The van der Pauw method utilises four probing points placed around the perimeter of the sample (Figure 3-10) [195]. The measurement is done by flowing a set current (excitation current) from one contact to another and measuring the voltage across the contacts on the opposite edge. In this study an excitation current of 1 nA was used, with the current being applied for 30 seconds before measurement. This was done to minimise ionic effects. Using Ohm's law the resistance can be calculated. The following example shows how the horizontal resistance ($R_{12,34}$) is calculated, with current measured across 1,2 (I_{12}) and voltage measured across 3,4 (V_{34}):

$$R_{12,34} = R_{horizontal} = \frac{V_{34}}{I_{12}} \quad (3\text{-}5)$$

This measurement is then conducted across all contacts and repeated with a reversed polarity to improve the accuracy. These measurements are combined in the following way:

$$R_{horizontal} = \frac{R_{12,34} + R_{34,12} + R_{21,43} + R_{43,21}}{4} \quad (3\text{-}6)$$

$$R_{vertical} = \frac{R_{23,41} + R_{41,23} + R_{32,14} + R_{14,32}}{4} \quad (3\text{-}7)$$

Using these values, the sheet resistance can be calculated using the van der Pauw formula [195]:

$$e^{-\pi R_{vertical}/Rs} + e^{-\pi R_{horizontal}/Rs} = 1 \quad (3\text{-}8)$$

Where Rs is the sheet resistance of the sample. By multiplying this value by the film thickness, the resistivity of the material can be determined.

3.4.4.3 Measuring Hall voltage

The Hall effect exploits the effect of the Lorenz force. This is a force that a charge particle experiences when it is travelling in a magnetic field. This force is proportional to the strength of the magnetic field and the velocity of the charged particle and is strongest when the particle is moving perpendicularly to the magnetic field. If a current is passed through a sample within a magnetic field, the Lorentz force

will cause electrons to accumulate on one side of the sample. This creates a potential difference across the sample, termed the Hall voltage (V_h).

To measure the V_h, a constant current is applied across the sample and the voltage is measured perpendicularly. This measurement is then repeated in a reversed magnetic field and the difference of the two values is taken. For instance, when injecting current across contacts 1 and 3, the voltage is determined as:

$$V_{24} = V_{24+} - V_{24-}$$

Similar to the resistivity measurements, the accuracy of the overall V_h can be therefore determined as follows:

$$V_h = \frac{V_{13} + V_{24} + V_{31} + V_{42}}{8}$$

3.4.4.4 Sample Preparation

The perovskites were deposited on glass substrates and mounted on a Lakeshore 840931 Sample card. The perimeter contacts were formed by using silver conductive paint (RS: 186-3600) on the four corners of the sample. The contacts were connected to the sample card using 0.03 mm copper wire, which was soldered directly to the card.

3.4.5 ToF

The time of flight system consisted of several components: excitation source, sample holder, signal generator and oscilloscope. The system was created by Theo Kreouzis, who significantly aided with the setup and measurements.

3.4.5.1 Excitation Source

The excitation source was a frequency tripled Big Sky Nd: YAG laser with a 355 nm wavelength. The laser had a pulse width of 8 ns, an output energy of 20 mJ, and was fired at the sample at 5 Hz controlled by a Q-switch. The intensity of the laser was reduced by an ND3 optical filter. This was done to reduce the number of excited charge carriers within the sample, so that they do not begin to screen the applied electric field.

3.4.5.2 Sample preparation and holder placement

Samples of MAPI were deposited on 3mm FTO coated glass, with dimensions of 20 mm x 20 mm. Electrodes were then evaporated using the method in described in section 3.2.3.5. The sample holder used in this study contained five pins. Four of the pins connect to the gold electrode, with the remaining pin connected directly to the FTO. To ensure a clean contact to the FTO, the deposited MAPI

is cleaned off using acetone, at one area of the sample. The sample is then mounted face down into the holder, with the glass side facing the window. This chamber is mounted in the path of the laser and is connected to the signal generator and oscilloscope.

3.4.5.3 Signal generator and timing

To apply the bias on the sample, an Aim-TTi TGA 1241 waveform generator was used to generate the voltage pulse. The generator is triggered using the laser's Q-switch. By adjusting a timing delay within the generator, one can adjust the time the sample experiences a bias before the laser strikes the sample. To monitor the timing of this bias, the output is split between the sample and oscilloscope.

3.4.5.4 Oscilloscope and data collection

The resulting signals are collected using a Wavesurfer 3024 Oscilliscope. A photodiode connected to the oscilloscope and placed in line with the sample, is used to trigger the collection of data. To improve the accuracy of the data, an average of 64 signals is taken. To reduce intrinsic electrical noise, data was collected whilst the sample was not illuminated. This was then subtracted from the original data to yield the final data.

3.4.6 Dektak Measurments

A Ntegra Prime (NT-MDT Spectrum Instruments) was used to determine the film thickness of the time of flight sample. To conduct the measurements a small area of the MAPI film was removed from the substrate using a scalpel. The tip of the surface profilometer was the placed on this area and scanned towards the coated area. The total distance for the scan was set at 2 mm. These, measurements were conducted by Thibault Degousée.

3.4.7 Kelvin Probe / APS

Kelvin Probe and APS measurements were conducted by Matyas Daboczi. All energy level measurements were performed using an APS04 System (KP Technology).

The Fermi level of the samples was determined in the dark by Kelvin probe (KP) applying a vibrating gold tip (2 mm diameter). A cleaned silver reference was used to calibrate the work function of the tip. The samples were deposited on a conductive substrate, grounded during the measurement and kept in the dark until an equilibrium value was reached.

Ambient pressure photoemission spectroscopy (APS) measurements were performed in order to determine the valence band edge of the semiconductor layer. The cube root of the photoemission signal was fitted with a linear and extrapolated to zero to extract the energy value of the valence band edge.

3.4.8 AFM and SKPFM

AFM measurements for AASA experiments were conducted by Vikki Bremmer using a Asylum MFP 3D AFM. Samples were probed using a Pt-Ir coated silicon tip (Nanosensors PPP-EFM-10). The total scan area was 3 µm x 3 µm.

3.4.9 TEM & EDS Imaging

TEM sample preparation, imaging and data processing was done by Felix Kosasih. The samples consisted of complete devices fabricated by Tian Du, using the methods detailed in section 3.3.5.

To prepare the samples for imaging, lamellae were cut and thinned to electron transparency with a FEI Helios Nanolab Dualbeam focused ion beam miller following a standard protocol [196]. The lamellae were then directly transferred into a FEI Osiris TEM operated at 200 kV, minimising air exposure to about 2 minutes. STEM-EDX data were collected using a Bruker Super-X silicon drift detector with ~0.9 sr collection solid angle. To minimise beam damage, a defocused beam (Δf = -1 µm) was used with a beam current of ~140 pA, dwell time of 40 ms/pixel, and spatial sampling of 10 nm/pixel. STEM-EDX data were acquired in TEM Imaging and Analysis (TIA) and analysed in HyperSpy [197].

3.4.10 Device Testing

The photovoltaic performance of AACVD devices were measured by this author and devices with the AASA experiments were measured by Tian Du.

3.4.10.1 J-V Measurements

Current density-voltage (J-V) characteristics were measured using a Keithley 2400 source meter. The cells were illuminated by an AM 1.5 filtered xenon lamp (Oriel Instruments) at 1 sun intensity, calibrated using a Si reference photodiode. The light source has an ABB spectral match rating. All devices were stored in the dark prior to measurement and were measured in a nitrogen-filled chamber. Measurements were taken after a 30 second light soaking period, at a rate of 0.03 V s^{-1} for AACVD devices and 0.1 V s^{-1} AASA. All devices in chapters 4 & 5 were measured by this author with Tian Du measuring all devices in chapter 6.

3.4.10.2 MPPT Testing

Maximum power point tracking (MPPT) was used to test the continuous power output of the PV devices. To accomplish this, measurements samples are placed within a chamber and connected to a Keithley 2400 source meter. The illumination source consists of a white-light LED area calibrated to AM 1.5 intensity. Using a MPPT algorithm the power output of the cell is continuously kept at maximum and recorded. Cells were tested in ambient air at 25°C at a relative humidity of 60%, or at 25°C in a nitrogen atmosphere. This testing was also completed by Tian Du.

3.4.11 Photoluminescence measurements

Measurements were conducted by Tian Du. All films were stored in a N_2 filled glovebox prior to measurement. Steady state photoluminescence (PL) spectroscopy of films were measured with a FL 1039 spectrometer (Horiba Scientific). Illumination is provided by a white light LED (B3590N) purchased from CREE with output wavelength from 400 nm to 700 nm. For this study an excitation wavelength of 635 nm was used.

Time resolved PL (TRPL) measurements were conducted using time-correlated single photon counting technique (TCSPC) delta flex system (Horiba Scientific). The excitation was produced by a NanoLED N-02B (Horiba scientific). The wavelength was set at 635 nm, with a pulse duration of < 200 µs and a 1 MHz repetition rate. The illumination intensity was set at 0.15 nJ cm^{-2}. The TRPL signal was collected using a PPD-900 single photon counting detector (Horiba Scientific).

3.4.12 Curve Fitting and data processing

All data processing and curve fitting was done using Origin Labs Origin Pro 2019b v9.6.5.169.

3.5 SUMMARY OF CONTRIBUTIONS

Afif Aziz, Masters student, Imperial College London
Assisted with data processing for high-temperature XRD Experiments

Dr Victoria Bremmer, Atomic Force Microscopy Facility, Imperial College London
SKPFM measurements of AASA samples

Matyas Daboczi, PhD student, Imperial College London
Kelvin probe and APS measurements

Thibault Degousée, PhD student, Queen Mary University of London
Dektak Measurement of ToF Film

Tian Du, PhD student, Imperial College London
Spin-coating of MAPI and interlayers for AASA experiments. Device testing for AASA experiments. PL and TRPL measurements.

Felix Kosasih, PhD student, University of Cambridge
STEM imaging and EDS analysis in AASA experiments

4 RESULTS: AACVD OF THICK PEROVSKITE FILMS

4.1 INTRODUCTION

As discussed in chapter 2, characterisation of AACVD deposited OMHP perovskite films has been previously explored by several studies. However, most of these studies have completed only limited characterisation, with most of the focus being on the confirmation of composition. Furthermore, there is also a lack of understanding of how perovskites form in the AACVD processes. This chapter will focus on the formation and intrinsic material properties of AACVD films produced via the method initially developed by Chen *et al.* [198]. This method utilises the AACVD setup described in section 3 and can produce thick MAPI films. Previous work within the group has attempted to utilise these films to produce photovoltaic devices, but due to the difficulty of producing sub 1µm films, this was never realised. In this study these thick AACVD films are extensively characterised using XRD, absorption spectroscopy ToF, Hall, Kelvin Probe and APS measurements.

4.2 2-STEP METHOD AND FILM FORMATION



Figure 4-1 Schematic showing the 2-Step AACVD process

Films are formed via a two-step process, with the first step depositing a layer of PbI_2. This is accomplished by aerosolising a (0.035) solution of PbI_2 in DMF and carrying it, via a nitrogen carrier gas, at 0.75 L/min into the reactor. Substrates were kept at 75 °C for this step. The second step involves the aerosolization of MAI in methanol, which then converts the initial PbI_2 film into MAPI. A schematic of the reaction can be seen in Figure 4-1 and the parameters for the deposition can be seen in Table 4-1.

Table 4-1 Deposition parameters used to deposit AACVD MAPI films

Step	Precursor	Solvent	Concentration (M/L)	Temperature (°C)	Flowrate (L min^{-1})	Time (min)
1	PbI_2	DMF	0.035	75	0.5	NA
2	MAI	MeOH	0.21	230	0.3	60

4.2.1 1st Step: Growth of PbI_2 film

To elucidate how the AACVD process deposits the initial PbI_2 layer, samples were removed at different points during the first of deposition. Samples were taken at 15, 30 and 60 min.

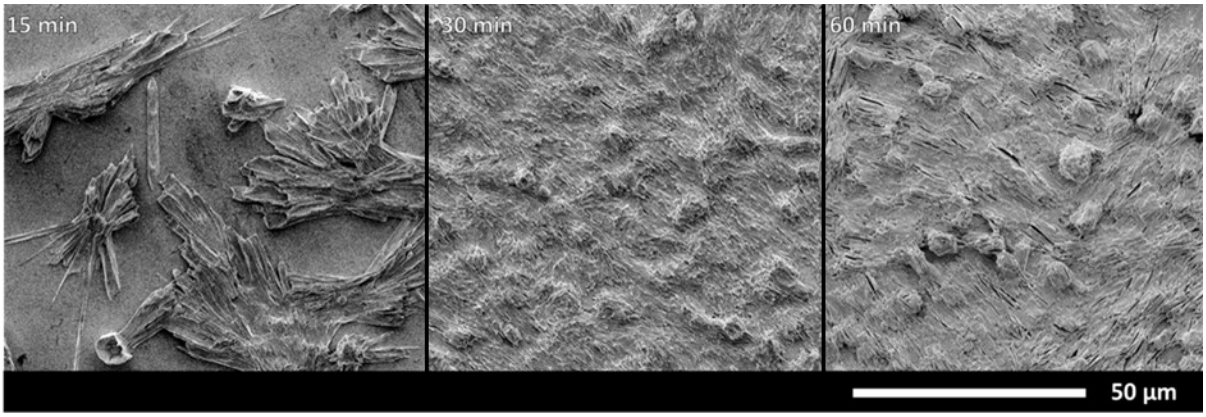


Figure 4-2 SEM images of the PbI_2 film deposited during the first step of the AACVD process for reaction durations shown on images.

Figure 4-2 shows the morphology development of the film during the first step of deposition. At 15 minutes, islands of PbI_2 are formed, which are composed of needle like grains. As time progresses the islands coalesce to form the final porous film. From these results it can be inferred that the film follows a Volmer-Webber type growth mechanism [186]. Furthermore, by visually observing the substrate during the deposition, droplet formation could be observed. This indicates that the process occurs in the AACVD pathway A, that is akin to spray coating. This is further corroborated by the porous and rough structure observed of the final PbI_2 film. Intriguingly, this morphology does not carry over to the final MAPI film.

4.2.2 2nd Step: Conversion to MAPI

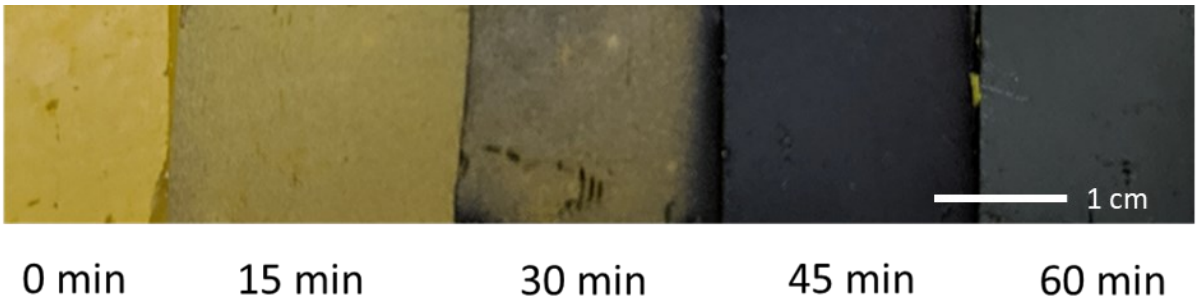


Figure 4-3 Photograph of samples taken at different points of the 2nd step reaction

The conversion of the film from PbI_2 to MAPI has been extensively explored in two-step spin coating solution processing methods. However, there have been no investigations carried out on the AACVD process. This study explored this by periodically taking films out of the reactor. For this experiment films were removed at 15, 30, 40, 50 and finally 60 minutes. Photographs of the resulting film can be

seen in Figure 4-3. When looking at SEM images (Figure 4-4), it can be observed that the conversion occurs from the surface of the film and propagates downwards towards the substrate. Moreover, original porous and platelet structure is completely transformed into the large dense columnar grain structure of the MAPI. This indicates a deconstruction-reconstruction type process, similar to that observed by Brenner *et al.* [199]. In their experiment, crystals of PbI_2 were exposed to gaseous and liquid MAI. When exposed to the gaseous MAI the PbI_2 crystals began to form large (~ 1µm) smooth spherical grains, like those observed in this study's films. Additionally, when they used a MAI solution grains tended to form sharp tetrahedron shaped crystals, similar to that observed in spin coated films.

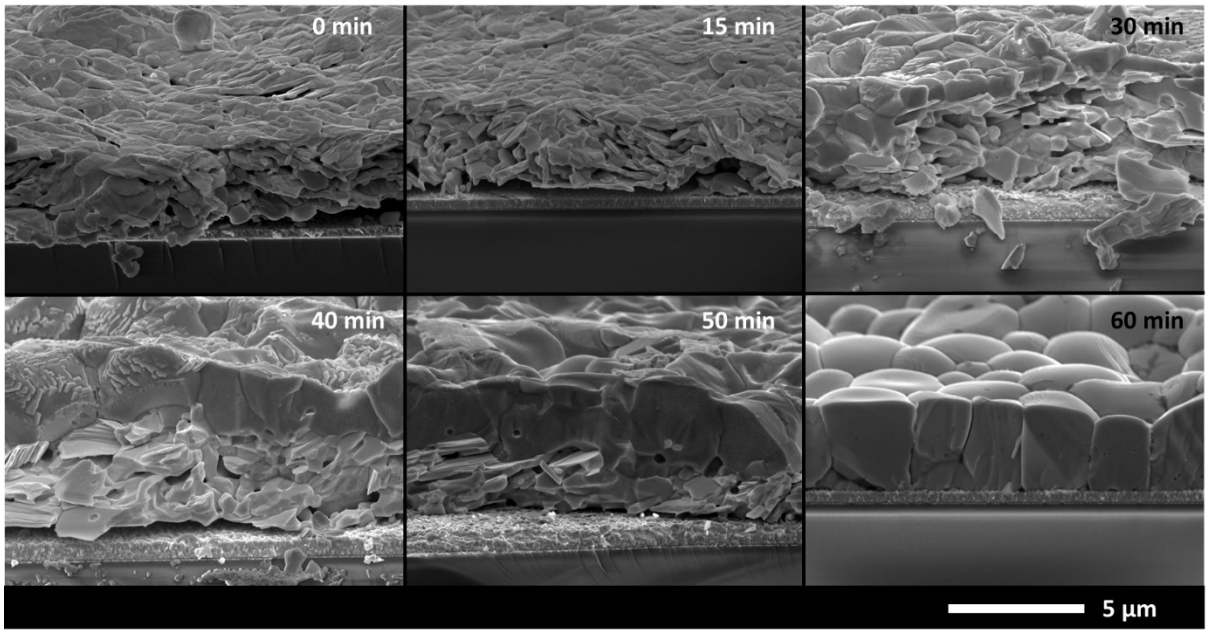


Figure 4-4 Cross-sectional SEM images of the PbI_2 film being converted to MAPI during the second step of the reaction

Therefore, it can be inferred that the second step conversion process does not occur in the AACVD reaction pathway A but is most likely in the true CVD pathway, with the chemical vapour being formed by MAI. This vapour then begins to deconstruct and reconstruct the surface of the PbI_2 into the final form. Furthermore, the swelling of the film during the early stages of conversion is due to the lower density of MAPI when compared to PbI_2 (4 g/cm^3 vs. 6 g/cm^3) [200,201]. As the reaction continuous the film thickness contracts slightly, which is due to the removal of porous voids originally found within the PbI_2 film. A schematic of the formation can be seen in Figure 4-5

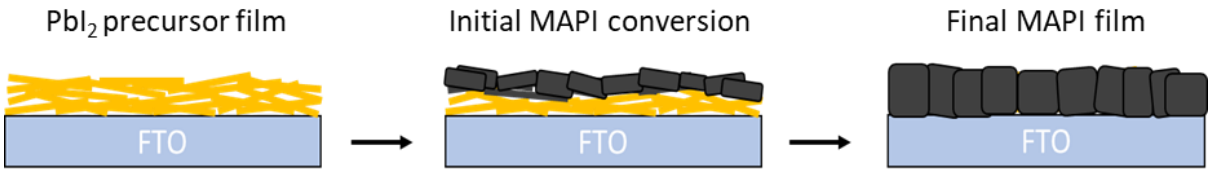


Figure 4-5 Schematic of the PbI2 to MAPI conversion process

To further elucidate the conversion process, samples were analysed using XRD and UV-Vis spectroscopy. Figure 4-6 shows the XRD patterns of the films during conversion. From this it can be seen that the initial PbI_2 layer formed crystals preferentially orientated around the (100) plane at 12.7°. The conversion can be followed more clearly when looking at the (100) peak of PbI_2 and the (110) peak of MAPI. As the conversion continues the (100) peaks slowly diminishes and the formation of the characteristic MAPI peak (110) can be observed beginning at 15 minutes. The final film shows no PbI_2 diffraction present, indicating complete conversion of the film.

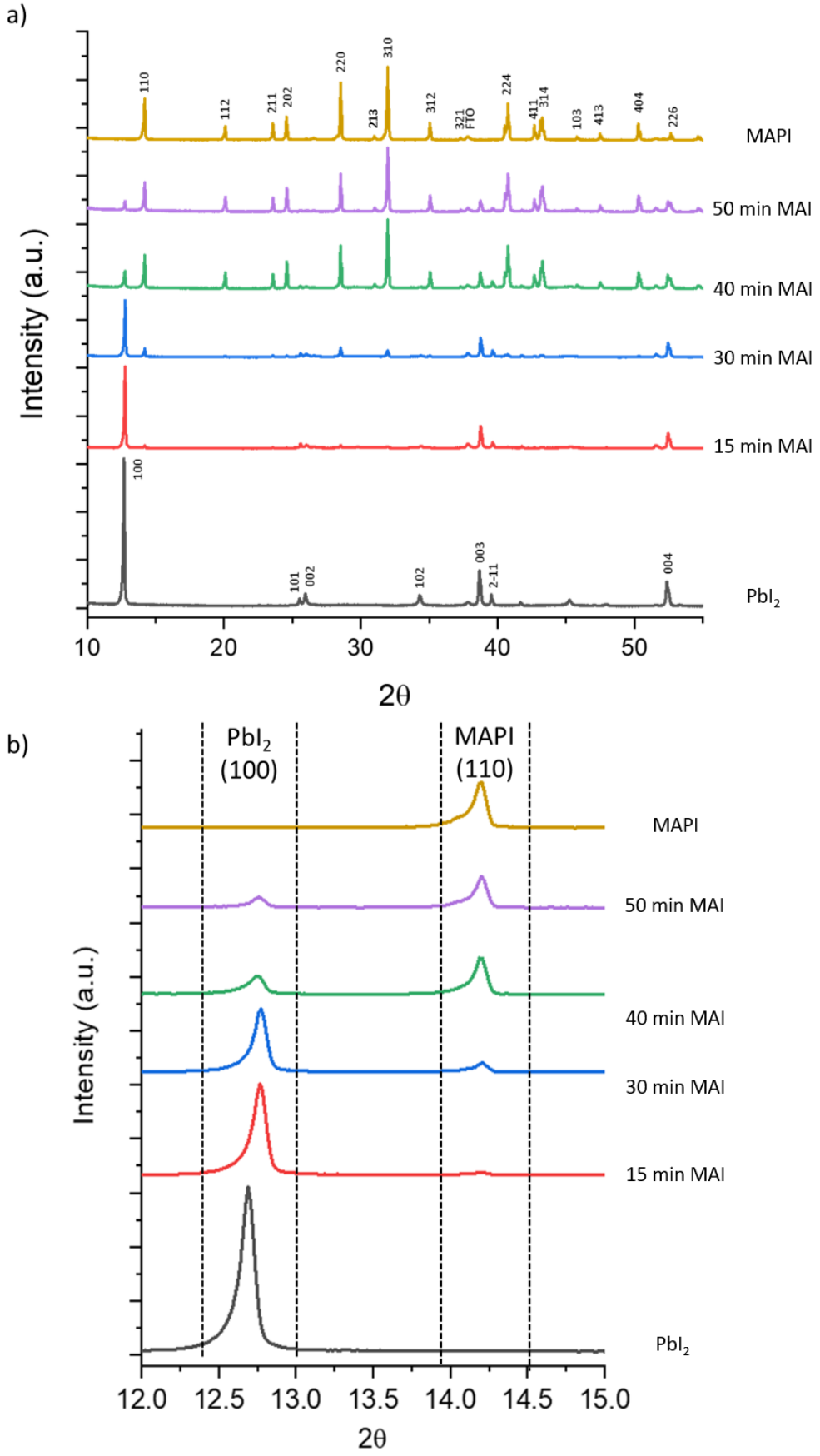


Figure 4-6 XRD patterns of substrates taken during the 2nd step AACVD conversion process. Right: Full XRD patterns Left: focusing on PbI_2 100 and MAPI 110 peak

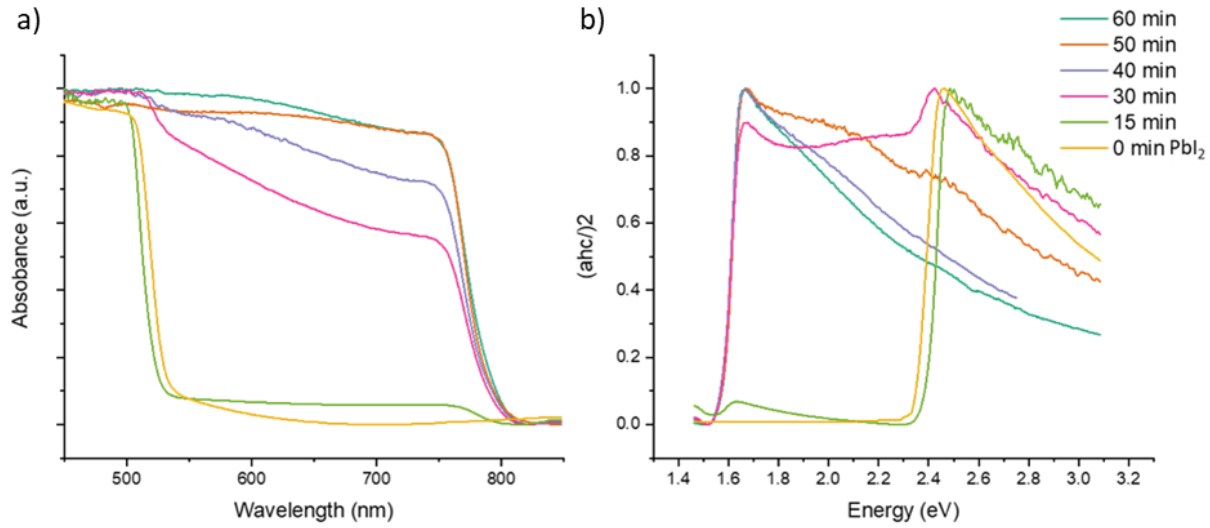


Figure 4-7 a) Absorption spectra of samples removed at different times. b) Tauc plots calculated for direct band gap

The UV-Vis spectra and calculated Tauc plots in Figure 4-7 supports the XRD data, with the initial film showing the characteristic absorption onset of PbI_2 at 540 nm corresponding to a band gap of 2.3 eV [202]. At 15 minutes the absorption onset of MAPI, at 800nm, begins to develop. Again, the bandgap matches the expected values at 1.55 eV. However, at this point the PbI_2 onset has blue shifted, resulting in an increase of the calculated bandgap. This can be partially explained when looking more closely at the XRD data. The (100) peak shows a shift towards higher 2θ, indicating a contraction in the lattice. What is likely occurring is that the higher temperature of the second step, 230 °C, begins to anneal the PbI_2 and relaxes the crystallographic strain. Therefore, this alters the density of states within the crystal and may alter the bandgap of the material. As the deposition commences, the absorption of the MAPI begins to dominate and at 60 minutes the film shows no absorption contributions of PbI_2. To evaluate the growth of MAPI crystals, the Scherrer equation was used to calculate the crystallite size during growth. The results can be seen in Table 4-2.

Table 4-2 Summary of FWHM and crystallite size calculated using Sherer equation. All values were calculated from 110 peaks.

Time	FWHM (°)	Crystallite size d_{110} (nm)
15	0.103	81.2
30	0.096	87.1
40	0.095	88.0
50	0.095	88.0
60	0.098	85.4

The crystallite sizes do indicate that large crystallites are formed as soon as 15 minutes. There does seem to be a slight growth as time progresses, however the FWHM values are close to the minimum instrumental broadening observed by the XRD measurement system. Therefore, the broadening may be masking the true crystallite size as the film is converted. Furthermore, the tetragonal peak splitting

which results in the (110) and (002) reflections overlapping may introduce artificial broadening, again masking the true crystallite size.

Combining the SEM observations, XRD and absorption spectra, the following facile reaction can be proposed:

$$PbI_{2(s)} + CH_3NH_3I_{(g)} \rightarrow CH_3NH_3PbI_{3(s)} \quad (4\text{-}1)$$

Here the solid PbI_2 is transformed into the MAPI via gaseous MAI to form the final solid MAPI film.

4.2.3 Future Work

Further study will be required to validate these results. True in situ experiments may show additional intermediary processes and chemical species. Potential modification of the reactor to allow in-situ XRD may allow for real time observation of the growth. Additionally, spectroscopic measurements, such as infrared spectroscopy, may allow for the identification of chemical species during the transformation process. Hu *et al.* utilised a similar combination of techniques to successfully evaluate the crystallisation of spin coated MAPI films [203]. However, implementing these techniques in AACVD will not be trivial, as there is a significant challenge in passing signals though an aerosol due to scattering effects of the droplets.

4.2.4 Film formation summary

In summary, these results indicate that the first step undergoes a Volmer-Webber type growth mechanism, likely in AACVD pathway A. As the second step commences, the original PbI_2 film undergoes a deconstruction-reconstruction type mechanism, due to exposure to vaporised MAI gas from the aerosol. The MAPI grains nucleate from the surface of the film and slowly grow down towards the substrate consuming the PbI_2 layer.

4.3 XRD STUDIES OF AACVD MAPI

This section looks more closely at the crystallographic information obtained from MAPI films utilising the aforementioned 2-step method. Additionally, the crystallographic information of the AACVD sample is compared with a spin-coated film of MAPI. This film was deposited using a 1-step antisolvent method, described in section 3.3.5, making it representative of most state-of-the-art research MAPI films, and were prepared by Tian Du. Note that the spin-coated sample was deposited on ITO, whereas the AACVD film was deposited on FTO. Direct deposition of spin coated samples on FTO proved difficult as the method was not optimised for ITO/glass substrates. However, the pattern observed in literature of spin coated films deposited on FTO substrates match closely to this study's spin-coated samples, therefore it is still a suitable comparison. [125,204]

4.3.1 Peak splitting and texture

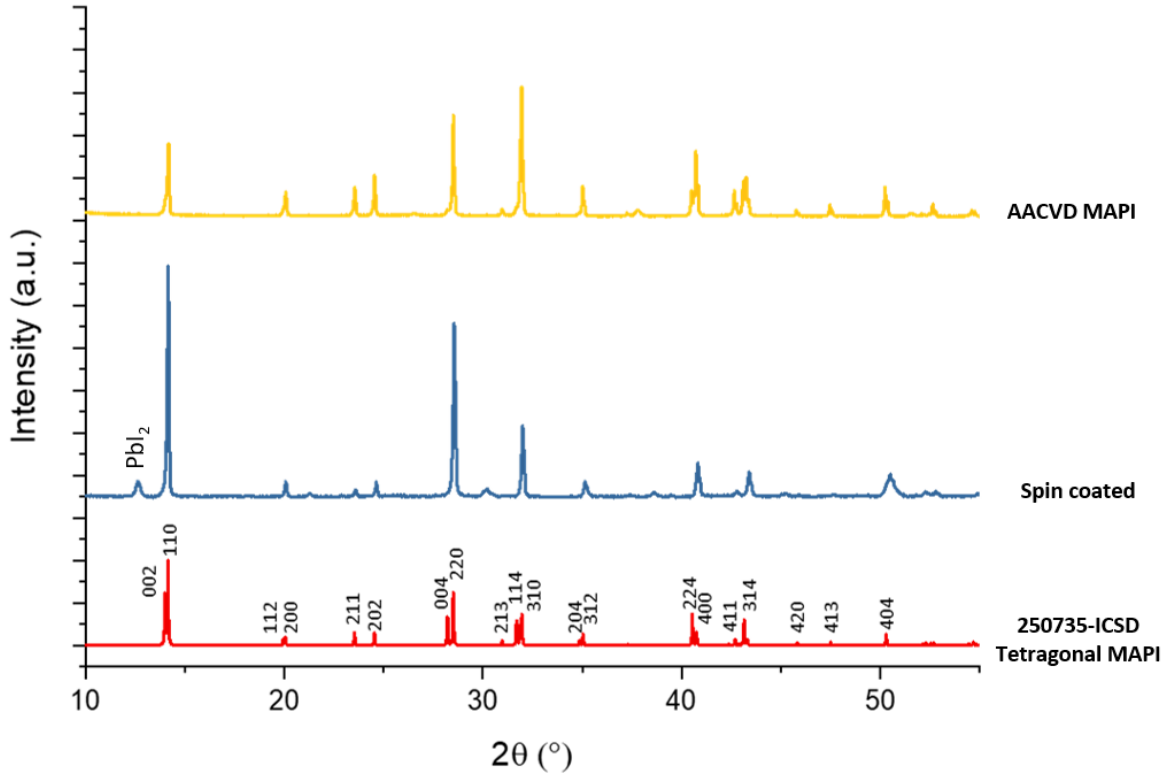


Figure 4-8 XRD patterns of AACVD, Spin coated and tetragonal reference MAPI 250735-ICSD [132]

The XRD diffraction data of the AAVCD MAPI shows a more tetragonal structure when compared to the reference pattern in Figure 4-8. The AACVD film shows stronger signs of tetragonal peak splitting indicated by the (004) and (220) reflection at 28.15° and 28.43° 2θ respectively. In the spin-coated sample the splitting is not visible, with an asymmetric peak observed at 28.53° which is typical of patterns observed in spin-coated samples literature. The splitting in the AACVD sample is most likely due to two factors. Firstly, the thicker (~5 µm) AACVD film may produce a stronger diffraction signal.

Additionally, the larger grains observed may indicate larger crystallite sizes. This would lead to a lower amount of peak broadening in the XRD pattern. This enables the smaller peak to be more clearly observable. When the crystallite sizes were evaluated using the Scherrer equation though, crystals in the AACVD films were found to be 85.4 nm and 85.1 nm for the spin coated films. However, the difference may be again masked by the instrumental limitation of the XRD system. The argument for larger domains is partially substantiated when looking at SEM images in Figure 4-9, as there are visibly larger grains in the AACVD film (180 nm for spin coated vs 1000 nm for AACVD).

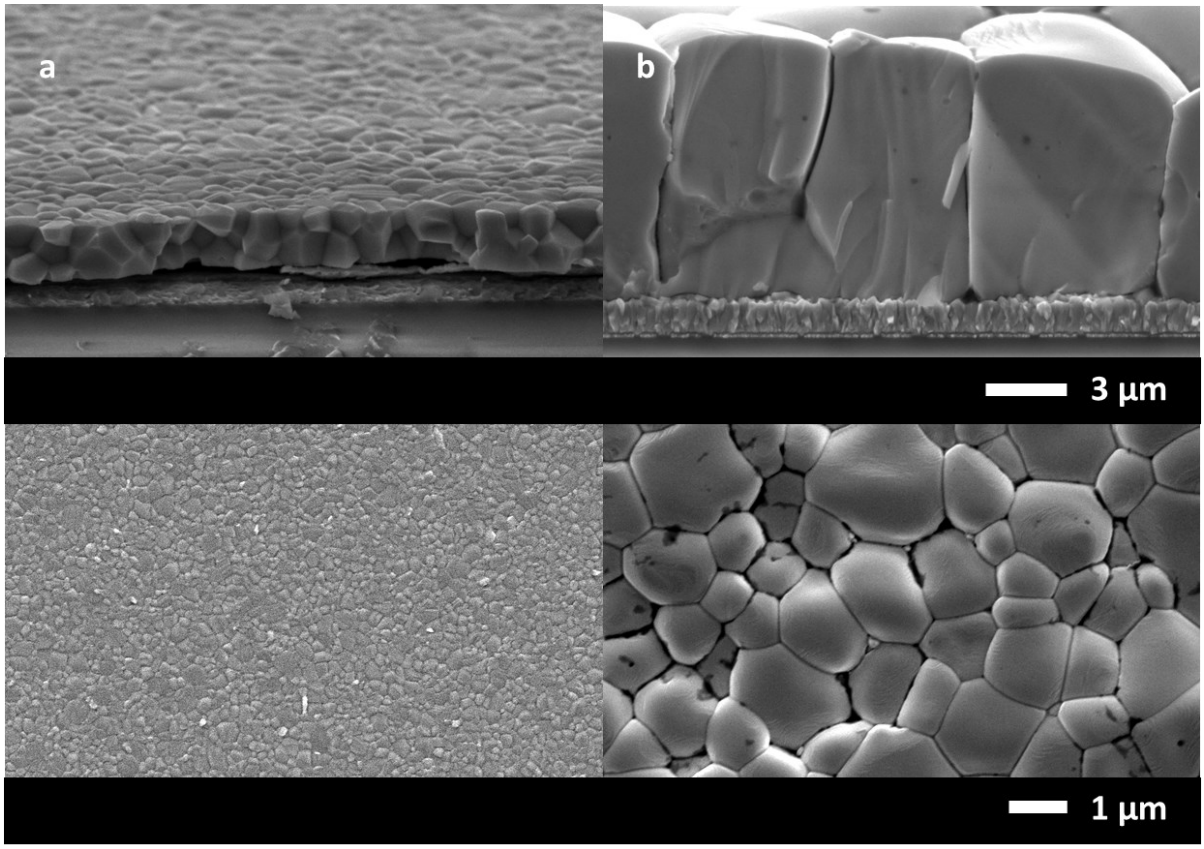


Figure 4-9 SEM images of (a) spin coated and (b) AACVD films of MAPI

Another major difference between the two films is their texture, with the AACVD films exhibiting significantly less preferred orientation (Figure 4-10). Spin coated films more closely match what is the reference pattern, with a preferred orientation around the {110} planes. In contrast, the AACVD films show a more even distribution of intensities, with a much stronger contribution from the (310) planes. A similar trend was observed by Brenner *et al.* when comparing vapour and liquid phase formation of MAPI, from single crystal PbI_2 [199]. Here, the PbI_2 reacted with MAI vapour and formed more randomly oriented MAPI, whereas, when exposed to a solution of solvent and MAI, the films exhibited a similar texture to spin coated films. This confirms the observations in section 4.2.2, where it was thought that the MAI aerosol step was forming a chemical vapour and reacting with the PbI_2 film.

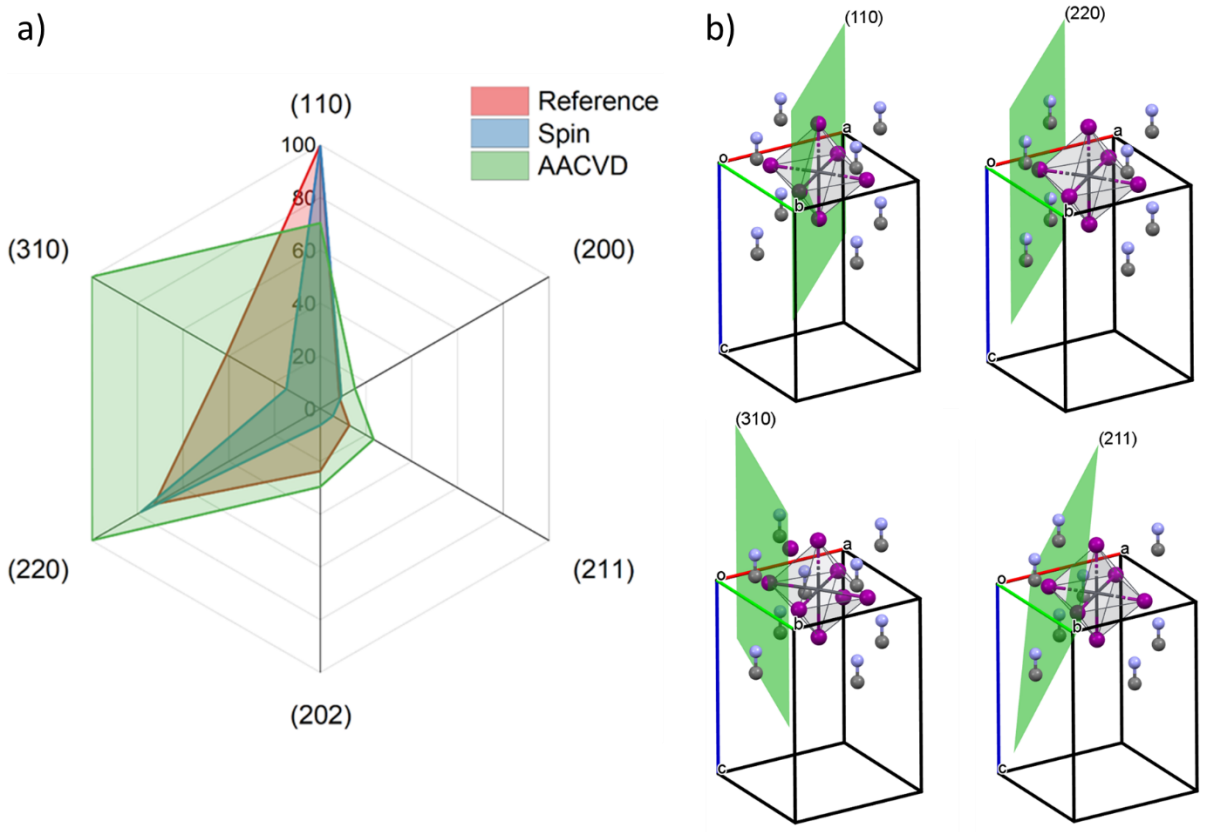


Figure 4-10 a) Relative intensity of peaks compared to MAPI reference pattern 250735-ICSD [201]. b) Illustration showing common diffraction planes in relation to perovskite crystal

4.3.1.1 Lattice parameters

Next, the crystal lattice dimensions of the films will be looked at more closely. By utilising Braggs Law and the formula for the tetragonal crystal system the dimensions of the crystal were calculated. The results are summarised in Table 4-3. The lattice parameters of the AACVD sample closely match reference patterns [201]. However, spin-coated MAPI exhibits significant elongation in the c-axis: 12.51 vs 12.67 Å respectively. This indicates that the rapid crystallisation during the 1-step antisolvent method, creates strain within the films. Additionally, epitaxial effects of the substrate could be more pronounced in the thinner spin coated film.

Table 4-3 Comparison of lattice parameters between AACVD and spin coated films

Film	Lattice constant	Calculated (Å)	Reference difference (%)	Primitive unit cell volume (Å^3)
AACVD	a	8.88	+0.33	249.8
	c	12.67	+0.24	
Spin coated	a	8.87	-0.10	246.1
	c	12.51	-1.03	

AACVD films exhibit a more contracted lattice when compared to its spin coated counterpart, with c/a ratio of 1.43 and 1.41 respectively. However, these are closer to the calculated reference pattern

indicating that the film is less strained. This is probably due to the longer and higher temperature process of formation. The intrinsic growth process of deconstruction and reconstruction tends to lead to more randomly orientated grains, further indicating that this is the process occurring in the AACVD method [199].

4.3.2 Thermal XRD studies

To further study the AACVD film, XRD measurements were undertaken at elevated temperatures. The experimental details can be seen in section 3.4.1.2. Samples were heated from 25-175°C ± 1°C at 25 °C intervals. 175°C was the maximum this study was able to run in the XRD system, as higher temperatures would lead to degradation material coating the inside of the measurement chamber. The samples were measured at ambient pressure and exposed to atmosphere. Again, the AACVD films are contrasted against a 1-step spin coated counterpart, which serves as a reference point. The total time of the process was 180 minutes, with each scan taking 5 minutes to complete. The results can be seen in Figure 4-11.

From this data it can be seen how the crystal structure of the spin coated and AACVD MAPI films changes at elevated temperature. The first notable change is the transition from β- tetragonal phase to the α-cubic phase, which occurs between 50°C ± 1°C and 75°C ± 1°C. This is evident from the disappearance of the (211) reflection, marking the transition between the two phases. At higher temperatures the formation of PbI_2 can be observed, indicating the onset of thermally induced degradation.

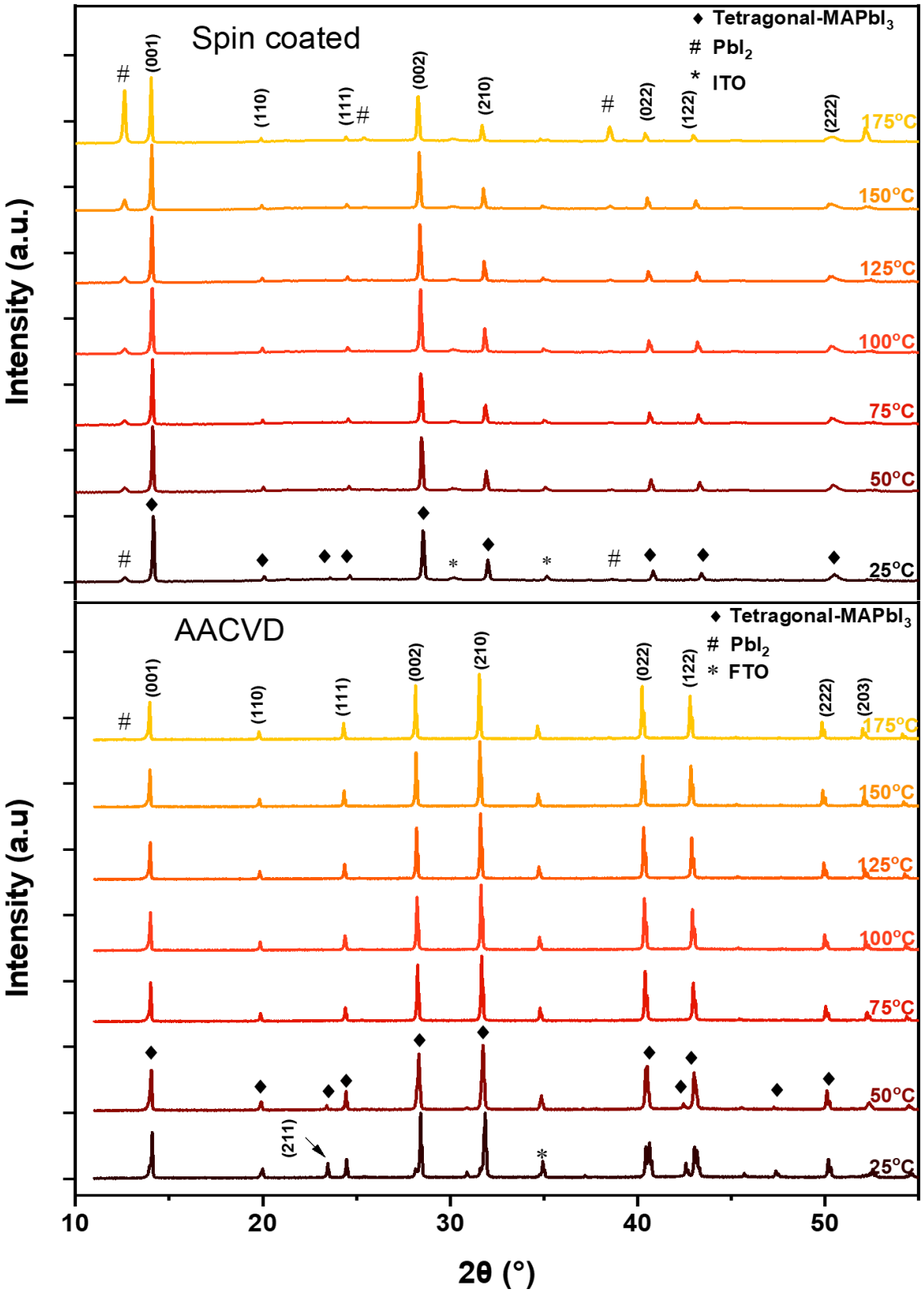


Figure 4-11 XRD data taken at different temperatures. Tetragonal indices are denoted by the diamond, with major cubic peaks indexed at higher temperatures

4.3.2.1 AACVD Phase transition

To confirm the phase transition in the AACVD sample, temperature scan measurements were conducted at smaller temperature increments. An initial room temperature pattern was firstly collected at 25°C ± 1°C, then at 2°C ± 1°C increments from 46°C ± 1°C to 64°C ± 1°C, with a final scan at 75°C ± 1°C (Figure 4-12).

Interestingly, the phase change occurs at approximately 50°C ± 1°C, with the (211) peak disappearing completely at 52°C ± 1°C. This is lower than that typically seen in literature, with the reported phase change occurring at approximately 330 K (57°C) [201,205–207]. Again, the reason may be due to a lower intrinsic strain within the film, allowing for a faster transition to occur. Previously, the McLachlan group has conducted similar experiments on spin coated films of MAPI. The phase transition was observed to occur at 55°C ± 1°C, more in line with reports in literature [208].

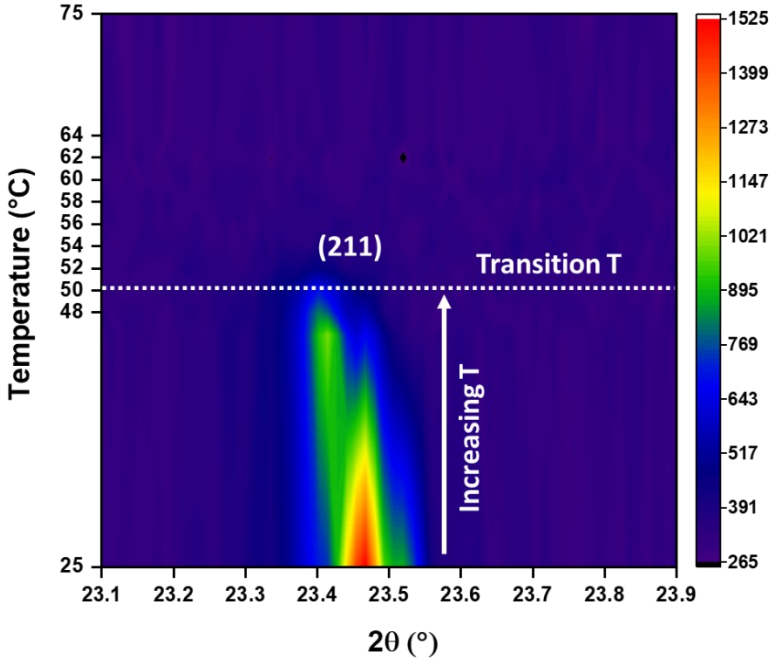


Figure 4-12 MAPI phase change from tetragonal to cubic upon heating

4.3.2.2 Determination of thermal expansion

Next, the expansion of the lattice with temperature will be outlined. This section contains contributions from Afif Aziz, who assisted with the data processing. As the temperature increases, the XRD patterns show a shift to lower angles; this is due to the expansion of the lattice. This data was used to calculate the lattice parameters at the different temperatures and the following equation was applied to calculate the thermal expansion coefficients [207].

$$\alpha_L = \frac{1}{L}\frac{dL}{dT} \qquad (4\text{-}2)$$

Where αL is the linear thermal expansion coefficient, L is the crystal dimension and T is the temperature in Kelvin. This calculation was done for the tetragonal system ($\alpha_{a/b}$ and α_c) from data collected between 25-50 °C ± 1°C and from 75-175 °C ± 1°C for cubic system (α_a). The results of this calculation can be seen in Table 4-4, and shows the increase in a/b parameters and a decrease in the c parameter during heating in the tetragonal phase. This is because the crystal is becoming more cubic as it is heated.

Table 4-4 Linear thermal expansion coefficients of AACVD film in tetragonal and cubic phase

Phase	AACVD Thermal expansion coefficient, α_x (K^{-1})	Spin coated Thermal expansion coefficient, α_x (K^{-1})
β Tetragonal	$\alpha_{a/b} = 1.27 \times 10^{-4}$	$\alpha_{a/b} = 1.36 \times 10^{-4}$
	$\alpha_c = -1.35 \times 10^{-4}$	$\alpha_c = -3.33 \times 10^{-5}$
α Cubic	$\alpha_a = 3.98 \times 10^{-5}$	$\alpha_a = 4.15 \times 10^{-5}$

The obtained values are close to previously determined expansion coefficients. Jacobsson *et al.* determined the linear expansion coefficients of spin coated MAPI to be: $\alpha_{a/b} = 1.32 \times 10^{-4}\ K^{-1}$, $\alpha_c = -1.06 \times 10^{-4}\ K^{-1}$ and $\alpha_a = 4.77 \times 10^{-5}\ K^{-1}$ [207]. Moreover, previous work in the M group also investigating spin-coated films, and determined the coefficients to be: $\alpha_{a/b} = 1.13 \times 10^{-4}\ K^{-1}$, $\alpha_c = -1.42 \times 10^{-4}\ K^{-1}$ and $\alpha_a = 3.17 \times 10^{-5}\ K^{-1}$ [208]. The largest difference is between the values of α_c between the AACVD sample and spin-coated sample. The spin-coated sample exhibits much lower expansion, which again bears credence to the idea that it is highly strained in the c axis.

Once the lattice parameters are determined, it is straight forward to calculate the volume of the primitive unit cells. Figure 4-13 shows the expansion across the phase change the volume of the primitive unit cells of the tetragonal and cubic phase. Note that at approximately 50 °C there is a discontinuity in the trend; this is most likely due to the phase change the material undergoes and corroborates the previous observation.

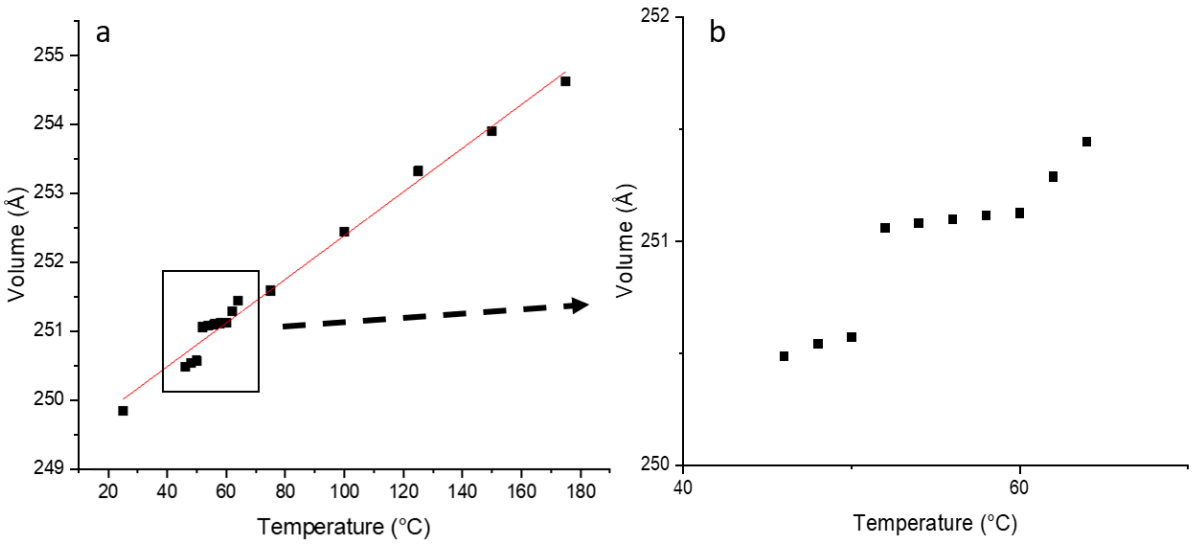


Figure 4-13 Results from AACVD film a) Volume of lattice plotted against temperature. b) Plot focusing on the point of phase change

Using a variation of equation 3-2, the volumetric expansion coefficient can be determined:

$$\alpha_v = \frac{1}{v}\frac{dv}{dT} \qquad (4\text{-}3)$$

Where V is the volume of the primitive unit cell. Using this equation an overall expansion coefficient, α_v can be calculated. However, as the expansion may not be linear across two different phases, separate values for tetragonal, $\alpha_{vt,}$ and cubic α_{vc} were calculated. The results are summarised in Table 4-5.

Table 4-5 Volumetric thermal expansion coefficients of AACVD film in tetragonal and cubic phase

Phase	Thermal expansion coefficient, α_x (K^{-1})
Overall	α_v = 1.27 x 10^{-4}
β Tetragonal	α_{vt} = 1.19 x 10^{-4}
α Cubic	α_{vc} = 1.97 x 10^{-4}

From these results the thermal expansion in the cubic phase is higher than in the tetragonal phase. However, as there is a lack of data in the lower temperature regions (25-45 °C), more data will need to be collected before the tetragonal expansion coefficient can be reliably determined. When comparing these values to literature, they are again very similar, with α_v = 1.57 x 10^{-4} K^{-1} being reported by Jacobsson *et al.* in spin-coated films [207]. Previous work within the McLachlan group also attempted to look at thermal expansion coefficients of the two individual phases in spin-coated films. The tetragonal expansion was calculated to be α_{vt} = 0.82 x 10^{-4} K^{-1} and the cubic α_{vc} = 2.43 x 10^{-4} K^{-1} [208]. This suggests that the results in this study are correct, with the tetragonal phase showing less thermal expansion than the cubic phase. Furthermore, these results indicate that AACVD MAPI films seem to

possess similar thermal expansion values to their spin-coated counterparts. Using this study's values, DFT calculations could be conducted to further understand the properties of films produced via AACVD.

When putting these results into context, they are relatively high compared to other common materials. For instance, soda lime glass has an expansion coefficient of $\alpha_V = 2.6 \times 10^{-5}$ K^{-1}, meaning that MAPI has a 5 times larger expansion coefficient. It is 8 times larger than stainless steel (316) ($\alpha_V = 1.6 \times 10^{-5}$ K^{-1}) and nearly double that of a common polymer acrylonitrile butadiene styrene (ABS) ($\alpha_V = 7.4 \times 10^{-5}$ K^{-1}). When comparing it to other solar cell materials, MAPI still has a much larger thermal expansion. Values for Si, CIGS and CdTe are: 0.3×10^{-5} K^{-1}, 2.7×10^{-5} K^{-1} and 1.4×10^{-5} K^{-1} respectively. MAPI's high thermal expansion coefficients could be a major obstacle when using these materials in photovoltaic cells. Thermal cycling that cells experience during a day will cause the active layer to swell and contract, creating mechanical stress within the layers and could lead to internal damage.

4.3.3 Isothermal XRD studies

When looking at Figure 4-11, there is a clear formation of PbI_2 at higher temperatures. This is due to the thermally induced degradation of MAPI. In the spin coated sample this process occurs to a greater degree, with a significant formation of lead iodide visible at 175 °C. Figure 4-14 shows the samples before and after the thermal sweep, which was detailed in section 4.3.2. On the other hand, the AACVD sample has remained more intact with only a small amount of PbI_2 observable in the pattern. This indicates that the AACVD sample may be more resistant to thermal degradation.

To try and quantify this difference in stability, a series of isothermal measurements were conducted and the evolution of the PbI_2 peaks were observed. Three different samples of AACVD and spin coated MAPI samples were measured at three elevated temperatures, 130 °C ± 1°C, 140 °C ± 1°C and 150 °C ± 1°C. The total time at each temperature was 93 minutes, with scans occurring every 10 minutes. This range of temperatures was chosen because it allows for practical observation of degradation in this short time frame. Lower temperatures did not show enough degradation to accurately analyse. Likewise, higher temperatures could not be used as this would cause the inside of the XRD chamber to be contaminated with excess degradation product, causing problems with the diffraction signal. Furthermore, only measurements between 12-16 ° 2θ were taken. This is the range where typically a strong (001) PbI_2 and (001) from the cubic MAPI is observable. Furthermore, this allowed for rapid scanning of the sample within 3 minutes and reducing of the lag time between each scan. Longer scans would cause problems in the measurement, as the sample would continue to degrade throughout the scan.

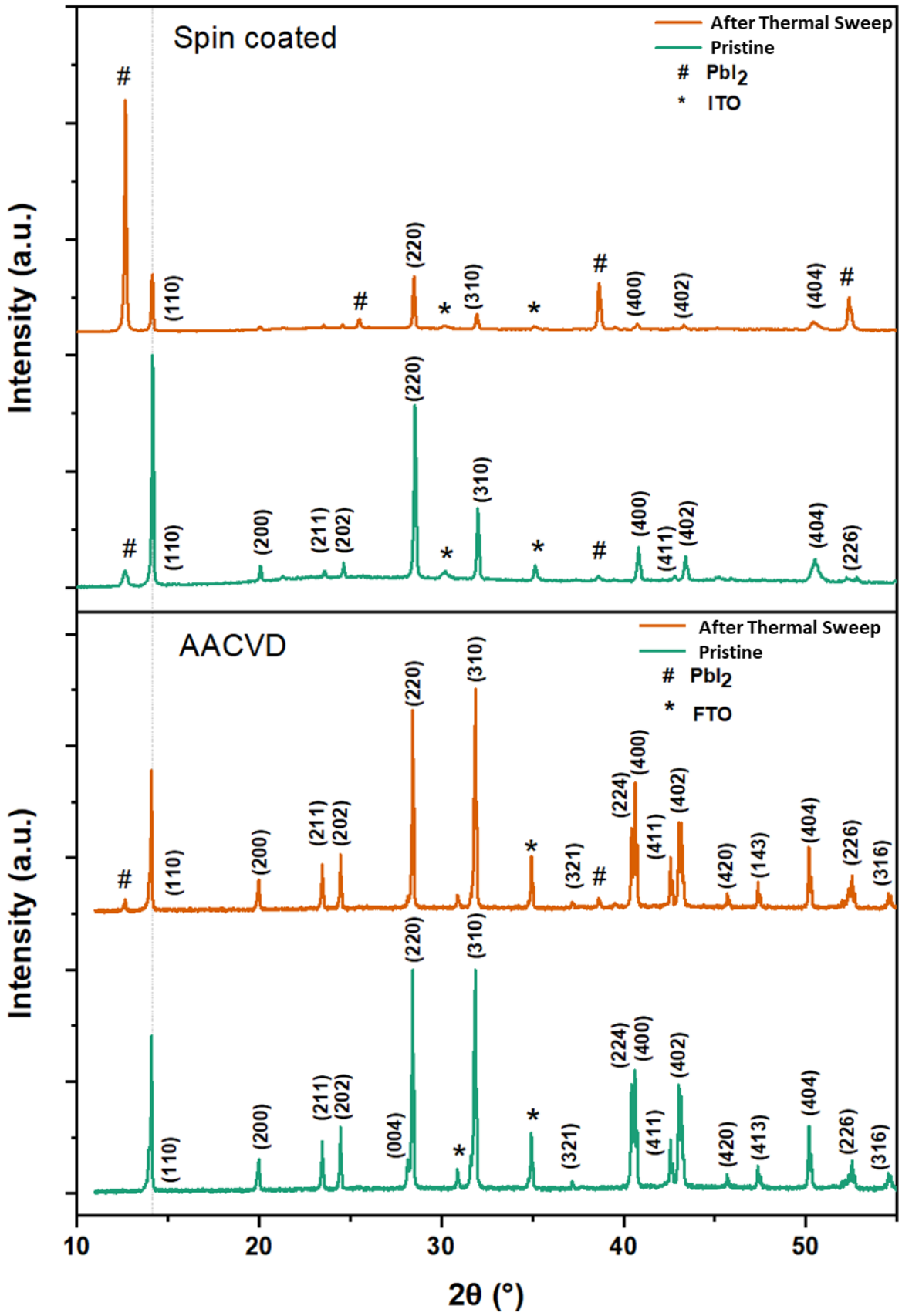


Figure 4-14 XRD patterns of samples before and after the thermal sweep experiment conducted in section 4.3.2. Figure 4-11 shows the full results of the sweep

The results of the three isothermal measurements on the AACVD film can be seen in Figure 4-16. See appendix (Figure 9-1) for spin-coated MAPI film. At 130 °C the degradation process is very slow, however at 150 °C the peak grows much more rapidly. Figure 4-15 shows the evolution of the (001) PbI_2 at 150 °C in both the spin coated and MAPI film. Interestingly, the intensity of the MAPI peak does not directly scale with the increasing intensity of the PbI_2 peak. This is because PbI_2 tends to nucleate highly orientated crystals, therefore the intensity of this peak is much stronger than the relative MAPI peaks, which have more evenly distributed intensities across diffraction peaks.

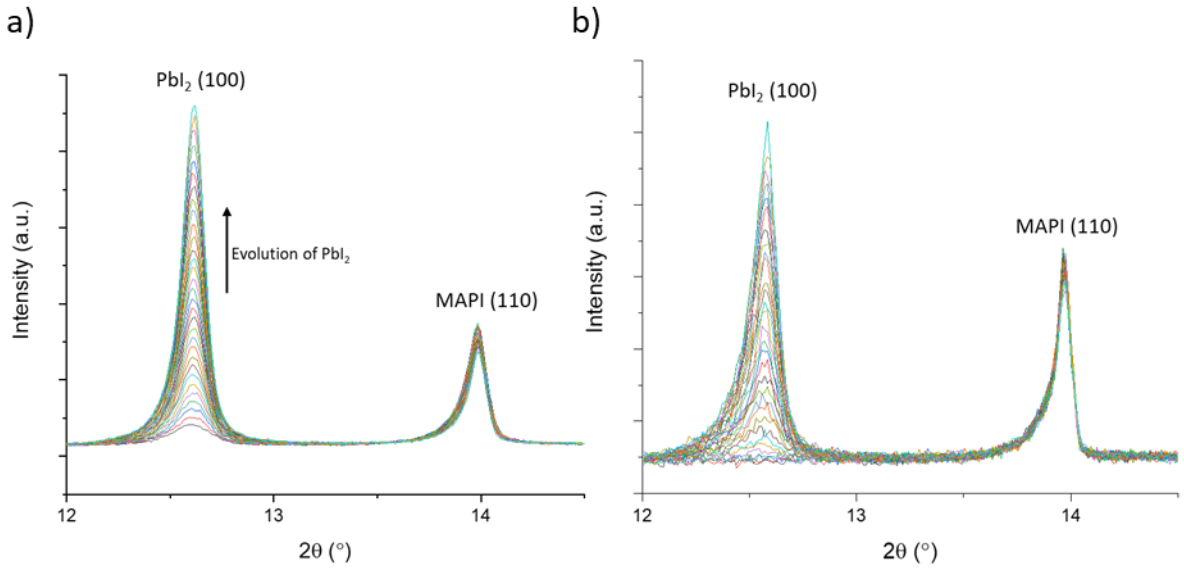


Figure 4-15 Isothermal XRD patterns overlaid to show the evolution of the 001 PbI_2 peak in spin-coated MAPI (a) and AACVD MAPI (b). Measurements taken at 150 °C for 93 minutes

Using this measurement, the relative ratios of the integrated peak areas can be taken to derive the parameter x(t):

$$x(t) = \frac{Area\ (001)PbI_2}{(Area\ (001)PbI_2 + Area\ (001)MAPI)} \quad (4\text{-}4)$$

Where x(t)= 0 is a completely pristine sample and x(t)=1 is a fully degraded sample. This assumes that the area of the peaks is related to the proportion of species within the film. It must also be assumed that any intensity changes are not due to realignment/recrystallisation processes within the film. Also, as an increase in background scattering has not been witnessed, it can be inferred that the degradation does not happen due to a dissolution process. There were some difficulties in correctly determining the area at lower temperatures and times, as the area of the PbI_2 peak was very small. To alleviate this problem, values from 24 minutes to 93 minutes were used. By plotting the x(t) vs time curves that show the fractional content of PbI_2 over time can be produced. By fitting a linear equation to this data, the time it takes for a certain fraction of degradation to occur can be calculated.

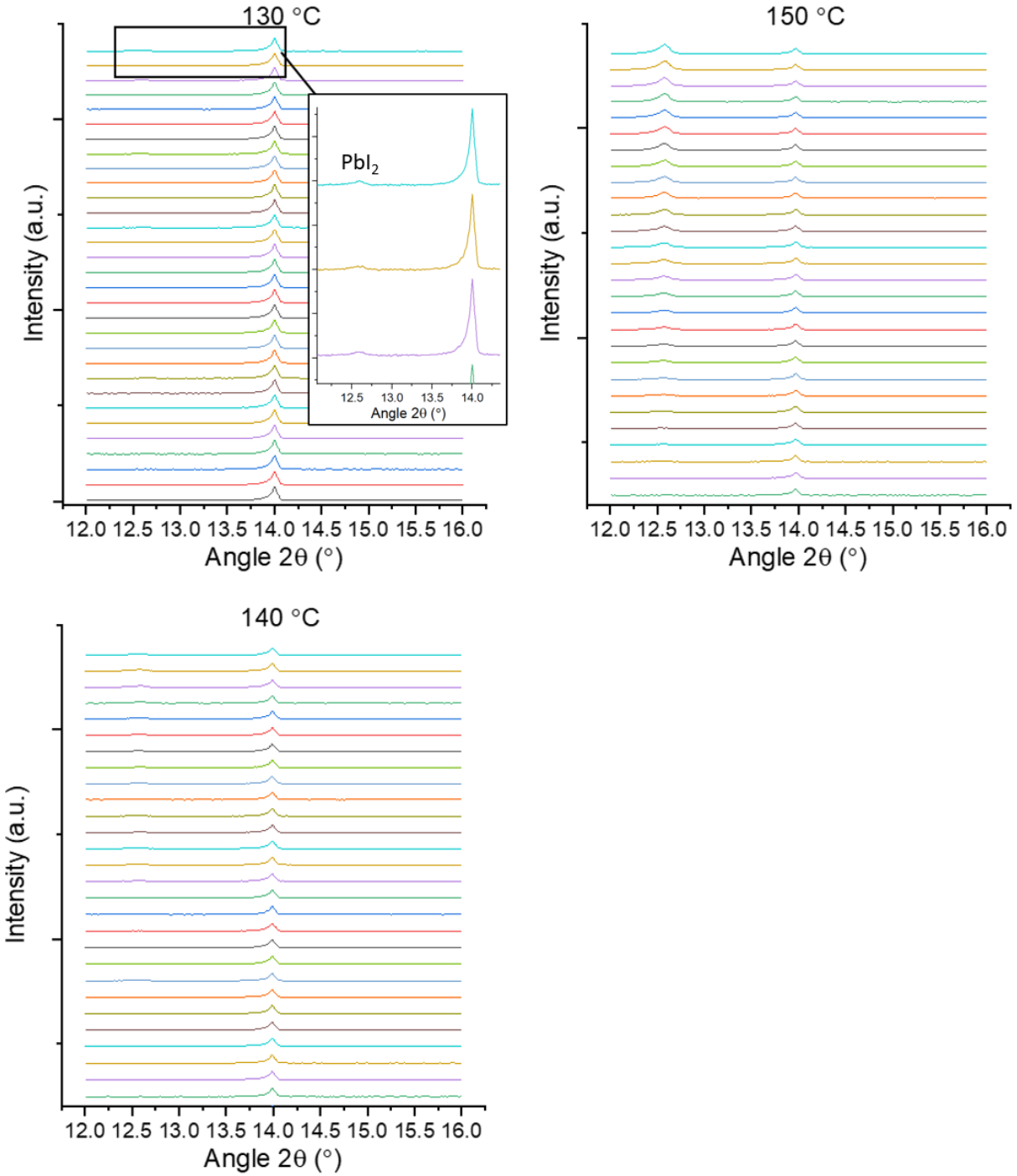


Figure 4-16 AACVD Isothermal XRD patterns taken from AACVD sample over 93 minutes. Insert shows small peak evolution due to PbI_2 formation

By using values of x(t) a simplified model of the Mittemeijer solid state reaction model can be applied, which itself is derived from the Arrhenius equation [209,210].

$$ln(t_{x2} - t_{x1}) = \frac{E_a}{RT} - lnK_m \qquad (4\text{-}5)$$

Where t_{xn} is the time taken for a certain fraction of PbI_2 to form, E_a is the effective activation energy for the nucleation and growth of PbI_2, R is the gas constant, T is the temperature in Kelvin and K_m is the pre-exponential rate constant. Plotting the data as $\ln(t_{x2}-t_{x1})$ vs. 1/RT and taking the slope of a linear fit will give the activation energy E_a. This analysis takes two times where the fraction of PbI_2 are 0.9 and 0.2, which will be the t_{x2} and t_{x1}. Choosing different volume fractions will result in shifting of the line, however the slope and therefore the calculated activation energy will be the same.

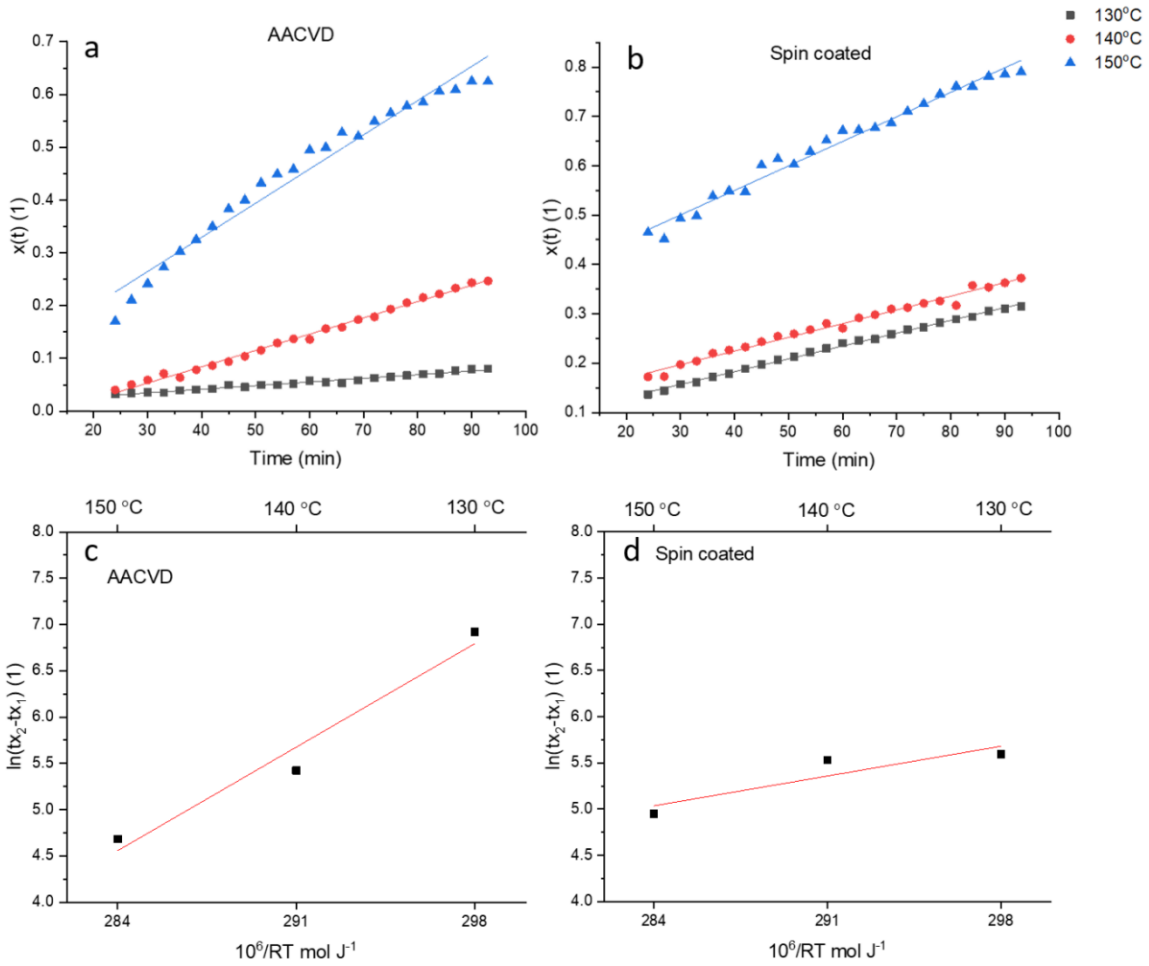


Figure 4-17 Graph showing volume fraction of (001) PbI_2 peak vs (001) MAPI over time for AACVD (a) and spin coated film (b). Below is the $\ln(tx_2\text{-}tx_1)$ vs. 1/RT plots. The gradient of the fitted line gives the activation energy

Figure 4-17 shows the results of the fractional fitting, where it can be seen that in the AACVD sample the growth of PbI_2 is faster at higher temperatures. At 150 °C the degradation begins to display a nonlinear pattern. At higher temperatures there may be different degradation mechanisms occurring, which could lead to this non monotonic behaviour. This effect should be first confirmed by

repeating the measurement, and potentially attempting the measurement over a longer time period or higher temperature. However, as the purpose of this study is comparative, a linear fit is used to simplify the model.

The spin coated sample shows a similar trend of increasing rate, however samples measured at 130 °C and 140 °C show very similar rates. This discrepancy may arise from the fact that every measurement is conducted on a different sample. Moreover, as the 1 -step spin-coating process is sensitive to process conditions and timing, the samples produced may have slight variations in morphology or composition. This may lead to different susceptibility to degradation between each sample, potentially affecting measured rate of degradation. Again, to verify these results multiple experimental runs should be conducted on multiple samples.

When looking at the (t_{x2}-t_{x1}) vs. 1/RT plot it is evident that the fit has a steeper gradient in the AACVD samples when compared to the spin coated samples. This indicates that the activation energy for degradation, E_a, is larger in the AACVD film. Table 4-6 shows the activation energies calculated by this method.

Table 4-6 Calculated activation energies of degradation for AACVD film and spin coated film

Film	Activation energy KJ mol^{-1}	Activation energy eV
AACVD	159 ± 31.3	1.66 ± 0.33
Spin-coated	46.1 ± 21.2	0.48 ± 0.22

The AACVD film has an activation energy that is over three times higher than the spin coated film. This strongly indicates that the AACVD films are more resistant to thermal stress. Previous studies in literature have shown that CVD based techniques produce perovskites that tend to show enhanced stability[211,212] . This enhanced stability may be due to several reasons. Firstly, the high temperature formation of the MAPI within the AACVD process would form a very dry film, with most of the solvent being evaporated during deposition. Whereas, the spin coated film would have residual solvent within it, potentially mediating the degradation pathway. Secondly, when looking at the sample XRD patterns, Figure 4-8, it can be observed that the spin-coated films already contain more PbI_2 than the AACVD film. This could mean that the spin coated film is not completely stoichiometric in composition, making the structure more defected, and this could lead to easier diffusion of ions due to thermal stress.

Previous work in the McLachlan group calculated the E_a of a spin-coated MAPI film to be 0.99 eV [208]. The film in this study had no visible PbI_2 before the experiments began. Therefore, this result may be more indicative of a higher quality spin-coated MAPI film. However, this value is still significantly lower

than that of the AACVD film. As the sample size is very limited, these results still need to be confirmed by repeat measurements. Moreover, the results should not necessarily be used as absolute values, but this methodology could be used to quantitatively compare the thermal stability of different deposition methods and compositions.

4.3.4 Future work and improvements

To substantiate these results a larger sample size should be used. This is especially required for the calculation of the lattice parameters, as the differences in values are quite small. As the growth process in AACVD is time consuming and inconsistent, producing many samples has proven to be problematic.

Electron beam diffraction would give more accurate crystallographic information and would also provide spatially resolved crystallographic information. Attempts have been made to prepare samples for this characterisation, however the thick films proved difficult to prepare. For electron beam diffraction, a thin slice of the film's cross section must be milled using a focused ion beam. Thick films have proven to be very difficult to mill, with the ion beam degrading the structure significantly before it is able to cut through the depth of the film. Therefore, development of a new protocol may be required to prepare samples for these kinds of measurements. Moreover, if samples could be successfully prepared, the diffraction information could be applied to the film formation study discussed in section 4.2. This would allow for the observation of crystal lattice constant evolution during growth.

Quantification of the strain via utilisation of sin2 Ψ XRD measurements would substantiate the claims of inbuilt strain. Attempts were made to conduct this measurement, however the measurement typically requires strong diffraction at high angles of 2θ (>50°) that this study's films do not possess. In work by Niu *et al.*, they utilised a grazing incidence arrangement of the XRD in combination with a sin2 Ψ to allow this measurement to work on peaks at lower angles [213]. Application of this method could allow for quantification of the stress of the strain within the film.

Again, a larger sample size would enable confirmation of the observations of the isothermal measurements. This would also allow for running of the samples at smaller temperature increments and give more data for the activation energy calculations. Utilising a system that would enable running measurements at higher temperatures could potentially shed light on the non-linearity observed in the AACVD film.

4.3.5 XRD study summary

This study shows that the AACVD films have a typical tetragonal MAPI crystal structure, with lattice parameters that are close to reference values. However, the films grown by this technique exhibit less preferred orientation to the spin coated analogue. This study also shows that the phase transition between tetragonal and cubic occurs at 50°C ± 1°C, lower than previously reported values for thin films. Utilising thermal XRD measurements this study also elucidated the thermal expansion coefficients of the system, again showing comparable results to spin coated films. Finally, isothermal XRD measurements were used to calculate the activation energies of degradation, showing that AACVD films are potentially more stable.

4.4 Optoelectronic and Electronic Measurements

This section will look at the optoelectronic and electronic properties of the AACVD films. Again, these properties have not been explored in previous studies and there is a lack of understanding of how materials deposited via AACVD behave in terms of charge generation and transport. By utilising ToF, Hall effects, 4- point probe and kelvin probe, this study reveals these intrinsic properties of the films.

4.4.1 Time of Flight measurements

Time of flight (ToF) is a common technique used to measure the charge carrier mobility of materials that has been seldom utilised in OMHPs [67,214]. The reason behind the lack of ToF studies in perovskites lies in the limitations of apparatus and the difficulties in both measuring and producing samples. ToF relies on measurement of transient currents as charges cross the sample. Therefore, if the films are relatively thin and have a high mobility, it will be difficult to measure the fast signals. Previous measurements in literature have been limited to single crystal samples which are thick enough for signals to arrive on timescales that are observable [67,215]. However, as AACVD films are typically much thicker than spin coated samples (> 5 µm vs 500 nm), it allows for the application of the ToF technique for one of the first times on a thin film.

These measurements were conducted on a sample of MAPI, which was deposited on FTO and coated with gold electrodes. The details of the sample preparation and experimental setup can be seen in 3.4.5. A schematic of the device stack can be seen in Figure 4-18. To photogenerate charges in the samples, a laser is fired through the FTO. The wavelength used for excitation was 355nm (3.55 eV), which is far higher in energy than the calculated band gap of the material 800nm (1.55 eV) (section 4.2.2). The absorption coefficient of MAPI at that wavelength is in the order of 10^5 cm^{-1} [216,217], which equates to a penetration depth of less than 100 nm. As this is far smaller than the thickness of the sample, it can be approximated that all the charges are being generated near the surface of the film.

Furthermore, a neutral density filter (ND3) was utilised to lower the intensity of the light. This is so that a large number photogenerated charges do not adversely affect the applied field.

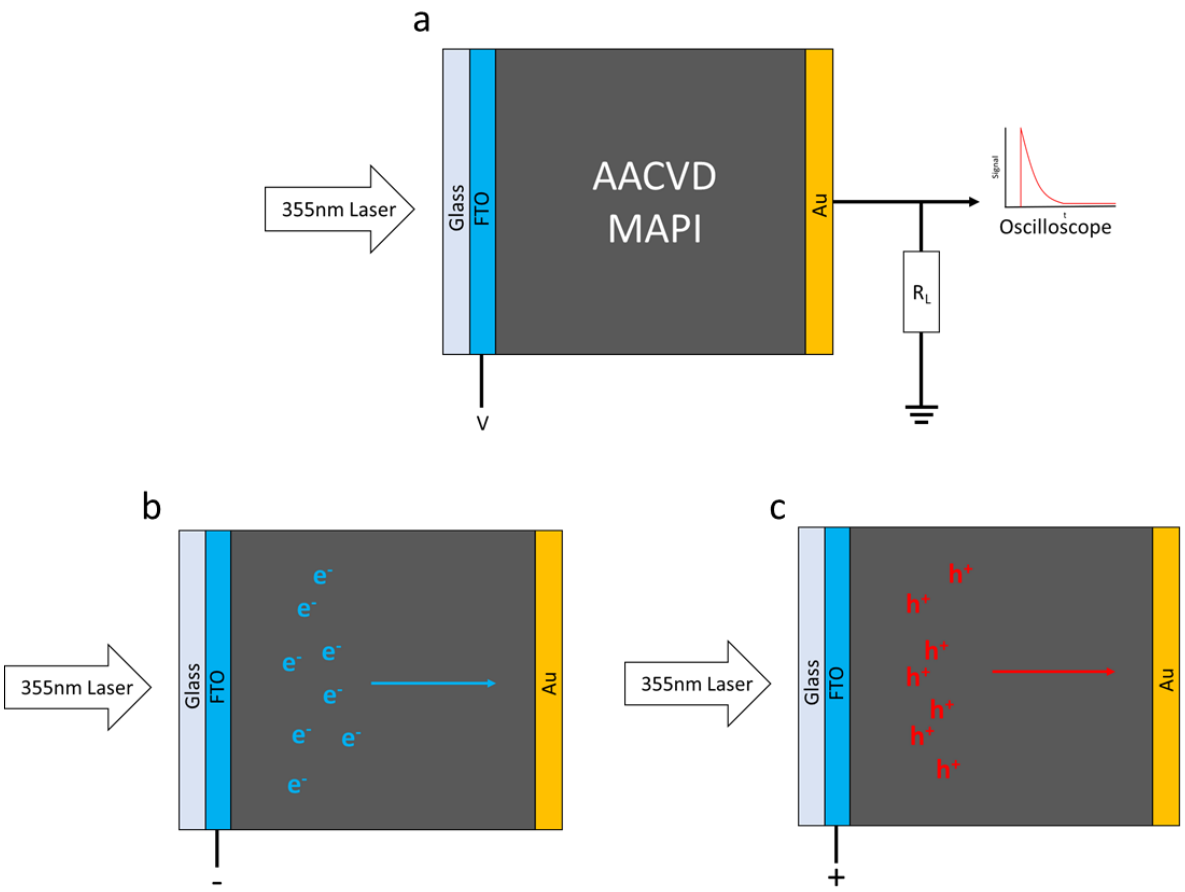


Figure 4-18 Schematic of AACVD ToF sample (a). (b) shows bias applied to FTO to collect holes and (c) shows the collection of electrons by applying the bias to gold

The charges are collected at the Au side of the device, with a positive applied bias on the FTO collecting holes at the FTO, and a negative bias collecting electrons. The resulting signals are then plotted as a double logarithmic plot. Here, the inflection point marks the transit time, t_x, of the charges. This point is determined by the intersection of tangents fitted on either side of the inflection point. A schematic of this process can be seen in Figure 4-19.

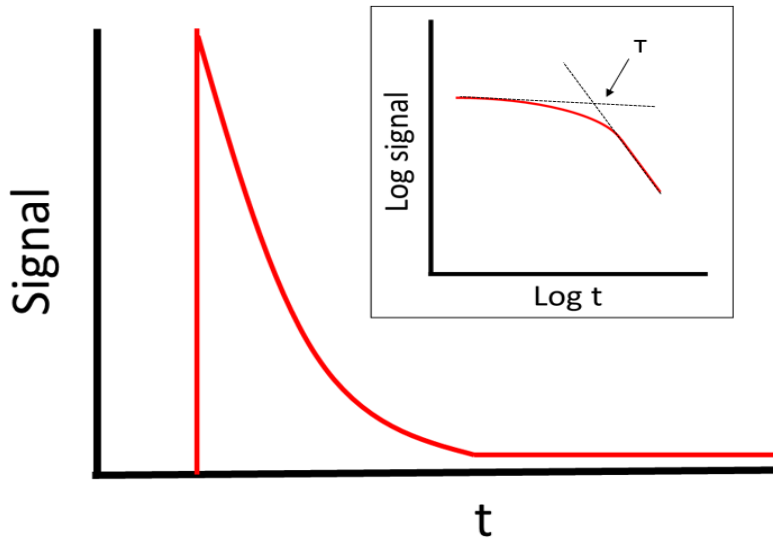


Figure 4-19 Graphical representation of time of flight signal as measured by the oscilloscope. Insert shows determination of arrival time by utilising a double logarithmic plot and the intersection of two tangents

Once the transit time is determined the mobility can be calculated using the following equation:

$$\mu = \frac{d^2}{V_{eff} t_x} \qquad (4\text{-}6)$$

Where μ is the mobility of the charge carrier, d is the film thickness, V_{eff} is the applied bias minus the inbuilt potential and t_x is the transit time determined from the measurement. The work function of FTO and Au is 4.4 and 5.1 eV respectively. Therefore, the applied voltage will be subtracted by 0.7 eV. This measurement is then repeated at different biases, to confirm the mobility dependence on the strength of electric field. The mobility value obtained should remain relatively constant as it should be a field independent value.

4.4.1.1 Development of the ToF technique for OMHPs

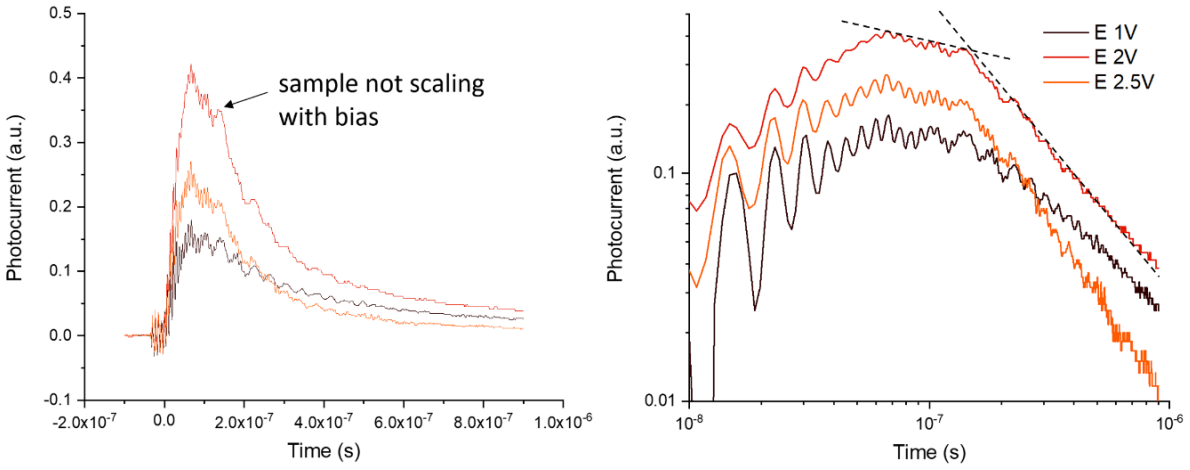


Figure 4-20 Photocurrent transients measured on sample with constant applied bias

Initial measurements of the samples showed anomalous results, with both the photocurrent and the arrival time not scaling with the applied bias. Figure 4-20 shows the electron photocurrent transients of a sample. Note how as the voltage is increased from 1 V to 2 V the amplitude of the signal increases, however, applying a higher bias causes an irreversible amplitude drop. This is due to the sample degrading under the applied bias, which causes a loss in photocurrent. When looking at the double logarithmic plot, there does not seem to be an observable shift in the transit time. Note that the noise of the signal makes determining the transit time difficult, creating a source of error in the absolute value. However, it is still clear that the signal is not responding to bias. This could be due to damage to the sample, or potential ionic effects interfering with the signal. As a bias is applied to the sample, ions may accumulate at the electrodes and screen the electric field (Figure 4-21). Several groups have witnessed this migration in weak electric field [115–117].

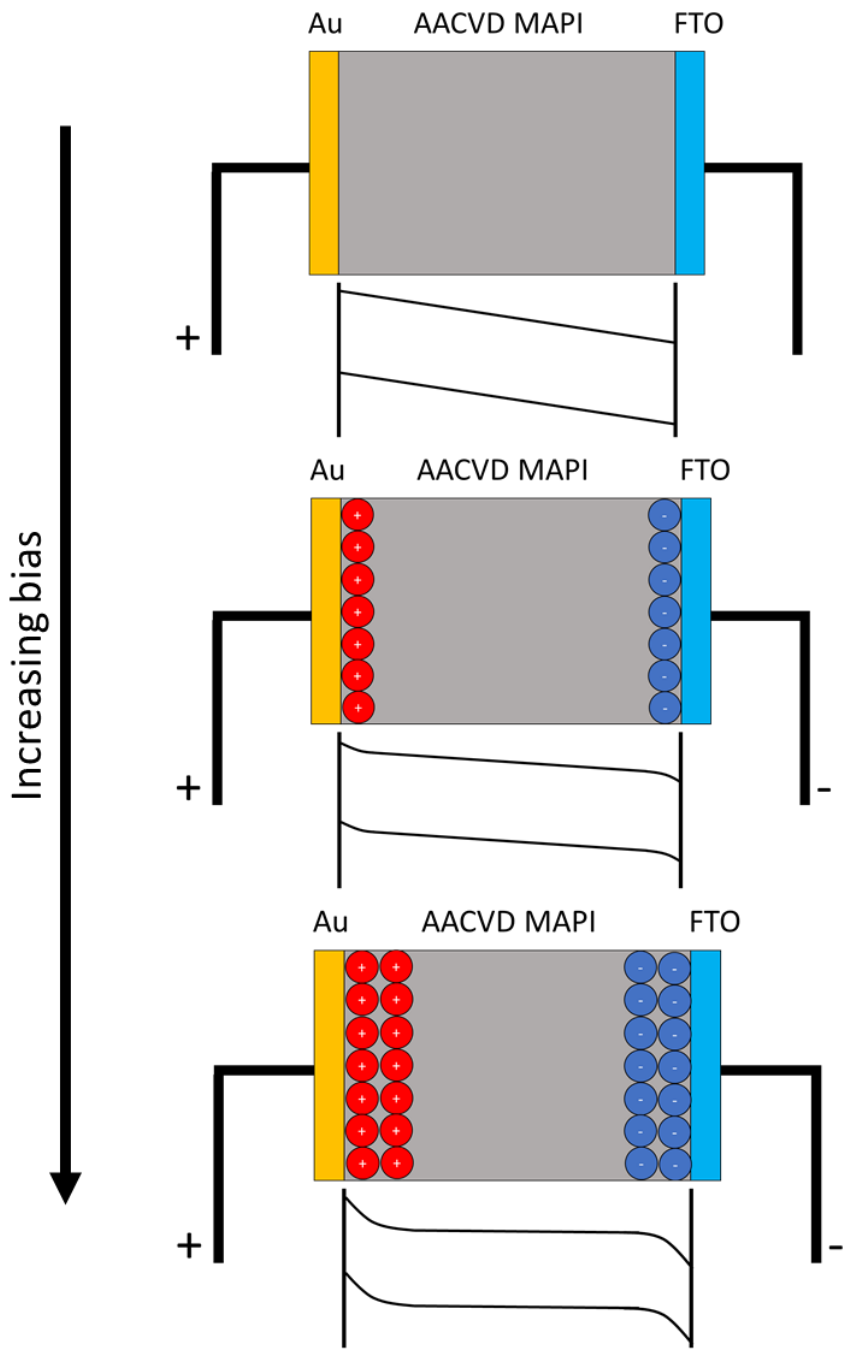


Figure 4-21 Schematic of ion migration screening with increasing electric field within the ToF sample

From this it can be observed that there are two significant issues when measuring these samples. Firstly, the potential of degradation of the sample under continuous bias and the non-scaling of the arrival time. To overcome these problems, a pulsing method was developed where the bias is applied to the sample over a set period. This means that the sample only experiences the bias for a short period of time, reducing the risk of damage and allowing for higher potentials to be used. Moreover, by adjusting the timing of the bias pulse this study attempted to decouple the influence of ions from the electronic response (Figure 4-22).

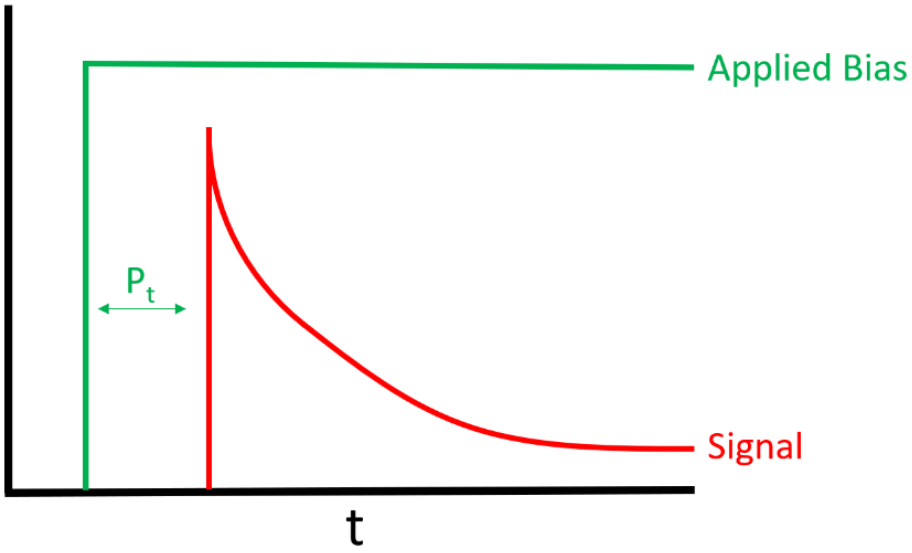


Figure 4-22 Schematic of voltage pulse timing in relation to photocurrent signal

Four different pulse delays (P_{dt}), 50 µs, 140 µs, 400 µs and 1000 µs were applied. The total length of each pulse was 1000 µs except for a pulse delay of 1000 µs, which used a total pulse time of 2000 µs. The timings relate to the time period between the first application of the bias and the laser excitation. 50 µs was the minimum time delay that could be used, as this allowed enough time for the bias to stabilise in the sample. Time periods over 2000 µs would lead to loss in photocurrent, indicating that this is the maximum duty cycle the sample can experience before degradation. Furthermore, due to the pulsing of the signal higher biases to the sample were able to be safely applied.

4.4.1.2 Pulse ToF measurements

Figure 4-23 shows data collected from one sample where this testing methodology was applied. The sample thickness was measured as 6.72 µm using a Dektak surface profilometer, with an average surface roughness of 0.76 µm. Additionally, tabulated data of arrival times and mobilities are shown in the appendix (Figure 9-2). What is clearly observable is that at longer pulse times the signal begins to quench, indicating the increasing influence of ionic screening. This is considerably more noticeable in the electron signal, which seems to be more strongly influenced by $P_{dt.}$ To confirm that this quenching is not due to degradation, the sample was remeasured after the set of experiments. Appendix Figure 9-3 shows the signal not degrading after the experiments were completed.

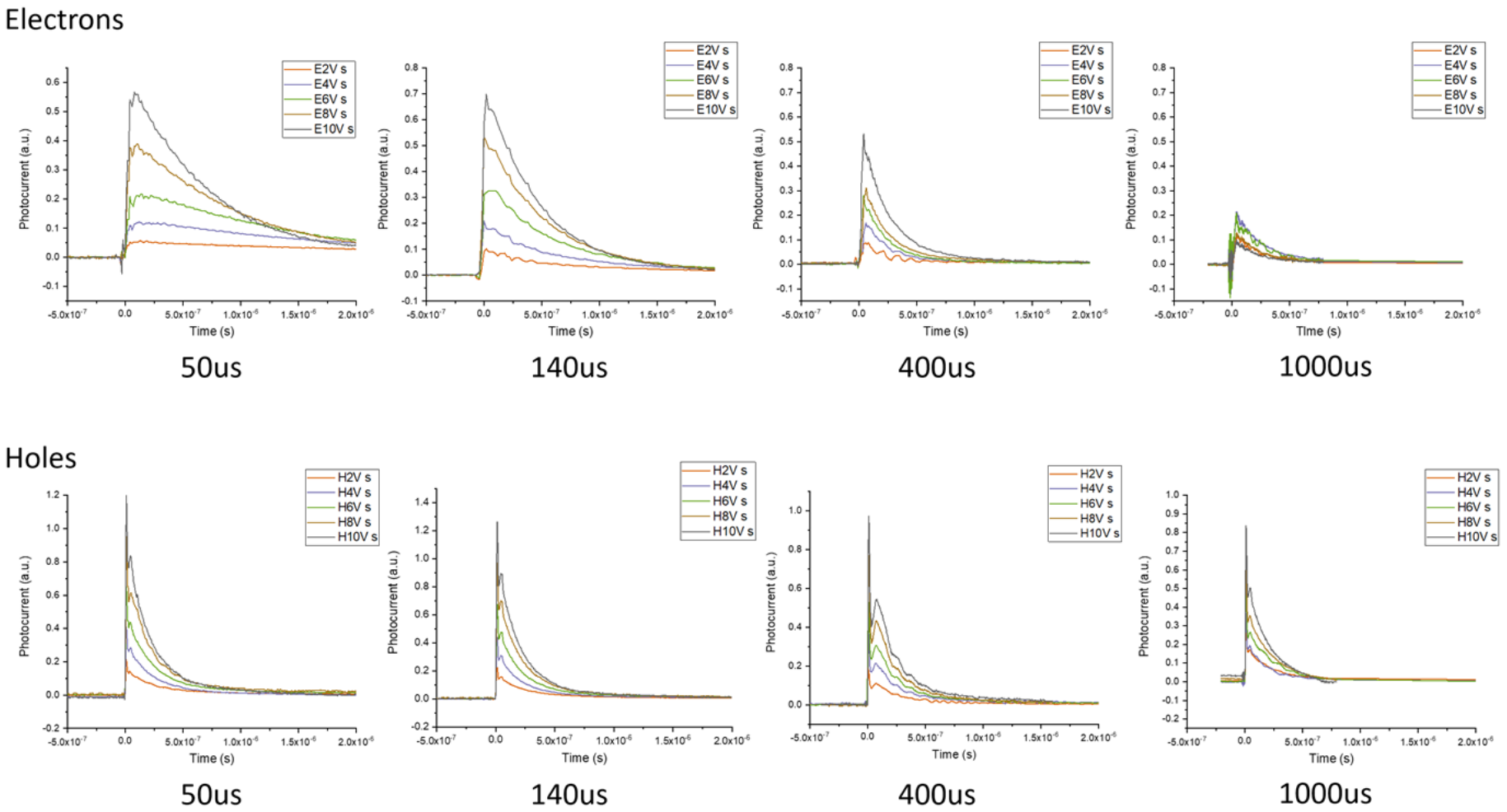


Figure 4-23 Photocurrent transients measured at different pulse delays

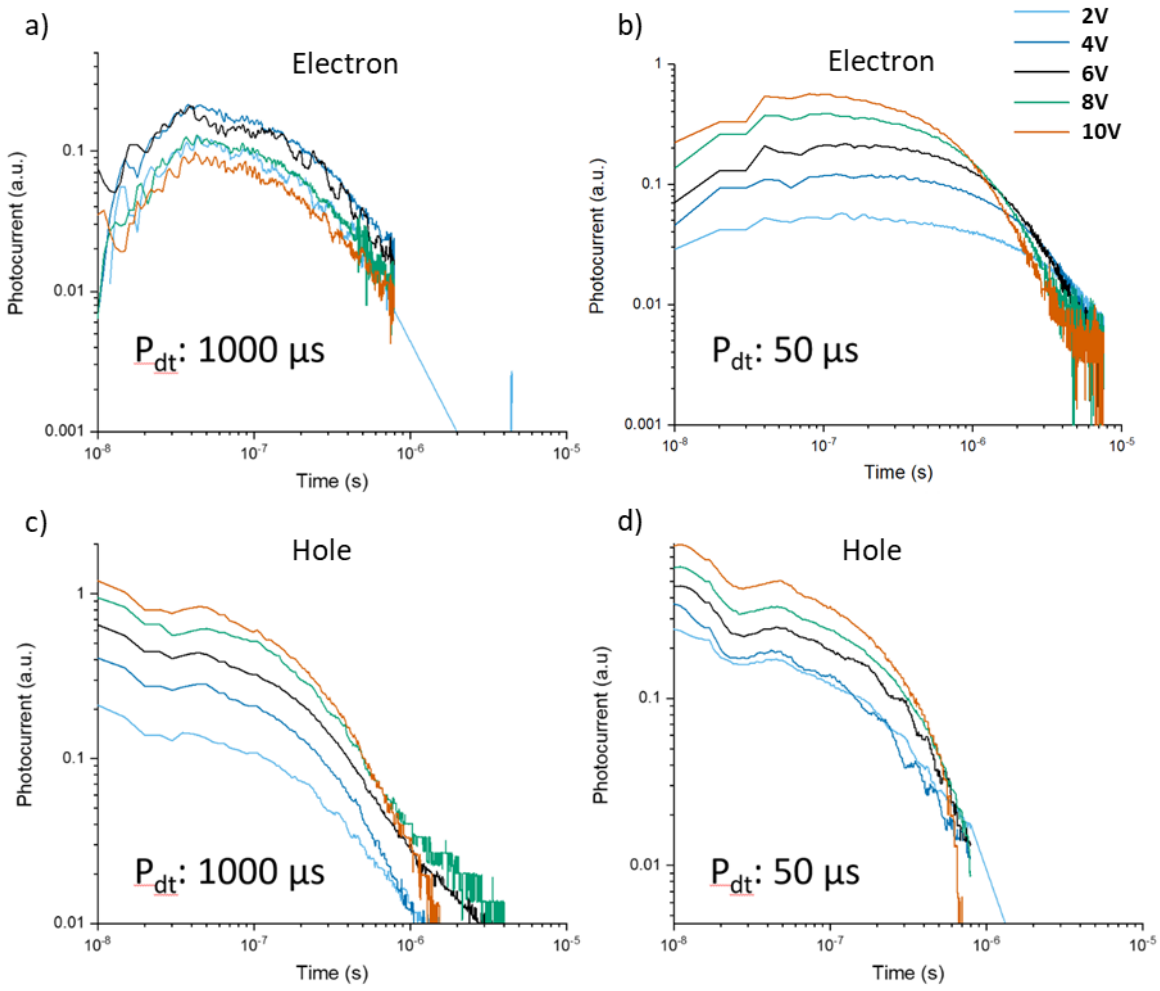


Figure 4-24 Log-log plots of sample tested with 50 µs and 1000 µs pulse delays. a) Electron signal with a bias pulse time of 1000 µs. b) Electron signal with a bias pulse time of 50 µs. c) Hole signal with a bias pulse time of 1000 µs .d) Hole signal with a bias pulse time of 50 µs

Figure 4-24 shows the log-log plot of the 50 µs and 1000 µs experiments. Here the onset of arrival time scaling in the 50 µs when compared to the longer pulse time can be clearly seen. Moreover, at 1000 µs the signals become very noisy and the inflection point becomes even more difficult to determine. Additionally, the time scale reduces as the delay increases. When looking at the holes, it is evident that the trend is not as clear. A lower delay does not seem to improve the measured signal, with both the amplitude and the arrival time not significantly changing. This data shows an anisotropic charge carrier behaviour, which indicates that the ionic effects do not affect both charge carrier species equally. Considering that V_I are potentially the dominant mobile, these results could be explained by the accumulation of these positively charged species at the collecting electrode [218–220]. During the hole measurement these vacancies would migrate towards the FTO contact, where the signals are collected. This would explain why the hole measurements show the invariant behaviour

when compared to the electron measurements. The overall time scale of the signals is similar between electron and holes, indicating balanced charge transport in the material. This matches what has been previously observed in MAPI [221]. Calculating the resulting mobilities using equation (4-6), gives values of 0.06 - 0.84 cm^2 $(V\ s)^{-1}$ for electrons, and 0.11 – 1.37 cm^2 $(V\ s)^{-1}$ for holes.

Using a Poole-Frenkel plot this data can be summarised by plotting the mobility derived via equation (4-6) vs. the square root of the electric field. The electric field is calculated using:

$$E = -\frac{V}{d} \qquad (4\text{-}7)$$

Where E is the electric field, V is the applied bias and d is the thickness of the sample. Note that in this case the effective electric field is unknown due to potential ionic screening.

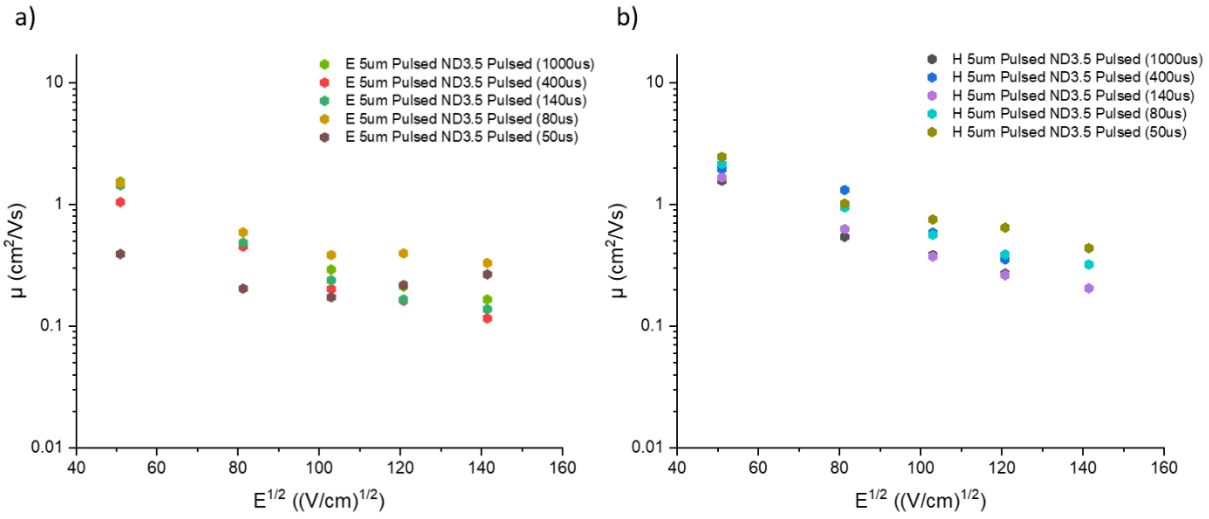


Figure 4-25 Poole-Frenkel of data gathered from ToF measurements. a) electron mobility b) hole mobility

Looking at Figure 4-25 it is evident that the electron mobilities scale negatively with the electric field until pulse times of 80 µs or below are used. This negative slope is a symptom of the arrival times not scaling with bias. In the holes the negative slope is present throughout all of the pulse time variations, again showing their invariance to the pulse delay.

Comparing these results with the few literature values available, thin film ToF measurments have not been conducted at different biases. Chen *et al.* utilised ToF to measure a 500 nm thin film of MAPI, however they only utilised a fixed bias of 20 V [214]. From their data it can be seen that their arrival times are in the same order of magnitude as this study's work (10^{-7} s), though their film is much thinner. Furthermore, they calculated their electron and hole mobilities to be in the order of 10^{-4} cm^2 $(V\ s)^{-1}$. In contrast this study measured mobilities approaching unity. Potentially, their values are so low because they experienced degredation during their measurment. However, it cannot be discounted that AACVD technique may produce films of higher quality and therefore better charge transport

properties. When comparing this study's results to single crystal measurments conducted by Dong *et al.*, they measured an electron mobility of 24 cm^2 $(V\ s)^{-1}$, with no results being shown for holes. Whilst the electron result are higher, this is expected as single crystals are more defect free and therefore have better charge carrier properties. Interestingly, they conducted their measurment from 2.5 – 20 V and show scaling of the arrival times with bias. Again, this may be due to the defect free nature of a single crystal, leading to lower amounts of ion accumulation at the interface. Additionally, when considering the electric field in their sample, at 20 V the field strength is 6.6 x 10^3 V m^{-1}. At 10 V this study's sample experiences 2 x10^6 V m^{-1}, therefore accumulation of the ions at the interface is far more likely to occur.

From these results, the timescales of ion migration using equation (4-6) could also be estimated. A significant effect of ion migration is seen at P_{dt}= 1000 µs. Using 1000 µs as an estimate of the time for ions to begin accumulating at the electrodes, equations can be applied to calculate an estimate of ion mobility. Using 6 V as the applied bias the ion mobility is 4.71 x 10^{-5} cm^2 $(V\ s)^{-1}$. This is five orders of magnitude slower than this study's calculated charge carrier mobilities. However, this assumes that the ions are drawn across the whole thickness of the film, but unlike photogenerated charge carriers ions are present throughout the film. Therefore, using 100 nm for d gives a value of 1.89 x 10^{-8} cm^2 $(V\ s)^{-1}$. These two values should be considered the upper and lower limit of the estimation. Comparing these values to literature, the highest calculated ion mobilities MAPI are in the order of 10^{-4} cm^2 $(V\ s)^{-1}$ [222]. The lowest measured mobilities are in the order of 10^{-6} cm^2 $(V\ s)^{-1}$ [223]. Therefore, it is plausible to assume that the effect this study witnessed is indeed due to ions. Furthermore, this would place this study's ionic mobility values in the upper region of most materials. If comparing this to Li^+ mobilities in $LiCoO_3$, a common battery electrode material, the values range between 10^{-8} to 10^{-10} cm^2 $(V\ s)^{-1}$. The ionic cionductivity in solid oxide fuel cell materials is in the order of 10^{-9} cm^2 $(V\ s)^{-1}$.

4.4.1.3 ToF future work

As these results have been collected using a single sample, repeat measurements should be used to validate these results. Furthermore, variation in thickness and temperature could be used to further decouple ionic and electronic influences. Measurement of the thinner and thicker samples could allow for determination of whether the arrival times scale with thickness. Additionally, different thickness may have different responses to the pulse. Likewise, measuring samples at lower temperatures, should reduce the influence of ions.

Another potential avenue of investigation is the exploration of different perovskite compositions and dopants. By altering the composition, it may be possible to reduce the ionic migration within the film [224]. Therefore, it may be possible to eliminate or reduce the signal from ionic effects.

4.4.1.4 ToF Summary

In conclusion, this study shows the development of a novel ToF technique to extract electron and hole mobilities in thick MAPI films deposited via AACVD films. Furthermore, the study elucidated the role that ionic migration has on the measurement and derive estimates on the timescales of ionic effects.

4.4.2 Hall and Electrical Measurments

To confirm the mobilities extracted by the ToF measurements the Hall effect was utilised. This measurement will not only allow for extraction of mobility values, but by the virtue of the measurement technique, resistivity and charge carrier concentrations can also be extracted. The results were compiled from three different samples, with each result being an average of 10 consecutive measurements. Details of the experimental setup and the Hall effect can be seen in section 3.4.4.

The mobility using the Hall effect is derived from the following equation:

$$\mu = \frac{|V_{hall}|}{R_S I B} \qquad (4\text{-}8)$$

Where μ is the hall mobility, V_{hall} is the measured hall voltage, I is the injected current, B is the magnetic field and R_s is the sheet resistivity. By utilising the Van der Pauw geometry, this study first measured the sheet resistivity, R_s, of the samples. The samples were probed using 1 nA, with the ohmic check being conducted from 0.1 to 1 nA. The ohmic check on the samples can be seen in appendix (Figure 9-4). Then using the same geometry, the Hall measurement was performed to derive the V_{hall}. This would give all the information required to calculate the hall mobility. Additionally, by using the following equation, the sheet carrier density can be derived:

$$n_s = \frac{IB}{q|V_{hall}|} \qquad (4\text{-}9)$$

Where n_s is the sheet carrier density and q is the elementary charge. By then dividing the thickness of the sample (6.72 μm), the bulk charge carrier density, n, can be determined. The following table summarises the results.

Table 4-7 Summary of data collected by Van der Pauw and Hall measurements

Sample	Resistivity Ω cm	Hall voltage V	Charge carrier density $(cm^3)^{-1}$	Hall mobility $cm^2 (V\ s)^{-1}$
1	2.65×10^6	6.95×10^{-3}	2.10×10^{11}	11.2
2	1.7×10^6	6.37×10^{-3}	2.3×10^{11}	15.9
3	2.07×10^6	5.10×10^{-3}	2.84×10^{11}	10.6
Avg.	2.14×10^6	6.14×10^{-3}	2.41×10^{11}	12.6

When comparing these values to literature, the electrical resistivity values of single crystal MAPI are typically in the order of $10^6 - 10^7$ Ω cm [225–228]. This indicates that the electrical properties of the AACVD deposited perovskite are single crystal like. When considering this is an in-plane measurement, the results are remarkable as the grain boundaries do not seem to have a significant effect. Thin film conductivity/resistivity measurements are difficult to find, especially for thin film MAPI. This could be due to the high resistivity making nm scale films very difficult to measure.

The Hall voltage measured was positive, which indicates that the sample is slightly p-type in nature. In MAPI defects and excess MAI can lead to a slight p-type doping in the film [229,230]. As the AACVD films are produced by exposing them to a vapour of MAI, excess of the organic cation is very likely to occur. Looking at the mobility values themselves they are well within the expected values for MAPI thin films, however they are lower than the single crystal counterparts [221]. The measured charge carrier concentrations also seem to correlate with what is typically observed in literature, with values for MAPI ranging from 10^{10} to 10^{13} [225–228,231].

When focusing on mobilities extracted by Hall measurements, again most reported results have been measured on single crystals. This is due to the difficulty of passing enough current through a very resistive sample. Single crystal values are reported to be between 20-105 $cm^2 (V s)^{-1}$ [225–228]. Chen *et al.* have reported values for thin film Hall measurements, however they utilise a laser to induce photoexcitation, which improves the conductivity. They report a mobility of 1.5 $cm^2 (V s)^{-1}$. However, they utilise a more sophisticated Faraday-induction corrected AC Hall measurement system to resolve the small hall voltage, therefore it is not a like for like comparison [232].

Figure 4-26 shows the Hall measurement plotted on a Poole-Frenkel plot with the results from the ToF measurement in section 4.4.1. As the Hall effect measures the drift of charge carriers perpendicular to an applied potential, this study plotted it at zero electric field. Essentially, the Hall measurement should show a mobility less affected by ionic screening, as the ions would be drawn to the current injecting contacts. This is the reason this study used long settling times as described in section 3.4.4. This leaves the injected charge carriers to form the Hall voltage due to the Lorentz forces, giving a potentially true intrinsic mobility value.

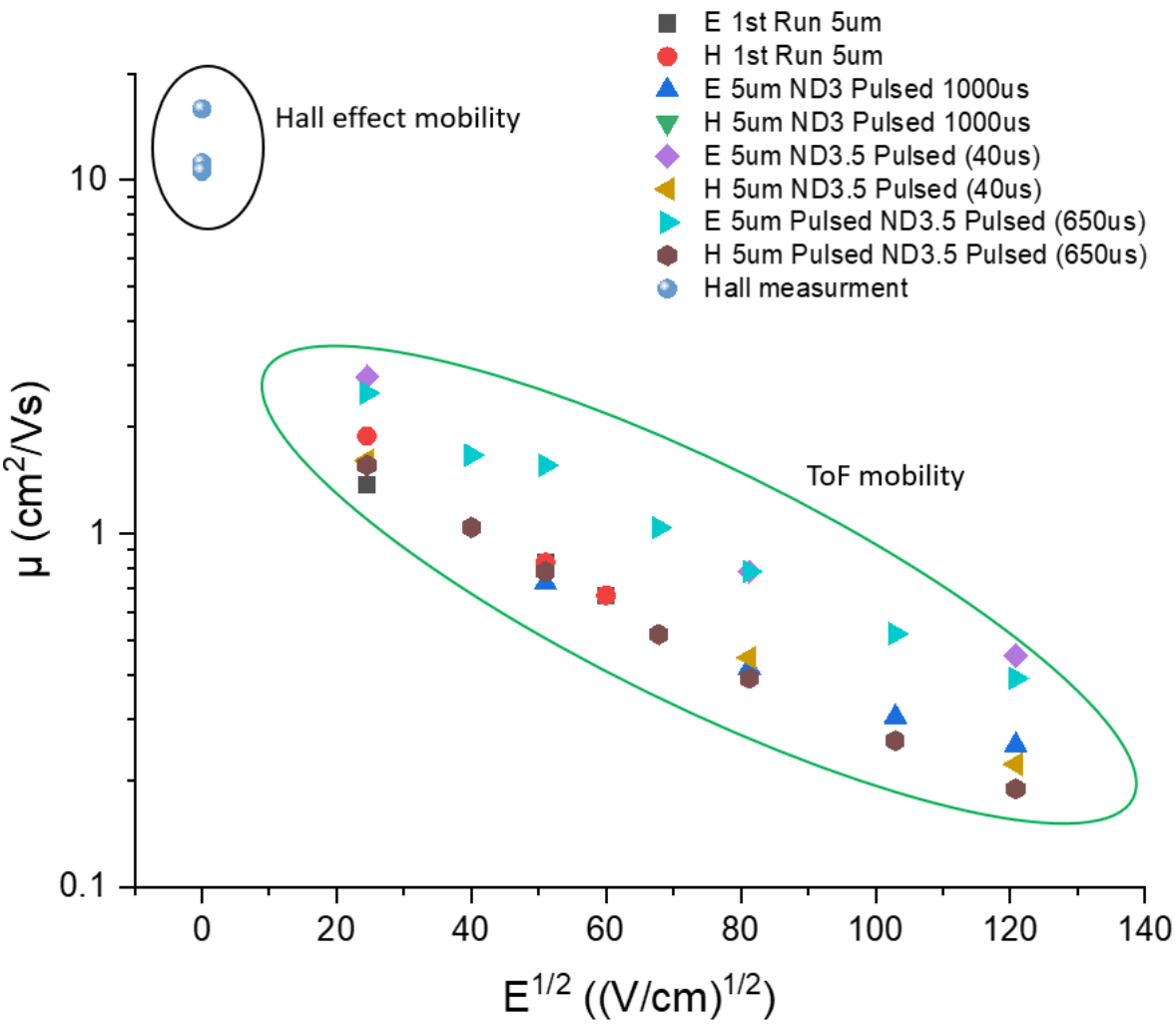


Figure 4-26 Poole-Frenkel plot showing combined extracted mobility values of Hall and ToF measurements

4.4.2.1 Comparison to ToF measurements

The results show that the Hall measurements are an order of magnitude higher. This may be because the Hall effect measures the in-plane mobility versus the out of plane mobility in the ToF measurement. However, the enhanced mobility may come from the lack of ionic screening experienced during this measurement. On the Poole-Frenkel plot, a linear dependence of the mobility based on the square root of the electric field can potentially be seen. The gradient of this slope could be related to the amount of ionic screening the sample experiences, and therefore an indication of the number of ionic defects within the sample. The following equation could be used to describe the effect:

$$\mu = i_s\left(E^{\frac{1}{2}}\right) + \mu_i \qquad (4\text{-}10)$$

Where μ is the measured mobility, i_s is the gradient due to ionic screening, E is the electric field and μ_i is the intrinsic mobility. Using this equation to process ToF mobilities, it is possible to solve for μ_i to

derive a "true" mobility of the material. Furthermore, the parameter i_s could be used to determine the quantity of ionic defects in the material, therefore giving a potential quantitative value for the quality of the perovskite.

4.4.2.2 Future Work

As these results are based on a limited range of samples and measurements, the value will need to be verified by repeat measurements. In terms of the Hall measurements themselves, measuring the samples at lower temperatures could "freeze out" ionic contributions, therefore improving the accuracy of the measurements. Moreover, utilising the same Faraday-induction compensated AC Hall technique as Chen *et al.* may also help to extract more accurate mobility value [232].

Furthermore, alternative techniques should be used to verify the mobility. Terahertz spectroscopy or charge extraction by a linearly increasing voltage (CELIV) could be used to further verify this study's obtained mobilities.

4.4.2.3 Hall and Electronic Summary

In conclusion, the results of this study show that the AACVD film has electrical properties that are comparable to single crystal MAPI literature values. In addition, the Hall mobilities are also comparable to literature values, though they are higher than the ToF results. Comparing these results, the study potentially shows a link of the measured mobility with the effect of ionic screening due to the application of electric fields.

4.4.3 Determining the Energy Levels: Kelvin probe, APS and optical band gap

Determining the energy levels of semiconducting material is crucial. Knowing the relative positions of the valence, conduction and Fermi level is key to device fabrication and can help with elucidating the origin of material characteristics. This study uses a mixture of Kelvin probe, ambient photoemission spectroscopy and absorption measurements to determine the energy levels of the AACVD MAPI film. All of the following measurements were performed by Matyas Daboczi. The experimental details for each of the techniques can be seen in section 3.4.7.

4.4.3.1 Kelvin Probe and APS results

To determine the valence band position, APS measurements were used. The resulting cube root vs. photon energy plot can be seen Figure 4-27 a). From this plot a valence band position of 5.32 eV ca be extrapolated; this is within the expected range of MAPI, with values ranging between 5.3-5.75 eV [233,234].

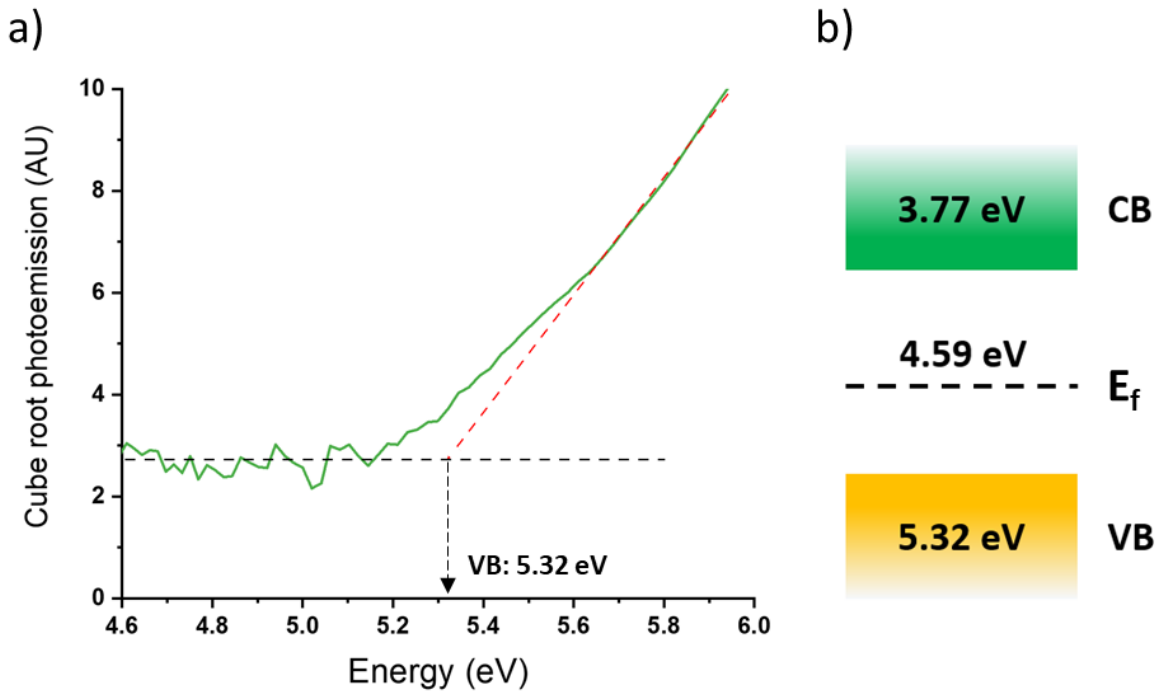


Figure 4-27 a) Ambient photoemission spectroscopy measurement of AACVD MAPI film. b) Energy level diagram of AACVD MAPI film. Valence band derived from APS measurements, Fermi level from Kelvin probe measurements and conduction band is calculated from the optical band gap

From the Kelvin probe measurements, a Fermi level value of 4.59 eV is derived. If we combine these measurements with the optical band gap values obtained in section 4.2.2, the following energy level diagram can be formed (Figure 4-27 b)). Comparing these values to literature, the AACVD film matches closely to the energy levels reported [49,161]. The mid-band position is 4.54 eV, therefore the Fermi level indicates a slight p-type doping of the film. However, the films show less doping when compared to spin coated films, which due to defects exhibit a deeper Fermi level [229]. This corroborates the Hall measurement results, which indicated p-type behaviour.

4.4.3.2 Summary

This study used APS, Kelvin probe and optical measurements to determine the key energy levels of the AACVD MAPI film. The results show that the film closely matches literature values for MAPI. Moreover, Kelvin probe measurements show that the films are slightly p-doped, which is also a typical feature of MAPI films.

4.5 Applications of Thick AACVD Films

Films made via this study's method have also shown promise in other material property studies. This section will briefly highlight some of the collaborative work that has utilised these films.

4.5.1 Thermal conductivity of AACVD MAPI films

The application of OMHPs in thermoelectric devices has been a relatively new area of research. Initial studies have shown excellent thermoelectric properties such as a low thermal conductivity, large Seebeck coefficient and high charge carrier mobilities [235–237].

By utilising the AACVD method to deposit films on specialised test chips, collaborators were able to measure the thermal conductivity of this study's AACVD MAPI films [238]. They contrasted the results with evaporated films. The results of this collaboration can be seen in Figure 4-28.

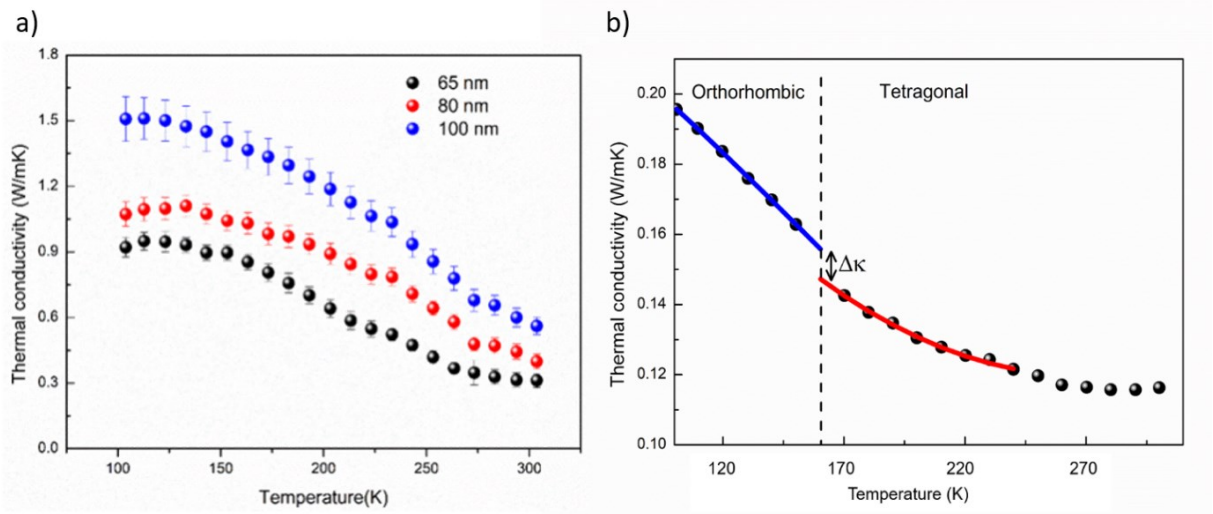


Figure 4-28 Thermal conductivity measurements of evaporated (a) and AACVD MAPI (b) [238]

The results show a clear discontinuity at the orthorhombic-tetragonal phase transition in the AACVD films. In contrast, this is not observed in thermally evaporated films. This is due to the increased mass of material in the AACVD film improving the sensitivity of the measurements. Again, this shows the value of producing these thick films for material property study.

4.5.2 Alpha radiation absorption

OMHPs have recently attracted attention for potential use in ionizing radiation detection, due to their strong absorption, particle radiation stopping power and large defect tolerance. To date there have been several studies showing the promise of these materials in X-ray, γ-ray and α-radiation detection [239,240].

Yet again, the AACVD films have shown promise in this area. With help of Theo Kreouzis et al., AACVD MAPI films, deposited on FTO, trialled as α-radiation detectors. The films were held at different biases

and exposed to α-radiation, produced by the decay of an americium 241. Figure 4-29 shows the results of this initial experiment.

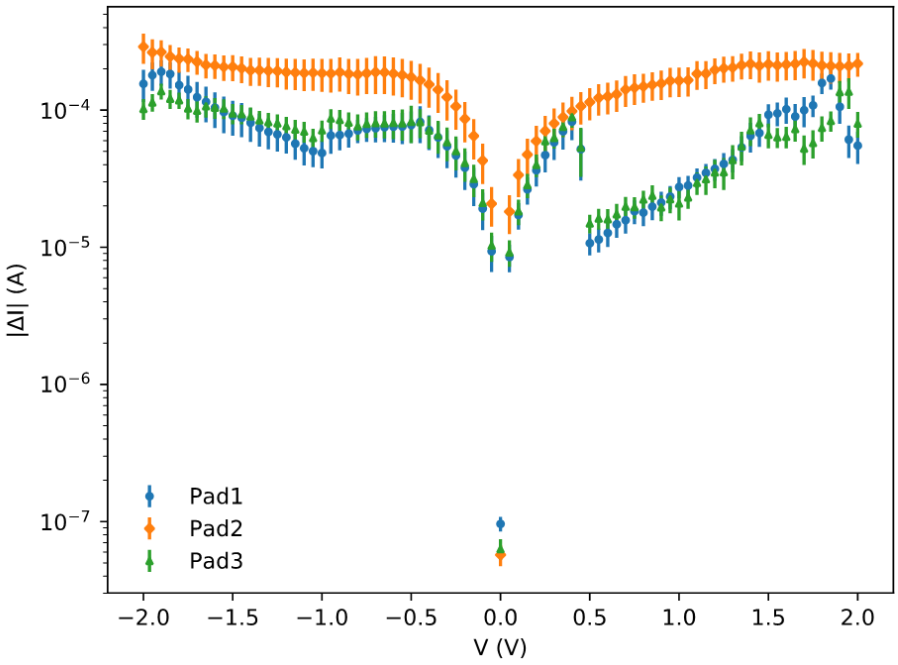


Figure 4-29 Average measured ΔI upon exposure to α-radiation, averaged over 16 measurements

Upon exposure, a detectable change in current was observed. These promising results indicate the potential for AACVD MAPI films to be used within α-radiation detectors.

4.6 CHAPTER 3 SUMMARY

By utilising several characterisation techniques, this study was able to monitor the growth of MAPI films via AACVD. Furthermore, these results shed light on the chemical and physical mechanisms involved in the formation of the films. Key characteristics of the films were then determined using a variety of analytical techniques, with the results indicating that the produced films closely match typical characteristic of MAPI. Table 4-8 summarises the key measured material properties of the AACVD film.

Table 4-8 Summary of AACVD MAPI film properties measured in Chapter 3. Conduction band, Valence band and Fermi Level values are relative to vacuum level.

Material Property	**Measured Value**
Lattice Parameters	a = 8.88Å c= 12.67 Å
Volumetric thermal expansion coefficient	1.27×10^{-4} K^{-1}
Tetragonal-Cubic phase change	50°C ± 1°C
Thermal degradation activation energy	1.66 eV
Optical Band Gap	1.55 eV
Conduction Band	3.94 eV
Valence Band	5.49 eV
Fermi level	4.59 eV (p-type)
Resistivity	2.14×10^{6}
Charge carrier concentration	2.41×10^{11} $(cm^3)^{-1}$
Hall mobility	12.6 cm^2 $(V\ s)^{-1}$ (p-type)
ToF e^- mobility	0.06 - 0.84 cm^2 $(V\ s)^{-1}$
ToF h^+ mobility	0.11 – 1.37 cm^2 $(V\ s)^{-1}$
ToF ion mobility estimate	10^{-5} – 10^{-8} cm^2 $(V\ s)^{-1}$

These values are derived from a few measurements and a limited set of samples, therefore they will have to be further validated experimentally. However, these are the first reported values of any kind for material deposited using AACVD. Moreover, they also indicate that the material is comparable to counterparts deposited with more conventional techniques.

5 AACVD LEAD ACETATE

5.1 INTRODUCTION

The main drawback of the method used in chapter 4 was that the resulting films were very thick. This limited their application for non-photovoltaic applications and intrinsic study. This chapter shows the development of a new AACVD technique that can produce thinner films (~ 1µm) and the application of these films in photovoltaic devices.

5.2 LEAD ACETATE AS A PRECURSOR

Over the past few years, there have been several different precursor systems used to form MAPI. The typical method involves using PbI_2 as the primary Pb^{2+} source, however, there have been recent developments in using alternative precursors. Non-halide lead precursors such as, lead nitrate ($Pb(NO_3)_2$), lead carbonate $PbCO_3$ and lead thiocyanate ($(Pb(SCN)_2$) have been reported to successfully produce perovskite films [241,242] . One of the more promising alternative precursors is lead acetate ($Pb(Ac)_2$), which was pioneered by Zhang *et al.* in 2015 to produce devices with a PCE of 14% [243]. $Pb(Ac)_2$ has been shown to allow for rapid crystallisation of the film, forming the perovskite in only a few minutes of annealing [244]. Furthermore, it has been shown that the hydrated form, lead acetate tri-hydrate ($(Pb(Ac)_2{\cdot}3H_2O$), enhances film stability [244,245] (See Figure 5-1).

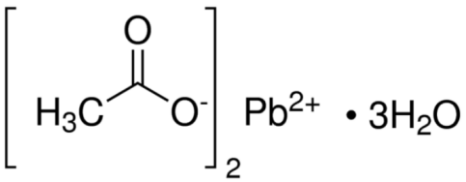


Figure 5-1 Chemical formula of lead acetate tri-hydrate ($(Pb(Ac)_2{\cdot}3H_2O$)

In terms of CVD, to date there have been no reported uses of $Pb(Ac)_2$ to fabricate any OMHPs. This is possibly due to the fact that lead acetate decomposes before being vaporised [246]. However, this limitation does not apply to the AACVD technique, as precursors do not need to be thermally vaporised. Moreover, as $Pb(Ac)_2{\cdot}3H_2O$ readily dissolves in many volatile solvents, it makes it a highly suitable precursor for AACVD.

5.3 DEVELOPMENT OF THE LEAD ACETATE 2-STEP AACVD

By utilising $Pb(Ac)_2{\cdot}3H_2O$ dissolved in MeOH, this study was able to substitute the PbI_2 in DMF step in the 2-step method detailed in chapter 4 (Figure 5-2). This came with several advantages. Firstly, MeOH is easier to volatilise due to its lower surface tension of 22.70 mNm^{-1} versus 38.16 mNm^{-1} [247,248].

Secondly, the solubility of $Pb(Ac)_2 \cdot 3H_2O$ in MeOH is higher than PbI_2 in DMF. Thirdly, MeOH is a safe and green solvent. This is notable as OMHPs are typically processed using toxic solvents, such as DMF and NMP, which limits their industrial applicability. Lastly, as the first (S1) and second step (S2) utilise common solvents, this could potentially make it easier to implement the systems and lower the cost.

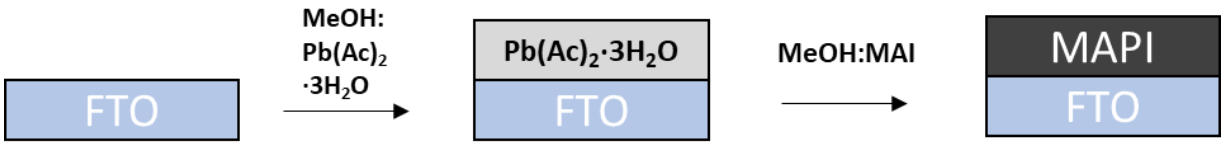


Figure 5-2 Schematic showing the 2-Step AACVD process using lead acetate ($Pb(Ac)_2 \cdot 3H_2O$)

5.3.1 Determining the deposition parameters

To determine the deposition parameters, this study first began by using a fixed concentration of $Pb(Ac)_2 \cdot 3H_2O$ in MeOH. To determine this concentration, half the concentration of the solubility limit was used, which was 0.13 M. This solution was aerosolised for 20 minutes and passed into the reactor at 0.5 l min^{-1}, where an FTO coated glass substrate was placed. Experimental details are presented in section 3.2. Several deposition temperatures were used to rapidly determine the ideal parameters. Table 5-1 summarises the experimental conditions used.

Table 5-1 Experimental conditions used for the determination of the first step deposition temperature. Notes describe the resulting film.

Concentration (M)	Flow Rate (l min^{-1})	S1 T (°C)	S2 T (°C)	Notes
0.13	0.5	500	230	No deposition with powdery residue on reactor
0.13	0.5	230	230	Sparse coverage with 3D structures
0.13	0.5	200	230	Smooth film with pinholes and incomplete coverage
0.13	0.5	175	230	Smooth film small pinholes and macro streaks
0.13	0.5	150	230	Smooth film large pinholes
0.13	0.5	125	230	Smooth film large pinholes

At 500 °C there was no visible deposition on the substrate, with powdery residue forming at the exit of the reactor. This indicated that the deposition temperature was far too high, resulting in homogenous nucleation of the precursor in the gas phase. At 230°C some deposition of material started to be seen on the substrate, however it is very sparse, with large three-dimensional flakes forming. Figure 5-3 shows the SEM images of the deposited material when using different first step temperatures. As the deposition temperature was lowered, a solid film began to form. At 200°C a

formation of a continuous film began to be observed, albeit very rough with large three-dimensional structures.

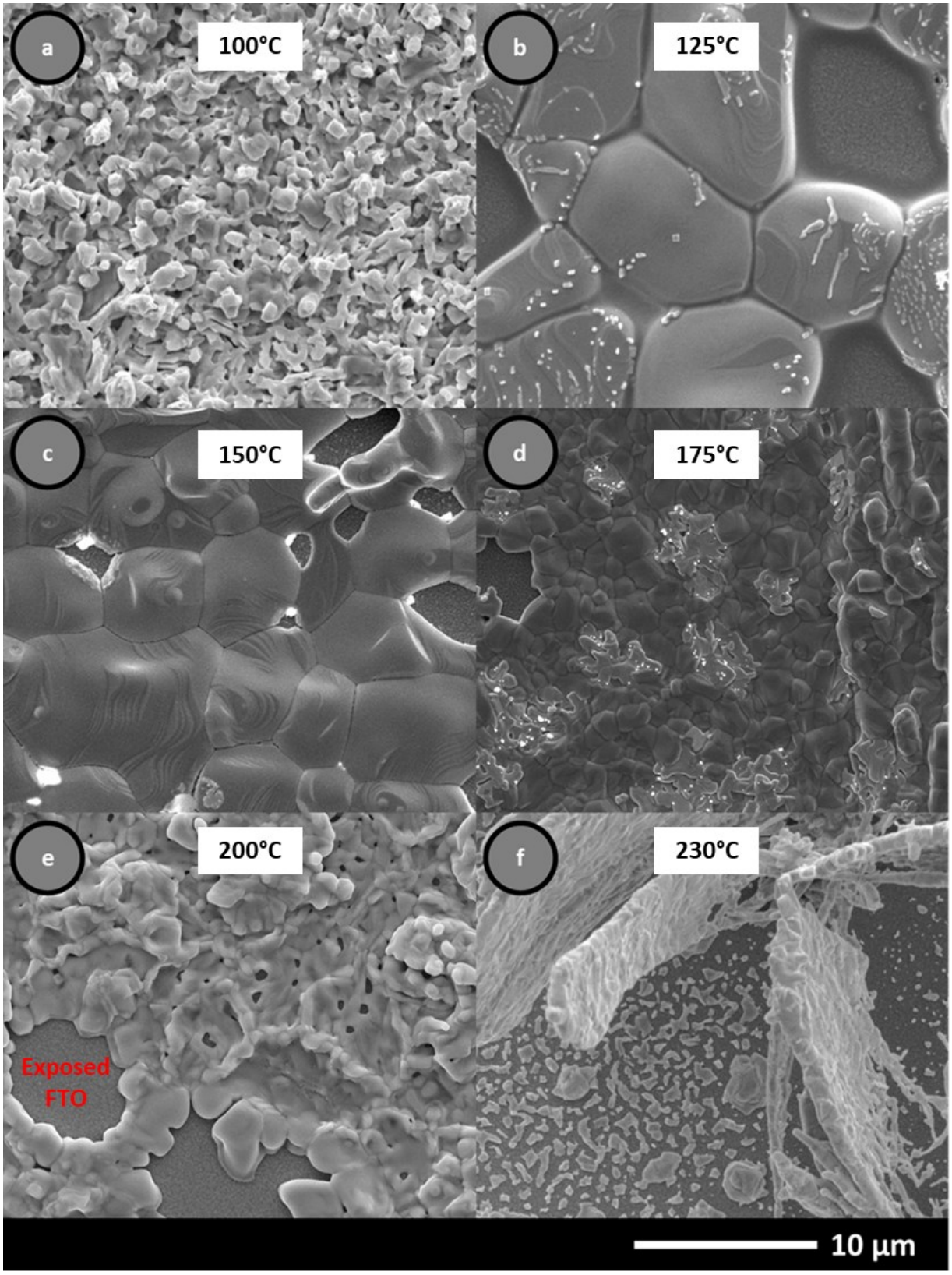


Figure 5-3 SEM images of films deposited at different first step temperatures using lead acetate $Pb(Ac)_2 \cdot 3H_2O$ a) 100°C, b) 125°C, c) 150°C, d) 175°C, e) 200°C and f) 230°C

175°C resulted in a continuous film with an average grain size of ~1.2 µm. However, there were still a significant number of pinholes present and the surface was still very rough. Note, the bright spots are the result of ambient degradation caused by lengthy storage and are not the result of the deposition. Lower temperatures of 150 – 125°C resulted in films with large grains (> 5 µm), however with poor film coverage. At 100°C, a very rough and porous film is formed. From these results, the most likely deposition temperature to produce films for PV devices is 175°C.

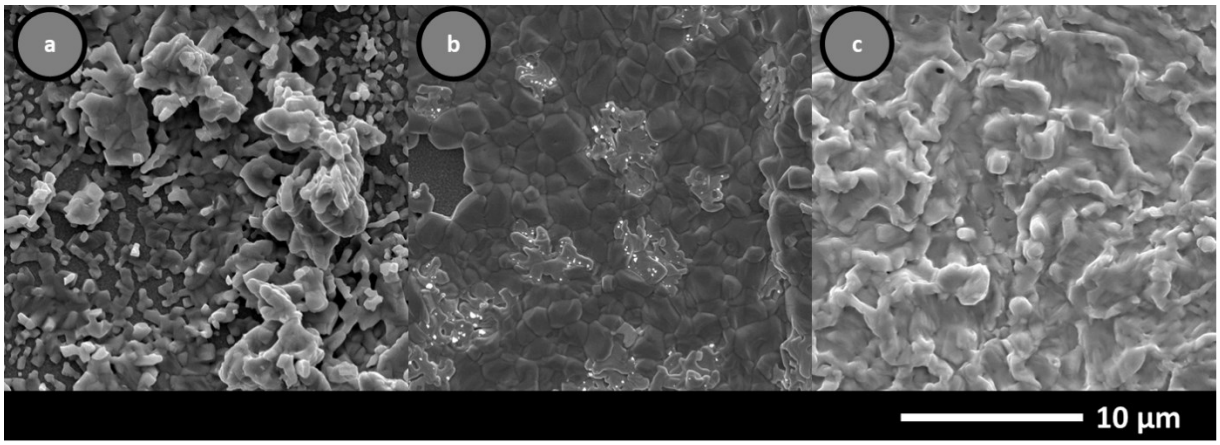


Figure 5-4 SEM images of films converted at different second step temperatures using lead acetate $Pb(Ac)_2{\cdot}3H_2O$ deposited at 175 °C. a) 220 °C b) 230 °C and 240 °C

This study also investigated the effect of the second step temperature on the morphology of the film. 230°C is the optimised temperature for the PbI_2 based method detailed in chapter 4. To confirm if this temperature is ideal for this method, depositions were carried out at 220 and 240°C. The results can be seen in Figure 5-4. As the temperature is lowered by 10 °C, the resulting film becomes sparsely covered and rough. An increase of 10 °C results again in a roughening of the film, with more three-dimensional structures forming. From these results it was determined that 230 °C produces a favourable morphology.

Further trials were conducted with concentration alterations and gas flow rate changes of the first step. The results can be seen in Figure 5-5. Halving the concentration of $Pb(Ac)_2{\cdot}3H_2O$ to 0.066 M led to a sparse film. In contrast, increasing the concentration to 0.198 M L^{-1} created a very rough film. This roughness is possibly caused by the promotion of homogenous nucleation as the solution becomes more concentrated. When altering the flow rate, the films became sparse when the flow was increased to 1.0 l min^{-1}. This indicates that at higher flow rates there is less time for the precursors to diffuse onto the substrate, leading to little precursor material being deposited to form a film. Reducing the flow rate to 0.25 l min^{-1} produces a rough film. This can be attributed to the increased turbulent flow at lower flow rates: see equation 2-34.

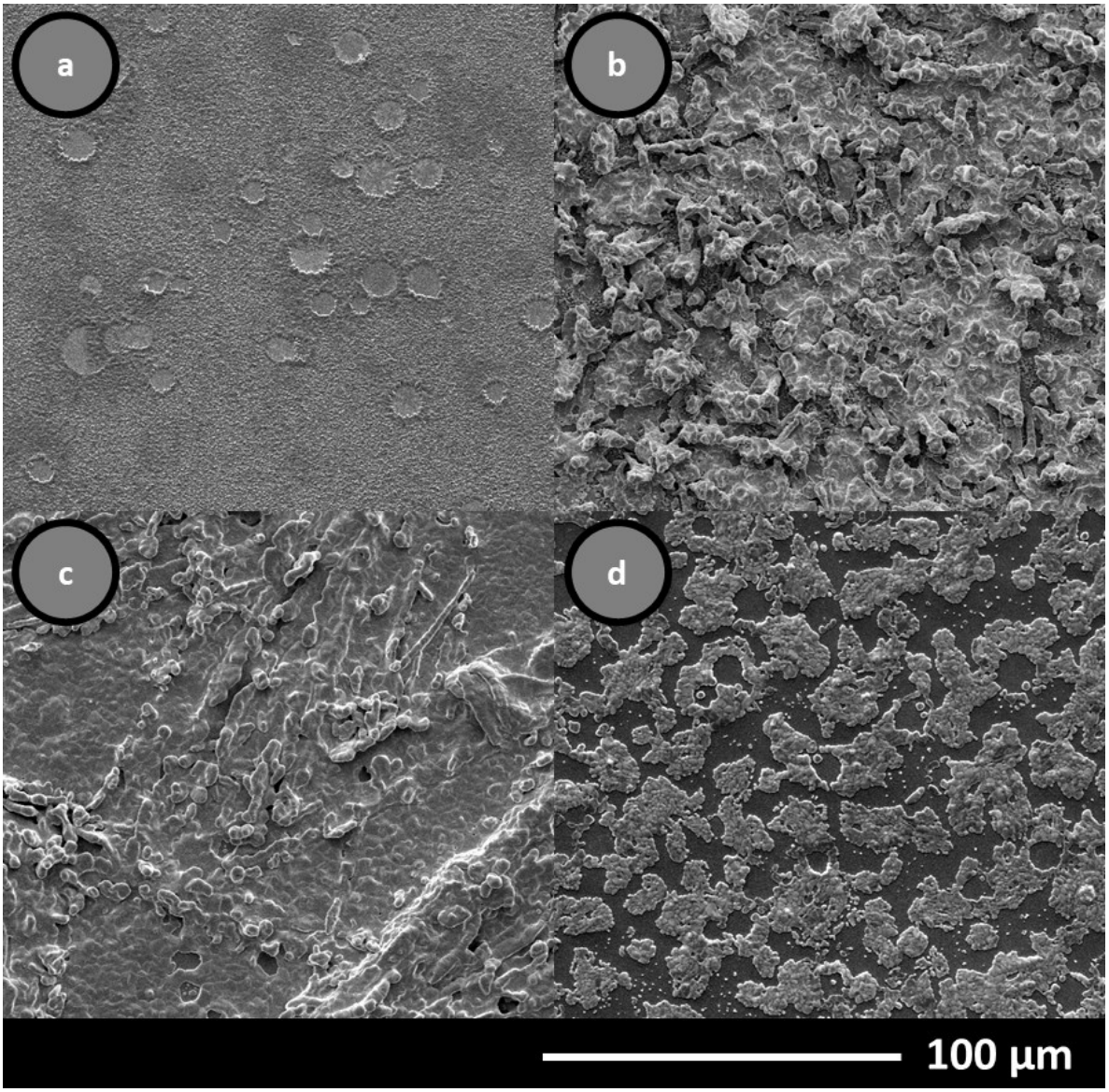


Figure 5-5 SEM images of films converted at different first step flow rates and concentrations of $Pb(Ac)_2 \cdot 3H_2O$ in MeOH. a) Concentration of 0.066 M with a flow rate of 0.5 l min^{-1}. b) Concentration of 0.198 M a flow rate of 0.5 l min^{-1}. c) Flow rate of 0.25 L min^{-1} with a concentration of 0.33 M d) Flow rate of 1 L min^{-1} with a concentration of 0.33 M

5.3.2 Deposition of mesoporous TiO_2

Due to the deposition temperature, this study was limited in the materials and architectures that could be employed to make a PV device. In terms of the TCO material, FTO was the most suitable due to its high resistance to temperature. ITO, for instance, suffers from resistivity increases when annealed at temperatures over 200 °C [249,250]. Most organic materials used for charge extraction, such as PTAA and PCBM also cannot endure the high temperatures of the second step. Therefore, it was necessary to utilise an inorganic charge extraction layer to deposit the perovskite onto. The chosen architecture was a n-i-p using mesoporous TiO_2 as the ETL layer. This is a well-known layout used for perovskite cells. Therefore, existing methods could be used to deposit the layers. Section 3.2.3 details the method

used to deposit the layer. This allows for focus on the perovskite layer performance, without having to introduce another variable into the device fabrication.

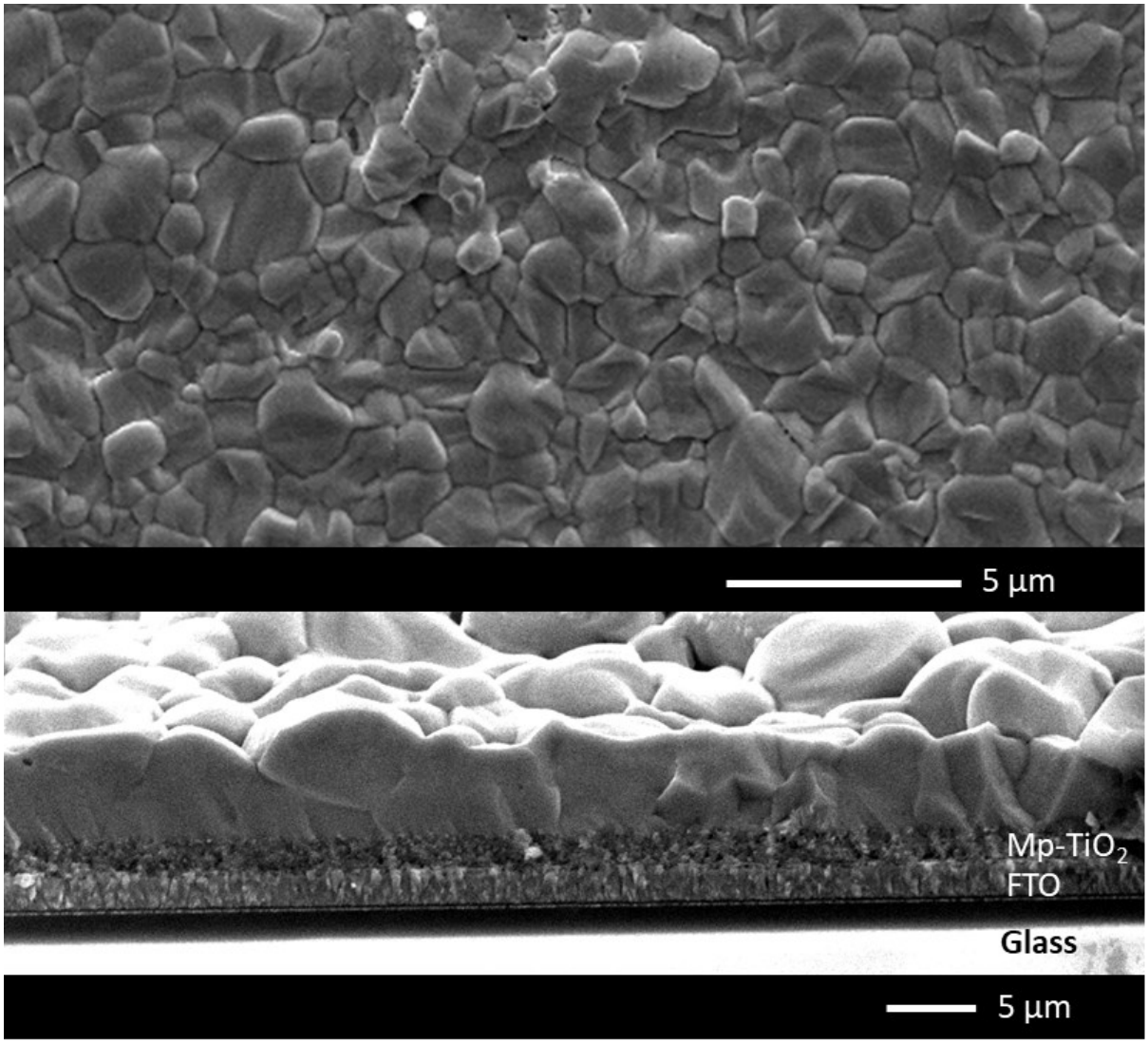


Figure 5-6 MAPI film deposited using lead acetate method on mesoporous TiO2 ETL

Figure 5-6 shows a MAPI film deposited using the previously established optimum deposition parameters (S1 T: 175 °C and S2 T: 230 °C). The resulting film had significantly improved coverage, with no pinholes visible when compared to the film deposited on bare FTO. Furthermore, the film retains a similar average grain size of ~1.2 µm. The cross-section shows the films have a thickness of approximately 1 µm, with grains spanning the entire thickness of the film. This morphology should be favourable in PV applications, as grain boundaries potentially host defects that can act as trap sites for charge carriers, induce shunts, and decrease the stability of the cell by allowing the ingress of moisture. Furthermore, whilst the film thickness is above the ideal for MAPI based devices, it was hoped that the lack of grain boundaries in the thickness of the film would allow charges to be extracted effectively. Also evident from the cross-section is the significant surface roughness, with the SEM

showing excess of 500 nm of thickness variation. This is confirmed by visual observation of a matte surface, rather than the ideal mirror-like finish of spin-coated film.

5.4 MATERIAL CHARACTERISATION

Whilst the resulting morphology looks to be suitable for PV applications, confirmation of the material properties is vital. Here, films deposited using the optimised method (S1 T: 175 °C and S2 T: 230 °C) are characterised. Figure 5-7 shows the XRD pattern of the MAPI film deposited on mesoporous TiO_2.

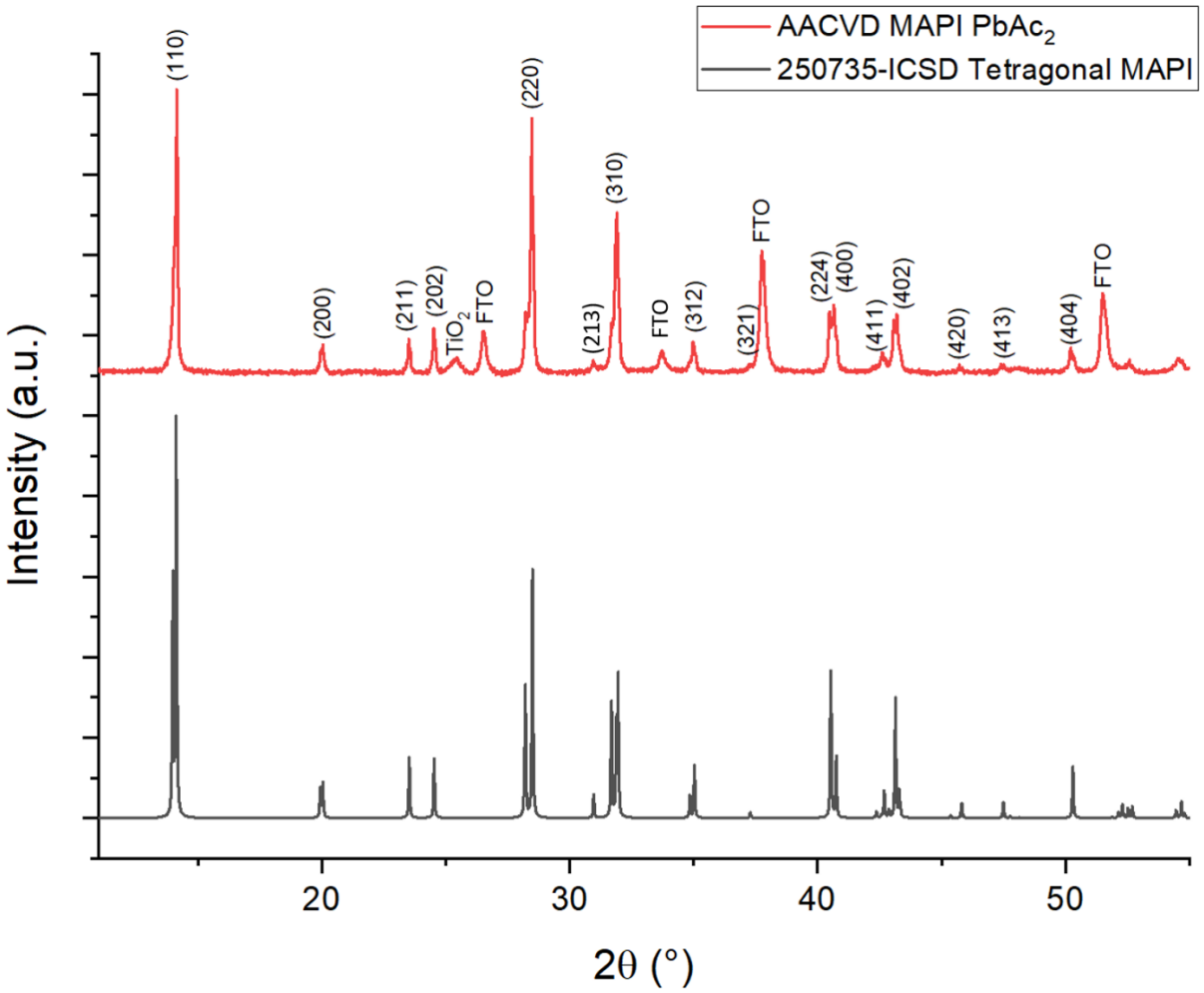


Figure 5-7 XRD patterns of AACVD MAPI and tetragonal MAPI reference pattern [132]

The patterns observed are in good agreement with the reference pattern for tetragonal MAPI. There are no observable precursor or degradation peaks visible, indicating good phase purity. Furthermore, the sharp and intense peaks indicate large crystallite sizes (d_{110}: 76 nm), which is substantiated by the larger observable grain sizes in SEM images. This increased crystallinity is generally desirable in perovskite cells and is typical of MAPI fabricated using an excess of MAI [251]. In the AACVD method, the films are exposed to MAI continuously until fully converted. Unlike films deposited utilising PbI_2, films deposited from $Pb(Ac)_2{\cdot}3H_2O$ do not appear to show a similar preferential orientation around (310)

reflection. Instead, they are more akin to that of spin coated samples, showing a preferred orientation around the (110) plane (See Figure 5-8).

Table 5-2 Calculated lattice parameters of MAPI films deposited using PbI2 and Pb(Ac)2·3H2O

Film	Lattice constant	Calculated (Å)	Reference difference (%)	c/a ratio	Primitive unit cell volume (Å^3)
PbI_2	a	8.88	+0.33	1.43	249.8
	c	12.67	+0.24		
$Pb(Ac)_2{\cdot}3H_2O$	a	8.84	-0.23	1.44	248.11
	c	12.70	+0.53		

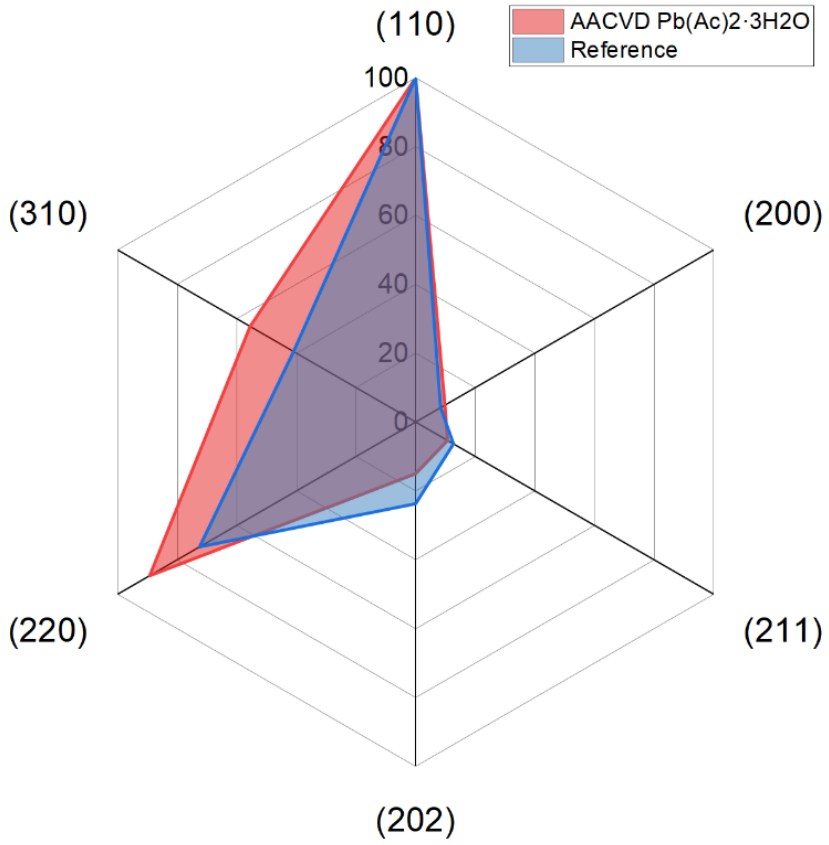


Figure 5-8 Relative intensity of peaks compared to MAPI reference pattern [201]

Utilising this data, the lattice parameters were calculated (Figure 5-8). When comparing this to the films made using PbI_2, it is evident that films produced by $Pb(Ac)_2{\cdot}3H_2O$ show more strain in the c-axis. The caveat with this comparison is that these films are deposited on mesoporous TiO_2, therefore there may be additional strain induced due to the substrate effects.

Uv-Vis measurements match the expected results, with a sharp absorption onset at 800nm and the Tauc plot indicating an optical band gap of 1.58 eV (Figure 5-9). Again, this supports the previous data, indicating that the formed film is indeed MAPI. Combining this study's optical measurements with APS

and Kelvin probe data allows for formation of a band diagram for the final film (Figure 5-9). The E_f and valence band positions were measured at -4.82 eV and -5.37 eV respectively. Using Tauc plot derived bandgap of 1.55 eV places the conduction band at approximately -3.82 eV. These results are comparable to literature values, however there are slight differences. The mid-band position of the Fermi level indicates a relatively defect-free film, where solution-processed samples typically show more p-type behaviour (Fermi level closer to valence band edge) due to defects [229]. Overall, this indicates that the AACVD MAPI is of high quality, with few intrinsic defects.

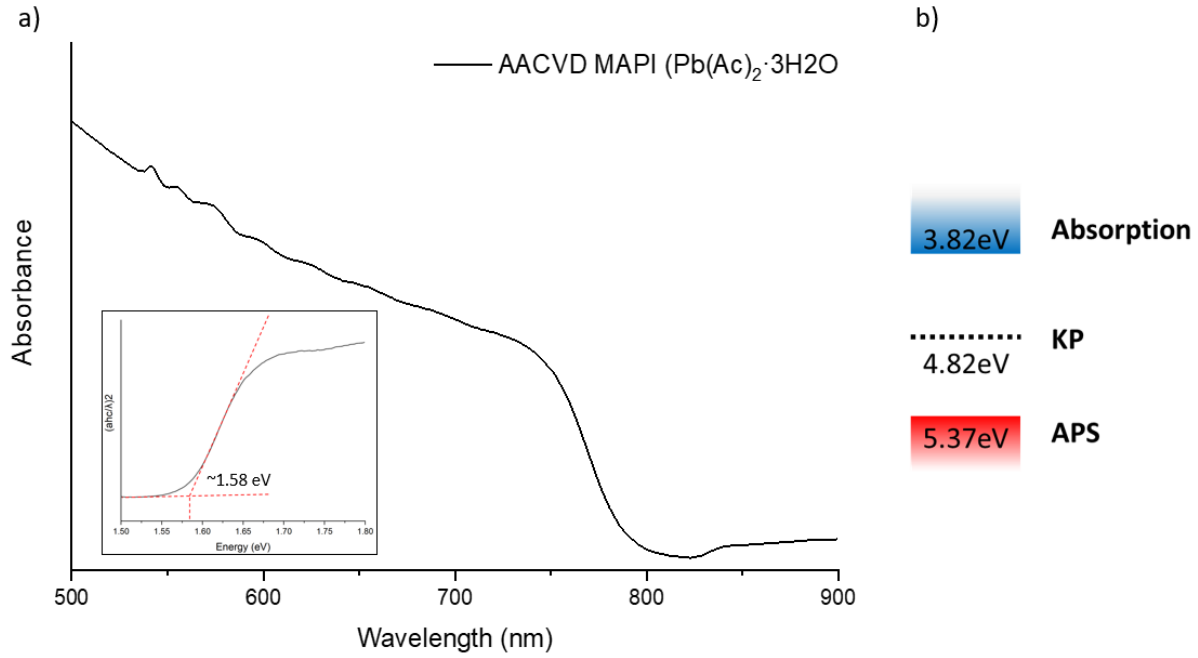


Figure 5-9 a) Absorption spectra of AACVD MAPI film deposited from $Pb(Ac)_2{\cdot}3H_2O$. Inset shows Tauc Plot b) Energy band diagram of deposited perovskite. Values were determined by absorption, APS and Kelvin Probe measurements

5.5 PV Devices

By utilising Spiro-OMeTAD as a hole transporting material, these films were tested in photovoltaic devices. The experimental method for cell fabrication can be seen in section 3.2. Figure 5-10 shows the SEM cross-section of a completed cell utilising Au as the top contact and the performance of the resulting devices.

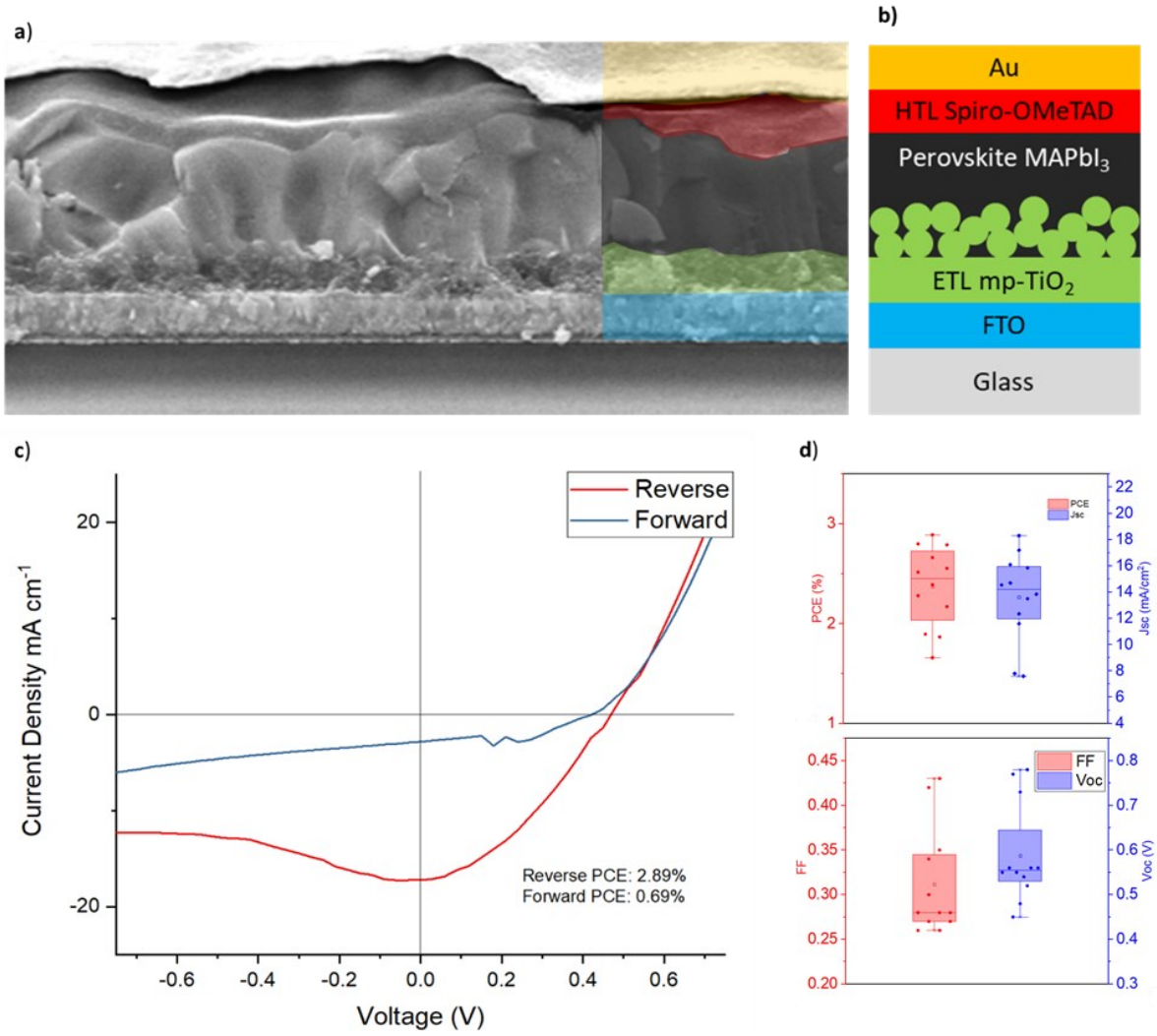


Figure 5-10 a) SEM Cross-section of a cell utilising AACVD MAPI film, with false colouring showing the TCO, ETL active layer and Au electrode. b) Schematic of the cell. c) J-V curve of champion device utilising Spiro-OMeTAD. d) Inset show box plots of data from 12 working cells, measured in a reverse J-V scan

The resulting devices suffered from low reproducibility, with approximately 50% of pixels on each substrate not functioning, either by shorting or giving no signal. Moreover, devices that did function suffered from low PCEs. The champion device had a Jsc of 17.2 mA cm^{-1}, V_{oc} of 0.48, FF of 0.35, resulting in a PCE of 2.89 %. Looking at these results, it is apparent that the largest loss is due to the low V_{oc}. Typically, state of the art devices utilising spiro-OMeTAD have a V_{oc} exceeding 1 V. This indicated that there were significant issues with the coverage of the HTM. Furthermore, looking more closely at the J-V scan revealed a significant amount of hysteresis (Figure 5-10), therefore these efficiencies are not

fully representative of the actual performance. Using equation 2-16, a large hysteresis index (HI) of 0.76 can be calculated. The potential origin of the hysteresis can be deduced by the shape of the reverse J-V curve. The bump observed in the reverse scan indicates a large amount of interfacial capacitance, which is potentially caused by a low interfacial quality of the device layers. This again points towards potential issues with the HTM perovskite interface, however the losses may also be caused by the mesoporous layer.

To circumvent the issues of a rough surface, CuSCN as the HTM was used. CuSCN possess a much higher hole mobility than organic equivalents, (upto 0.1 $cm^2 V^{-1}$) [252]. Therefore, thicker layers can be utilised and still effectively transport charge. Using the spray coating developed in the McLachlan group, detailed in section 3.2.3.3, this study was able to deposit a >500 nm layer of CuSCN. This thicker layer compensated for the surface roughness and ensured complete coverage of the film. Moreover, spray-coating is also a scalable technique and therefore complements the AACVD technique in this regard. The cross-section SEM of the resulting device can be seen in Figure 5-11.

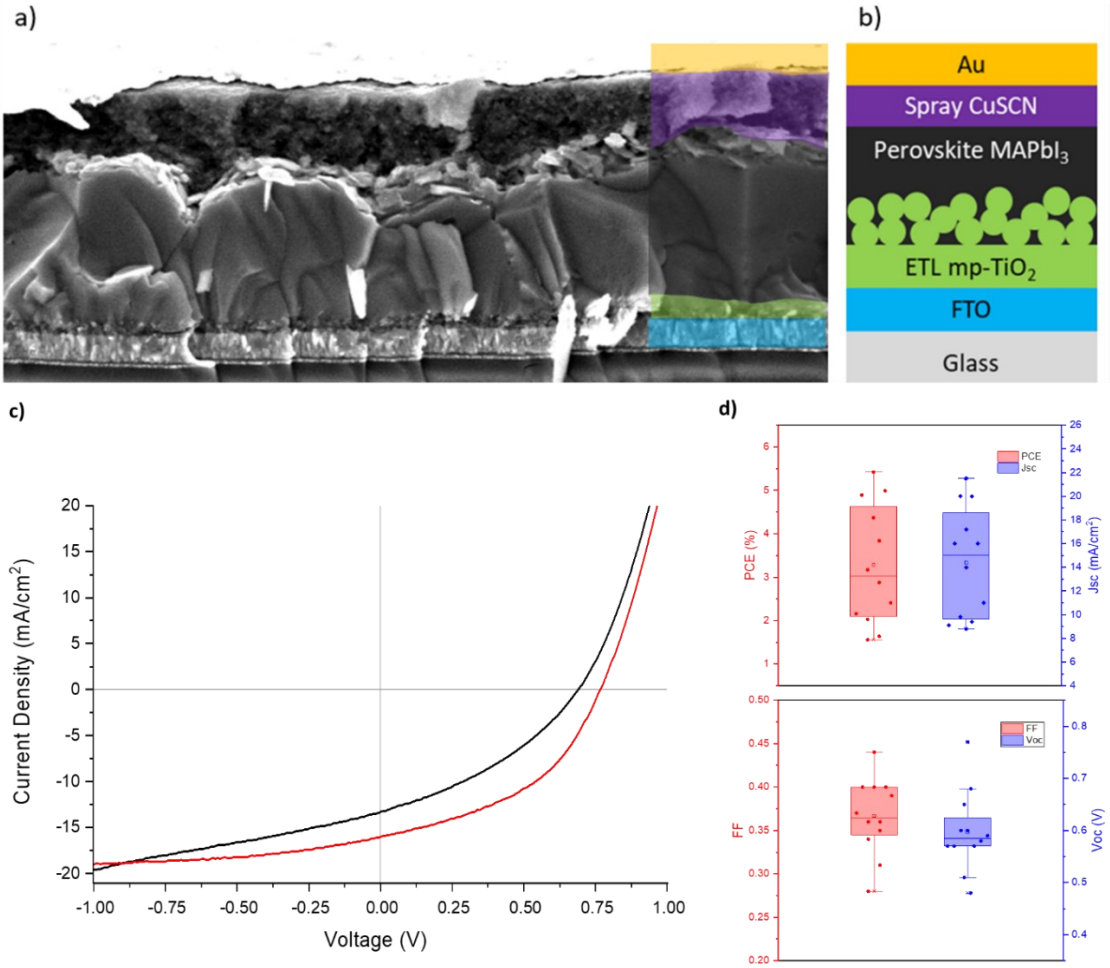


Figure 5-11 a) SEM Cross-section of a cell utilising AACVD MAPI film, with false colouring showing the TCO, ETL active layer and Au electrode. b) Schematic of the cell. c) J-V curve of champion device utilising spray-coated CuSCN. d) Inset show box plots of data from 12 working cells, measured in a reverse J-V scan

Distribution of device performances and the J-V curve of the champion cell can be seen in Figure 5-11. This device had a short circuit current density (J_{sc}) of 16.01 mA/cm^2, open circuit voltage (V_{oc}) of 0.77, and a fill factor (FF) of 0.44 resulting in a PCE of 5.42%. These are results taken from the reverse sweep of the device, with the forward sweep showing a significantly reduced hysteresis when compared to the cells using spiro-OMeTad. Moreover, the substantial increase in V_{oc} indicates that the coverage issues are alleviated by using the thick CuSCN layer. Looking at the J-V curve it seems that the cell also suffers from a low FF induced by both a high series resistance of ~20 Ω and low shunt resistance of 129 Ω. The high series resistance could be attributed to the sub-optimal thicknesses of the layer and the shunt resistance could still be linked to bad interfaces or pinholes present in the device. Looking closely at the cross-section of the cells reveals that the CuSCN layer adopts a bi-layer type structure, with an initial layer of larger crystals followed by a smoother thicker layer. This may be the origin for the hysteresis and still sub-optimal FF and V_{oc}. Looking at the distribution of PCEs, it is evident that the performance varies greatly, even more so in the devices utilising spiro-OMeTAD. This indicates that the constant application of the CuSCN layer is not facile. However, the champion efficiency still represents the potential for this process.

In terms of OMHPs being processed by AACVD, these results are the first successful application of this technique to produce working cells. Additionally, these are the highest recorded efficiencies of any device utilising an AACVD active layer. The previous non-certified record PCE was 1.0 % using copper indium selenide ($CuInS_2$), achieved by Hepp *et al.* in 2006 at NASA [253].

5.5.1 Comparison to spin-coated films

To confirm the origin of the losses leading to low PCEs in the aforementioned devices, cells utilising spin coated MAPI layers were tested. Figure 5-12 shows the results utilising the same architecture as the AACVD devices using mesoporous TiO_2 and spiro-OMetad. The resulting J-V curve of the champion device shows a significant amount of hysteresis, with a calculated HI of 0.54. This hysteresis manifests itself in a similar way to the AACVD devices, with a "bump" clearly observable in the reverse sweep. Looking at the V_{oc} of the device, it can be observed that the values are well within the expected range for spiro-OMeTAD, with all the devices having a value over 1 V. This indicates complete coverage of the active layer with the p-type material. Combining these observations, it can be inferred that the origin of the hysteresis lies in the ETL layer.

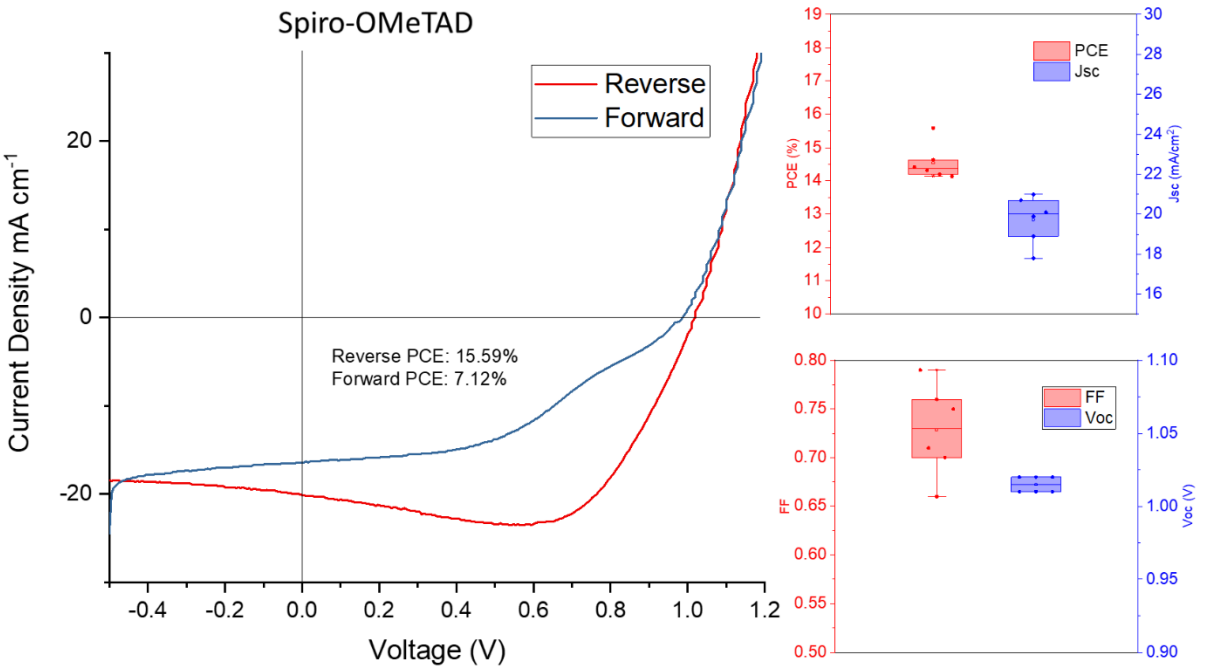


Figure 5-12 J-V curve of champion spin coated device utilising spin- coated spiro-OMeTAD. Inset show box plots of data from 6 working cells, measured in a reverse J-V scan

Figure 5-13 shows devices with the spray coated CuSCN, which had a drastically reduced PCE of 8.23% when compared to the original Spiro-OMeTAD device. This was primarily caused by a low FF and V_{oc}. The large distribution of V_{oc} values corroborates the observation in the all AACVD cell, indicating that this layer is difficult to apply consistently. In terms of hysteresis, it is significantly reduced when compared to the cell utilising spiro-OMeTad, with a HI value of 0.18. However, the true hysteresis may be masked by the drop off in performance. The way the hysteresis manifests itself is different, showing a clear crossover between forward and reverse scans. This behaviour is typically linked to unequal charge transport in the cell, potentially caused by the thicker spray coated layer not effectively extracting charge.

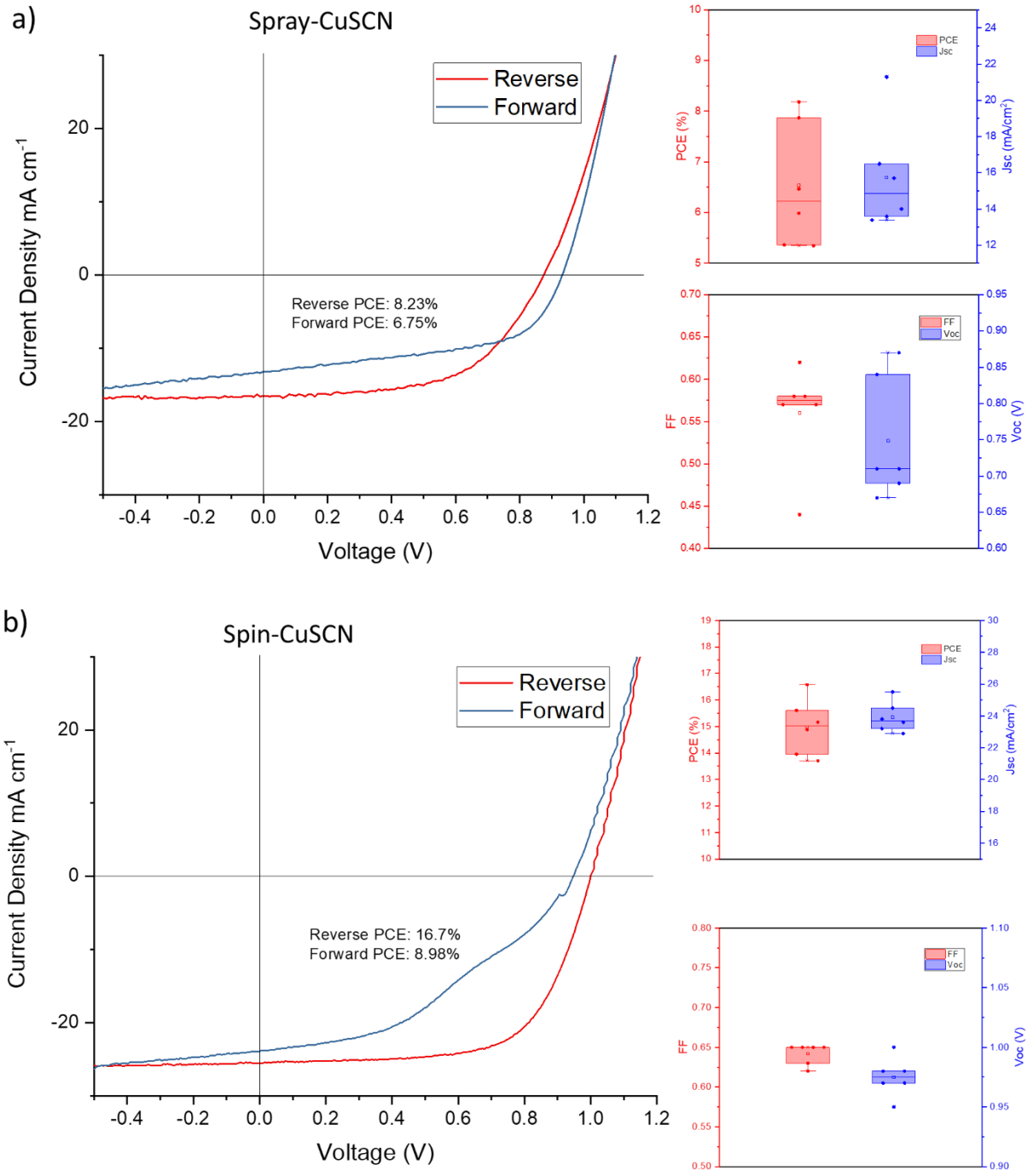


Figure 5-13 a) J-V curve of champion spin coated device utilising spray-coated CuSCN. Inset show box plots of data from 6 working cells, measured in a reverse J-V scan. b) J-V curve of champion spin coated device utilising spin- coated CuSCN. Inset show box plots of data from 6 working cells, measured in a reverse J-V scan

To confirm this hypothesis another set of devices were prepared using a thin spin-coated layer of CuSCN (Figure 5-13). These devices show much improved device performance, displaying a significant recovery in the FF and V_{oc}. In particular, the V_{oc} almost matches the performance of spiro-OMeTAD. Conversely, the hysteresis greatly increased with a calculated HI value of 0.46. This gives credence to the cause of the effect being linked to the ETL layer, and in the spray coated CuSCN device the

limitation of the charge transport masks this effect. Moreover, this result shows that it is not the CuSCN itself that reduces the performance, rather it is the morphology that dictates the performance.

5.5.2 Film formation

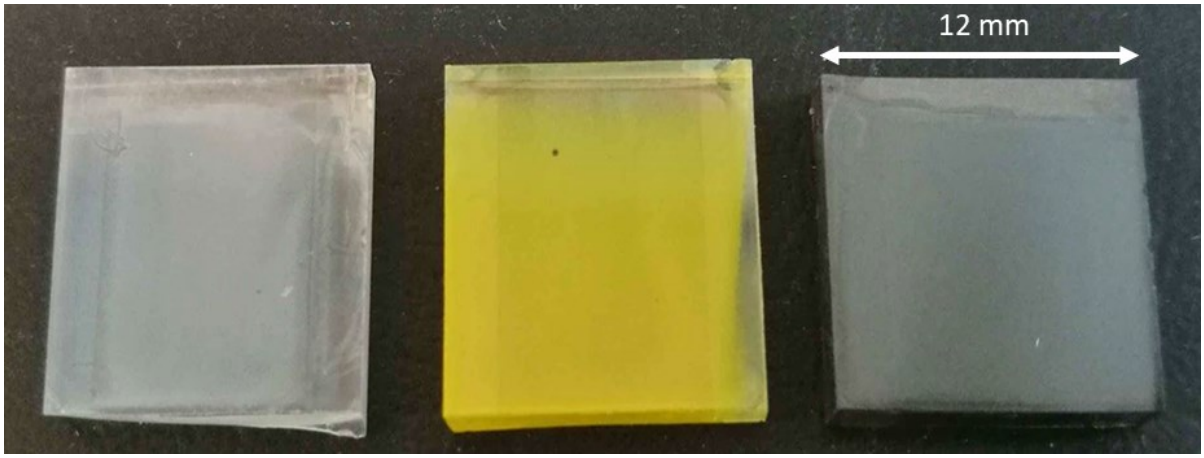


Figure 5-14 Photographs of three films removed at different stages of the AACVD deposition. Left: Film after first step. Center: Film halfway through MAI aerosol exposure. Right: Completed MAPI film

To further investigate the poor device performance and better understand the film formation process, the films were characterised at various stages of the deposition procedure. Figure 5-14 shows a set of substrates removed at different points during the reaction. In the first step, a white translucent film of $PbAc_2$ is formed and upon exposure to the MAI aerosol an intermediate yellow phase forms, which with further time converts into a characteristic dark MAPI film.

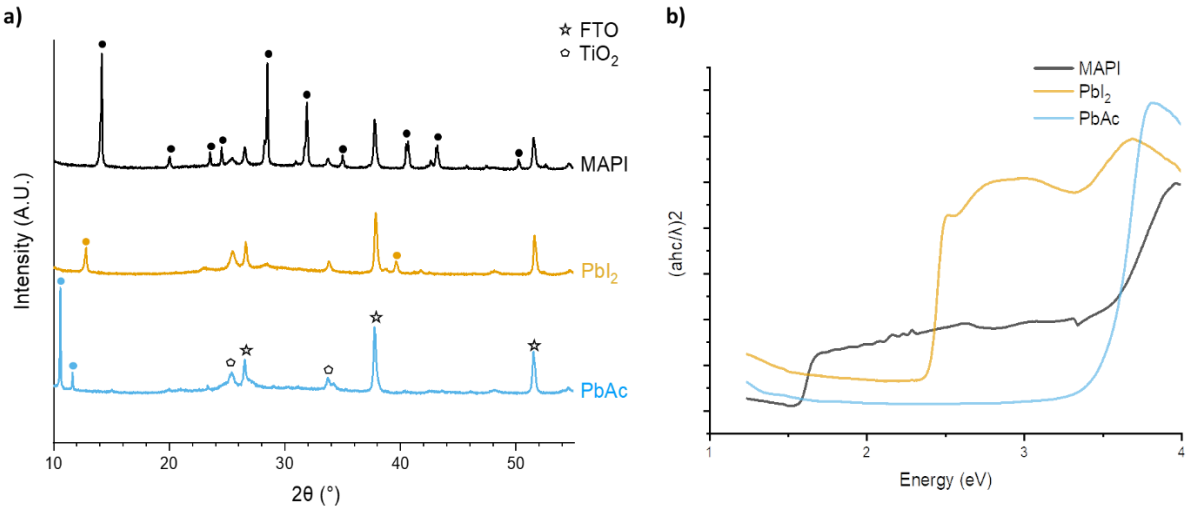


Figure 5-15 a) XRD patterns correspond to initial lead acetate (PbAc) film, lead iodide intermediary and final methylammonium lead triiodide (MAPI) film b) Tauc plots of film extracted from absorption data

XRD patterns of the films at these stages indicate the yellow phase to be PbI_2, with the typical (001) and (003) reflection being present. Furthermore, the lack of $PbAc_2$ reflections during the intermediate stage suggests complete conversion to PbI_2 before being converted to MAPI. This indicates a different

film formation mechanism compared to solution-processed counterparts, where there are no intermediate phases formed. Absorption measurements seen in Figure 5-15 further support the proposed film formation mechanism, with absorption onset and bandgap values matching literature values of $PbAc_2$, PbI_2 and MAPI (3.5 eV, 2.3 eV and 1.55 eV) [202]. The linear regime in the $PbAc_2$ data is likely due to the mesoporous TiO_2, showing a band gap of 3.5 eV.

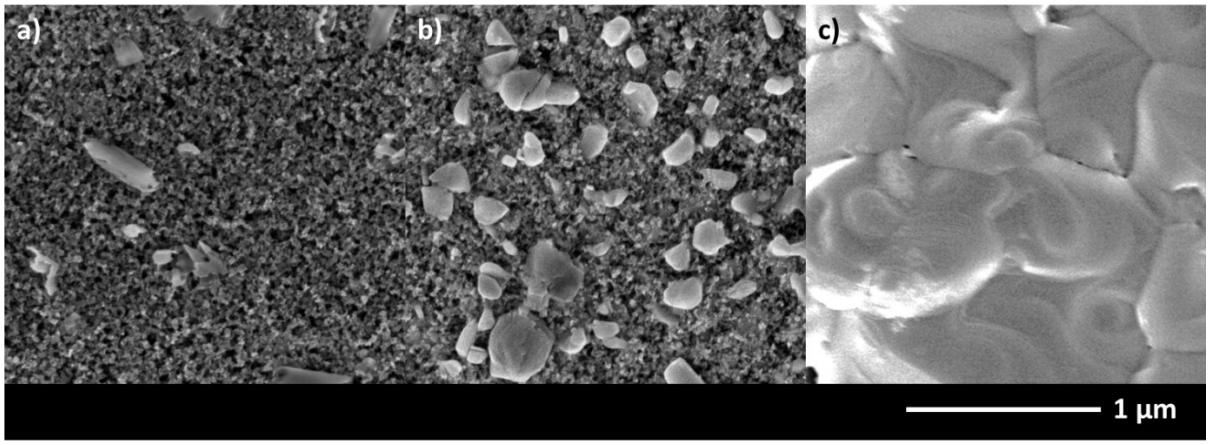


Figure 5-16 SEM images of three films removed at different stages of the AACVD deposition. a) Film after first step. b) Film halfway through MAI aerosol exposure. c) Completed MAPI film

SEM images of the films reveal an interesting film formation mechanism. After the first step, the acetate seems to infiltrate the mesoporous TiO_2 layer. Upon exposure to the MAI, lead iodide crystals begin to form on the substrate surface. With continued exposure these crystals begin to transform into MAPI and the film begins to coalesce. This process is illustrated in figure 5-17.

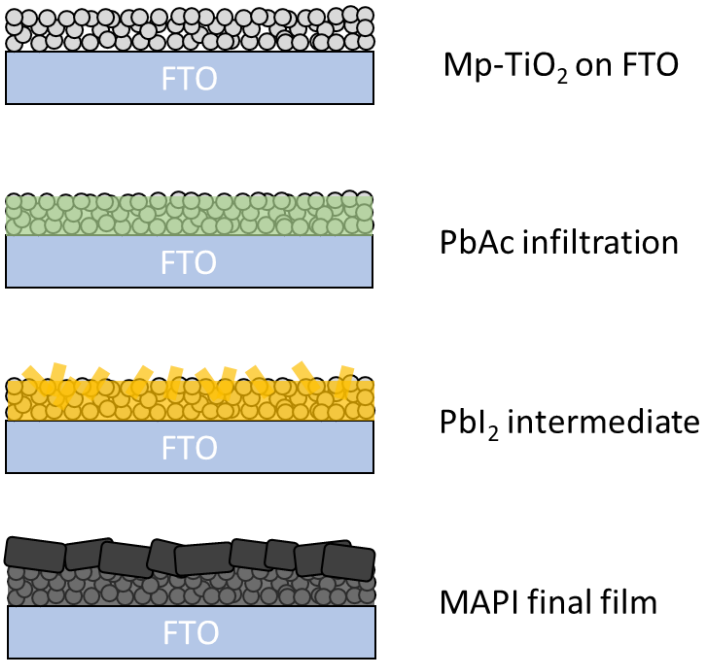


Figure 5-17 Schematic illustrating the growth and conversion of the AACVD MAPI film

From these observations, it can be deduced that there are multiple reactions that occurs during the formation of these films. Equation (5-1) shows the typically-reported scheme of MAPI formation when using $PbAc_2$ as the Pb(II) source[254].

$$Pb(CH_3COO)_2 + 3CH_3NH_3I \rightarrow CH_3NH_3PbI_3 + 2CH_3NH_3CH_3COO\uparrow \quad (5\text{-}1)$$

In that process, the $PbAc_2$ reacts with the MAI to form MAPI and a volatile by-product $CH_3NH_3CH_3COO$ (MAAc), which is removed via the annealing process. From observations of the AACVD process, this study proposes a different reaction scheme with two parts, as can be seen in equation (5-2) and (5-3).

$$Pb(CH_3COO)_2 + 3CH_3NH_3I \rightarrow PbI_2 + CH_3NH_3CH_3COO\uparrow \quad (5\text{-}2)$$

$$PbI_2 + CH_3NH_3I \rightarrow CH_3NH_3PbI_3 \quad (5\text{-}3)$$

The first part of the process involves the transformation of $PbAc_2$ to PbI_2, and the formation of the volatile species MAAc. As the reactor is at an elevated temperature (220 °C) it is feasible to assume that MAAc will be removed during the reaction. The second process is akin to a typical solution process and involves the reaction of PbI_2 with MAI, leading to the formation of MAPI.

This film formation mechanism could also in part explain the surface roughness observed in the final film. The large density changes during film formation, beginning from 3.25g/cm^3 (PbAc)[255] to 6.16g/cm^3 (PbI_2)[256] and then finally to 4g/cm^3 (MAPI)[257] would cause the films to swell and contract, leaving a rough surface. Moreover, work by Brenner *et al.* explored vapour phase transformation of PbI_2 single crystals exposed to gaseous MAI [199]. Similar to this study's work, the transformation of the films was accompanied by a roughening of the surface, likely attributed to the expansion and growth of the MAPI grains. Further work will be needed to find a suitable set of precursors that may minimize the density change and therefore improve final film quality.

5.6 Methyl Ammonium Lead Bromide

The acetate method developed in this chapter is potentially a flexible route for the deposition of a variety of OMHP materials. As this process uses lead acetate in the first step, it was predicted that halide substitution may be facile. Therefore, to test the versatility of this method, MAI was substituted for methylammonium bromide (MABr) with the aim of forming Methyl ammonium lead tri-bromide (MAPbBr). Lead acetate precursor films deposited on mesoporous TiO_2 were used at the optimised parameters used in section 4.2.1. These films were then exposed to an aerosol of MABr in MeOH (0.21M per litre), at 230 °C, to complete the second step (Figure 5-18).

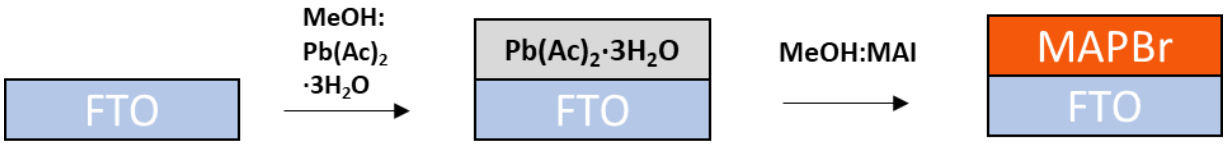


Figure 5-18 Schematic showing the 2-Step AACVD process using lead acetate ($Pb(Ac)_2 \cdot 3H_2O$) and *methylammonium bromide*

The resulting film had the characteristic orange colour of MAPBr, with the SEM showing a typical OMHP grain structure. The average grain size was calculated to be 870nm, which is comparable to the MAPI counterpart. However, film coverage was poor with large uncovered areas showing the mesoporous TiO_2 substrate. The cross-section SEM images reveal a film thickness of approximately 1 µm (Figure 5-19).

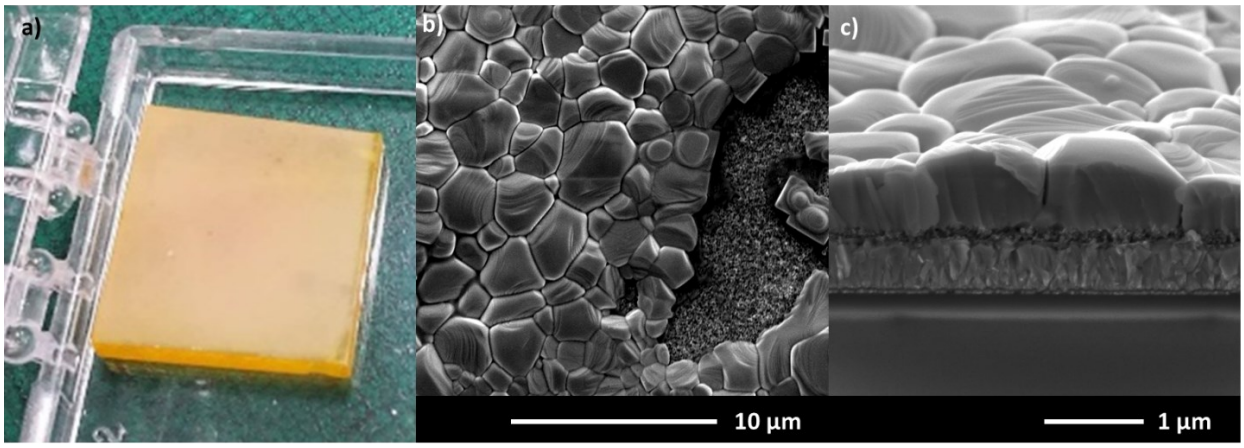


Figure 5-19 a) Photograph of resulting MAPbBr film. b) top down SEM image of film and c) cross-section of film

To confirm the composition of the film, optical absorption and XRD measurements were performed. Figure 5-20 shows the diffraction pattern of the MAPBr film compared to the previously discussed MAPI film. The pattern shows that the deposited MAPBr possess the expected cubic perovskite structure. Furthermore, the pattern indicates a high phase purity with no trace of PbBr or other

degradation products visible. By applying the Scherrer equation, a large crystallite size of 89nm was calculated. This again is similar to what was observed in the MAPI film.

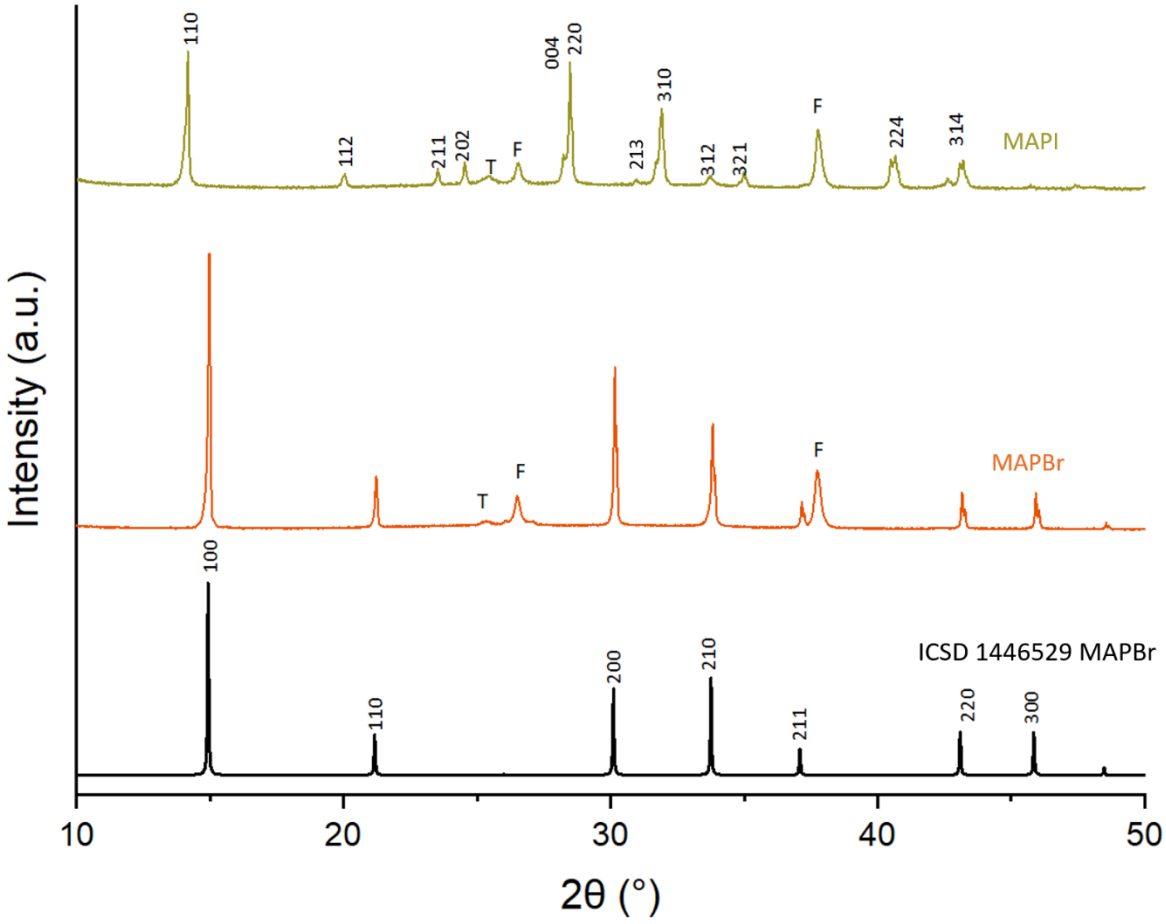


Figure 5-20 XRD patterns of AACVD MAPI and AACVD MAPBr both deposited using led acetate ($Pb(Ac)_2{\cdot}3H_2O$) as the Pb(II) source. Reference pattern ICSD 1446529

Table 5-3 shows the lattice parameters calculated using the cubic crystal system equation. The results again match closely with the values calculated from the reference pattern. In comparison, MAPI atoms within MAPBr are more closely spaced, which can be observed by the higher angles of diffraction. Moreover, the lattice volume of the MAPBr film is approximately 16% smaller than the MAPI counterpart (208.8 vs 248.1 Å).

Table 5-3 Calculated lattice parameters of AACVD MAPbBr film

Film	Lattice constant	Calculated (Å)	Reference difference (%)	Primitive unit cell volume (Å^3)
AACVD MAPBr	a	5.933	+0.01	208.8

To further confirm the composition of the material, optical absorption measurements were conducted (Figure 5-21). A sharp absorption onset was observed at approximately ~540 nm. Using a Tauc plot a bandgap of 2.28 eV was determined, which is close to the expected value for MAPBr, 2.3 eV [258].

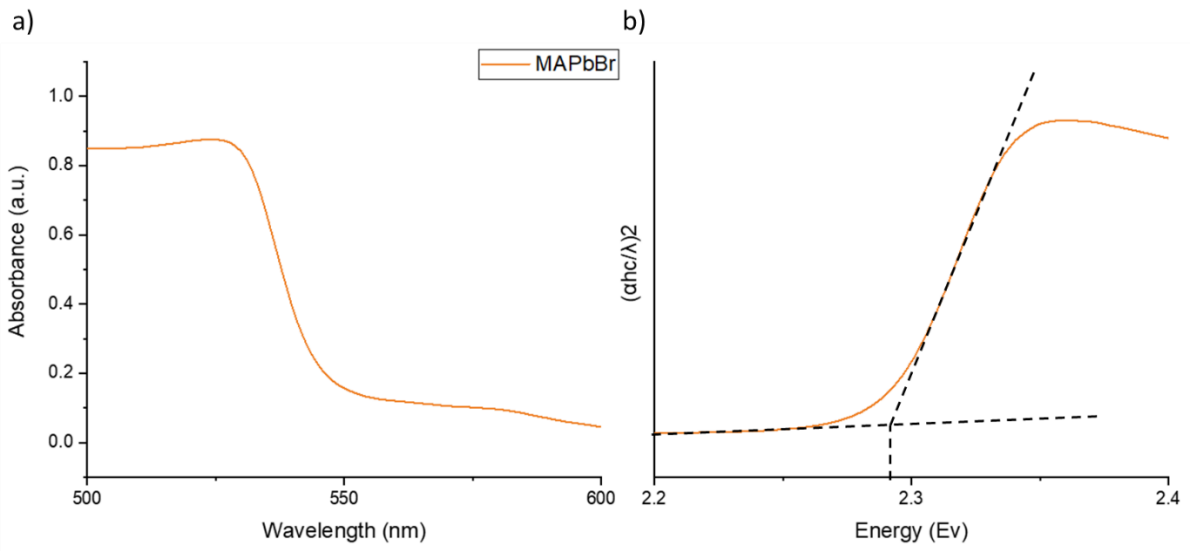


Figure 5-21 a) Absorption spectra of AACVD MAPBr film deposited from $Pb(Ac)_2{\cdot}3H_2O$. b) Tauc Plot indicating band gap of 2.28 eV

In summary, these results show the successful deposition of MAPBr using the lead acetate based AACVD method. This demonstrates the potential flexibility of this method to produce lead based OMHPs.

5.7 FUTURE WORK

To improve the PV performance several issues will need to be investigated and solved. Primarily, the consistency of the deposition will need to be improved. The variability of the process can be strongly linked to the continuum flow regime the method takes place within. Due to the reaction occurring in this regime, aerodynamic effects dominate the precursor flow and delivery. Therefore, to achieve consistent results, there must be a well-defined aerosol flow in the reactor. Another area of improvement is the aerosol formation itself. The piezoelectric system utilised in this study creates a polydisperse aerosol, therefore the droplet evaporation rates vary greatly within the reactor. Utilising a more advanced aerosol delivery system to create a monodisperse aerosol may drastically improve the consistency of the deposition.

There are several different architectural changes that could be implemented to improve performance. This study primarily utilised mesoporous TiO_2 due to its prevalent use in literature, allowing for quick development of a consistent ETL. However, alternatives such as SnO_2 or porous carbon could be viable to further develop this technique. Moreover, this study's results strongly indicate that optimisation of the p-type layer is necessary. Alternative materials or deposition techniques could be applied to circumvent the surface roughness issues. As scalability is the goal, applying AACVD or other scalable deposition techniques for the ETL/HTM layer would create a proof of concept for an entirely line processable cell. However, this would require significant amount of research, and potentially would require reactors utilising multiple aerosol streams.

In terms of composition, the lead acetate technique could be used to produce a variety of OMHPs. Moreover, other metal acetates could be utilised to deposit a variety of non-lead, inorganic or double perovskite materials. Investigation into different compositions may further showcase the flexibility of this system and perhaps could lead to novel material development.

5.8 CHAPTER 5 SUMMARY

In terms of OMHPs being processed by AACVD, these results are the first successful application of lead acetate as a precursor to produce a thin film of MAPI. The method utilises a facile green solvent based precursor mixture, potentially making it compatible with large scale production. Using this method PV devices were successfully fabricated, achieving a champion device efficiency of 5.4 %. These are the first reported cells using an AACVD deposited OMHP and are the highest recorded efficiencies of any device utilising AACVD active layer. Moreover, this technique has been shown to be versatile, demonstrating the ability to also deposit MAPbBr.

6 AEROSOL ASSISTED SOLVENT ANNEALING (AASA)

6.1 INTRODUCTION

Until this point, the focus of this research has been to utilise AACVD to deposit OMHP. However, this has been proven to be a challenging technique to master. Despite this, there are valuable lessons that have been learned during this endeavour. Primarily, the development of a system that can aerosolise solutions and solvents commonly used in OMHP processing. In this chapter, the focus will be on utilising these aerosols to improve existing spin coated OMHP films. Additionally, the potential mechanisms behind the improvements are elucidated.

6.2 SOLVENT ANNEALING OF PEROVSKITES

The key factors affecting the performances of OMHP devices is their microstructure and morphology. Grain boundary density, crystal orientation, crystal quality and defects can significantly affect performance. Therefore, scalable deposition of materials and controlling these parameters poses a great technical challenge. Studies have demonstrated improvements in morphology utilising chemical approaches, such as using additives and alterations in stoichiometry. For instance, a mixed halide and mixed cation systems have been proven to significantly enhance the performance and stability of cells [161]. In terms of processing there are many different approaches that have been used. During the spin-coating, application of an antisolvent has been shown to dramatically improve morphology, resulting in uniform films with large crystals. However, this technique has proven to be difficult to master consistently, as the timing window for successful application is small (order of s). Solvent annealing has been shown to be an effective post-processing technique [164]. It utilizes a solvent vapour to recrystallise perovskite films and increase crystallinity and grain size, therefore improving the performance of the device. However, this technique also suffers from scalability and consistency issues. Most examples of this technique in publication utilise an upturned petri dish and a very precise amount of solvent. Similar to the anti-solvent technique, controlling the effect is a challenge.

6.3 DEVELOPING THE AASA

Using the previously developed aerosol system, this study was able to effectively aerosolise DMF solutions to produce MAPI films. Therefore, it was feasible to use a pure DMF aerosol to treat an existing MAPI film, akin to the petri dish method solvent annealing method [164]. To conduct these experiments, 1-step spin coated MAPI films on ITO were used, as this method has been fully optimised

and yields high performance device. This allows for the critical evaluation of the influence that the aerosol treatment has on the film.

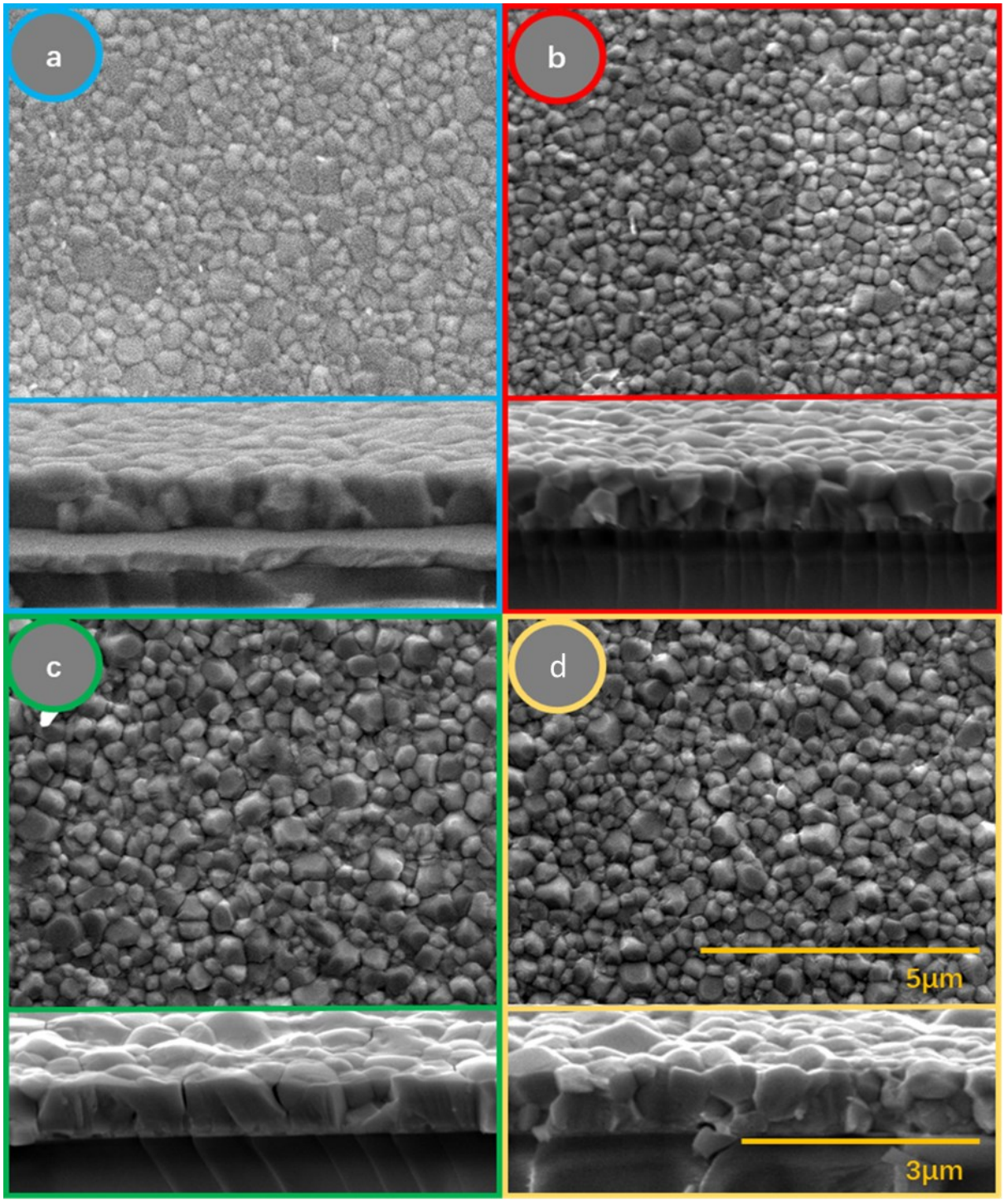


Figure 6-1 SEM images of spin coated MAPI films treated with the AASA method. Corresponding cross sections are below each image. a) Untreated control film b) Film treated with 0.1 L min^{-1} c) 0.5 L min^{-1}and d) 1 L min^{-1}

To develop the method, a simple parameter sweep was conducted. Films were kept at 100 °C for 5 minutes, whilst different aerosol flows were trialled. This temperature and time were initially chosen as they are the typical annealing parameters for MAPI films. Experimental details can be seen in

section 3.2. Figure 6-1 shows the influence of flow rate on the morphology of the film. The control film has an average grain size of 240 nm. At 0.1 L min^{-1} there is no discernible difference in the film. Increasing the flow to 0.5 L min^{-1} yielded an average grain size increase to 380 nm. Moreover, the cross section reveals a monolithic grain structure, which is favourable for PV applications. As charges move out of plane in PV devices, this structure would present no grain boundaries to impede charge transport. At 1.0 l min^{-1} the average grain size is 330 nm, showing less effect than rate. Additionally, the cross-section does not reveal the same monolithic grain structure. Thus, similar to the work in previous chapters, faster flow rates may reduce the time for the aerosol to interact with the film. Therefore, the effect will become less pronounced at faster flow rates.

To more closely look at the microstructural effect of the AASA treatment, XRD measurements were taken. Figure 6-2 shows the (110) reflection of the treated films. Note how the peaks shifted to a higher angle in the samples that are treated at higher flows, 0.5 and 1 L min^{-1}. This indicates that the unit cell of the perovskite has contracted. In the sample treated at 0.5 L min^{-1}, the peak is more intense and hints of tetragonal peak splitting can be seen, with a small hump forming due to the (002) plane. This suggests that the crystallites within the film are larger and more highly orientated, leading to more defined diffraction peaks.

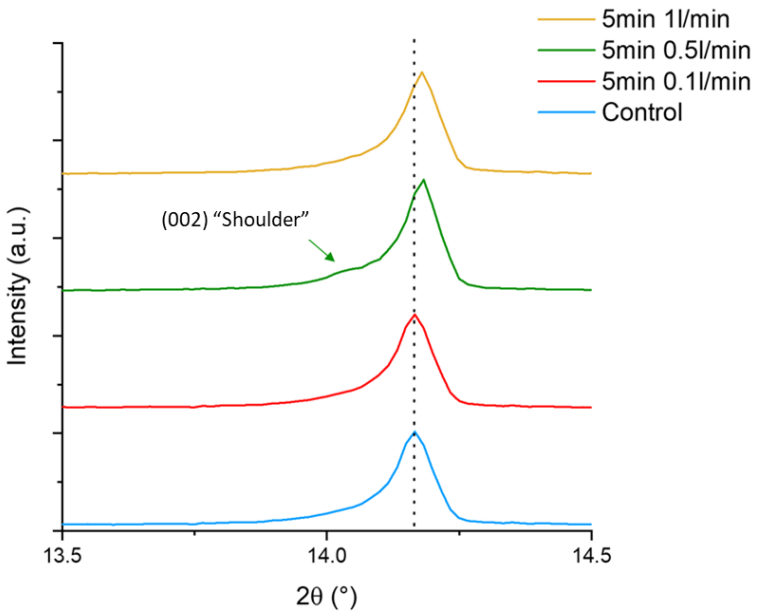


Figure 6-2 XRD pattern centred around (110) reflection of films treated by AASA with varying aerosol flow rates

To confirm this, the Scherrer equation was used to calculate the crystal size and the results can be seen in Figure 6-2. The resulting crystallite sizes are very close, with the 0.5 L min^{-1} sample indicating a slightly larger crystallite size, 103 nm vs 98.5 nm. However, as these results are close to the detection limit of the method, the results should be verified with further experimentation.

Table 6-1 FWHM and Crystallite sizes of films treated with varying aerosol flow rates

Flow rate (L min^{-1})	FWHM (°)	Crystallite size d_{110} (nm)
Control	0.085	98.5
0.1	0.085	98.5
0.5	0.081	103
1	0.085	98.5

Figure 6-3 shows the preferential orientation of the samples and again a subtle yet clear difference in the sample treated at 0.5 L min^{-1} is observable. The film shows a slight increase in preferential orientation around the (110) plane, corroborating the visual observations can be seen from the SEM data.

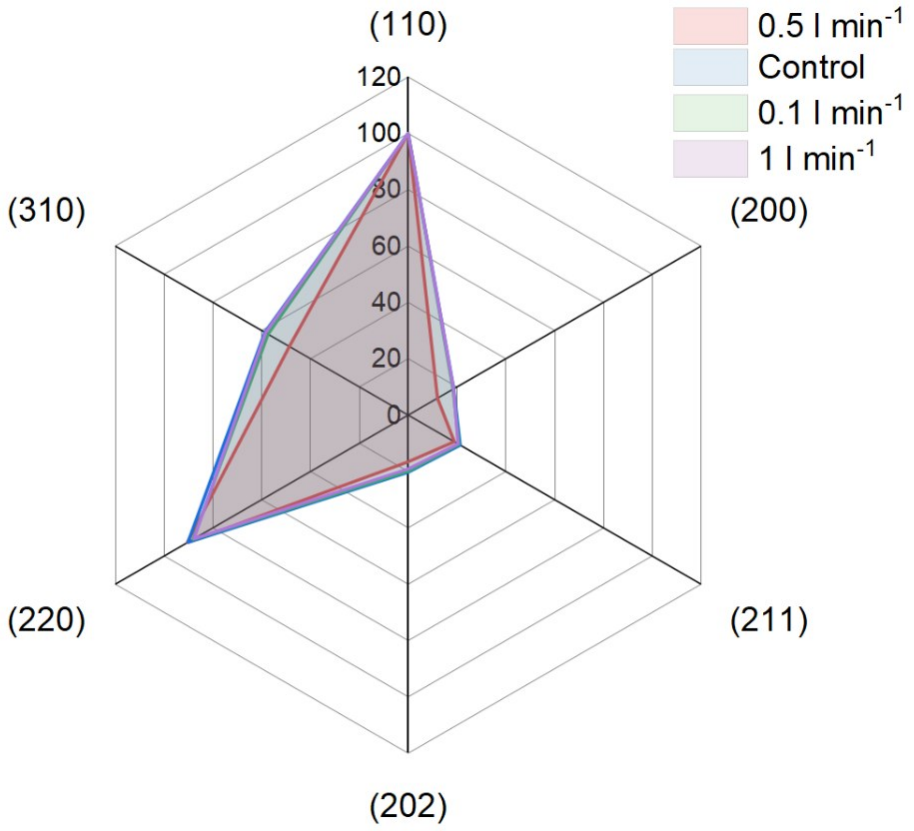


Figure 6-3 Radar diagram showing relative peak intensities of films treated with different aerosol flow rates. Only the 0.5l min $^{-1}$shows a significant difference

Using the XRD data, the lattice parameters of the treated films were calculated. The results can be seen in table . Here again it is evident that the aerosol effect is more pronounced in the samples treated at 0.5 and 1 L min^{-1}, with both samples showing a more contracted lattice. As expected, the 0.5 L min^{-1} sample shows the largest change. However, the ratio between a and c increases, indicating a more tetragonal lattice, which is why the sample shows the (002) “shoulder” in the XRD pattern.

Table 6-2 Lattice parameters calculated from XRD patterns of films treated at different aerosol flow rates

Flow Rate (L min^{-1})	**Lattice constant**	**Calculated (Å)**	**Control difference (%)**	**Unit cell volume (Å^3)**	**c/a**
Control	a	8.84	N/A	247.5	1.433
	c	12.67	N/A		
0.1	a	8.84	0	247.5	1.437
	c	12.67	0		
0.5	a	8.82	0.23	246.9	1.439
	c	12.70	0.24		
1	a	8.83	0.12	247.2	1.437
	c	12.68	0.16		

6.4 AASA Devices and Optoelectronic Properties

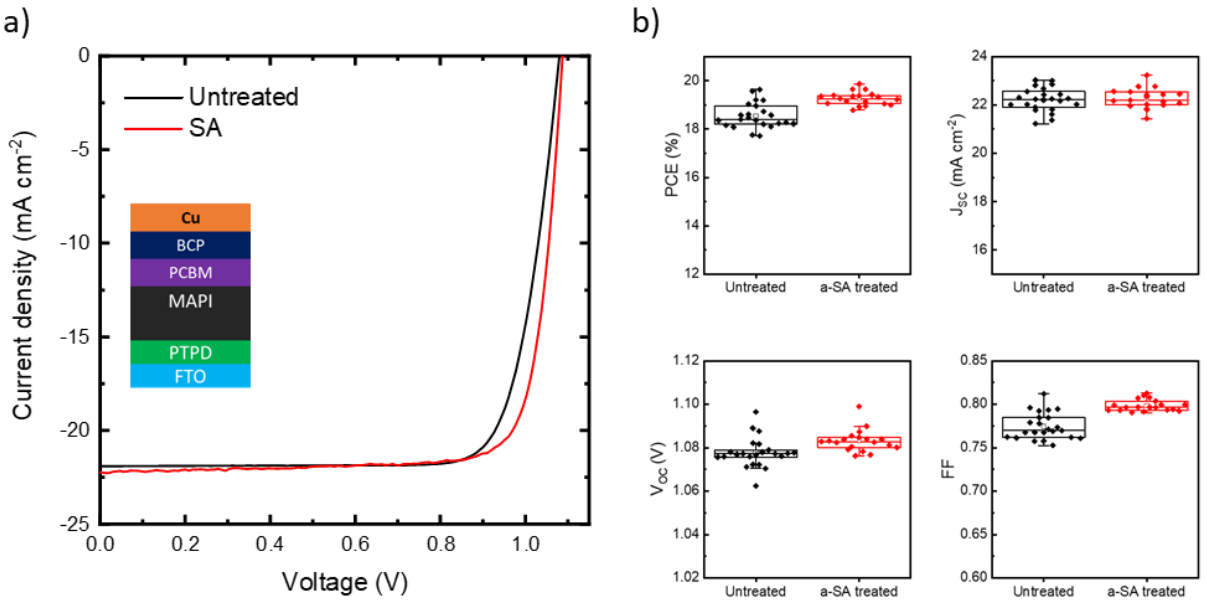


Figure 6-4 a) J-V curve of champion treated and untreated champion cells. b) PCE distribution of 24 treated and untreated cells c) Schematic of cell architecture used

In section 5.3, it was shown that a 5-minute treatment with an aerosol flow rate of 0.5 L/min resulted in the most promising film morphology. Hence, films treated with these parameters were incorporated into devices and their performance was evaluated. The details of device fabrication can be seen in section 3.3. Figure 6-4 shows the resulting performances of the devices measured in reverse sweep. Note as p-i-n devices do not show significant hysteresis only reverse sweeps are evaluated; appendix Figure 9-5 shows an example of a forward and reverse sweep. Non-treated films had an average PCE of 18.58%, with a champion PCE of 19.64%. Treated films show an improved average PCE of 19.26% with a champion efficiency of 19.87%. Moreover, the AASA treatment not only improves the average PCE of the cell, but also reduces the distribution of device performance. Comparing the J-V curve of the two champion devices, it is clear that there is an improvement in J_{sc}, V_{oc} and, more significantly, the FF. This increase could be primarily attributed to the reduction of grain boundaries in the treated films, which would act as potential charge trap sites. Observations in literature similarly link FF losses with parasitic resistances caused by grain boundaries [259,260].

6.4.1 Elucidating the performance increase

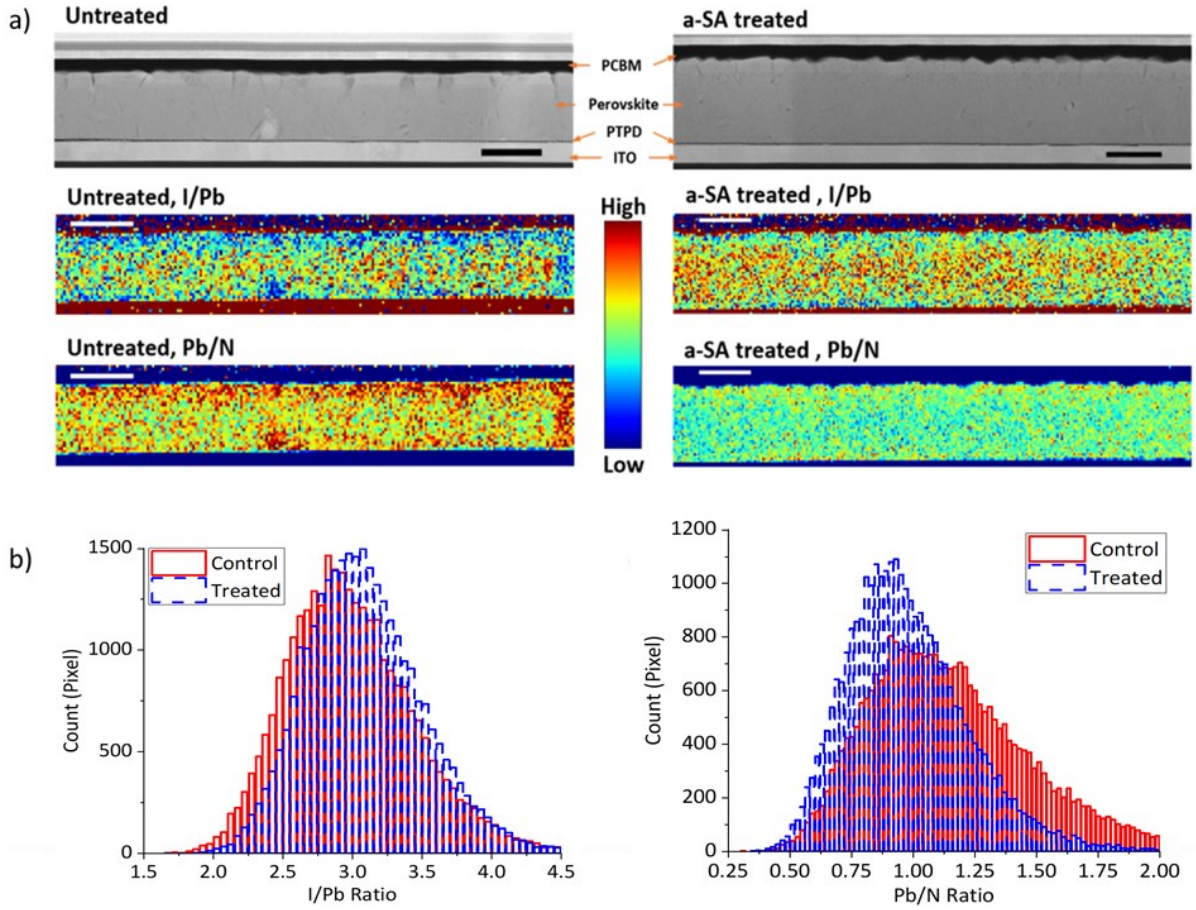


Figure 6-5 a) Cross-sectional scanning transmission electron microscopy (STEM) images (top row) of complete solar cells, scale bar corresponds to 500 nm. Energy dispersive x-ray spectroscopy (EDS) mapping of the of I/Pb (center row) and Pb/N (bottom row) molar ratio, colour scale bar corresponds to elemental molar ratio from high (red) to low (blue). b) and c) Histogram of pixels of varied elemental molar ratio

To better understand the effect of the AASA and the resulting device performance, scanning transmission electron microscopy (STEM) was employed. These measurements were conducted by Felix Kosasih at the university of Cambridge materials science department. Figure 6-5 shows the cross-sections of a treated and untreated device. The reduction of grain boundaries in the treated film can clearly be seen. Additionally, the untreated films displayed more inhomogeneity, with bright spots visible near the HTM interface. Using EDS, these brighter areas were shown to be Pb rich, indicating that these are areas may be PbI_2 left over from the initial fabrication of the film. These areas act as potential trap sites for charges and would reduce the PCE potential of the device. Furthermore, when looking at the overall I:Pb ratio, the treated samples show a more ideal 3:1 stoichiometry. Appendix Figure 9-6 shows further the atomic ratios of key elements within the treated and untreated films. Again, these results clearly show that the treated films have a more homogenous distribution of atomic species. This indicates that the AASA not only promotes the recrystallisation of the film, but also homogenises the stoichiometry of the film.

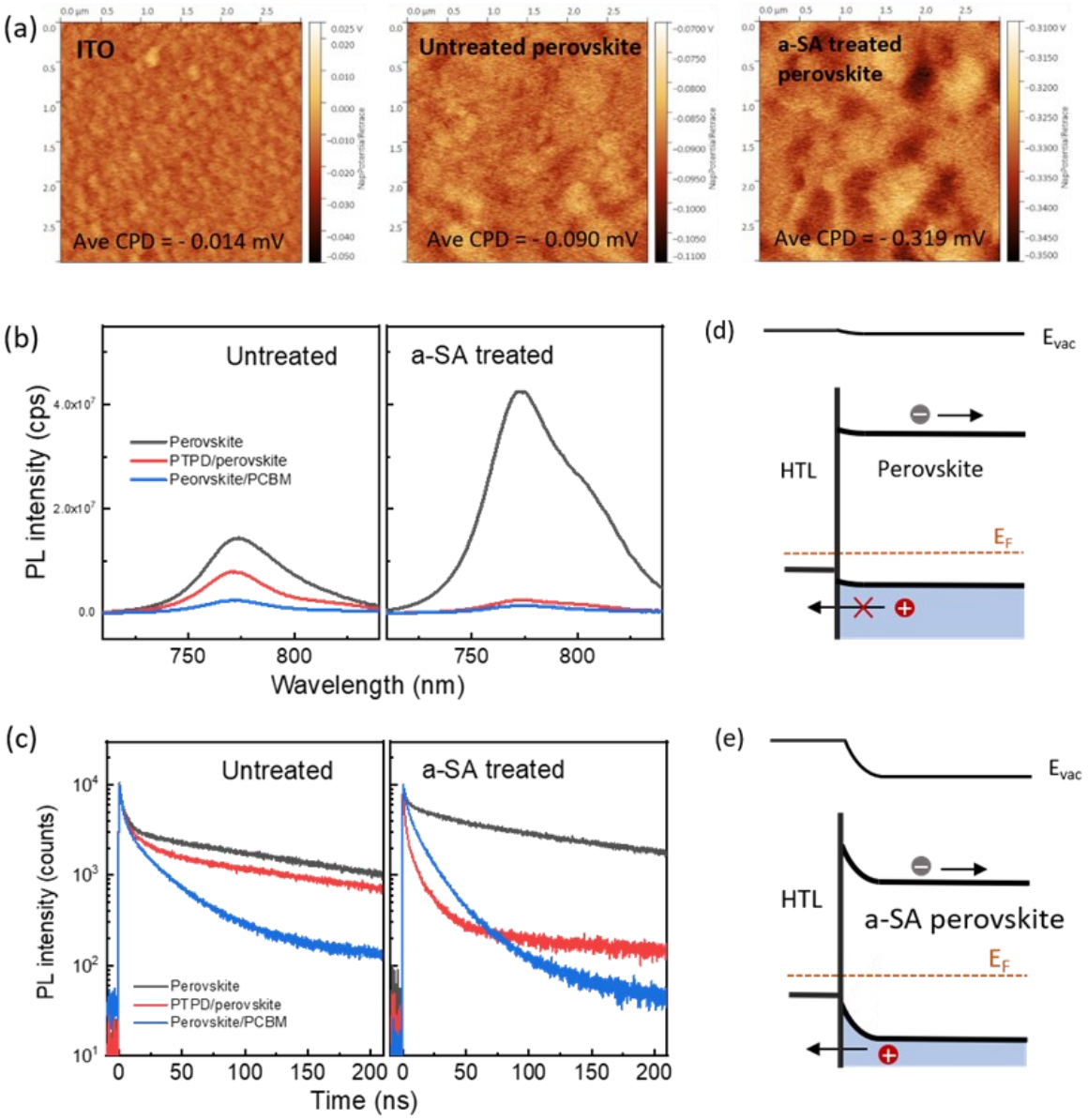


Figure 6-6 Electronic and optoelectronic characterization of untreated perovskite film and AASA treated perovskite film. a) the surface contact potential difference. b) steady-state PL emission spectra of perovskite, HTL/perovskite and perovskite/ETL. c) PL decay dynamics. d) and e) schematic drawing of HTL/perovskite band bending.

To better understand the effects of these microstructural and stoichiometric improvements, a variety of electronic and optoelectronic measurements were applied. Firstly, the work function was probed using scanning Kelvin probe force microscopy (SKPFM), which was measured by Victoria Bremmer. Figure 6-6 a) shows the average surface contact potential difference (CPD) of ITO and treated and untreated films. The average CPD of untreated perovskite film (-0.09 mV) is slightly more negative than ITO (-0.014 mV). After the treatment this becomes more negative after a-SA treatment (-0.319 mV). Whilst the absolute WF cannot be reliably determined, the negative shift in respect to the untreated film shows the reduction of p-type doping. The data suggests that the untreated films are intrinsically more p-type as deposited, which is typical of spin-coated films [229]. It also shows that after the treatment the films become more intrinsic as the unreacted species/defects are reincorporated

into the film. These results substantiate the EDS measurements and show the relationship of non-stoichiometry and electronic properties.

To probe the effect of these energetic changes, steady state and transient photo luminescence (PL) spectroscopy was used. Figure 6-6 b) shows the steady state PL emission spectra of treated and untreated films on glass and charge extraction layers. On glass substrates, treated films show a fivefold increase in emission, indicating a strong reduction of non-radiative recombination processes. Or, in other words, removal of defects leads to less quenching caused by trap states. In the transient measurements the typical bi-exponential decay dynamics observed in OMHPs can be clearly observed. However, the magnitude of the initial fast decay is reduced by more than half after treatment, again indicating a considerable suppression of the charge trapping due to defects.

By conducting these measurements on half cells utilising only an ETL or HTM, this study was able to look at the differences of charge transfer dynamics. In the untreated film more significant quenching of the steady state PL can be seen, when the film is contacted with the ETL, when compared to the HTM. Likewise, in the transient measurement a more rapid decay in the ETL contacted film is observable. This indicates that the hole transfer is significantly slower than the electron transfer. After treatment however, this becomes more balanced. Both the ETL and HTM contacted film show significant and more equal quenching. Again, the transient measurement verifies this, showing a considerable faster decay. This improvement can be ascribed to the change in WF of the film, resulting in more favourable band bending that facilitates better charge transfer. This is illustrated in Figure 6-6 d) and e).

Overall, these results illustrate that the AASA treatment not only improves the morphology and stoichiometry, but also alters fundamental electronic properties of the film that aid in device charge carrier dynamics.

6.4.2 Future work

To further investigate the effects of the AASA treatment on the fundamental optoelectronic properties, several key techniques could be utilised. One key factor that is lacking within this study is the determination of the charge carrier mobility of the films. From the results it would be expected that the mobility of the charge carriers would be improved. The microstructural, morphological and optoelectronic properties all indicate that out of plane mobility should improve. However, deriving the true mobility is not trivial. SCLC or ToF may be used to give accurate values, however they rely on specific architectures and film thicknesses to give accurate results. Preliminary work has been conducted using the AASA treatment on the thick perovskite films deposited utilising the method detailed in chapter 3. Figure 6-7 shows the improvement in measured mobility after the AASA

treatment. This supports the assumption that the AASA process would improve charge carrier mobility. However, as these results utilise AACVD films they cannot be used as a like-for-like companions. These results, however, do give credibility to the argument of improved mobility due to the AASA treatment.

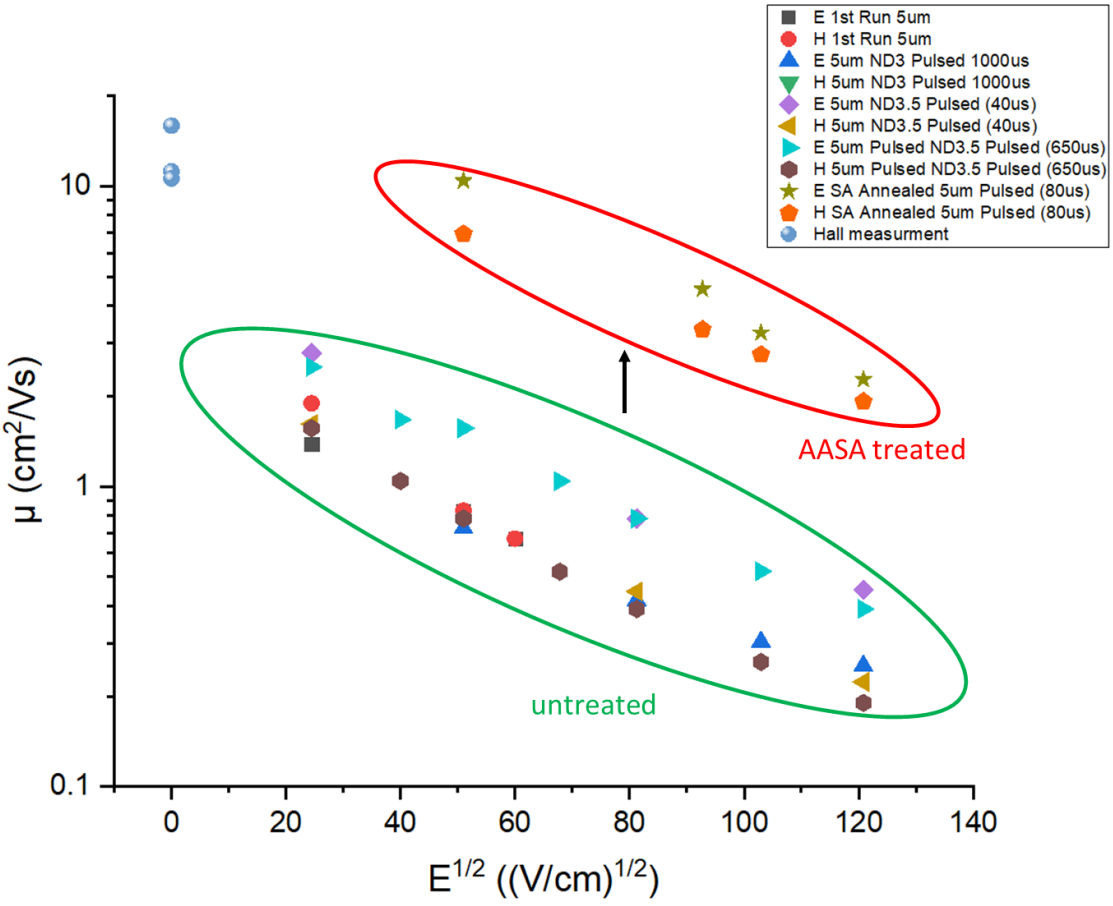


Figure 6-7 Poole-Frenkel plot of ToF measurements conducted on AASA treated and untreated MAPI films deposited by AACVD. Films were deposited using the method detailed in chapter 4, with the treated films using the 5 minute protocol detailed in this chapter.

6.5 Scalability of AASA

One of the main benefits of using the AASA versus conventional solvent annealing techniques is the potential scalability of the method. Typical solvent annealing of OMHPs is conducted by placing a substrate in a sealed vessel containing a small quantity of solvent. The substrate is then heated, which also evaporates the solvent within the vessel. The evaporated solvent then interacts with the film, recrystalising it and promoting grain growth. The caveat with this system is that the solvent delivery is dominated by convective flows, which are difficult to control. On the contrary, within this study's AACVD based system, the aerosol/solvent flow is more controlled. Figure 6-8 shows a schematic comparing both the methods, illustrating the use of the boundary layer to control the delivery of the solvent. This means that the AASA should be more controllable and consistent over large areas.

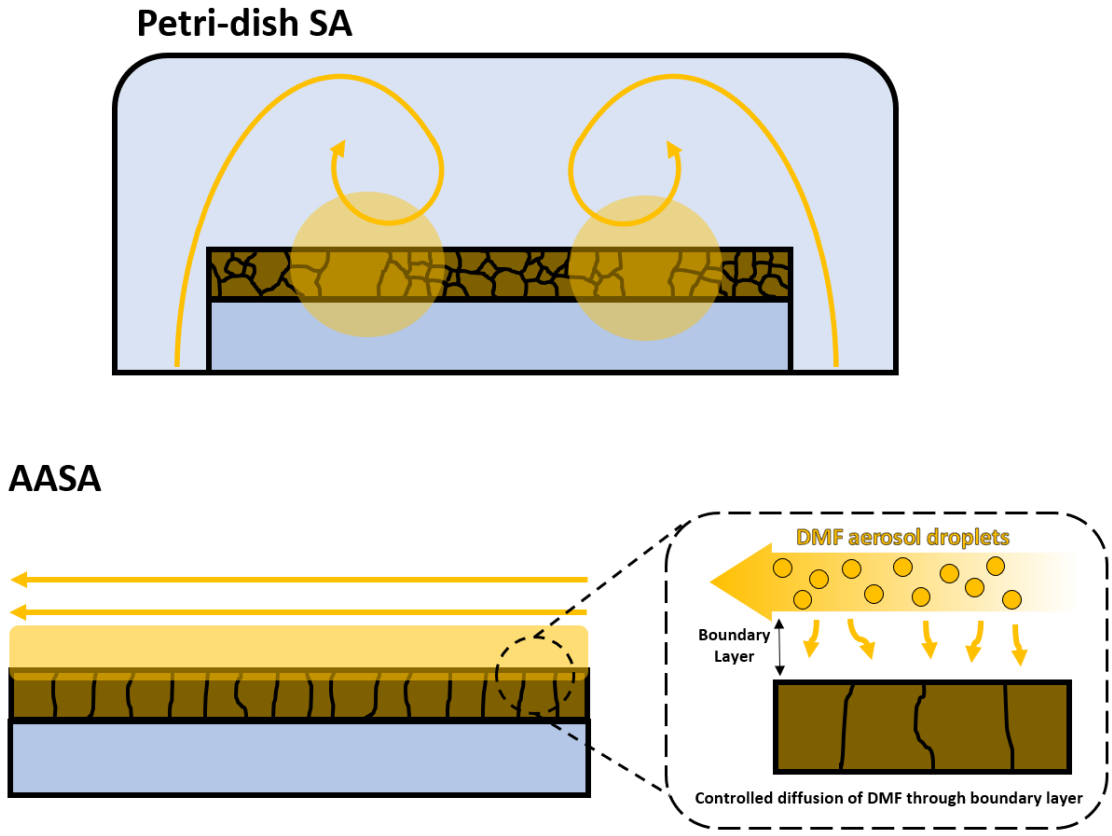


Figure 6-8 Schematic illustrating petri-dish solvent annealing and the AASA process

6.5.1 Uniformity over large areas

To demonstrate the scalability of the AASA technique, the grain size was evaluated over a larger area within the reactor. This is a simple approach to assess the uniformity of the solvent annealing effect. The experiment was carried out by using large glass substrates coated with MAPI, that were placed within the reactor and treated. The substrates had a total area of 19.35 cm^2 (2.54 cm x 7.62 cm). The substrates were then divided into 36 individual areas and the grain size was measured in the centre of each area using SEM images. For comparison, a petri dish solvent annealed analogue was also

measured. Due to the size limitation of the petri dish, the substrate was a third of the size with an area of 6.45 cm^2 (2.54 cm x 2.54 cm). The results of this experiment can be seen in Figure 6-9, with results of an untreated sample in appendix Figure 9-7. Note that as these samples are spin coated on large glass substrates, they have intrinsically smaller grains.

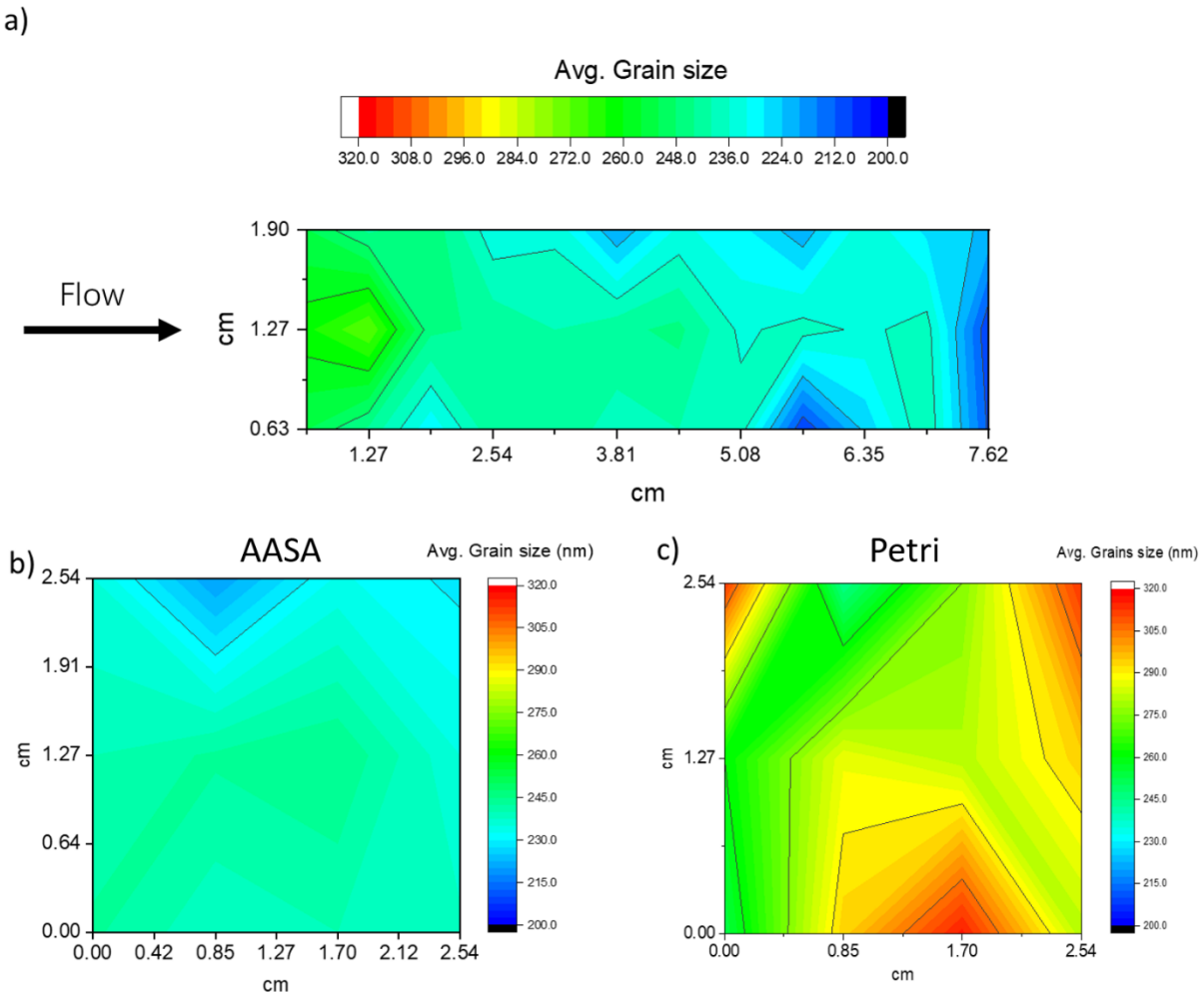


Figure 6-9 Heatmap showing the average grain size of MAPI films on glass substrates. a) Shows the distribution of grain sizes after the AASA treatment. b) Grain sizes of centre slice of the AASA sample c) Grain size distribution in petri-dish solvent annealed sample

The average grain size across the entire length of the substrate was 236 nm, however it is clear that the distribution is not entirely uniform. Near the entrance of the reactor the grain size is larger, and towards the back of the reactor the grain sizes approach the untreated values. This inhomogeneity can be explained by gas flow effects detailed in section 2.3.3.3. Essentially, as the aerosol flows over the substrate, the boundary layer begins to form at the leading edge of the substrate. At this point the boundary layer is very thin and the solvent can easily diffuse through this layer and recrystallise the film. As the aerosol flows further down the substrate, a stable boundary layer is formed, and the solvent annealing effect begins to become more homogenous. Towards the latter part of the reactor

the laminar flow will begin to detach from the surface of the substrate, transitioning to turbulent flow. This reduces the amount of aerosol near the surface of the substrate, thereby reducing the effect. This inhomogeneity is a result of the limited size of the reactor. For instance, in a wider reactor, the homogenous area would make up a larger total proportion.

The petri dish treatment yielded an average grain size of 284 nm, slightly larger than the AASA treatment (Figure 6-9c). However, there was more significant grain size variation across the substrate. When comparing the centre section of the AASA, the homogeneity advantages become more apparent. Figure 6-10 shows the box plots of both the AASA centre section and the petri dish treated sample. The results clearly show how much more even the effect of the AASA treatment is, and how the more traditional petri dish method could be unsuitable for scalable implementation.

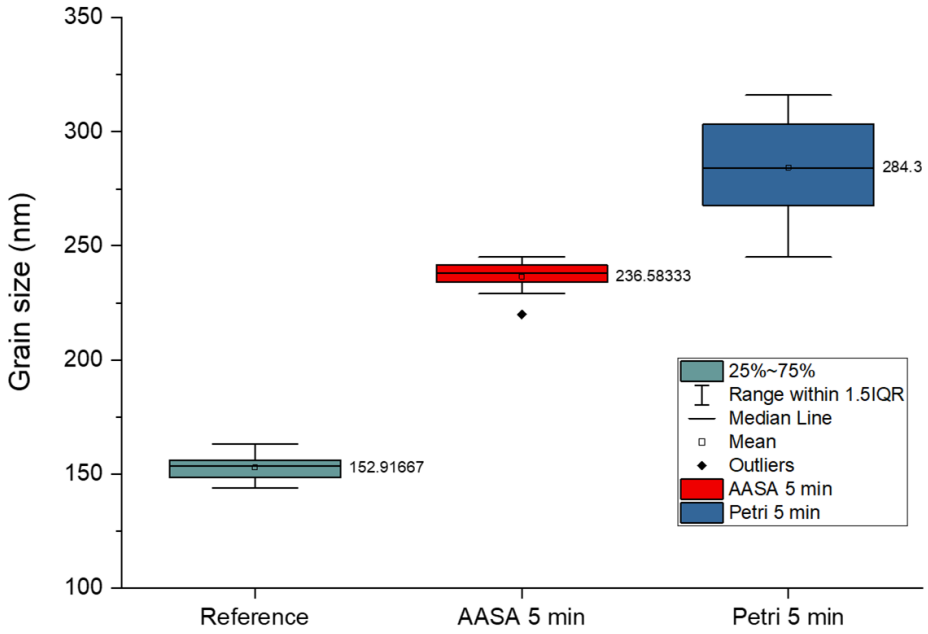


Figure 6-10 Box plots of average grain size collected from untreated and treated MAPI films spin-coated on glass

To further test the spatial uniformity of the AASA, a set of cells were fabricated utilising treated MAPI films. The AASA treated films were placed within an approximately 2.54 cm^2 area in the centre of the reactor, which simulated the aforementioned glass substrate. A second set of films were treated using the petri dish solvent anneal method. Figure 6-11 shows the resulting J-V curves of the devices treated by both methods. Here it can be clearly seen that the all devices treated by AASA showed a smaller distribution in performance. Conversely, in the petri dish method there was a large variation, with multiple devices performing worse than the reference device. AASA treated devices also had a higher average PCE of 19.4 % as opposed to 18.0 % for petri-dish method. Appendix Figure 9-8 shows the distribution of cell parameters. These results highlight the advantage of the AASA method, as it can more consistently solvent anneal perovskite films over a large area.

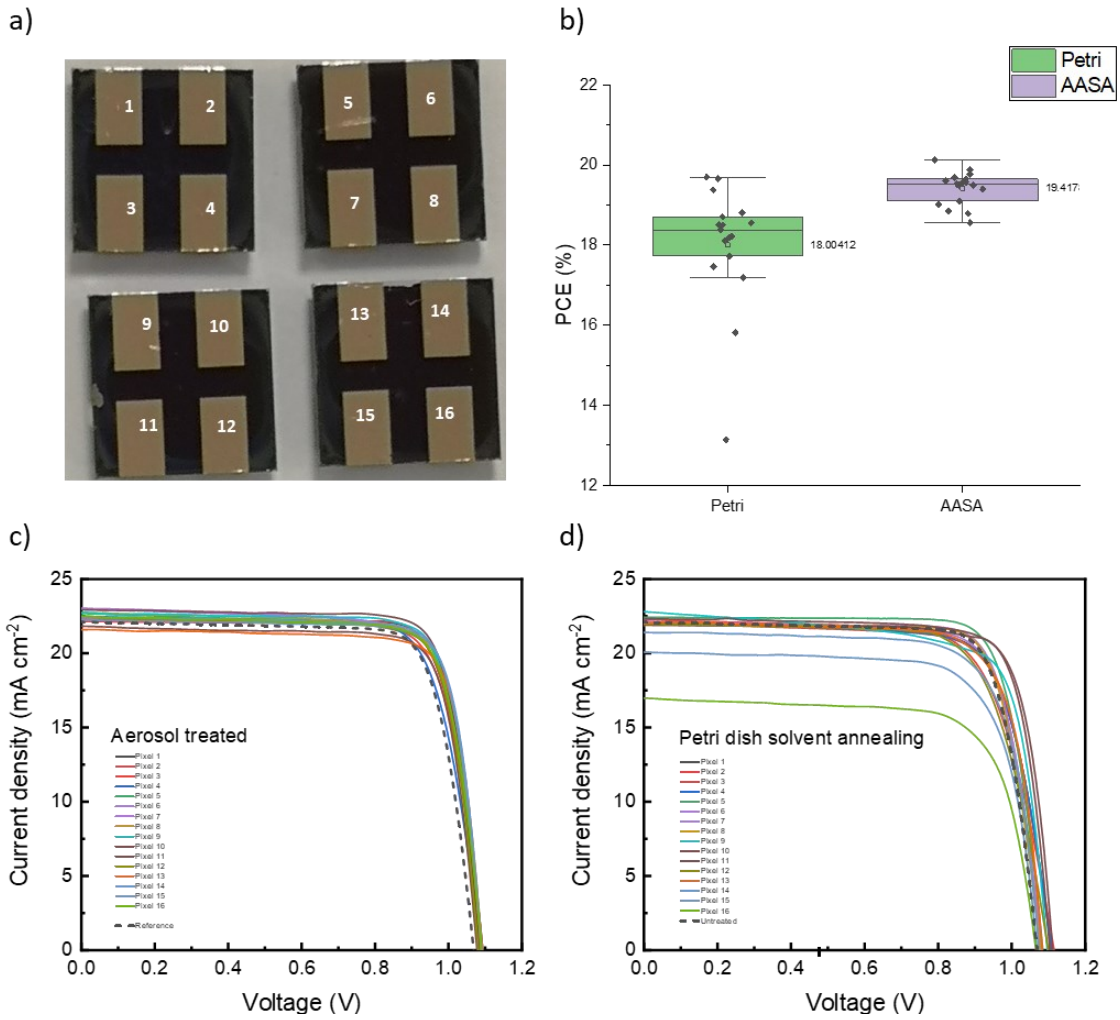


Figure 6-11 a) Photograph of device arrangement used to test spatial uniformity. b) Box plot showing PCE distribution of treated devices. c) J-V curves of devices treated by AASA at different reactor positions. d) J-V curves of devices treated by petri dish solvent anneal at different reactor positions.

6.5.2 Large area devices

To further prove the viability of AASA in industrial applications, one of the key requirements is the use of large pixel devices. Currently, all the results have been collected using devices with active areas smaller than 10 mm^2, which is far smaller than what would be required in a typical industrial cell. From this study's previous results, it can be seen that AASA performs consistently over a large area. Therefore, it was anticipated that it could be effectively applied to large area cells. Additionally, as the treatment has been shown to reduce the number of defects in the film, it was hoped that the AASA can preserve the performance of a device when the area is scaled up.

To evaluate the effect of AASA in regard to device area, substrates were patterned with two different electrode areas. This produced two devices on each substrate, one with an area of 0.25 cm^2, and the other with 1.025 cm^2. Details of device fabrication and electrode design can be found in section 3.3. By evaluating the area effect per substrate, it minimises the effect of substrate-to-substrate film

quality variation. However, as the electrodes are at different points on the substrate, there may be still some variation caused by the inhomogeneity of the spin coated film. Moreover, due to the difficulty of fabricating large-area devices using spin-coating, the results were limited by the number of working devices. Figure 6-12 shows the results of one AASA treated and one untreated substrate. Whilst this is a small sample set, the results indicate that AASA has a positive effect on the area scaling. At 0.25 cm^2 the untreated device had a PCE of 18.7 % and this reduced to 16.7 % in the larger area. On the other hand, in the treated device the small area PCE was 18.9 %, which reduced to 17.8%. In other words, as the area increases the untreated devices suffer from an 11.1% reduction in PCE, whereas in the AASA treated samples this is 6.02 %. From this it can be seen that the AASA treatment not only causes the expected PCE uplift, but it also preserves the performance when scaling up the device.

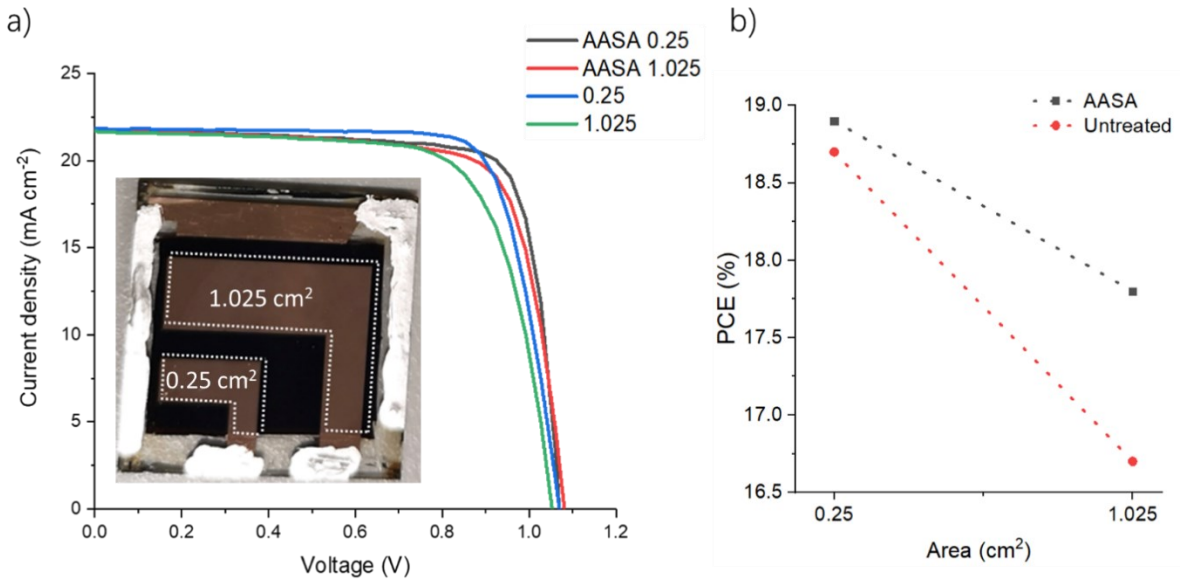


Figure 6-12 a) J-V curves of two-pixel substrates, showing results for AASA treated and untreated films. b) PCE values of devices plotted against area.

Table 6-3 shows the detailed parameters extracted from the devices. Here it can be seen that the AASA improves the FF and J_{sc} retention as the device is scaled up. Interestingly, the V_{oc} shows a significant improvement as the device is scaled up. Again, whilst these results corroborate this study's hypothesis, a larger sample size would be required to truly substantiate the claim.

Table 6-3 Two-pixel device parameters for AASA treated and untreated films

	Untreated			AASA		
Area (cm^2)	0.25	1.025	Diff. (%)	0.25	1.025	Diff. (%)
PCE (%)	18.7	16.7	- 11.1	18.9	17.8	- 6.02
V_{oc} (V)	1.1	1.08	- 1.91	1.08	1.10	+ 1.85
Jsc (mA/cm^2)	21.9	21.8	- 0.46	21.8	21.8	- 0.23
FF	0.78	0.71	- 8.97	0.8	0.74	- 7.50

6.5.3 Future Work

Firstly, further work should be conducted on the large-area experiments to substantiate the initial findings in this study. Moreover, utilising smaller increments of pixel sizes may give a more accurate representation on how the effect scales with size. Additionally, utilising more optimised deposition techniques better suited for large area devices would give a better starting film. This would remove the uncertainty caused by the spin coating technique. Utilising cells based on inkjet or slot-die coating may not only give more reproducible results but would also test the cross applicability of AASA on different deposition techniques.

In terms of further characterisation, utilisation of electro luminesces (EL) measurements could be used to prove the AASA effect over the large area. As these measurements are conducted by injecting charges into the cell and measuring the radiative recombination, they are a good indicator of the quality of the film. Moreover, as these measurements are conducted by taking an image of the entire cell, they could provide strong evidence for the area effect of the treatment [261]. Spatial photoluminescence measurements could be also used in a similar effect to EL measurements, however this would probe radiative emission on a more local area and could be used to look at potential grain boundary trap states [262].

6.6 ENABLING THICKER FILMS

Typically, the active layer within high-performing perovskite cells is around 500 nm thick. Whilst, OMHPs have shown diffusion lengths in excess of this length, grain boundaries and the resulting trap states have limited the optimal thickness. This limits the maximum amount of light the active layer can absorb and therefore limits the potential efficiency the device can reach. This is especially true in non-AM1.5 conditions. For instance, at dusk and dawn longer wavelengths of light dominate the spectrum, which require a larger absorption depth. Therefore, if the microstructure of the absorbing layer can be improved the cells would become more efficient in real world use cases. As AASA has demonstrated the transformation of perovskite film morphology to a monolithic grain structure, it seems plausible to apply this method to thick films of perovskite.

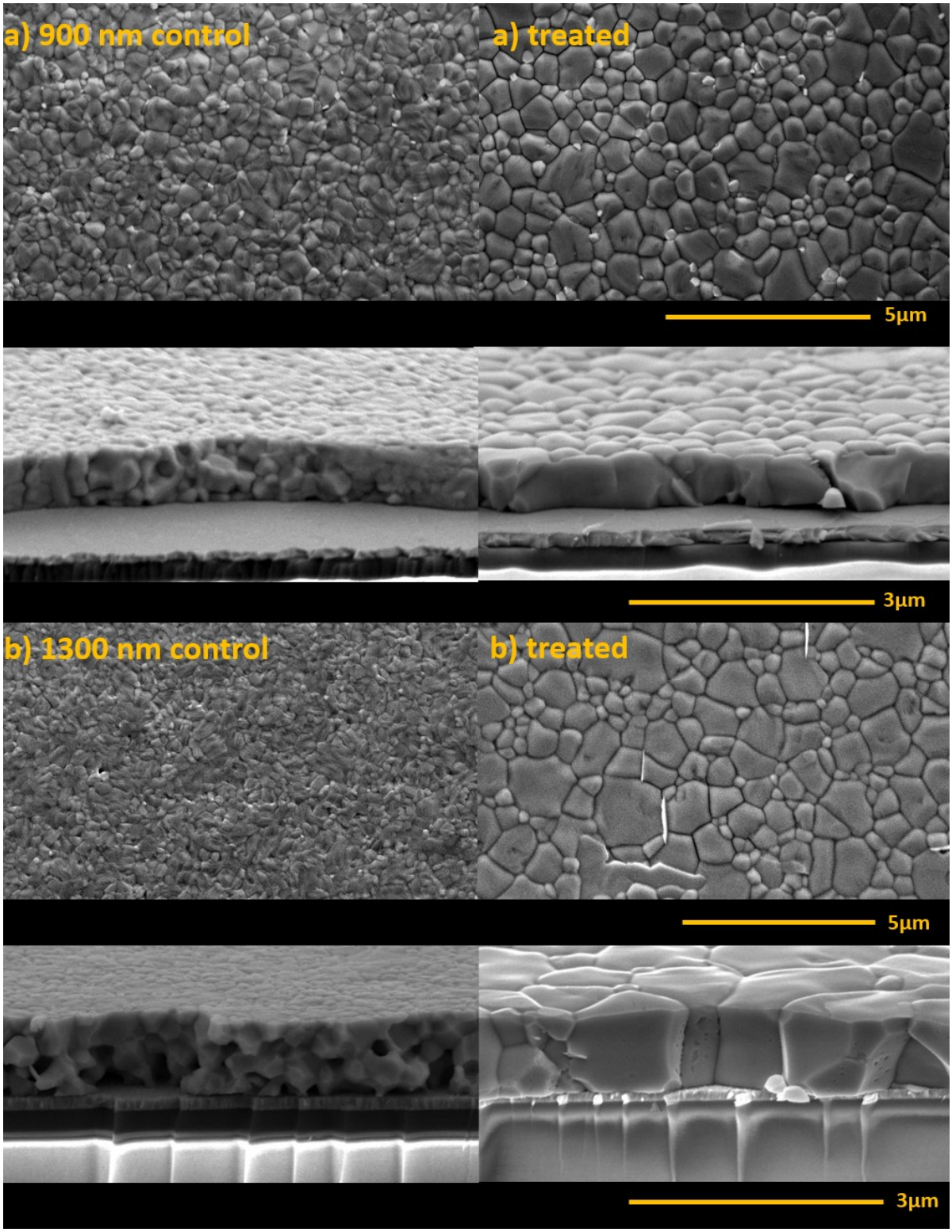


Figure 6-13 SEM images of thick MAPI films treated with AASA. a) 900 nm film control left and treated right with corresponding cross sections below. b) 1300 nm film control left and treated right with corresponding cross sections below.

To test the AASA effect on thicker films, films with two different thicknesses were spin coated: 900 nm and 1300 nm. The technique and method were developed by Tian Du and was detailed in section 3.3.5. Intriguingly, as thickness increases the as-spin coated grain structure becomes finer. This is most

probably due to the thicker films requiring higher concentrations of precursor material, which in turn would lead to more rapid nucleation of the film and therefore produce a finer grain structure. However, after the AASA treatment both films show much improved morphology. Figure 6-13 shows the microstructure of the respective films before and after AASA treatment. In the 900 nm thick film, the treatment increases the average planar grain size from 330 nm to 550 nm. When looking at the cross-section, the formation of a monolithic grain structure can be clearly observed. This trend is also seen in the 1300 nm thick film. Here, the planar average grain size increases from 220 nm to 800 nm and again the grains are monolithic in the z-axis.

This change in morphology is again visible in the XRD measurements, with the (110) reflection showing a shift to higher angles (Figure 6-14). This is consistent with the observations in the 500 nm films. However, the effects of the AASA are stronger as the film thickness increases. This is possibly due to the aforementioned rapid crystallisation creating strain in the parent film as they are spin coated. Alternatively, thicker films may have more of an ability to relax as they are less epitaxially confined.

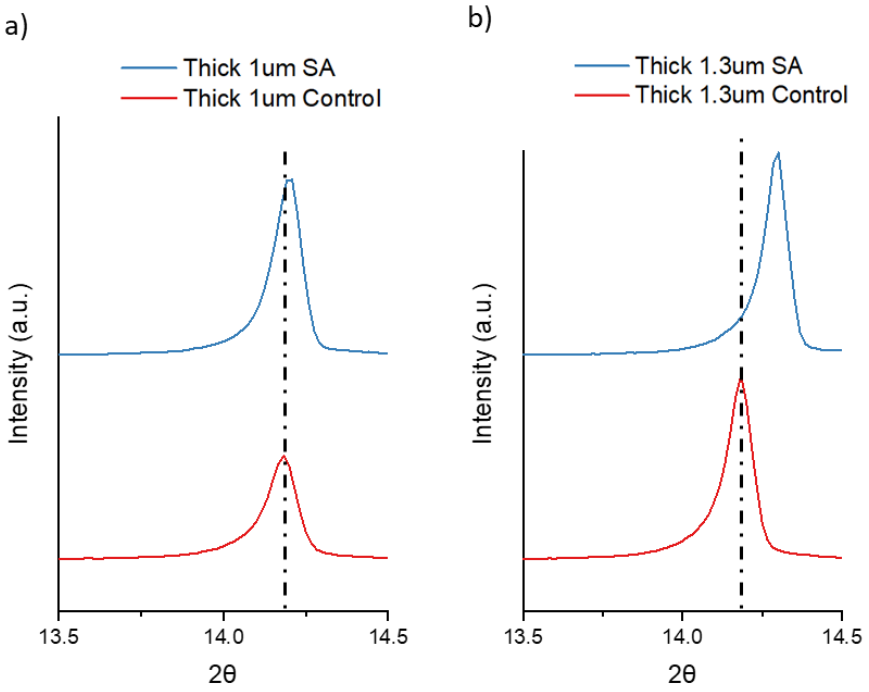


Figure 6-14 XRD diffractograms of treated and untreated film focusing on the (110) reflection. a) Results for 900 nm film before and after treatment. b) Results of 1300 nm film

Table 6-4 shows the lattice parameters of the films before and after treatment. The 1300 nm film shows the largest lattice contraction, with a primitive lattice volume change of 1.4 %. The 900 nm shows a change of 0.55 %. Both of these films exhibit a larger lattice volume contraction than the 500 nm counterpart, which only showed a 0.22 % contraction.

Table 6-4 Lattice parameters for AASA treated and untreated thick perovskite films

Sample	Lattice constant	Length (Å)	Control difference (%)	Primitive unit cell volume (Å^3)	Control difference (%)
Control 900 nm	a	8.83	N/A	247.75	N/A
	c	12.71	N/A		
AASA 900 nm	a	8.82	0.12	246.41	0.55
	c	12.67	0.32		
Control 1300 nm	a	8.83	N/A	247.16	N/A
	c	12.68	N/A		
AASA 1300 nm	a	8.752	0.89	243.77	1.4
	c	12.73	0.40		

In Figure 6-15 the device performances of treated and untreated thick films can be seen. Appendix Figure 9-9 contains more detailed cell parameter results. Like the 500 nm films there was a significant uplift in PCE. The origin of this uplift seems to primarily come from an increase in J_{sc}, with the thickest 1300 nm films showing the largest improvement. These results are consistent with the observable monolithic grain structure in the films, as this would allow for more changes to be extracted without them getting trapped at the numerous grain boundaries in the as-spun film. Moreover, the champion devices utilising a treated 900 nm film had a PCE of 20.68 %. This is a high value for a device utilising unalloyed MAPI. The current record for a p-i-n type cell is 21 %, held by Luo *et al.* However, they utilise a mixed composition perovskite with guanidinium bromide as a dopant to attain this performance. This indicates that AASA can potentially produce state of the art cells without the need for complex stoichiometry or dopants.

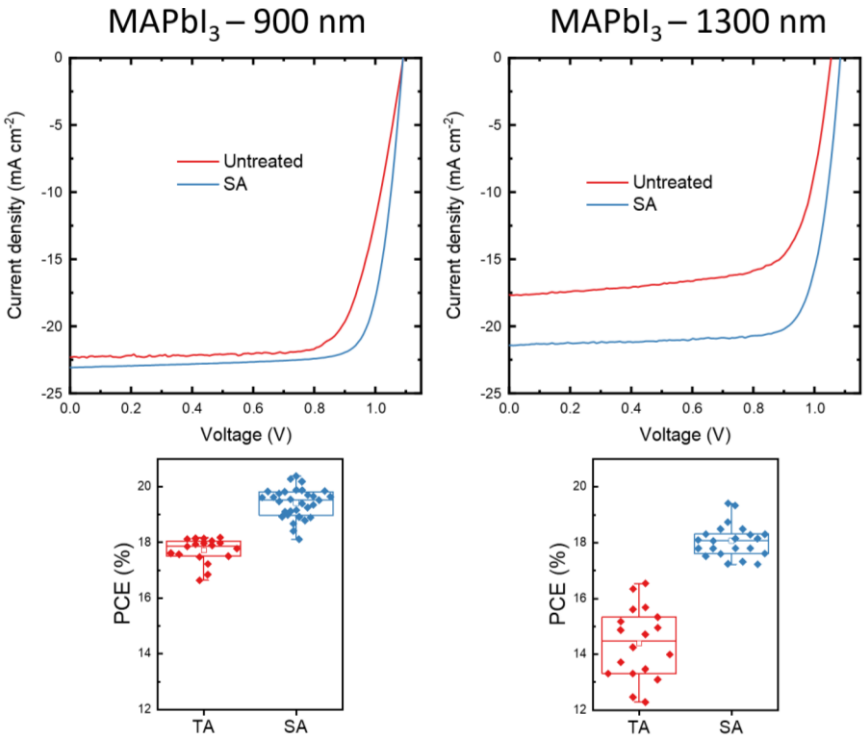


Figure 6-15 J-V curves of champion devices fabricated from AASA treated and untreated thick perovskite films. Below each curve are the PCE distribution of fabricated cells

These results have several major implications. Firstly, AASA can potentially remedy charge collection issues of overly thick films. This means that the treatment can be used to relax the stringent thickness requirements during deposition, making scalable production easier as variation in thicknesses will not lead to detrimental device performance. Secondly, as AASA enables the use of thicker films, these devices may show enhanced performance in low light conditions and can produce more power during the day. Lastly, the results show how much performance can be extracted from a pure MAPI device. This gives credence to the idea that reducing defects and not doping is the key to ultimate device performance.

6.6.1 Future work

The motivation behind utilising thicker films was both the potential benefit to industrial manufacturing and the potential low-light performance. Whilst the results have indicated that the performance of thicker cells can be significantly improved, the low light performance has not been assessed. Going forward this should be tested, and it is anticipated that there would be an increased performance in the AASA treated devices.

In terms of the absolute performance, the AASA treated 900 nm film exhibited near record levels of PCE. This result would need to be verified using independent and certified testing to ensure the obtained PCE value is valid. Moreover, by conducting optical modelling of these devices, the thickness of the transport layers could be optimised to further boost the PCE.

6.7 AASA Effect on Stability

As the AASA treatment has been shown to improve the stoichiometry and morphology of the device, it is natural to assume that there may be some observable stability improvements. Moreover, as pure MAPI is utilised within this study, any improvements in stability can be solely attributed to the AASA treatment. All of the following results utilise the same 5 min treatment previously described in this chapter.

6.7.1 Ambient stability via XRD

As shown in chapter 4, a facile approach to monitor stability is to track the development of the PbI_2 peaks within XRD diffractograms. To evaluate the effect of AASA on ambient stability, two 500 nm MAPI films deposited on ITO were exposed to ambient atmosphere for 48 hours. Additionally, these films were not exposed to light, meaning that any observable degradation is most likely due to atmospheric moisture and not due to light-induced degradation. The results of this experiment can be seen in Figure 6-16.

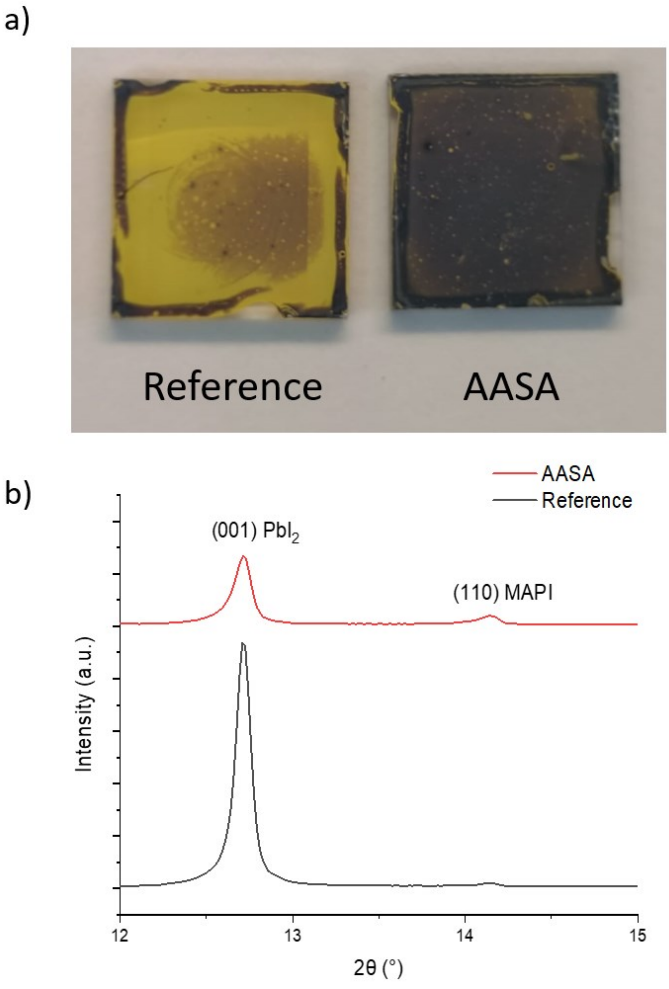


Figure 6-16 a) Photographs of AASA treated and untreated MAPI films after 48 hours of exposure to ambient air. b) XRD patterns of aged films

From the photographs it is immediately apparent that the reference film shows almost complete degradation to PbI_2, with nearly the entire substrate being yellow. Conversely, the treated film retains more of the characteristic dark brown/black colour. The XRD measurements also corroborate the visual results, with a much larger (001) peak visible for the untreated film. By taking the total area of the (001), it was estimated that the reference film has more than three times the amount of PbI_2 than the AASA treated film. The origin of the stability may be due to several factors. Firstly, the increased grain size results in fewer grain boundaries, which means that there are less points of ingress for moisture. Furthermore, as it has been shown that PbI_2 nucleates at grain boundaries, a treated film may have fewer points at which the degradation can progress from. Another cause could be linked to the improvements in stoichiometry and crystal geometry. A less defected crystal would be more stable, and therefore, would be more resistant to degradation.

6.7.2 Long-Term Device Stability

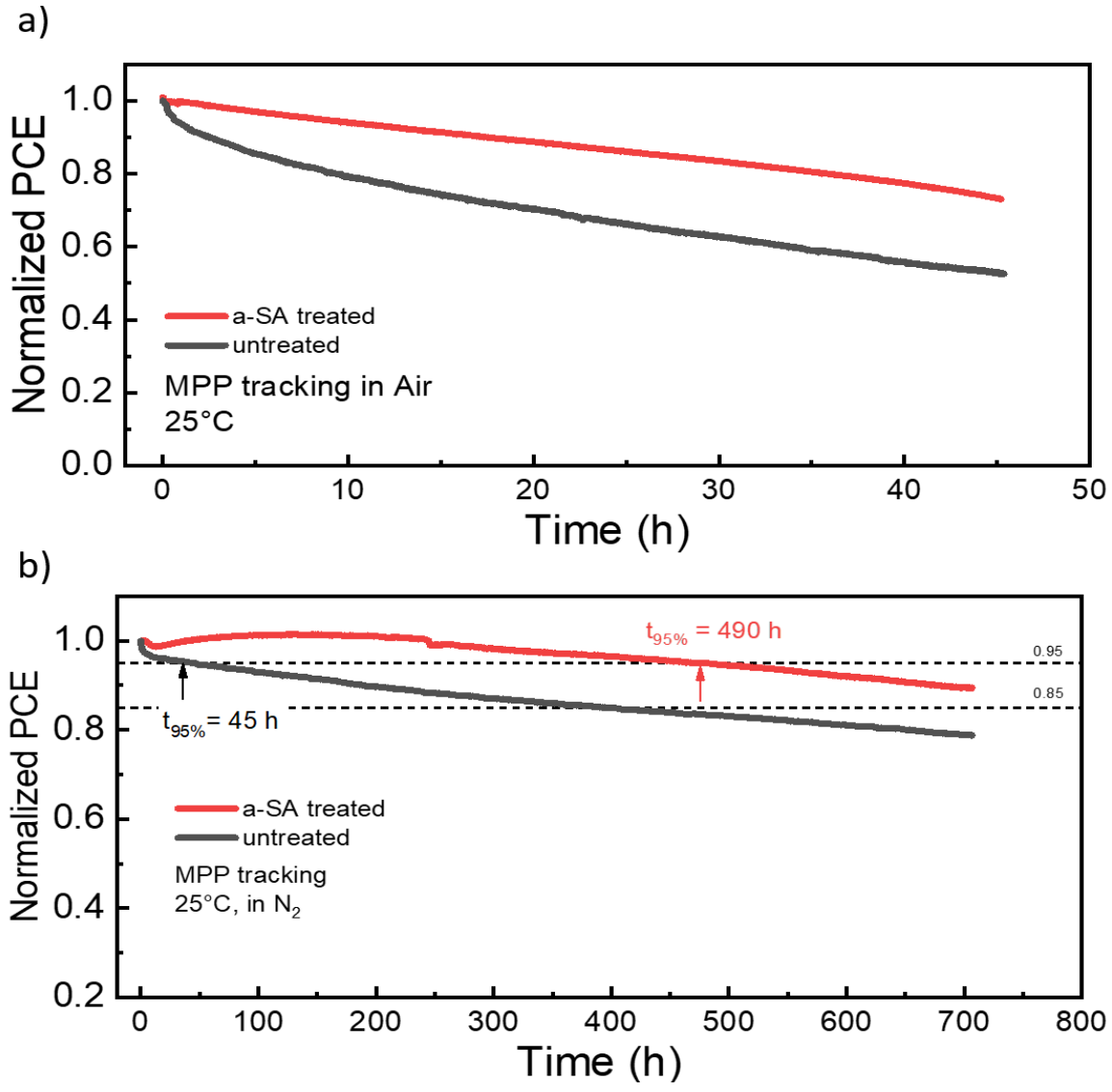


Figure 6-17 MPP tracking results of AASA treated and untreated devices measured in a) ambient and b) N_2 atmospheres

To test the effect of AASA on device stability, the output of treated and untreated cells was measured using maximum power point tracking (MPP). The details of the method are given in section 3.4.10.2. This method was used to compare the PCE of AASA treated and untreated MAPI devices over time. The devices were illuminated in both atmospheric and nitrogen atmospheres whilst at ambient temperatures. These two atmospheres in essence can be used to simulate encapsulated and unencapsulated devices. However, effects of humidity and ambient moisture may still influence the results.

Figure 6-17 shows the results of both AASA treated and untreated samples, in atmosphere and nitrogen atmospheres. In both cases, the treated sample experiences a slower performance decline, indicating that the AASA treatment has indeed improved the stability. However, unencapsulated results still show rapid degradation over the course of only a few hours. This degradation is most likely caused by super oxide induced degradation of the active layer, or oxidation of the electrodes [150,263]. Therefore, whilst AASA improves ambient stability, it will not enable the use of these devices without encapsulation.

The results of cells tested in N_2 show much slower degradation, therefore measurements were taken over a much longer time period. The data indicates that the untreated cell experiences an initial rapid drop-off in performance, followed by a slower degradation. After just 45 hours, the untreated cell drops below 95% of its initial PCE; this point is known as $t_{0.95}$ and is a known metric evaluate cell longevity. In the treated cell the degradation in performance acts very differently. Over the course of the first 200 hours, the AASA cell experiences a slight boost in performance, after which the performance begins to drop off. This boost during the initial part of testing the cell is typically seen in high-performing p-i-n cells [264]. The $t_{0.95}$ point is reached after 490 hours, showing a considerable improvement over the untreated cell. This is the highest result reported for a pure MAPI device, matching more advanced mixed composition and doped OMHP devices [265–267]. Therefore, from these results it can be inferred that the stoichometry and crystal defects are the dominant factors that influence device stability.

In summary, the data shows that the AASA treatment can effectively improve the stability of devices. This, in conjuction with the performance uplift, makes this a very promising post deposition treatment method.

6.7.3 Future Work

To explore the full effect that AASA has on stability, several different experiments will need to be conducted. To elucidate the ambient stability further, it will be necessary to track the degradation over time. XRD or optical absorption measurements can be used to give the rate of ambient

degradation. Furthermore, SEM and TEM imaging can help identify how the films degrade and show how the AASA treatment impedes this on a morphological level.

In terms of device stability, MPP tests should be conducted in ambient atmosphere and at elevated temperatures. If the measurement was conducted at 85°C, the results could be used to evaluate the performance against the IEC 8125 standard. However, as MAPI tends to suffer from thermal instability, this test could perhaps utilise a different OMHP.

The effect on thermal stability should also be evaluated. For instance, this could be conducted with the process developed in section 4.3.3, and using the calculated E_a, this can be contrasted against a reference film.

6.8 Applicability to Different Architectures and Compositions

From the previous results it can be seen that AASA can successfully improve the properties of MAPI devices, and this study has also shown how the treatment may be scalability applied. To further demonstrate the flexibility of AASA, different compositions and device architectures were experimented with.

6.8.1 HTM Free

One of the most expensive components of an OMHP cell is typically the p-type HTM. These are primarily composed of small molecules or polymers that can cost in excess of £1000/g. For instance, the current quoted cost of PTAA from Merck is £1800/g. Therefore, replacing or omitting these layers would significantly reduce the material costs of the cell. From the work in section 6.4.1, it was shown that the AASA may create more favourable band bending, allowing for more efficient hole extraction. This motivated the experimentation of applying AASA to HTM free devices.

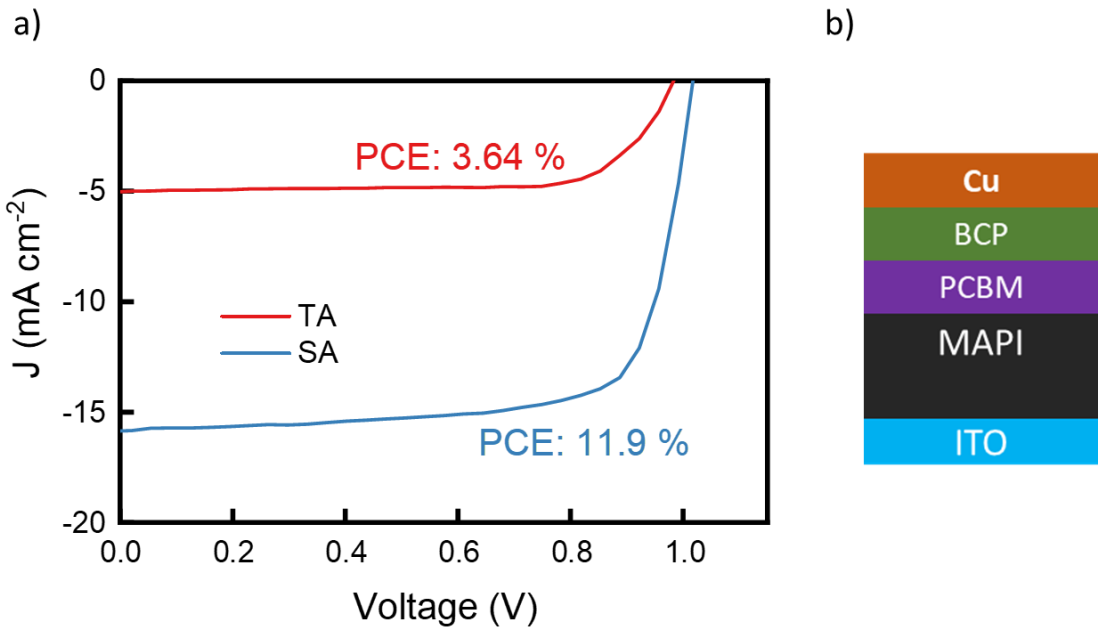


Figure 6-18 a) J-V curves of HTM free devices treated with AASA and untreated. b) Schematic of HTM free device

Figure 6-18 shows the results of treated and untreated HTM champion devices, utilising a i-n architecture. The untreated device has an expectantly low PCE of 3.6 %, caused primarily by a lack of J_{sc}. This is a typical result for an HTM free device, as the extraction of holes becomes problematic. This study's previous measurements indicated that the Fermi level of the untreated perovskite nearly matches that of the ITO. Therefore, there would little energetic offset to drive the extraction of holes. Conversely, the AASA treated device shows a much higher PCE of 11.9 %, a result of a large increase in J_{sc}. This three-fold increase in PCE suggests that the extraction of holes is at least partially remedied by the AASA treatment. The result also vindicates this study's hypothesis of more favourable band

bending, due to a more mid band Fermi level. However, the cells still do not reach the maximum PCE observed in the standard devices, suggesting that there are still some barriers to hole extraction.

In conclusion, AASA could be used to produce reasonably efficient HTM free devices by creating more favourable band offsets. This again shows how this method can be used to potentially enable lower cost OMHP devices.

6.8.2 AASA with mixed composition OMHP

To test the applicability of AASA on different compositions three common mixed cation/halide perovskites that are utilised within the McLachan research group were trialled. The device architecture was kept the same, utilising PTPD and PCBM as the HTM and ETL layers. The details of fabrication and composition is detailed in section 3.3.6. Figure 6-19 shows champion device J-V curves of treated and untreated mixed composition devices.

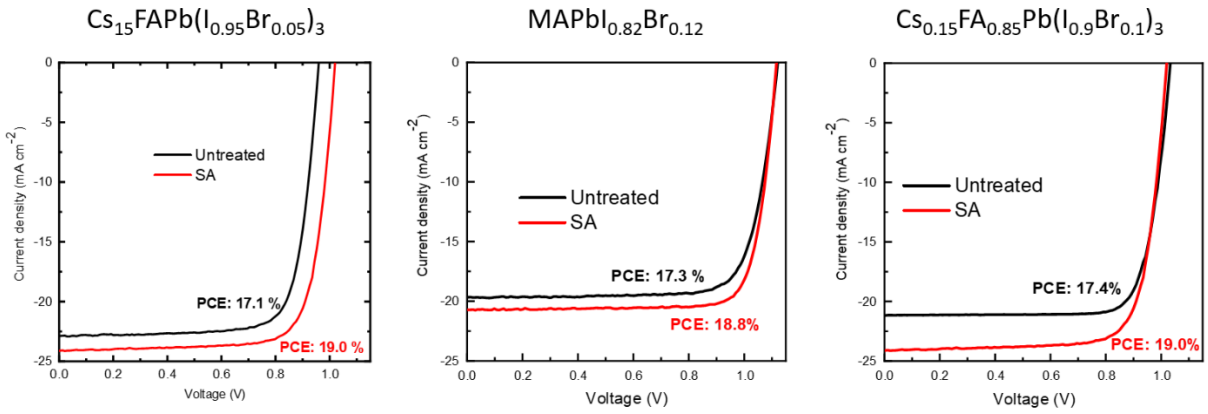


Figure 6-19 Champion J-V curves of AASA treated and untreated devices utilising mixed composition OMHP's. a) J-V curve of film utilsing $Cs_{15}FAPb(I_{0.95}Br_{0.05})_3$. a) J-V curve of film utilsing $MAPb(I_{0.82}Br_{0.12})_3$. a) J-V curve of film utilsing $Cs_{0.15}FA_{0.85}Pb(I_{0.9}Br_{0.1})_3$.

Here it can be seen that the AASA has the expected effect with a similar uplift of PCE visible for every example. Interestingly, all compositions show an uplift in J_{sc}, suggesting that the mechanism of improvement is like that of the MAPI based devices. This gives strong evidence for the cross-applicability of the AASA treatment.

6.8.3 Future work

To further evaluate the versatility of AASA, the technique could be applied to a variety of different architectures. The work in this study has primarily focused on the use of OMHP devices utilising the inverted p-i-n architecture structure, however this technique should be evaluated using conventional n-i-p devices. It is expected that these devices would also show improvements, however the impact of the treatment may be different. More unusual architectures such as the mesostructured carbon-

based cells should also be trialled. As these cells use a line-processable technology, AASA could be easily incorporated into the technology and be used to boost performance to acceptable levels.

As AASA is a potentially scalable technique it should be tested on perovskite devices that utilise scalable deposition methods. Currently cells that use CVD, spray coating, slot-die coating or thermal evaporation are yet to match the performance of spin-coated analogues. Therefore, AASA could provide a facile route to scalable produced high performance OMHP devices.

7 SUMMARY, CONCLUSIONS AND RESEARCH OUTCOMES

7.1 BACKGROUND AND AIMS

As OMHPs research has matured over the last decade, one of the key barriers to mass adoption is the difficulty in scalably manufacturing these materials. To date, there has been a large focus on developing scalable methods, with many different technologies emerging as potential candidates. Some examples include Inkjet, spray-coating, slot die coating, thermal evaporation and CVD. Whilst scalable, so far none of these technologies has yet managed to reach the same record efficiencies as devices based on spin-coating processes. Therefore, developing new alternative processing techniques that may help realise scalable OMHP production is of vital importance.

One such alternative deposition technique is AACVD, which is a CVD based technique that utilises aerosols to deliver precursor material. This technique has numerous advantages, primarily as it is a low-cost and low complexity technique. OMHPs have been fabricated using this technique, however, most studies have been limited to rudimentary material characterisation. To date there has been little focus on the intrinsic properties of AACVD films, or the fabrication of working devices utilising this technique.

Therefore, the aim of this study was to further develop the AACVD method, with the ultimate goal of producing the first working OMHP device utilising an AACVD deposited active layer. Moreover, it was also hoped that by studying the properties of films deposited via this technique, how the deposition technique affected intrinsic material properties could be investigated.

7.2 RESEARCH OUTCOMES

7.2.1 Chapter 3

In chapter 3 this study utilised the previously developed 2-step AACVD method to deposit perovskite films. As this method tends to produce overly thick films (>1 µm), it is unsuitable for PV device fabrication. Therefore, it was hoped that by understanding how these films form and their properties, an attempt could be made to try and improve the system to make PV devices.

Film formation using XRD, SEM and optical absorption measurements was observed. From this data this study was able to observe the growth of the precursor film, which showed island growth-like characteristics, forming large islands that only coalesce once a > 1 µm thickness is reached. This therefore is the origin of the thickness limitation. Further observations show that the final film is formed via a deconstruction-reconstruction type process, which converts the precursor PbI_2 to MAPI.

Moreover, it was shown that the final morphology bears very little resemblance to the precursor morphology.

These films were then analysed in depth using a variety of characterisation techniques to determine the films' intrinsic properties. XRD measurements revealed that the films are slightly different from spin-coated counterparts. The crystals within the film showed less preferential orientation and lattice parameters indicated a more tetragonal crystal structure. By conducting XRD measurements at elevated temperatures, this study was able to deduce the thermal expansion coefficient of the film. Furthermore, by conducting isothermal XRD measurements the thermal stability of the material was evaluated. Using the Mittemeijer solid state reaction model the E_a of PbI_2 formation due to degradation was determined. The results show that the 2-step AACVD films are more temperature resistant, something that is common trait of films deposited by conventional CVD.

This study then proceeded to probe the optoelectronic properties of these films, to both ascertain and verify the properties. Fortunately, due to the thickness of the films, it was possible to apply the ToF technique to measure the charge carrier mobility. During the measurements, artefacts in the measurement that were potentially related to the ion migration were discovered. This led to the development of a new measurement protocol, which applies a pulsed bias to the sample. Using this this study was able to show the decoupling of the ionic and electronic signals. This allowed not only for the determination of charge carrier mobilities, but also indicated at what time scales the ionic contribution occur. These results were then contrasted against Hall effect measurements, which show similar mobility values, further validating the results. By virtue of the Hall measurement technique, this study was also able to extract key electrical properties of the films, which approached values of single crystal measurements. Additionally, by combining optical, Kelvin probe and APS measurements, the energy diagram of the films was determined.

This data indicates that the material itself is comparable to that of MAPI deposited via other methods, in some cases matching single crystal values. Therefore, it can be inferred that the MAPI deposited via AACVD is of high quality. Lastly, potential applications for these thick films in thermo electric and radiation detection applications were shown.

7.2.2 Chapter 4

In chapter 4, a new precursor solution composed of $Pb(Ac)_2{\cdot}3H_2O$ dissolved in MeOH was developed to form the precursor film. This allowed for production of thinner films, more suitable for PV applications. The films were characterised using SEM, XRD, optical absorption spectroscopy, Kelvin probe and APS measurements. All results indicated that the resulting MAPI was of a high quality and comparable to that of spin coated films. Moreover, as this method utilises MeOH as the common

solvent throughout the deposition, it is one of the few reported synthesis processes that utilises entirely green solvents. This makes it a potentially attractive method for scalable manufacturing.

By optimising parameters to produce higher quality films, this study was then able to incorporate these films into working devices. However, the device performance was low, with the best performing device achieving 2.89%. It was then identified that the potential shortcoming of the device is caused by the rough nature of the deposited MAPI film; this created interfacial issues with the thin layer of organic HTM. This led to the application of a thicker spray coated layer of CuSCN, which resulted in a slightly improved PCE of 5.4%. Whilst these results are quite low in comparison to record efficiencies for OMHP's, these are the first reported devices that utilise an AACVD deposited OMHP active layer. Furthermore, these are the highest reported efficiencies using an AACVD active layer of any material.

To further understand the deposition process, this study looked at how the film formed. By removing substrates from the reactor half way during the deposition and by conducting XRD, SEM and optical absorption measurements, the formation of a species was tracked. It was discovered that the precursor $Pb(Ac)_2$ film transforms into an intermediate PbI_2 film upon exposure to MAI. Upon continued exposure the final MAPI film is finally formed. The large density changes that the film undergo during this process is the likely origin of the surface roughness in the final MAPI film.

As this method splits the metal and halide sources between the first and second step, it potentially makes it more flexible in terms of producing other compositions. To test this, MAI was substituted with MABr in the second step, whilst keeping most parameters the same. This resulted in the successful deposition of MAPbBr, which was confirmed using XRD and optical absorption measurements. Therefore, the results show that this is indeed a relatively flexible technique.

7.2.3 Chapter 5

The focus of chapter 5 was to utilise the aerosol delivery system within the AACVD setup to treat existing films with a solvent aerosol. This was termed aerosol-assisted solvent annealing (AASA). As the flow of aerosol can be carefully controlled within the system, it was thought to be a more controllable way to solvent anneal OMHP films.

To develop the technique, spin-coated films of MAPI were placed into the reactor and treated with aerosolised DMF at different flow rates and exposure times. SEM images revealed that the treatment induced the expected grain growth and the formation of a monolithic grain structure through the thickness of the film. This was corroborated by XRD measurements, which indicated higher crystallinity and a more contracted lattice. Furthermore, it was revealed that the tetragonality of the lattice was increased after the treatment, evidenced by more visible peak splitting in the XRD pattern.

Treated films were then incorporated into devices, which showed significant improvements in the average PCE and reduced the distribution of device performance. These results suggested that the treatment can be used to normalize the device efficiency, making it an attractive proposition as a more controllable post-process treatment.

To understand the origin of the device performance, the films were measured using a variety of optoelectronic and material characterisation techniques. STEM imaging corroborated this study's previous SEM observations. However, they also revealed inhomogeneity in the untreated films, which were not present after treatment. Using the EDS functionality in STEM, it was possible to evaluate the compositional variation across the cross-section of the film. The results revealed that the AASA had homogenised the compositional variation across the film, thereby reducing potential defect sites that would degrade cell performance.

To investigate the effect that this compositional change had on the film, KPFM measurements were used to probe the work function of the film. It was revealed that the treated films have a more intrinsic doping level with the Fermi level shifting to a more mid band position. This is what would be expected from a film with a more even composition. This shift in Fermi level would also create more favourable band bending within a device, allowing for more effective charge carrier collection. Using PL and TRPL measurements it was possible to show that the number of trap states was significantly reduced after the treatment. Moreover, by measuring the perovskite films in contact with either ETL or HTM, improved charge carrier injection in treated films was demonstrated. This again corroborates this study's other findings.

As AASA is a potentially scalable technique, it was useful to validate its effectiveness over larger areas. To do this, several substrates were placed along the length of the reactor and the average grain size across several positions was measured. These results were then contrasted with a conventional petri dish solvent annealing method. The results showed that the AASA led to a more even distribution of grain sizes, whereas the petri dish method showed a large variation across the substrate area. To further validate these results, this experiment was repeated and used to fabricate a set of devices. The results corroborated the previous findings, with the device performance being more consistent across the AASA treated substrates.

Due to these promising results, this study then turned to application of AASA on large area devices. It was hoped that the AASA treatment can mitigate the performance loss that is associated with area scaling. To evaluate this, substrates containing one small and one large electrode were utilised. This allowed for comparison of the area effect per spin coated substrate. As expected, the AASA treated devices showed better area scaling than the untreated counterparts, with only a 6% reduction in PCE

vs. 11%. These results show that AASA can not only treat films more evenly over larger areas but can also be used to improve the performance of larger area devices.

The influence of parental film thickness was also investigated. By applying AASA on 900 nm and 1300 nm perovskite films, this study was able to show that the effect still produces a monolithic crystal structure through the thickness of the films. Likewise, XRD measurements showed a similar trend of lattice volume contraction, as seen in the thin films. Devices fabricated using the treated films show a significant increase in PCE and a narrower distribution of performances. Moreover, the 900 nm film showed a champion efficiency of 20.68 %, making it competitive with state-of-the-art OMHP devices. This shows that AASA can enable the practical application of thicker active layers within a device, which could potentially boost low light performance of OMHP devices. Furthermore, by enabling higher device performance with thicker active layers, AASA can be potentially used to relax the optimal thickness requirements. This would allow for more facile large-scale production of OMHP.

As stability is an ongoing concern in OMHPs, it was important to ensure that AASA does not have a detrimental effect on device lifetimes. XRD measurements of films aged in ambient conditions revealed that AASA has a positive effect on stability. After 48 hours, the treated films showed less PbI_2 present than the corresponding untreated film. To test the effect on device stability, MPP tracking was used to measure device performance decline over time. Measurements were taken in both ambient and nitrogen atmospheres, and in both cases the AASA treated devices showed improved stability. In N_2 the treated devices have shown only a 5% PCE drop off after 490 hours, whereas untreated devices suffered a 5% PCE drop after only 45 hours. These result demonstrate that the healing effect of the AASA on the perovskite can significantly improve the longevity of devices, most probably a result of the improved local stoichiometry and lower number of defects.

To test the versatility of AASA this study attempted different device architectures and OMHP compositions. This method was tested on HTM free devices, which showed a significant improvement in performance, with the PCE increasing from 3.6% to 11.9% due to a large J_{sc} increase. This performance increase was attributed to more favourable energy band alignments, due to the more intrinsic nature of the MAPI film after the treatment. As previously stated, the Fermi level of the treated films are shallower, being closer to the mid band position. This means that when contacted with the ITO there would be more favourable band bending, allowing for charge to be extracted more efficiently. These results therefore support this study's initial KPFM measurements. Moreover, this shows the potential of using AASA to remove the requirement of an HTM layer, which is significant as these are some of the most expensive materials used within OMHP devices.

This study further probed the versatility by testing the AASA on mixed composition OMHP devices. Three different compositions were trialled, all of which showed an improvement after the AASA treatment. This is strong evidence to show that the AASA method can be used to treat a variety of OMHP compositions.

7.3 CONCLUSION

In summary, this study has successfully advanced the field of AACVD of OMHPs by elucidating film formation, key material properties and the fabrication of working devices. Therefore, the goals set out in this project have been successfully achieved. Additionally, the AASA treatment technique was developed, which has shown great potential in improving the morphology, crystallinity, performance and stability of already deposited OMHP films.

8 REFERENCES

1. NREL. Best Research-Cell Efficiency Chart | Photovoltaic Research | NREL. *National Renewable Energy Laboratory* https://www.nrel.gov/pv/cell-efficiency.html (2019).
2. Powell, M. J. & Carmalt, C. J. Aerosols: A Sustainable Route to Functional Materials. *Chem. - A Eur. J.* **23**, 15543–15552 (2017).
3. Ritchie, H. & Roser, M. Energy Production & Changing Energy Sources. *Our World Data* (2019).
4. BP. 67 th edition Contents is one of the most widely respected. *Stat. Rev. World Energy* (2018).
5. Smil, V. *Energy : a beginner's guide*.
6. Trenberth, K. E., Fasullo, J. T. & Kiehl, J. Earth's global energy budget. *Bull. Am. Meteorol. Soc.* (2009) doi:10.1175/2008BAMS2634.1.
7. Ewald, F., Zinner, T., Kölling, T. & Mayer, B. Remote sensing of cloud droplet radius profiles using solar reflectance from cloud sides – Part 1: Retrieval development and characterization. *Atmos. Meas. Tech.* (2019) doi:10.5194/amt-12-1183-2019.
8. Coley, P. F. & Jonas, P. R. Back to basics: Clouds and the earth's radiation budget. *Weather* (1999) doi:10.1002/j.1477-8696.1999.tb06428.x.
9. Loster, M. Total Primary Energy Supply — From Sunlight. *ez2c* 1 https://www.ez2c.de/ml/solar_land_area/ (2010).
10. Ortega, J. I., Burgaleta, J. I. & Téllez, F. Central Receiver System Solar Power Plant Using Molten Salt as Heat Transfer Fluid. *J. Sol. Energy Eng.* **130**, 024501 (2008).
11. Swanson, R. M. A vision for crystalline silicon photovoltaics. *Prog. Photovoltaics Res. Appl.* **14**, 443–453 (2006).
12. New Energy Outlook 2019 | Bloomberg New Energy Finance | Bloomberg Finance LP. *Bloomberg* https://about.bnef.com/new-energy-outlook/ (2019).
13. Philips, D. S. & Warmuth, W. Fraunhofer ISE: Photovoltaics Report, updated: 14 March 2019. *Fraunhofer ISE Photovoltaics Report, Updat. 14 March 2019* (2019).
14. Kakiage, K. *et al.* Highly-efficient dye-sensitized solar cells with collaborative sensitization by silyl-anchor and carboxy-anchor dyes. *Chem. Commun.* **51**, 15894–15897 (2015).
15. Extance, A. The reality behind solar power's next star material. *Nat. 2019 5707762* (2019).

16. Rong, Y. *et al.* Challenges for commercializing perovskite solar cells. *Science (80-.).* **361**, eaat8235 (2018).

17. De Gennes, P.-G. Recherches sur les effets de la radiation chimique de la lumiere solaire au moyen des courants electriques. *Comptes Rendus L'Academie des Sci.* (1839).

18. Adams, W. G. & Day, R. E. The Action of Light on Selenium. *Proc. R. Soc. London* **A25**, 113 (1877).

19. Einstein, A. Concerning an Heuristic Point of View Toward the Emission and Transformation of Light. *English Am. J. Phys.* (1905) doi:10.1119/1.1971542.

20. Millikan, R. A. A direct photoelectric determination of planck's 'h'. *Phys. Rev.* (1916) doi:10.1103/PhysRev.7.355.

21. Chapin, D. M., Fuller, C. S. & Pearson, G. L. A new silicon p-n junction photocell for converting solar radiation into electrical power. *Journal of Applied Physics* vol. 25 676–677 (1954).

22. Singleton, J. Band theory and electronic properties of solids. *Oxford Univ. Press* (2001) doi:10.1063/1.1537918.

23. Band gap comparison.svg. *Wikimedia* https://commons.wikimedia.org/wiki/File:Band_gap_comparison.svg (2006).

24. Serway, R. & Jewett, J. *Physics for Scientists and Engineers, Volume 5, Chapters 39-46*. (Brooks Cole, 2010).

25. WILSON, A. H. The Internal Photoelectric Effect in Crystals. *Nature* **130**, 913–915 (1932).

26. Hersch, P. & Zweibel, K. *Basic photovoltaic principles and methods*. https://www.nrel.gov/docs/legosti/old/1448.pdf (1982) doi:10.2172/5191389.

27. Andreani, L. C., Bozzola, A., Kowalczewski, P., Liscidini, M. & Redorici, L. Silicon solar cells: toward the efficiency limits. *Adv. Phys. X* **4**, 1548305 (2019).

28. Honsberg, C. & Bowden, St. Absorption Coefficient | PVEducation. https://www.pveducation.org/pvcdrom/pn-junctions/absorption-coefficient.

29. Shockley, W. & Queisser, H. J. Detailed balance limit of efficiency of p-n junction solar cells. *J. Appl. Phys.* (1961) doi:10.1063/1.1736034.

30. Nelson, J. *The physics of solar cells*. (Imperial College Press, 2003).

31. Ohl, R. Light-sensitive electric device. (1941).

32. Schubert, E. F. *Doping in III-V semiconductors*. (Cambridge University Press, 2005).

33. R Nave. Doped Semiconductors. *Hyperphysics* http://hyperphysics.phy-astr.gsu.edu/hbase/Solids/dsem.html.

34. Britt, M. Pn junction equilibrium.svg. *Wikimedia* https://commons.wikimedia.org/wiki/File:Pn_junction_equilibrium.svg (2016).

35. Böer, K. W. The pin Junction with Light. in *Survey of Semiconductor Physics* 820–835 (Springer Netherlands, 1992). doi:10.1007/978-94-011-2912-1_25.

36. Van Zeghbroeck, B. Carrier recombination and generation. *University of Boulder Colorado* https://ecee.colorado.edu/~bart/book/book/chapter2/ch2_8.htm (2007).

37. Mcevoy, A., Markvart, T. & Castañer, L. *Practical Handbook of Photovoltaics: Fundamentals and Applications: Fundamentals and Applications*. (2003). doi:10.1016/B978-0-12-385934-1.X0001-3.

38. Einstein, A. Über die von der molekularkinetischen Theorie der Wärme geforderte Bewegung von in ruhenden Flüssigkeiten suspendierten Teilchen. *Ann. Phys.* (1905) doi:10.1002/andp.19053220806.

39. Kojima, A., Teshima, K., Shirai, Y. & Miyasaka, T. Organometal halide perovskites as visible-light sensitizers for photovoltaic cells. *J. Am. Chem. Soc.* **131**, 6050–1 (2009).

40. Im, J.-H., Lee, C.-R., Lee, J.-W., Park, S.-W. & Park, N.-G. 6.5% efficient perovskite quantum-dot-sensitized solar cell. *Nanoscale* **3**, 4088–93 (2011).

41. Kim, H.-S. *et al.* Lead iodide perovskite sensitized all-solid-state submicron thin film mesoscopic solar cell with efficiency exceeding 9%. *Sci. Rep.* **2**, 591 (2012).

42. Lee, M. M., Teuscher, J., Miyasaka, T., Murakami, T. N. & Snaith, H. J. Efficient hybrid solar cells based on meso-superstructured organometal halide perovskites. *Science* **338**, 643–7 (2012).

43. Kojima, A., Ikegami, M., Teshima, K. & Miyasaka, T. Highly Luminescent Lead Bromide Perovskite Nanoparticles Synthesized with Porous Alumina Media. *Chem. Lett.* **41**, 397–399 (2012).

44. Stranks, S. D. *et al.* Electron-Hole Diffusion Lengths Exceeding 1 Micrometer in an Organometal Trihalide Perovskite Absorber. *Science (80-.).* **342**, 341–344 (2013).

45. Wehrenfennig, C., Eperon, G. E., Johnston, M. B., Snaith, H. J. & Herz, L. M. High Charge Carrier

Mobilities and Lifetimes in Organolead Trihalide Perovskites. *Adv. Mater.* **26**, 1584–1589 (2014).

46. Wolfram, T. & Ellialtioglu, S. *Electronic and Optical Properties of d-Band Perovskites*. (Cambridge University Press, 2006).

47. Weber, D. CH3NH3SnBrxI3-x (x = 0-3), ein Sn(II)-System mit kubischer Perowskitstruktur / CH3NH3SnBrxI3-x(x = 0-3), a Sn(II)-System with Cubic Perovskite Structure. *Zeitschrift für Naturforsch. B* **33**, 862–865 (1978).

48. Goldschmidt, V. M. Die Gesetze der Krystallochemie. *Naturwissenschaften* (1926) doi:10.1007/BF01507527.

49. Chen, Q. *et al.* Under the spotlight: The organic–inorganic hybrid halide perovskite for optoelectronic applications. *Nano Today* **10**, 355–396 (2015).

50. Li, C. *et al.* Formability of ABX3 (X = F, Cl, Br, I) halide perovskites. *Acta Crystallogr. B.* **64**, 702–707 (2008).

51. Bartel, C. J. *et al.* New tolerance factor to predict the stability of perovskite oxides and halides. *Sci. Adv.* **5**, eaav0693 (2019).

52. Brivio, F., Walker, A. B. & Walsh, A. Structural and electronic properties of hybrid perovskites for high-efficiency thin-film photovoltaics from first-principles. *APL Mater.* **1**, 042111 (2013).

53. Chang, Y. H., Park, C. H. & Matsuishi, K. First-principles study of the structural and the electronic properties of the lead-halide-based inorganic-organic perovskites (CH3NH3)PbX3 and CsPbX3 (X = Cl, Br, I). *J. Korean Phys. Soc.* **44**, 889–893 (2004).

54. Stoumpos, C. C. *et al.* Semiconducting tin and lead iodide perovskites with organic cations: phase transitions, high mobilities, and near-infrared photoluminescent properties. *Nat. Commun.* **6**, n/a-n/a (2015).

55. Jena, A. K., Kulkarni, A. & Miyasaka, T. Halide Perovskite Photovoltaics: Background, Status, and Future Prospects. *Chem. Rev.* **119**, 3036–3103 (2019).

56. Ogomi, Y. *et al.* CH3NH3SnxPb(1-x)I3 Perovskite Solar Cells Covering up to 1060 nm. *J. Phys. Chem. Lett.* **5**, 1004–1011 (2014).

57. Qiu, J. *et al.* All-solid-state hybrid solar cells based on a new organometal halide perovskite sensitizer and one-dimensional TiO2 nanowire arrays. *Nanoscale* **5**, 3245–8 (2013).

58. Jiang, Y., Green, M. A., Sheng, R. & Ho-Baillie, A. Room temperature optical properties of organic–inorganic lead halide perovskites. *Sol. Energy Mater. Sol. Cells* **137**, 253–257 (2015).

59. Pellet, N. *et al.* Mixed-organic-cation perovskite photovoltaics for enhanced solar-light harvesting. *Angew. Chemie - Int. Ed.* **53**, 3151–3157 (2014).

60. Koh, T. M. *et al.* Formamidinium-containing metal-halide: An alternative material for near-IR absorption perovskite solar cells. *J. Phys. Chem. C* **118**, 16458–16462 (2014).

61. Beal, R. E. *et al.* Cesium lead halide perovskites with improved stability for tandem solar cells. *J. Phys. Chem. Lett.* 746–751 (2016) doi:10.1021/acs.jpclett.6b00002.

62. Saliba, M. *et al.* Cesium-containing Triple Cation Perovskite Solar Cells: Improved Stability, Reproducibility and High Efficiency. *Energy Environ. Sci.* **9**, (2016).

63. Deschler, F. *et al.* High photoluminescence efficiency and optically pumped lasing in solution-processed mixed halide perovskite semiconductors. *J. Phys. Chem. Lett.* **5**, 1421–1426 (2014).

64. Ponseca, C. S. *et al.* Organometal halide perovskite solar cell materials rationalized: Ultrafast charge generation, high and microsecond-long balanced mobilities, and slow recombination. *J. Am. Chem. Soc.* **136**, 5189–5192 (2014).

65. Ponseca, C. S. *et al.* Organometal Halide Perovskite Solar Cell Materials Rationalized: Ultrafast Charge Generation, High and Microsecond-Long Balanced Mobilities, and Slow Recombination. *J. Am. Chem. Soc.* **136**, 5189–5192 (2014).

66. Piatkowski, P. *et al.* Unraveling Charge Carriers Generation, Diffusion, and Recombination in Formamidinium Lead Triiodide Perovskite Polycrystalline Thin Film. *J. Phys. Chem. Lett.* **7**, 204–210 (2016).

67. Herz, L. M. Charge-Carrier Mobilities in Metal Halide Perovskites: Fundamental Mechanisms and Limits. *ACS Energy Letters* (2017) doi:10.1021/acsenergylett.7b00276.

68. Chung, I. *et al.* $CsSnI_3$: Semiconductor or Metal? High Electrical Conductivity and Strong Near-Infrared Photoluminescence from a Single Material. High Hole Mobility and Phase-Transitions. *J. Am. Chem. Soc.* **134**, 8579–8587 (2012).

69. Stoumpos, C. C., Malliakas, C. D. & Kanatzidis, M. G. Semiconducting Tin and Lead Iodide Perovskites with Organic Cations: Phase Transitions, High Mobilities, and Near-Infrared Photoluminescent Properties. *Inorg. Chem.* **52**, 9019–9038 (2013).

70. Hu, Y. *et al.* Understanding the Role of Cesium and Rubidium Additives in Perovskite Solar Cells:

Trap States, Charge Transport, and Recombination. *Adv. Energy Mater.* **8**, 1703057 (2018).

71. Turren-Cruz, S.-H. *et al.* Enhanced charge carrier mobility and lifetime suppress hysteresis and improve efficiency in planar perovskite solar cells. *Energy Environ. Sci.* **11**, 78–86 (2018).

72. Rehman, W. *et al.* Charge-Carrier Dynamics and Mobilities in Formamidinium Lead Mixed-Halide Perovskites. 7938–7944 (2015) doi:10.1002/adma.201502969.

73. Zhang, F., Yang, B., Li, Y., Deng, W. & He, R. Extra long electron–hole diffusion lengths in $CH_3NH_3PbI_{3-x}Cl_x$ perovskite single crystals. *J. Mater. Chem. C* **5**, 8431–8435 (2017).

74. Bi, Y. *et al.* Charge Carrier Lifetimes Exceeding 15 µs in Methylammonium Lead Iodide Single Crystals. *J. Phys. Chem. Lett.* **7**, 923–928 (2016).

75. Brenes, R. *et al.* Metal Halide Perovskite Polycrystalline Films Exhibiting Properties of Single Crystals. *Joule* **1**, 155–167 (2017).

76. Sha, W. E. I., Ren, X., Chen, L. & Choy, W. C. H. The efficiency limit of $CH_3NH_3PbI_3$ perovskite solar cells. *Appl. Phys. Lett.* **106**, 221104 (2015).

77. Baloch, A. A. B., Hossain, M. I., Tabet, N. & Alharbi, F. H. Practical Efficiency Limit of Methylammonium Lead Iodide Perovskite ($CH_3NH_3PbI_3$) Solar Cells. *J. Phys. Chem. Lett.* **9**, 426–434 (2018).

78. Pazos-Outón, L. M., Xiao, T. P. & Yablonovitch, E. Fundamental Efficiency Limit of Lead Iodide Perovskite Solar Cells. *J. Phys. Chem. Lett.* **9**, 1703–1711 (2018).

79. Adhyaksa, G. W. P. *et al.* Carrier Diffusion Lengths in Hybrid Perovskites: Processing, Composition, Aging, and Surface Passivation Effects. *Chem. Mater.* **28**, 5259–5263 (2016).

80. Liu, Y. *et al.* Ultrahydrophobic 3D/2D fluoroarene bilayer-based water-resistant perovskite solar cells with efficiencies exceeding 22%. *Sci. Adv.* **5**, eaaw2543 (2019).

81. Chen, Y. *et al.* Design of an Inorganic Mesoporous Hole-Transporting Layer for Highly Efficient and Stable Inverted Perovskite Solar Cells. *Adv. Mater.* **30**, 1805660 (2018).

82. Wu, S. *et al.* Efficient large guanidinium mixed perovskite solar cells with enhanced photovoltage and low energy losses. *Chem. Commun.* (2019) doi:10.1039/c9cc00016j.

83. Luo, D. *et al.* Enhanced photovoltage for inverted planar heterojunction perovskite solar cells. *Science* **360**, 1442–1446 (2018).

84. Li, Y. *et al.* Hole-conductor-free planar perovskite solar cells with 16.0% efficiency. *J. Mater.*

Chem. A **3**, 18389–18394 (2015).

85. Huang, C. *et al.* Facile fabrication of highly efficient ETL-free perovskite solar cells with 20% efficiency by defect passivation and interface engineering. *Chem. Commun.* **55**, 2777–2780 (2019).

86. Zhang, F., Yang, X., Cheng, M., Wang, W. & Sun, L. Boosting the efficiency and the stability of low cost perovskite solar cells by using CuPc nanorods as hole transport material and carbon as counter electrode. *Nano Energy* **20**, 108–116 (2016).

87. Tian, C. *et al.* Oxygen management in carbon electrode for high-performance printable perovskite solar cells. *Nano Energy* **53**, 160–167 (2018).

88. Qiu, J. *et al.* All-solid-state hybrid solar cells based on a new organometal halide perovskite sensitizer and one-dimensional TiO2 nanowire arrays. *Nanoscale* **5**, 3245 (2013).

89. Kim, H.-S. *et al.* High Efficiency Solid-State Sensitized Solar Cell-Based on Submicrometer Rutile TiO_2 Nanorod and $CH_3NH_3PbI_3$ Perovskite Sensitizer. *Nano Lett.* **13**, 2412–2417 (2013).

90. Gao, X. *et al.* Enhanced photovoltaic performance of perovskite $CH_3NH_3PbI_3$ solar cells with freestanding TiO_2 nanotube array films. *Chem. Commun.* **50**, 6368–6371 (2014).

91. Bera, A. *et al.* Perovskite Oxide $SrTiO_3$ as an Efficient Electron Transporter for Hybrid Perovskite Solar Cells. *J. Phys. Chem. C* **118**, 28494–28501 (2014).

92. Okamoto, Y. & Suzuki, Y. Mesoporous $BaTiO_3$ /TiO_2 Double Layer for Electron Transport in Perovskite Solar Cells. *J. Phys. Chem. C* **120**, 13995–14000 (2016).

93. Bi, D. *et al.* Efficient luminescent solar cells based on tailored mixed-cation perovskites. *Sci. Adv.* **2**, e1501170 (2016).

94. Leijtens, T. *et al.* Overcoming ultraviolet light instability of sensitized TiO_2 with meso-superstructured organometal tri-halide perovskite solar cells. *Nat. Commun.* **4**, 2885 (2013).

95. Kim, H.-S. & Park, N.-G. Parameters Affecting I-V Hysteresis of CH3NH3PbI3 Perovskite Solar Cells: Effects of Perovskite Crystal Size and Mesoporous TiO2 Layer. *J. Phys. Chem. Lett.* Ahead of Print (2014) doi:10.1021/jz501392m.

96. Liu, P., Wang, W., Liu, S., Yang, H. & Shao, Z. Fundamental Understanding of Photocurrent Hysteresis in Perovskite Solar Cells. *Adv. Energy Mater.* **9**, 1803017 (2019).

97. Nemnes, G. A. *et al.* Normal and Inverted Hysteresis in Perovskite Solar Cells. *J. Phys. Chem. C*

121, 11207–11214 (2017).

98. Unger, E. L. *et al.* Hysteresis and transient behavior in current–voltage measurements of hybrid-perovskite absorber solar cells. *Energy Environ. Sci.* **7**, 3690–3698 (2014).

99. Gottesman, R. *et al.* Extremely slow photoconductivity response of CH3NH 3PbI3 perovskites suggesting structural changes under working conditions. *J. Phys. Chem. Lett.* **5**, 2662–2669 (2014).

100. Snaith, H. J. *et al.* Anomalous Hysteresis in Perovskite Solar Cells. *J. Phys. Chem. Lett.* **5**, 1511–1515 (2014).

101. Ravishankar, S. *et al.* Influence of Charge Transport Layers on Open-Circuit Voltage and Hysteresis in Perovskite Solar Cells. *Joule* **2**, 788–798 (2018).

102. Xiong, L. *et al.* Fully High-Temperature-Processed SnO_2 as Blocking Layer and Scaffold for Efficient, Stable, and Hysteresis-Free Mesoporous Perovskite Solar Cells. *Adv. Funct. Mater.* **28**, 1706276 (2018).

103. Zhang, Y. *et al.* Charge selective contacts, mobile ions and anomalous hysteresis in organic–inorganic perovskite solar cells. *Mater. Horizons* **2**, 315–322 (2015).

104. Meng, L., You, J., Guo, T.-F. & Yang, Y. Recent Advances in the Inverted Planar Structure of Perovskite Solar Cells. *Acc. Chem. Res.* **49**, 155–165 (2016).

105. McMeekin, D. P. *et al.* A mixed-cation lead mixed-halide perovskite absorber for tandem solar cells. *Science (80-.).* (2016) doi:10.1126/science.aad5845.

106. Tress, W., Correa Baena, J. P., Saliba, M., Abate, A. & Graetzel, M. Inverted Current-Voltage Hysteresis in Mixed Perovskite Solar Cells: Polarization, Energy Barriers, and Defect Recombination. *Adv. Energy Mater.* **6**, 1600396 (2016).

107. Wei, J. *et al.* Hysteresis Analysis Based on the Ferroelectric Effect in Hybrid Perovskite Solar Cells. *J. Phys. Chem. Lett.* **5**, 3937–3945 (2014).

108. Stroppa, A., Quarti, C., De Angelis, F. & Picozzi, S. Ferroelectric Polarization of $CH_3NH_3PbI_3$: A Detailed Study Based on Density Functional Theory and Symmetry Mode Analysis. *J. Phys. Chem. Lett.* **6**, 2223–2231 (2015).

109. Leguy, A. M. A. *et al.* The dynamics of methylammonium ions in hybrid organic–inorganic perovskite solar cells. *Nat. Commun.* **6**, 7124 (2015).

110. Chen, B., Yang, M., Priya, S. & Zhu, K. Origin of J – V Hysteresis in Perovskite Solar Cells. *J. Phys. Chem. Lett.* **7**, 905–917 (2016).

111. Wetzelaer, G.-J. A. H. *et al.* Trap-Assisted Non-Radiative Recombination in Organic-Inorganic Perovskite Solar Cells. *Adv. Mater.* **27**, 1837–1841 (2015).

112. Singh, T. *et al.* Tuning of perovskite solar cell performance via low-temperature brookite scaffolds surface modifications. *APL Mater.* **5**, 016103 (2017).

113. Eames, C. *et al.* Ionic transport in hybrid lead iodide perovskite solar cells. *Nat. Commun.* **6**, 7497 (2015).

114. Haruyama, J., Sodeyama, K., Han, L. & Tateyama, Y. First-Principles Study of Ion Diffusion in Perovskite Solar Cell Sensitizers. *J. Am. Chem. Soc.* **137**, 10048–10051 (2015).

115. Xiao, Z. *et al.* Giant switchable photovoltaic effect in organometal trihalide perovskite devices. *Nat. Mater.* **14**, 193–198 (2015).

116. Yuan, Y. *et al.* Photovoltaic Switching Mechanism in Lateral Structure Hybrid Perovskite Solar Cells. *Adv. Energy Mater.* **5**, 1500615 (2015).

117. Yuan, Y. *et al.* Electric-Field-Driven Reversible Conversion Between Methylammonium Lead Triiodide Perovskites and Lead Iodide at Elevated Temperatures. *Adv. Energy Mater.* **6**, 1501803 (2016).

118. Li, Z. *et al.* Extrinsic ion migration in perovskite solar cells. *Energy Environ. Sci.* **10**, 1234–1242 (2017).

119. Eames, C. *et al.* Ionic transport in hybrid lead iodide perovskite solar cells. *Nat. Commun.* **6**, 7497 (2015).

120. Jacobs, D. A. *et al.* Hysteresis phenomena in perovskite solar cells: the many and varied effects of ionic accumulation. *Phys. Chem. Chem. Phys.* **19**, 3094–3103 (2017).

121. Pockett, A. *et al.* Microseconds, milliseconds and seconds: deconvoluting the dynamic behaviour of planar perovskite solar cells. *Phys. Chem. Chem. Phys.* **19**, 5959–5970 (2017).

122. Bella, F. *et al.* Improving efficiency and stability of perovskite solar cells with photocurable fluoropolymers. *Science (80-.).* **354**, 203–206 (2016).

123. Tsai, H. *et al.* High-efficiency two-dimensional Ruddlesden–Popper perovskite solar cells. *Nature* **536**, 312–316 (2016).

124. Wang, Z. *et al.* Efficient ambient-air-stable solar cells with 2D–3D heterostructured butylammonium-caesium-formamidinium lead halide perovskites. *Nat. Energy* **2**, 17135 (2017).

125. Leguy, A. M. A. *et al.* Reversible Hydration of CH3NH3PbI3 in Films, Single Crystals, and Solar Cells. *Chem. Mater.* **27**, 3397–3407 (2015).

126. Leguy, A. M. A. *et al.* Reversible Hydration of $CH_3NH_3PbI_3$ in Films, Single Crystals, and Solar Cells. *Chem. Mater.* **27**, 3397–3407 (2015).

127. Eperon, G. E. *et al.* The Importance of Moisture in Hybrid Lead Halide Perovskite Thin Film Fabrication. *ACS Nano* **9**, 9380–9393 (2015).

128. Noh, J. H., Im, S. H., Heo, J. H., Mandal, T. N. & Seok, S. Il. Chemical Management for Colorful, Efficient, and Stable Inorganic–Organic Hybrid Nanostructured Solar Cells. *Nano Lett.* **13**, 1764–1769 (2013).

129. Zhang, M. *et al.* Composition-dependent photoluminescence intensity and prolonged recombination lifetime of perovskite $CH_3NH_3PbBr_{3-x}Cl_x$ films. *Chem. Commun.* **50**, 11727–11730 (2014).

130. Lee, M. M., Teuscher, J., Miyasaka, T., Murakami, T. N. & Snaith, H. J. Efficient Hybrid Solar Cells Based on Meso-Superstructured Organometal Halide Perovskites. *Science (80-.).* **338**, 643–647 (2012).

131. Holzhey, P. & Saliba, M. A full overview of international standards assessing the long-term stability of perovskite solar cells. *J. Mater. Chem. A* **6**, 21794–21808 (2018).

132. Stoumpos, C. C., Malliakas, C. D. & Kanatzidis, M. G. Semiconducting Tin and Lead Iodide Perovskites with Organic Cations: Phase Transitions, High Mobilities, and Near-Infrared Photoluminescent Properties. *Inorg. Chem.* **52**, 9019–9038 (2013).

133. Heo, J. H. *et al.* Efficient inorganic–organic hybrid heterojunction solar cells containing perovskite compound and polymeric hole conductors. *Nat. Photonics* **7**, 486–491 (2013).

134. Dualeh, A. *et al.* Effect of Annealing Temperature on Film Morphology of Organic-Inorganic Hybrid Pervoskite Solid-State Solar Cells. *Adv. Funct. Mater.* **24**, 3250–3258 (2014).

135. Dualeh, A., Gao, P., Seok, S. Il, Nazeeruddin, M. K. & Gr??tzel, M. Thermal behavior of methylammonium lead-trihalide perovskite photovoltaic light harvesters. *Chem. Mater.* **26**, 6160–6164 (2014).

136. Conings, B. *et al.* Intrinsic Thermal Instability of Methylammonium Lead Trihalide Perovskite. *Adv. Energy Mater.* **5**, 1500477 (2015).

137. Brunetti, B., Cavallo, C., Ciccioli, A., Gigli, G. & Latini, A. On the Thermal and Thermodynamic (In)Stability of Methylammonium Lead Halide Perovskites. *Sci. Rep.* **6**, 31896 (2016).

138. Kim, N.-K. *et al.* Investigation of Thermally Induced Degradation in CH3NH3PbI3 Perovskite Solar Cells using In-situ Synchrotron Radiation Analysis. *Sci. Rep.* **7**, 4645 (2017).

139. Latini, A., Gigli, G. & Ciccioli, A. A study on the nature of the thermal decomposition of methylammonium lead iodide perovskite, $CH_3NH_3PbI_3$: an attempt to rationalise contradictory experimental results. *Sustain. Energy Fuels* **1**, 1351–1357 (2017).

140. Eperon, G. E. *et al.* Formamidinium lead trihalide: a broadly tunable perovskite for efficient planar heterojunction solar cells. *Energy Environ. Sci.* **7**, 982 (2014).

141. Binek, A., Hanusch, F. C., Docampo, P. & Bein, T. Stabilization of the Trigonal High-Temperature Phase of Formamidinium Lead Iodide. *J. Phys. Chem. Lett.* **6**, 1249–1253 (2015).

142. Wang, Z., Shi, Z., Li, T., Chen, Y. & Huang, W. Stability of Perovskite Solar Cells: A Prospective on the Substitution of the A Cation and X Anion. *Angew. Chemie Int. Ed.* **56**, 1190–1212 (2017).

143. Nazarenko, O. *et al.* Guanidinium-Formamidinium Lead Iodide: A Layered Perovskite-Related Compound with Red Luminescence at Room Temperature. *J. Am. Chem. Soc.* **140**, 3850–3853 (2018).

144. Saliba, M. *et al.* Incorporation of rubidium cations into perovskite solar cells improves photovoltaic performance. *Science* **354**, 206–209 (2016).

145. Aristidou, N. *et al.* The Role of Oxygen in the Degradation of Methylammonium Lead Trihalide Perovskite Photoactive Layers. *Angew. Chemie Int. Ed.* **54**, 8208–8212 (2015).

146. Zhao, Y. & Zhu, K. Optical bleaching of perovskite (CH3NH3)PbI3 through room-temperature phase transformation induced by ammonia. *Chem. Commun. (Camb).* **50**, 1605–7 (2014).

147. Niu, G. *et al.* Study on the stability of CH 3 NH 3 PbI 3 films and the effect of post-modification by aluminum oxide in all-solid-state hybrid solar cells. *J. Mater. Chem. A* **2**, 705–710 (2014).

148. Niu, G., Guo, X. & Wang, L. Review of Recent Progress in Chemical Stability of Perovskite Solar Cells. *J. Mater. Chem. A* Advance (2015) doi:10.1039/C4TA04994B.

149. Song, J. *et al.* Low-temperature SnO_2-based electron selective contact for efficient and stable

perovskite solar cells. *J. Mater. Chem. A* **3**, 10837–10844 (2015).

150. Wang, R. *et al.* A Review of Perovskites Solar Cell Stability. *Adv. Funct. Mater.* 1808843 (2019) doi:10.1002/adfm.201808843.

151. Kato, Y. *et al.* Silver Iodide Formation in Methyl Ammonium Lead Iodide Perovskite Solar Cells with Silver Top Electrodes. *Adv. Mater. Interfaces* **2**, 1500195 (2015).

152. Domanski, K. *et al.* Not All That Glitters Is Gold: Metal-Migration-Induced Degradation in Perovskite Solar Cells. *ACS Nano* **10**, 6306–6314 (2016).

153. Zhao, J. *et al.* Is Cu a stable electrode material in hybrid perovskite solar cells for a 30-year lifetime? *Energy Environ. Sci.* **9**, 3650–3656 (2016).

154. Babayigit, A., Ethirajan, A., Muller, M. & Conings, B. Toxicity of organometal halide perovskite solar cells. *Nat. Mater.* **15**, 247–251 (2016).

155. Li, J. *et al.* Biological impact of lead from halide perovskites reveals the risk of introducing a safe threshold. *Nat. Commun.* **11**, 310 (2020).

156. Hailegnaw, B., Kirmayer, S., Edri, E., Hodes, G. & Cahen, D. Rain on methylammonium lead iodide based perovskites: Possible environmental effects of perovskite solar cells. *J. Phys. Chem. Lett.* **6**, 1543–1547 (2015).

157. Poll, C. G. *et al.* Electrochemical recycling of lead from hybrid organic–inorganic perovskites using deep eutectic solvents. *Green Chem.* **18**, 2946–2955 (2016).

158. Kadro, J. M. *et al.* Proof-of-concept for facile perovskite solar cell recycling. *Energy Environ. Sci.* **9**, 3172–3179 (2016).

159. Binek, A. *et al.* Recycling Perovskite Solar Cells to Avoid Lead Waste. *ACS Appl. Mater. Interfaces* (2016) doi:10.1021/acsami.6b03767.

160. Chen, P.-Y. *et al.* Environmentally responsible fabrication of efficient perovskite solar cells from recycled car batteries. *Energy Environ. Sci.* **7**, 3659–3665 (2014).

161. Jena, A. K., Kulkarni, A. & Miyasaka, T. Halide Perovskite Photovoltaics: Background, Status, and Future Prospects. *Chem. Rev.* **119**, 3036–3103 (2019).

162. Jeon, N. J. *et al.* Solvent engineering for high-performance inorganic-organic hybrid perovskite solar cells. *Nat. Mater.* **13**, 1–7 (2014).

163. Li, J. *et al.* Optimization of anti-solvent engineering toward high performance perovskite solar

cells. *J. Mater. Res.* **34**, 2416–2424 (2019).

164. Xiao, Z. *et al.* Solvent Annealing of Perovskite-Induced Crystal Growth for Photovoltaic-Device Efficiency Enhancement. *Adv. Mater.* **26**, 6503–6509 (2014).

165. Liu, J. *et al.* Improved Crystallization of Perovskite Films by Optimized Solvent Annealing for High Efficiency Solar Cell. *ACS Appl. Mater. Interfaces* **7**, 24008–24015 (2015).

166. Luo, J., Qiu, R. Z., Yang, Z. S., Wang, Y. X. & Zhang, Q. F. Mechanism and effect of γ-butyrolactone solvent vapor post-annealing on the performance of a mesoporous perovskite solar cell. *RSC Adv.* **8**, 724–731 (2018).

167. Wang, B., Wong, K. Y., Yang, S. & Chen, T. Crystallinity and defect state engineering in organo-lead halide perovskite for high-efficiency solar cells. *J. Mater. Chem. A* **4**, 3806–3812 (2016).

168. Mou, J. *et al.* Butanol-assisted solvent annealing of CH3NH3PbI3 film for high-efficient perovskite solar cells. *J. Mater. Sci. Mater. Electron.* **30**, 746–752 (2019).

169. Chen, Q. *et al.* Planar Heterojunction Perovskite Solar Cells via Vapor-Assisted Solution Process. *J. Am. Chem. Soc.* **136**, 622–625 (2014).

170. Yin, J. *et al.* Vapor-assisted crystallization control toward high performance perovskite photovoltaics with over 18% efficiency in the ambient atmosphere. *J. Mater. Chem. A* **4**, 13203–13210 (2016).

171. Leyden, M. R. *et al.* High performance perovskite solar cells by hybrid chemical vapor deposition. *J. Mater. Chem. A* **2**, 18742–18745 (2014).

172. Luo, P. *et al.* Chemical Vapor Deposition of Perovskites for Photovoltaic Application. *Advanced Materials Interfaces* (2017) doi:10.1002/admi.201600970.

173. Tavakoli, M. M. *et al.* Fabrication of efficient planar perovskite solar cells using a one-step chemical vapor deposition method. *Sci. Rep.* **5**, 14083 (2015).

174. Lewis, D. J. & O'Brien, P. Ambient pressure aerosol-assisted chemical vapour deposition of (CH3NH3)PbBr3, an inorganic-organic perovskite important in photovoltaics. *Chem. Commun.* **50**, 6319–21 (2014).

175. Bhachu, D. S. *et al.* Scalable route to $CH_3NH_3PbI_3$ perovskite thin films by aerosol assisted chemical vapour deposition. *J. Mater. Chem. A* **3**, 9071–9073 (2015).

176. Nishinaka, H. & Yoshimoto, M. Solution-based mist CVD technique for CH 3 NH 3 Pb(Br 1− x Cl

x) 3 inorganic–organic perovskites. *Jpn. J. Appl. Phys.* **55**, 100308 (2016).

177. Chen, S. *et al.* A simple, low-cost CVD route to high-quality $CH_3NH_3PbI_3$ perovskite thin films. *CrystEngComm* **17**, 7486–7489 (2015).

178. Afzaal, M., Salhi, B., Al-Ahmed, A., Yates, H. M. & Hakeem, A. S. Surface-related properties of perovskite $CH_3NH_3PbI_3$ thin films by aerosol-assisted chemical vapour deposition. *J. Mater. Chem. C* 8366–8370 (2017) doi:10.1039/C7TC02968C.

179. Ke, C.-R. *et al.* Air-Stable Methylammonium Lead Iodide Perovskite Thin Films Fabricated via Aerosol-Assisted Chemical Vapor Deposition from a Pseudohalide $Pb(SCN)_2$ Precursor. *ACS Appl. Energy Mater.* acsaem.9b01124 (2019) doi:10.1021/acsaem.9b01124.

180. Aamir, M. *et al.* Controlled synthesis of all inorganic CsPbBr2I perovskite by non-template and aerosol assisted chemical vapour deposition. *Mater. Lett.* **190**, 244–247 (2017).

181. Ke, J. C. *et al.* Ambient-air-stable inorganic Cs 2 SnI 6 double perovskite thin films via aerosol-assisted chemical vapour deposition. *J. Mater. Chem. A* (2018) doi:10.1039/C8TA03133A.

182. K. L. Choy. Chemical vapour deposition of coatings. *Prog. Mater. Sci.* **48**, 57–170 (2003).

183. Omura, K., Veluchamy, P., Tsuji, M., Nishio, T. & Murozono, M. A Pyrosol Technique to Deposit Highly Transparent, Low-Resistance SnO[sub 2]:F Thin Films from Dimethyltin Dichloride. *J. Electrochem. Soc.* **146**, 2113 (1999).

184. Dobkin, D. M. & Zuraw, M. K. *Principles of chemical vapor deposition*. (Kluwer Academic Publishers, 2003).

185. Rečnik, A., Stanković, N. & Daneu, N. Topotaxial reactions during the genesis of oriented rutile/hematite intergrowths from Mwinilunga (Zambia). *Contrib. to Mineral. Petrol.* **169**, 19 (2015).

186. Venables, J. *Introduction to surface and thin film processes*. (Cambridge University Press, 2000).

187. Flanker. File:Laminar boundary layer scheme.svg - Wikipedia. *Wikimedia* https://en.wikipedia.org/wiki/File:Laminar_boundary_layer_scheme.svg (2008).

188. Park, J.-R., Song, Y. K., Rie, K.-T. & Gebauer, A. Hard coating by plasma-assisted CVD on plasma nitrided stellite. *Surf. Coatings Technol.* **98**, 1329–1335 (1998).

189. Lee, N. H., Park, J. H. & Choi, K. H. A study on fuel spray of spark-ignited direct injection engine using laser image technology. *KSME Int. J.* **13**, 286–293 (1999).

190. Lee, D. O. Aerosols, an industrial and environmental science, G. M. Hidy, Academic Press, London, 1984. *J. Climatol.* (1985) doi:10.1002/joc.3370050214.

191. May, K. R. The collison nebulizer: Description, performance and application. *J. Aerosol Sci.* (1973) doi:10.1016/0021-8502(73)90006-2.

192. Lang, R. J. Ultrasonic Atomization of Liquids. *J. Acoust. Soc. Am.* **34**, 6–8 (1962).

193. Filipovic, L. Topography Simulation of Novel Processing Techniques. (Technischen Universität Wien Fakultät für Elektrotechnik und Informationstechnik, 2012).

194. Hatch, S. M., Briscoe, J. & Dunn, S. Improved CuSCN–ZnO diode performance with spray deposited CuSCN. *Thin Solid Films* **531**, 404–407 (2013).

195. van der Pauw, L. J. A method of measuring the resistivity and Hall coefficient on lamellae of arbitrary shape. *Philips Technical Review* (1958) doi:537.723.1:53.081.7+538.632:083.9.

196. Kosasih, F. U. & Ducati, C. Characterising degradation of perovskite solar cells through in-situ and operando electron microscopy. *Nano Energy* **47**, 243–256 (2018).

197. Peña, F. de la *et al.* hyperspy/hyperspy v1.4.1. (2018) doi:10.5281/ZENODO.1469364.

198. Chen, S. Thin Films Deposition for Energy Efficient Windows and Solar Cells. (Queen Mary University of London, 2016).

199. Brenner, T. M. *et al.* Conversion of Single Crystalline PbI2 to CH3 NH3 PbI3 : Structural Relations and Transformation Dynamics. *Chem. Mater.* **28**, 6501–6510 (2016).

200. National Center for Biotechnology Information. PubChem Database. Lead iodide, CID=24931. https://pubchem.ncbi.nlm.nih.gov/compound/Lead-iodide.

201. Stoumpos, C. C., Malliakas, C. D. & Kanatzidis, M. G. Semiconducting Tin and Lead Iodide Perovskites with Organic Cations: Phase Transitions, High Mobilities, and Near-Infrared Photoluminescent Properties. *Inorg. Chem.* **52**, 9019–9038 (2013).

202. Ahuja, R. *et al.* Electronic and optical properties of lead iodide. *J. Appl. Phys.* **92**, 7219–7224 (2002).

203. Hu, Q. *et al.* In situ dynamic observations of perovskite crystallisation and microstructure evolution intermediated from [PbI 6] 4- cage nanoparticles. *Nat. Commun.* **8**, 15688 (2017).

204. Liu, H. *et al.* A facile room temperature solution synthesis of SnO_2 quantum dots for perovskite solar cells. *J. Mater. Chem. A* **7**, 10636–10643 (2019).

205. Quarti, C. *et al.* Structural and optical properties of methylammonium lead iodide across the tetragonal to cubic phase transition: implications for perovskite solar cells. *Energy Environ. Sci.* **9**, 155–163 (2016).

206. Baikie, T. *et al.* Synthesis and crystal chemistry of the hybrid perovskite (CH3NH3)PbI3 for solid-state sensitised solar cell applications. *J. Mater. Chem. A* **1**, 5628 (2013).

207. Jacobsson, T. J., Schwan, L. J., Ottosson, M., Hagfeldt, A. & Edvinsson, T. Determination of Thermal Expansion Coefficients and Locating the Temperature-Induced Phase Transition in Methylammonium Lead Perovskites Using X-ray Diffraction. *Inorg. Chem.* **54**, 10678–10685 (2015).

208. Davidson, M. (Imperial C. Understanding Environmentally Induced Degradation in Methylammonium Lead Iodide Thin Films for Solar Cell Devices. (Imperial College, 2018).

209. Liu, F., Sommer, F., Bos, C. & Mittemeijer, E. J. Analysis of solid state phase transformation kinetics: models and recipes. *Int. Mater. Rev.* **52**, 193–212 (2007).

210. Mittemeijer, E. J. Analysis of the kinetics of phase transformations. *J. Mater. Sci.* **27**, 3977–3987 (1992).

211. Pammi, S. V. N., Lee, H.-W., Eom, J.-H. & Yoon, S.-G. Predominant Stable $MAPbI_3$ Films Deposited via Chemical Vapor Deposition: Stability Studies in Illuminated and Darkened States Coupled with Temperature under an Open-Air Atmosphere. *ACS Appl. Energy Mater.* **1**, 3301–3312 (2018).

212. Leyden, M. R., Jiang, Y. & Qi, Y. Chemical vapor deposition grown formamidinium perovskite solar modules with high steady state power and thermal stability. *J. Mater. Chem. A* **4**, 13125–13132 (2016).

213. Zhu, C. *et al.* Strain engineering in perovskite solar cells and its impacts on carrier dynamics. *Nat. Commun.* **10**, 815 (2019).

214. Chen, Y., Peng, J., Su, D., Chen, X. & Liang, Z. Efficient and balanced charge transport revealed in planar perovskite solar cells. *ACS Appl. Mater. Interfaces* **7**, 4471–4475 (2015).

215. Wang, J. *et al.* Performance enhancement of perovskite solar cells with Mg-doped TiO2 compact film as the hole-blocking layer. *Appl. Phys. Lett.* **106**, 121104 (2015).

216. De Wolf, S. *et al.* Organometallic halide perovskites: Sharp optical absorption edge and its relation to photovoltaic performance. *J. Phys. Chem. Lett.* **5**, 1035–1039 (2014).

217. Ball, J. M. *et al.* Optical properties and limiting photocurrent of thin-film perovskite solar cells. *Energy Environ. Sci.* **8**, 602–609 (2015).

218. Yu, H., Lu, H., Xie, F., Zhou, S. & Zhao, N. Native Defect-Induced Hysteresis Behavior in Organolead Iodide Perovskite Solar Cells. *Adv. Funct. Mater.* **26**, 1411–1419 (2016).

219. Senocrate, A. *et al.* The Nature of Ion Conduction in Methylammonium Lead Iodide: A Multimethod Approach. *Angew. Chemie Int. Ed.* **56**, 7755–7759 (2017).

220. Delugas, P., Caddeo, C., Filippetti, A. & Mattoni, A. Thermally Activated Point Defect Diffusion in Methylammonium Lead Trihalide: Anisotropic and Ultrahigh Mobility of Iodine. *J. Phys. Chem. Lett.* **7**, 2356–2361 (2016).

221. Herz, L. M. Charge-Carrier Mobilities in Metal Halide Perovskites: Fundamental Mechanisms and Limits. *ACS Energy Lett.* **2**, 1539–1548 (2017).

222. Yang, D., Ming, W., Shi, H., Zhang, L. & Du, M.-H. Fast Diffusion of Native Defects and Impurities in Perovskite Solar Cell Material $CH_3NH_3PbI_3$. *Chem. Mater.* **28**, 4349–4357 (2016).

223. Yang, T.-Y., Gregori, G., Pellet, N., Grätzel, M. & Maier, J. The Significance of Ion Conduction in a Hybrid Organic-Inorganic Lead-Iodide-Based Perovskite Photosensitizer. *Angew. Chemie Int. Ed.* **54**, 7905–7910 (2015).

224. Yang, W. S. *et al.* Iodide management in formamidinium-lead-halide–based perovskite layers for efficient solar cells. *Science (80-.).* **356**, 1376–1379 (2017).

225. Saidaminov, M. I. *et al.* Planar-integrated single-crystalline perovskite photodetectors. *Nat. Commun.* **6**, 8724 (2015).

226. Shi, D. *et al.* Solar cells. Low trap-state density and long carrier diffusion in organolead trihalide perovskite single crystals. *Science* **347**, 519–22 (2015).

227. Dong, Q. *et al.* Electron-hole diffusion lengths > 175 μm in solution-grown $CH_3NH_3PbI_3$ single crystals. *Science (80-.).* **347**, 967–970 (2015).

228. Xiao, Z. *et al.* Efficient, high yield perovskite photovoltaic devices grown by interdiffusion of solution-processed precursor stacking layers. *Energy Environ. Sci.* **7**, 2619–2623 (2014).

229. Frolova, L. A., Dremova, N. N. & Troshin, P. A. The chemical origin of the p-type and n-type doping effects in the hybrid methylammonium–lead iodide ($MAPbI_3$) perovskite solar cells. *Chem. Commun.* **51**, 14917–14920 (2015).

230. Wang, Q. *et al.* Qualifying composition dependent *p* and *n* self-doping in $CH_3NH_3PbI_3$. *Appl. Phys. Lett.* **105**, 163508 (2014).

231. Peng, J., Chen, Y., Zheng, K., Pullerits, T. & Liang, Z. Insights into charge carrier dynamics in organo-metal halide perovskites: from neat films to solar cells. *Chem. Soc. Rev.* **46**, 5714–5729 (2017).

232. Chen, Y. *et al.* Extended carrier lifetimes and diffusion in hybrid perovskites revealed by Hall effect and photoconductivity measurements. *Nat. Commun.* **7**, 12253 (2016).

233. Hellmann, T. *et al.* The difference in electronic structure of MAPI and MASI perovskites and its effect on the interface alignment to the HTMs spiro-MeOTAD and CuI. *J. Mater. Chem. C* **7**, 5324–5332 (2019).

234. Harwell, J. R. *et al.* Probing the energy levels of perovskite solar cells via Kelvin probe and UV ambient pressure photoemission spectroscopy. *Phys. Chem. Chem. Phys.* **18**, 19738–19745 (2016).

235. Mettan, X. *et al.* Tuning of the Thermoelectric Figure of Merit of $CH_3NH_3MI_3$ (M═Pb,Sn) Photovoltaic Perovskites. *J. Phys. Chem. C* **119**, 11506–11510 (2015).

236. Ye, T. *et al.* Ultra-high Seebeck coefficient and low thermal conductivity of a centimeter-sized perovskite single crystal acquired by a modified fast growth method. *J. Mater. Chem. C* **5**, 1255–1260 (2017).

237. Elbaz, G. A. *et al.* Phonon Speed, Not Scattering, Differentiates Thermal Transport in Lead Halide Perovskites. *Nano Lett.* **17**, 5734–5739 (2017).

238. Liu, T. *et al.* Unusual thermal boundary resistance in halide perovskites: A way to tune ultralow thermal conductivity for thermoelectrics. *ACS Appl. Mater. Interfaces* acsami.9b14174 (2019) doi:10.1021/acsami.9b14174.

239. Wei, H. & Huang, J. Halide lead perovskites for ionizing radiation detection. *Nat. Commun.* **10**, 1066 (2019).

240. Gao, L. & Yan, Q. Recent Advances in Lead Halide Perovskites for Radiation Detectors. *Sol. RRL* solr.201900210 (2019) doi:10.1002/solr.201900210.

241. Aldibaja, F. K. *et al.* Effect of different lead precursors on perovskite solar cell performance and stability. *J. Mater. Chem. A* **3**, 9194–9200 (2015).

242. Kim, M. K. *et al.* Effective control of crystal grain size in $CH_3NH_3PbI_3$ perovskite solar cells

with a pseudohalide Pb(SCN) $_2$ additive. *CrystEngComm* **18**, 6090–6095 (2016).

243. Zhang, W. *et al.* Ultrasmooth organic–inorganic perovskite thin-film formation and crystallization for efficient planar heterojunction solar cells. *Nat. Commun.* **6**, 6142 (2015).

244. Wu, F. & Zhu, L. Fast preparation of compact and stable perovskite films derived from PbCl2 and Pb(Ac)2·3H2O mixed-lead-halide precursors. *Sol. Energy Mater. Sol. Cells* **167**, 1–6 (2017).

245. Guo, Z. *et al.* Improving the performance of lead acetate-based perovskite solar cells *via* solvent vapor annealing. *CrystEngComm* **21**, 4753–4762 (2019).

246. Martínez-Casado, F. J. *et al.* Unraveling the Decomposition Process of Lead(II) Acetate: Anhydrous Polymorphs, Hydrates, and Byproducts and Room Temperature Phosphorescence. *Inorg. Chem.* **55**, 8576–8586 (2016).

247. Wu, M., Cubaud, T. & Ho, C. M. Scaling law in liquid drop coalescence driven by surface tension. *Phys. Fluids* (2004) doi:10.1063/1.1756928.

248. Kahl, H., Wadewitz, T. & Winkelmann, J. Surface tension of pure liquids and binary liquid mixtures. *J. Chem. Eng. Data* (2003) doi:10.1021/je0201323.

249. Thilakan, P. & Kumar, J. Investigations on the Annealing Effects on Reactively Deposited ITO Thin Films. *Phys. status solidi* **160**, 97–104 (1997).

250. Ahmed, N. M. *et al.* The effect of post annealing temperature on grain size of indium-tin-oxide for optical and electrical properties improvement. *Results Phys.* **13**, 102159 (2019).

251. Du, T. *et al.* Elucidating the Origins of Subgap Tail States and Open-Circuit Voltage in Methylammonium Lead Triiodide Perovskite Solar Cells. *Adv. Funct. Mater.* (2018) doi:10.1002/adfm.201801808.

252. Wijeyasinghe, N. *et al.* Copper(I) Thiocyanate (CuSCN) Hole-Transport Layers Processed from Aqueous Precursor Solutions and Their Application in Thin-Film Transistors and Highly Efficient Organic and Organometal Halide Perovskite Solar Cells. *Adv. Funct. Mater.* **27**, 1701818 (2017).

253. Hepp, A. F. *et al.* Aerosol-assisted chemical vapor deposited thin films for space photovoltaics. *Collect. Tech. Pap. - 4th Int. Energy Convers. Eng. Conf.* **1**, 100–114 (2006).

254. Chen, Y. *et al.* Control of the Nucleation and Growth of the Lead Acetate Solution Derived CH3NH3PbI3 Films Leads to Enhanced Power Conversion Efficiency. *ACS Appl. Energy Mater.* (2018) doi:10.1021/acsaem.8b00561.

255. National Center for Biotechnology Information. PubChem Database. Lead(II) acetate, CID=9317,. https://pubchem.ncbi.nlm.nih.gov/compound/Lead_II_-acetate (2019).

256. Lead iodide | PbI2 - PubChem. https://pubchem.ncbi.nlm.nih.gov/compound/24931.

257. Stuckelberger, M. *et al.* Charge Collection in Hybrid Perovskite Solar Cells: Relation to the Nanoscale Elemental Distribution. *IEEE J. Photovoltaics* (2017) doi:10.1109/JPHOTOV.2016.2633801.

258. Sheng, R. *et al.* Methylammonium Lead Bromide Perovskite-Based Solar Cells by Vapor-Assisted Deposition. *J. Phys. Chem. C* **119**, 3545–3549 (2015).

259. Chiang, C.-H. & Wu, C.-G. A Method for the Preparation of Highly Oriented $MAPbI_3$ Crystallites for High-Efficiency Perovskite Solar Cells to Achieve an 86% Fill Factor. *ACS Nano* **12**, 10355–10364 (2018).

260. Wu, N. *et al.* Identifying the Cause of Voltage and Fill Factor Losses in Perovskite Solar Cells by Using Luminescence Measurements. *Energy Technol.* **5**, 1827–1835 (2017).

261. Mastroianni, S. *et al.* Analysing the effect of crystal size and structure in highly efficient $CH_3NH_3PbI_3$ perovskite solar cells by spatially resolved photo- and electroluminescence imaging. *Nanoscale* **7**, 19653–19662 (2015).

262. El-Hajje, G. *et al.* Quantification of spatial inhomogeneity in perovskite solar cells by hyperspectral luminescence imaging. *Energy Environ. Sci.* **9**, 2286–2294 (2016).

263. Aristidou, N. *et al.* The Role of Oxygen in the Degradation of Methylammonium Lead Trihalide Perovskite Photoactive Layers. *Angew. Chemie - Int. Ed.* **54**, 8208–8212 (2015).

264. Saliba, M., Stolterfoht, M., Wolff, C. M., Neher, D. & Abate, A. Measuring Aging Stability of Perovskite Solar Cells. *Joule* **2**, 1019–1024 (2018).

265. Tan, H. *et al.* Efficient and stable solution-processed planar perovskite solar cells via contact passivation. *Science (80-.).* **355**, 722–726 (2017).

266. Alharbi, E. A. *et al.* Perovskite Solar Cells Yielding Reproducible Photovoltage of 1.20 V. *Research* **2019**, 1–9 (2019).

267. Li, N. *et al.* Cation and anion immobilization through chemical bonding enhancement with fluorides for stable halide perovskite solar cells. *Nat. Energy* **4**, 408–415 (2019).

9 APPENDIX

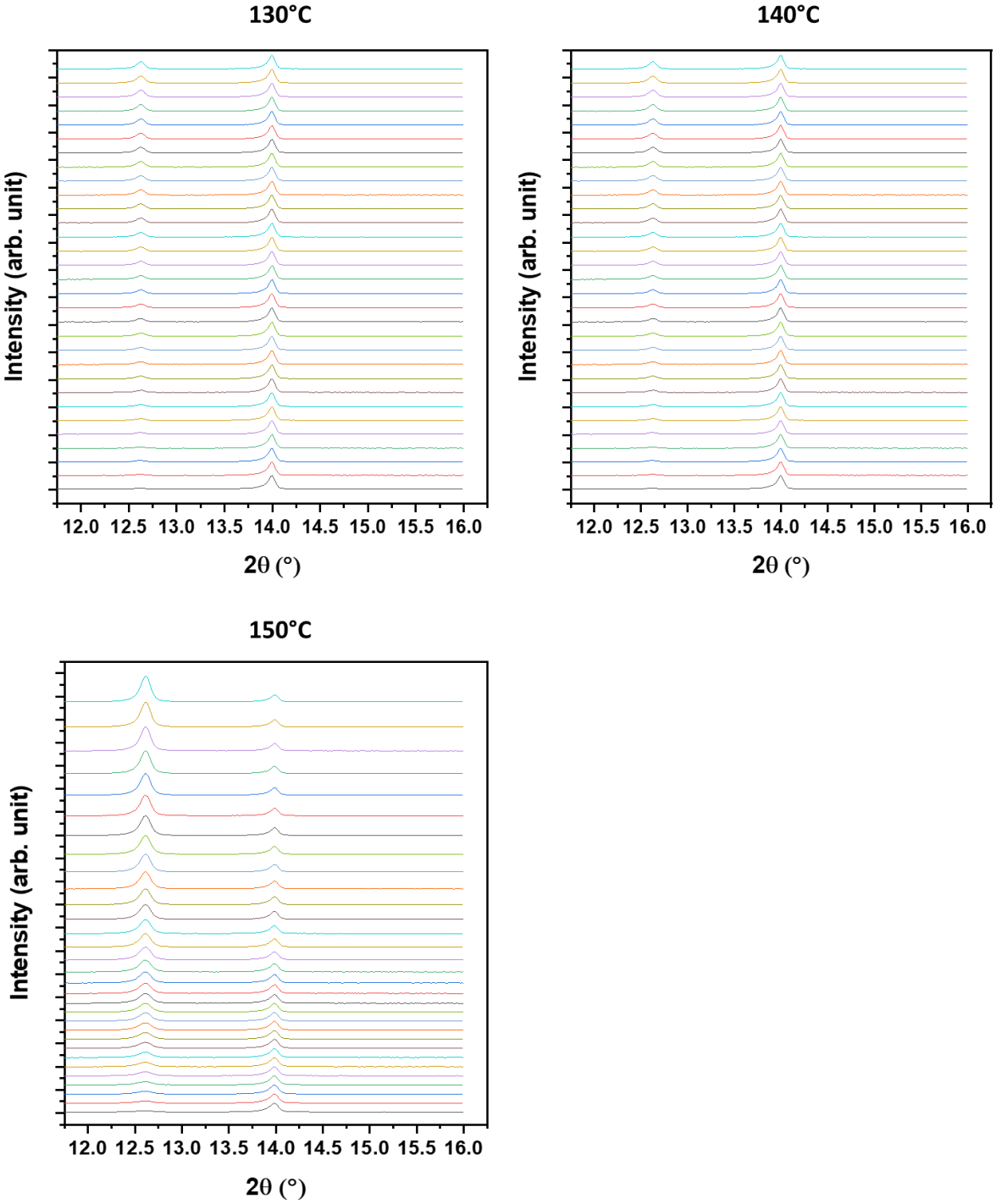


Figure 9-1 spin-coated MAPI Isothermal XRD patterns taken from AACVD sample over 93 minutes

1000 µs pulse time

Applied Bias (V)	t_e (s)	t_h (s)	μ_e ($cm^2 (V s)^{-1}$)	μ_h ($cm^2 (V s)^{-1}$)
2	2.30E-07	2.20E-07	1.50E+00	1.57E+00
4	2.30E-07	2.50E-07	5.91E-01	5.44E-01
6	2.90E-07	2.20E-07	2.92E-01	3.85E-01
8	2.90E-07	2.27E-07	2.12E-01	2.71E-01
10	2.90E-07	2.35E-07	1.66E-01	2.05E-01

400 µs pulse time

Applied Bias (V)	t_e (s)	t_h (s)	μ_e ($cm^2 (V s)^{-1}$)	μ_h ($cm^2 (V s)^{-1}$)
2	3.30E-07	1.76E-07	1.05E+00	1.96E+00
4	3.00E-07	1.03E-07	4.53E-01	1.32E+00
6	4.20E-07	1.44E-07	2.02E-01	5.88E-01
8	3.80E-07	1.73E-07	1.62E-01	3.55E-01
10	4.17E-07	1.50E-07	1.16E-01	3.22E-01

140 µs pulse time

Applied Bias (V)	t_e (s)	t_h (s)	μ_e ($cm^2 (V s)^{-1}$)	μ_h ($cm^2 (V s)^{-1}$)
2	2.40E-07	2.07E-07	1.44E+00	1.67E+00
4	2.80E-07	2.16E-07	4.86E-01	6.30E-01
6	3.54E-07	2.26E-07	2.39E-01	3.75E-01
8	3.70E-07	2.34E-07	1.66E-01	2.63E-01
10	3.50E-07	2.36E-07	1.38E-01	2.05E-01

80 µs pulse time

Applied Bias (V)	t_e (s)	t_h (s)	μ_e ($cm^2 (V s)^{-1}$)	μ_h ($cm^2 (V s)^{-1}$)
2	2.30E-07	1.60E-07	1.50E+00	2.16E+00
4	2.30E-07	1.44E-07	5.91E-01	9.48E-01
6	2.20E-07	1.42E-07	3.85E-01	5.95E-01
8	1.55E-07	1.58E-07	3.97E-01	3.89E-01
10	1.46E-07	1.50E-07	3.31E-01	3.22E-01

50 µs pulse time

Applied Bias (V)	t_e (s)	t_h (s)	μ_e ($cm^2 (V s)^{-1}$)	μ_h ($cm^2 (V s)^{-1}$)
2	8.80E-07	1.40E-07	3.92E-01	2.47E+00
4	6.68E-07	1.34E-07	2.04E-01	1.02E+00
6	4.90E-07	1.12E+00	1.73E-01	7.56E-08
8	2.82E-07	9.50E-01	2.18E-01	6.47E-08
10	1.81E-07	1.10E+00	2.67E-01	4.39E-08

Figure 9-2 ToF table of results, showing arrival times and calculated mobilities of AACVD MAPI film. The film thickness was 6.72 ± 0.76 µm

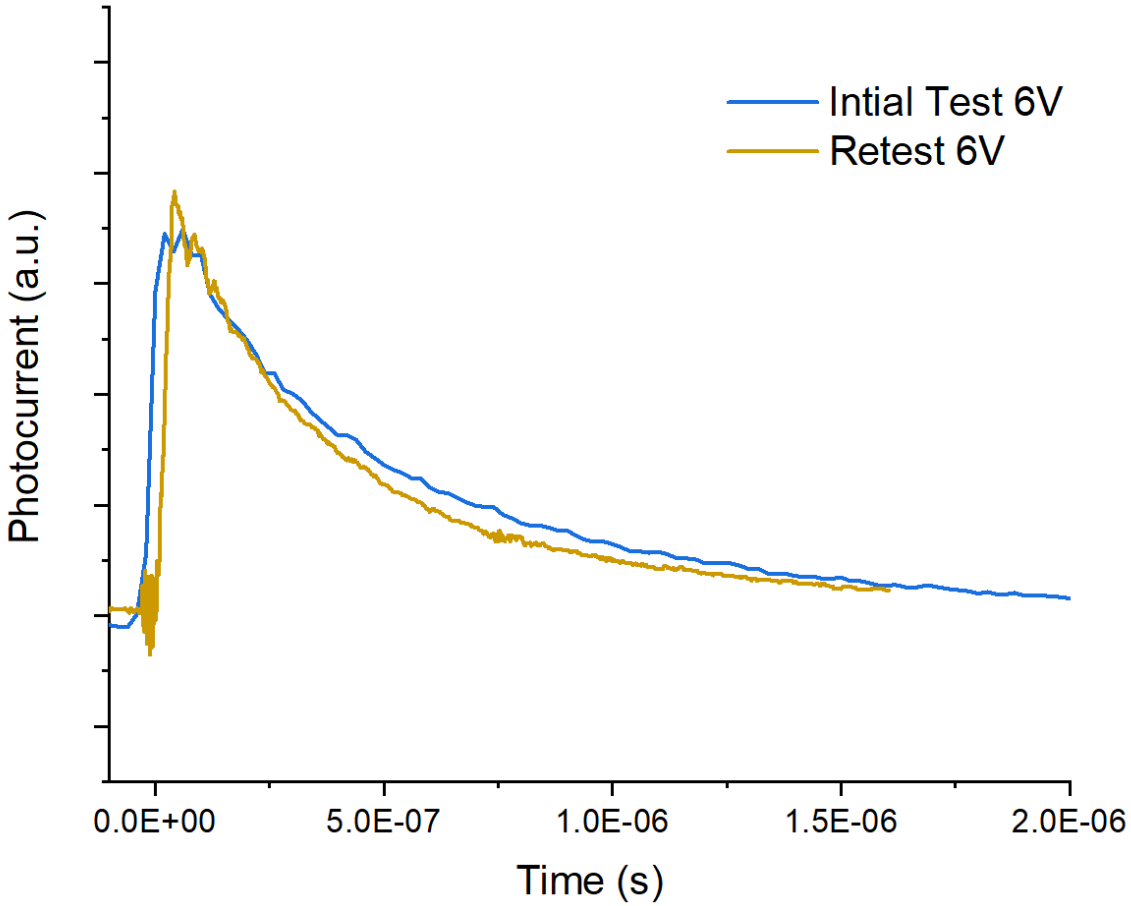


Figure 9-3 ToF signal before and after pulsing experiments. This shows that the sample did not degrade after the application of a pulsed bias.

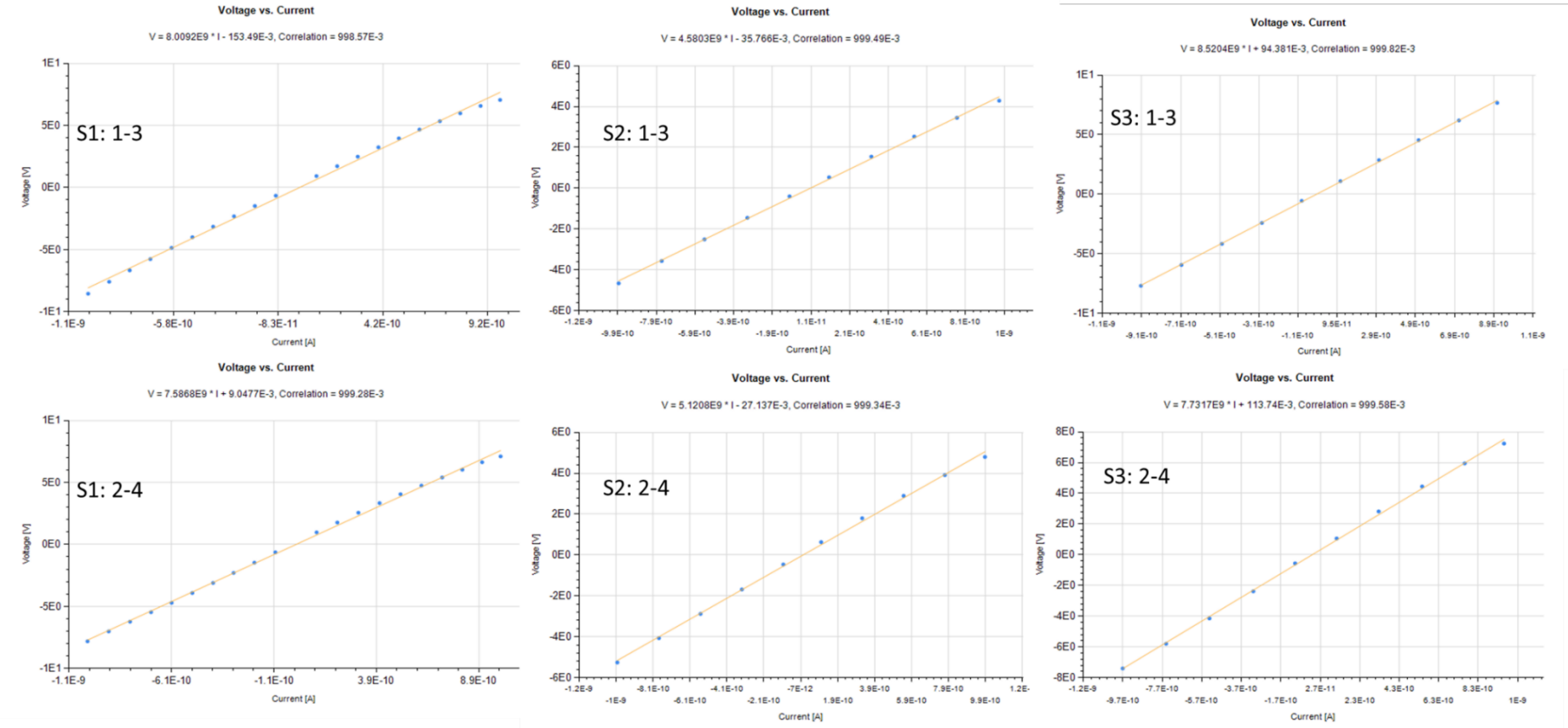


Figure 9-4 Ohmic check results conducted for Hall measurements.

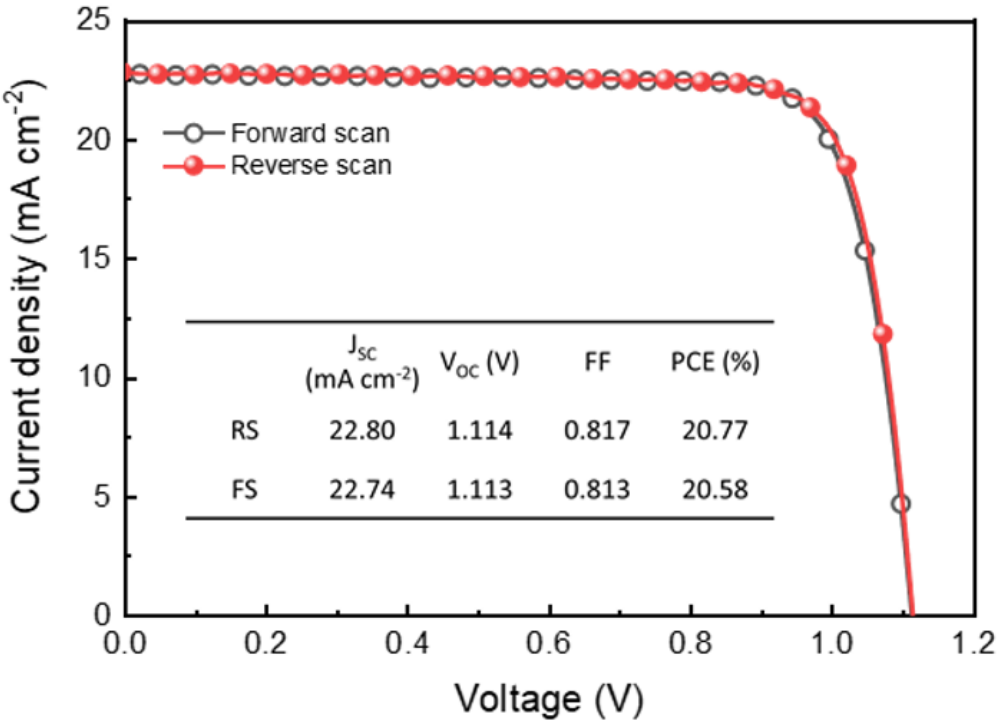


Figure 9-5 Example of neglibile hysteresis within p-i-n cell used in AASA experiments.

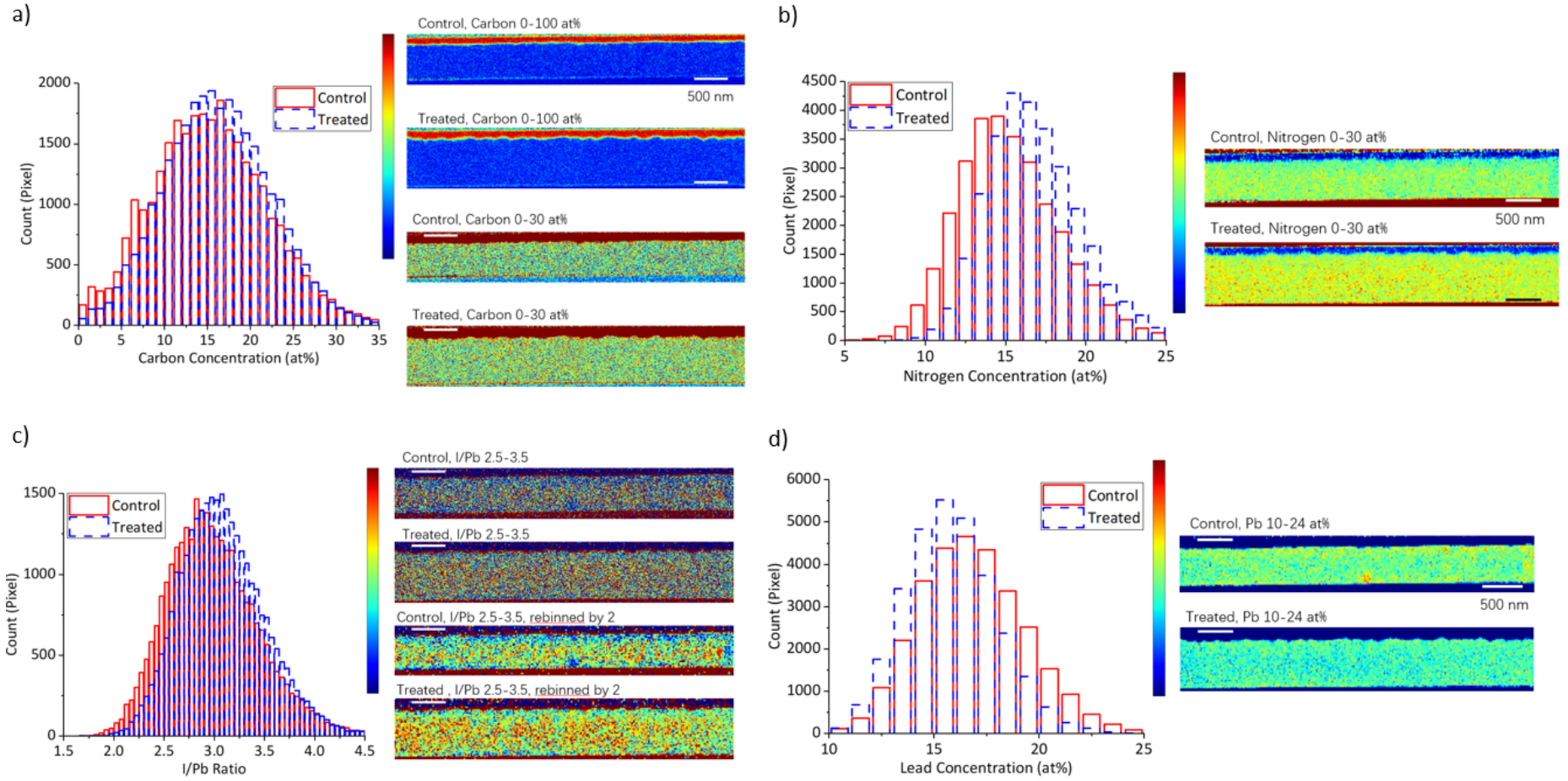


Figure 9-6 Energy dispersive x-ray spectroscopy (EDS) mapping of the destruction of a) C at%, b) N at% c) I/Pb Ratio d) Pb at%.

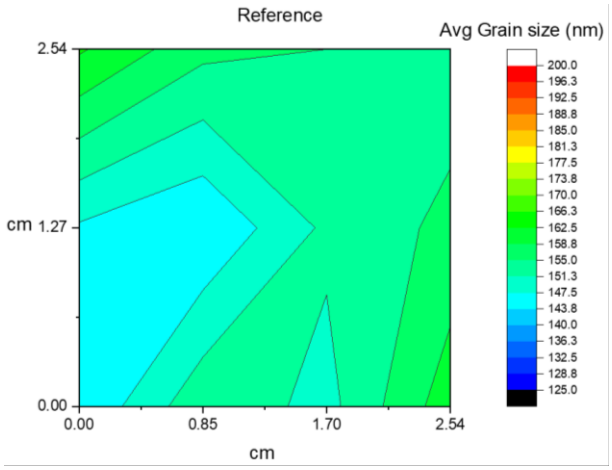


Figure 9-7 Grain size distribution of untreated MAPI spin coated on glass

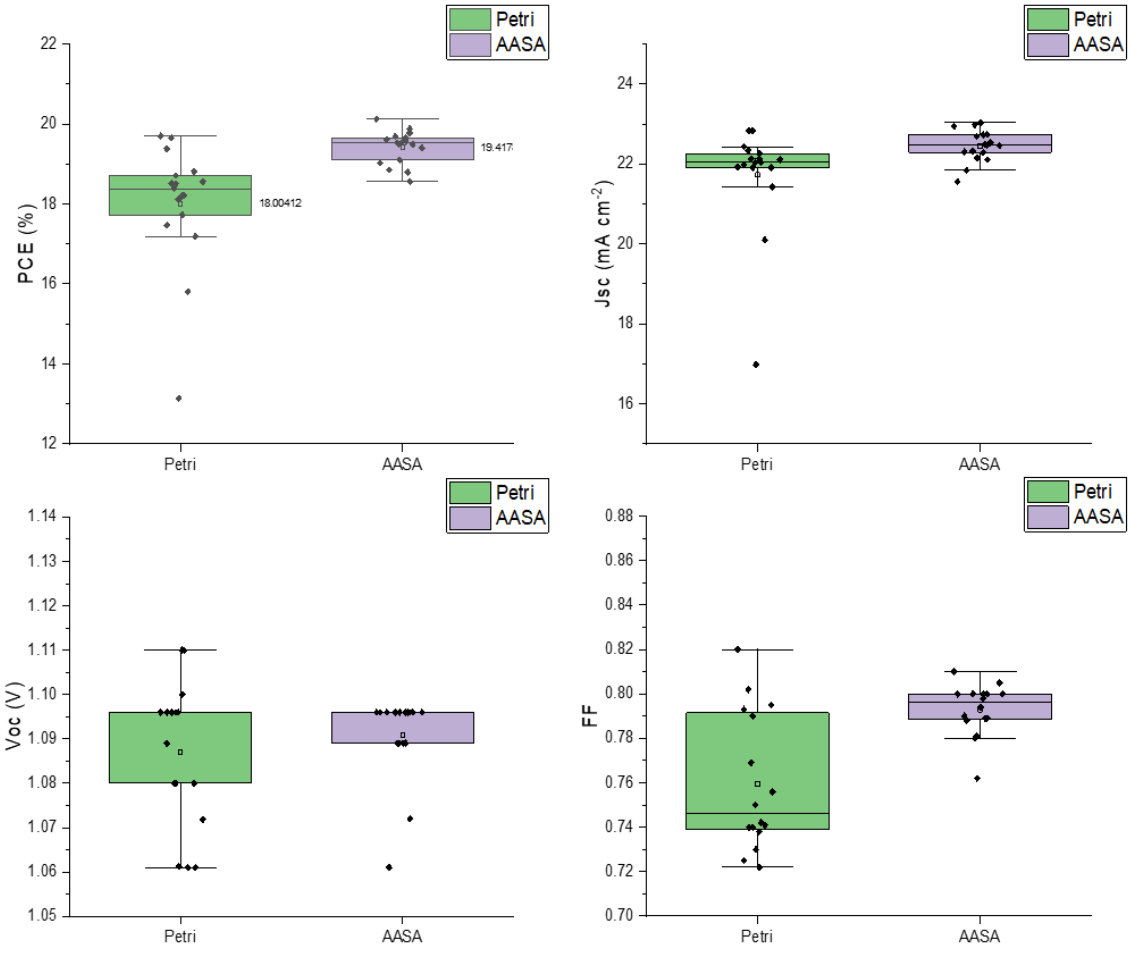


Figure 9-8 Box-plots of cell parameters of AASA and Petri-dish solvent annealed devices

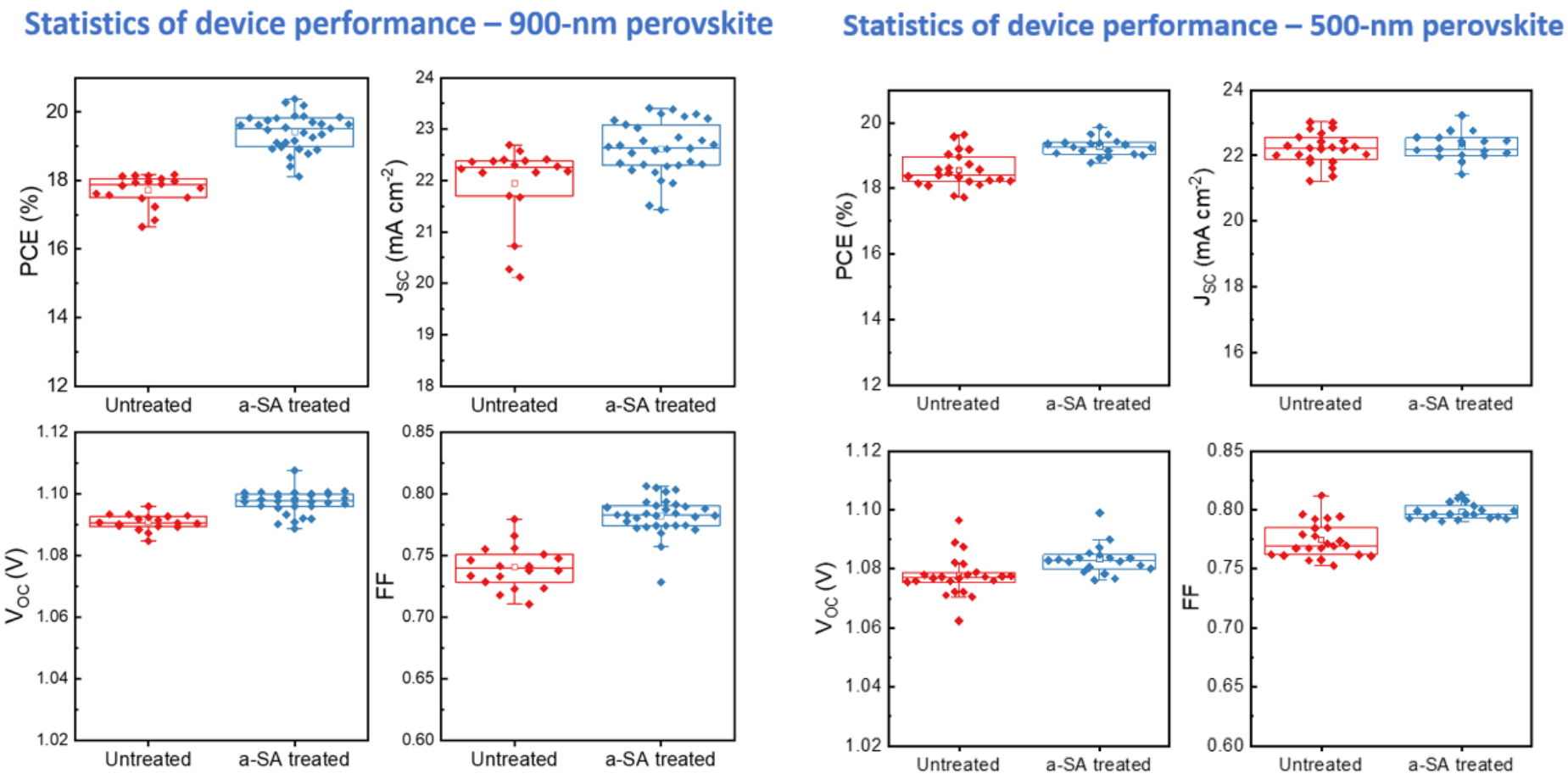


Figure 9-9 Box-plots showing the distribution of cell parameters for AASA treated and untreated thick MAPI devices